universität
wien

MASTERARBEIT / MASTER'S THESIS

Titel der Masterarbeit / Title of the Master's Thesis

"Search for signatures of s-process elements in cool stars in the near infrared (NIR)"

verfasst von / submitted by

Dr. Manfred Zendel

angestrebter akademischer Grad / in partial fulfilment of the requirements for the degree of

Master of Science / (MSc)

Wien, 2021/ Vienna 2021

Studienkennzahl lt. Studienblatt / degree programme code as it appears on the student record sheet:	UA 066 861
Studienrichtung lt. Studienblatt / degree programme as it appears on the student record sheet:	Masterstudium Astronomie UG 2002
Betreut von / Supervisor:	Dozent Dr. Thomas Lebzelter

Abstract

Signatures of high resolution NIR-spectra can provide specific identification of elements and molecules to determine the composition of elements at the surface of the observed star. A high resolution near infrared (NIR) absorption spectrum of the K-star 10 Leonis, processed and published by the CRIRES-POP project, is used for the analysis. The published spectrum includes wavelength calibration, various corrections for velocity and instrumental properties as well as the removal of telluric lines. It supplies the wavenumber and the corresponding normalized flux. The NIR spectrum covers a wavelength range from 962 nm to 5225 nm, which is divided into YJ, H, K, L and M bands.

The focus of this work is on the identification of unknown absorption lines in the different segments of this NIR spectrum which could originate from elements more massive than Fe, which are formed by neutron capture.

In addition to a large number of metal lines, which mainly originate from Fe I, Si I, Mn I, Cr I, Ni I and Ti I, absorption lines from molecules such as CO, CN and OH dominate the spectrum. The complexity and large number of observed absorption lines require a differentiated search for signatures in order to enable an unambigous assignment to a certain element/molecule. Unfortunately, the published line lists of many metals lack the necessary completeness and accuracy of the line parameters, some of which are determined by model calculations only. This work identifies major inconsistencies and finds hints that the majority of the unknown lines are attributable to Fe and elements less massive than Fe.

The analysis of the spectra and data management is mainly performed by standard Excel spreadsheet applications that are tailored to the specific task. Small, self-developed Python programs facilitate the analysis and graphical presentation of the data.

Most of the molecular absorption lines could be identified and attributed to their respective rotational-vibrational bands. Bandheads and wavelengths of the individual line transitions are calculated using polynomial fits and matched with the observed spectrum. In addition, the NIR-spectrum of the K-star Arcturus is used to support line identification. Equivalent widths are determined in order to compare the strength of lines and to estimate limit values for the detection of different elements.

A large number of synthetic spectra, generated with atmospheric models and parameters for the Sun, 10 Leonis and Arcturus, are compared with the observed spectra of 10 Leonis and Arcturus. Differences in element abundance and isotope abundance of ^{12}CO, ^{13}CO, $C^{17}O$ and $C^{18}O$ between 10 Leonis and Arcturus are observed.

Extended data analysis for the molecule CO provide a range of specific parameter such as rotational constants, distortion constants and coupling constants.

Zusammenfassung

Signaturen von hochaufgelösten NIR-Spektren können eine spezifische Identifizierung von Elementen und Molekülen ermöglichen, um die Zusammensetzung der Elemente an der Oberfläche des beobachteten Sterns zu bestimmen. Ein hochaufgelöstes Nahinfrarot (NIR)-Absorptionsspektrum des K-Sterns 10 Leonis, aufbereitet und veröffentlicht durch das CRIRES-POP-Projekt, wird benutzt zur Analyse. Das publizierte Spektrum umfasst Wellenlängenkalibrierung, verschiedene Korrekturen für Geschwindigkeit und instrumentelle Eigenschaften sowie die Entfernung von atmosphärischen Absorptionslinien. Es liefert die Wellenzahl und den entsprechenden normierten Fluss. Das NIR-Spektrum deckt einen Wellenlängenbereich von 962 nm bis 5225 nm ab, der in YJ-, H-, K-, L- und M-Band unterteilt ist.

Der Fokus dieser Arbeit liegt auf der Identifizierung unbekannter Absorptionslinien in den verschiedenen Segmenten dieses aufbereiteten NIR-Spektrums, die von Elementen schwerer als Fe stammen könnten, welche durch Neutroneneinfang gebildet werden können.

Neben einer Vielzahl von Metalllinien, die hauptsächlich von Fe I, Si I, Mn I, Cr I, Ni I und Ti I stammen, dominieren Absorptionslinien von Molekülen wie CO, CN und OH das Spektrum. Die Komplexität und Vielzahl der beobachteten Absorptionslinien erfordert eine differenzierte Suche nach Signaturen, um eine eindeutige Zuordnung zu einem bestimmten Element/Molekül zu ermöglichen. Leider mangelt es in den publizierten Linienlisten vieler Metalle an Vollständigkeit und Genauigkeit der spektralen Parameter, die teilweise modellabhängig ermittelt sind. Diese Arbeit identifiziert größere Widersprüche und findet Hinweise, dass die Mehrheit der unbekannten Linien Fe und den Elementen leichter als Fe zugeschrieben werden kann.

Die Analyse der Spektren und die Handhabung der Daten erfolgen hauptsächlich durch Anwendung von Standard-Excel-Tabellenkalkulationen, die auf die jeweilige Aufgabe zugeschnitten sind. Kleine, selbst entwickelte Python-Programme erleichtern die Analyse und graphische Darstellung der Daten.

Die meisten molekularen Absorptionslinien können identifiziert und ihren jeweiligen Rotation-Vibrationsbanden zugeordnet werden. Bandenköpfe und Wellenlängen der einzelnen Linienübergänge werden durch Polynome berechnet und mit dem beobachteten Spektrum verglichen. Darüber hinaus wird das NIR-Spektrum des K-Sterns Arktur zur Unterstützung der Linienidentifikation verwendet. Äquivalentbreiten werden bestimmt, um die Stärke von Linien zu vergleichen und Grenzwerte für den Nachweis verschiedener Elemente abzuschätzen.

Eine Vielzahl von synthetischen Spektren, erzeugt mit atmosphärischen Modellen und Parametern für Sonne, 10 Leonis und Arktur, werden mit den beobachteten Spektren von 10 Leonis und Arktur verglichen. Unterschiede in Elementhäufigkeit und Isotopenhäufigkeit von ^{12}CO, ^{13}CO, C^{17}O und C^{18}O zwischen 10 Leonis und Arktur werden beobachtet.

Die erweiterte Datenanalyse für das Molekül CO liefert eine Reihe spezifischer Parameter wie Rotationskonstanten, Verzerrungskonstanten und Kopplungskonstanten.

Contents

List of Figures

List of Tables

1 Introduction and Motivation

Spectroscopy is subdivided according to the mechanism of energy absorption/emission and related energy range. Near-infrared spectroscopy works in the region from about 1000 nm to 5000 nm of the electromagnetic spectrum. By excitation energy, it mainly studies how molecules absorb infrared radiation which causes molecules to vibrate and rotate and ultimately convert it to heat. In chemistry, IR-spectroscopy is the most commonly used spectroscopic method and is widely used as a standard analysis tool to determine chemical structure and quantify chemical compounds. The infrared region can be subdivided into far-IR (FIR), mid-IR region (MIR) and near IR (NIR).
The main spectral features in the NIR region stem from molecular absorption bands with closely spaced lines. They are caused by low energy transitions within rotational and vibrational excitation states of molecules. Electronic states of atoms and ions are also excited within the IR region of the electronic spectrum and their quantum specific absorption of the photons from the flux is a fingerprint that can be used to identify the respective atom/ion. In the case of a star, the resulting spectra are a complex mixture of absorption and emission lines of molecules and atoms on a continuous background spectrum. In most cases lines are blended with various contributing species. **High** resolution NIR spectroscopy is needed to resolve spectral lines in such an environment to enable the unique identification of transitions and the assignment to a specific element/molecule.
With recent advances in technology, high resolution NIR spectroscopy has become available and has gained the attention of astronomers. Stars generate a continous flux of photons over a large spectral range as a result of their energy production. The photons travel to the surface of the star passing through the stellar atmosphere, which is forming the outermost layer of the star. Passing through the atmosphere, these photons will interact with layers of atoms/molecules. Photons with the appropriate quantum energy can excite specific energy levels in atoms/molecules and are absorbed from the continuous flux of photons. The interaction depends on the electronic configuration of the atom/molecule and the probability of populating the excited states in the specific atom/molecule. Photons which have been absorbed to excite the atom/molecules are missing from the measurable flux and are visible at distinct energies (wavelengths) as spectral lines. The de-excitation can be observed as emission lines of the specific absorbed energy. However, emission in the direction of the observer is much less as the excited specie emits the absorbed energy isotropically.
The observed radiation escapes from a very thin layer (e.g. 300 km in Sun) = "photosphere". The photosphere, which is the atmosphere's outermost and coolest layer, is normally its only visible part. Light escaping from the surface of the star stems from this region and passes through the higher layers. The absorption lines formed in stellar atmospheres provide a multitude of information, e.g. on temperature, gravity, rotational velocity and chemical composition of a star. However, ground-based spectroscopic observations are limited and disturbed by the strong absorption of radiation by the earth's atmosphere. This absorption of the radiation is not uniform across the wavelength region and there are various windows in the wavelength scale featuring high transmission of IR radiation. Figure 1 shows various bandpasses used for the recording of a high resolution NIR-spectrum. The chemical composition of a star is of major interest as it shows the history of nucleosynthesis by previous generations of stars and identifies the current stage of their life cycle. All elements with atomic number Z >26 (Fe) are the result of three main processes of stellar nucleosynthesis: the *s*- (slow neutron capture), *r*-(rapid neutron capture) and *p*-process (proton process). A detailed discussion of the various processes of nucleosynthesis (see also Burbidge *et al.* (1957); Truran (1984); Käppeler *et al.* (1989); Sneden *et al.* (2008);

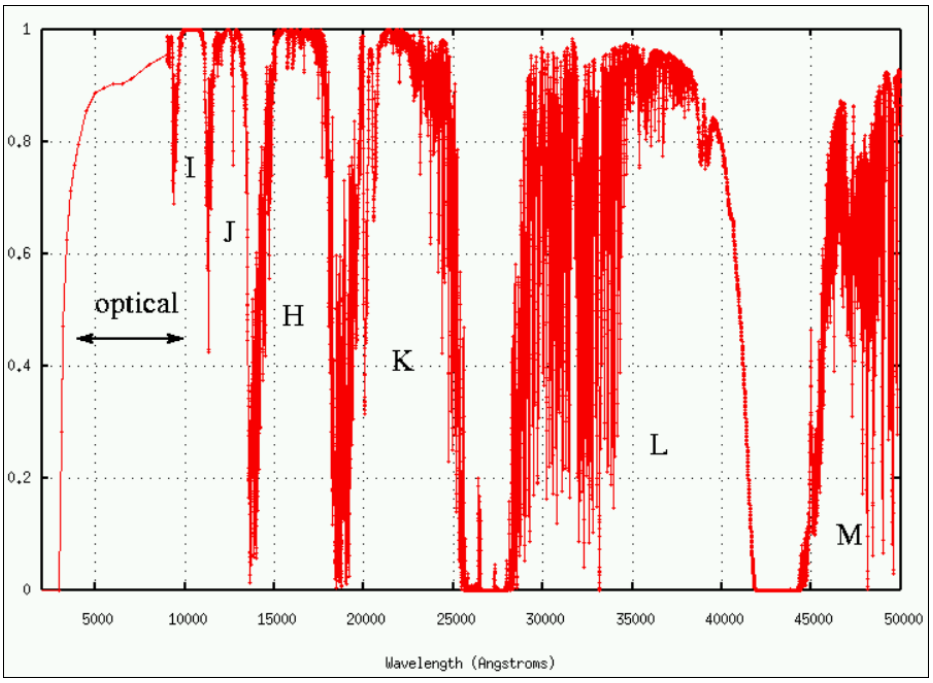

Figure 1: Atmospheric transmission and bandpasses for NIR-detection (picture from http://spiff.rit.edu/classes/phys440/lectures/filters/filters.html)

Karakas & Lattanzio (2014); Arnould & Goriely (2020) for review articles) would go far beyond the scope of this work and therefore is limited to a short description of the s-process.
The *s*-process is a neutron capture process, whereby a nucleus absorbs a neutron and produces an unstable neutron-rich isotope, and the latter then decays by β^--decay (n→proton + electron + antineutrino) forming an isotope with increased atomic number Z by one. Nuclear reactions such as ^{13}C(α, n)^{16}O and ^{22}Ne(α, n)^{25}Mg act as neutron sources. The capture of neutrons occurs on timescales that are long enough to enable unstable nuclei to decay via the emission of a β^--particle before absorbing another neutron. Depending on the nuclear properties, such as cross-section and half-life of the generated unstable isotope, the process repeats and elements up to bismuth (Bi, Z= 83) can be obtained.
Stars below 10 $M_\odot$ become asymptotic giant branch (AGB) stars toward the end of their lives. These stars are the main sites for the production of elements by the *s*-process (Busso *et al.*, 1999). The synthesized elements, which have been transported from the star's inner region to its surface by convection, are then ejected into the interstellar medium (ISM) by intensive stellar winds during the final stages of the star's life cycle. These elements, together with hydrogen and helium gases, are the ingredients to form the next generation of stars. The investigation of young stars and atmospheres of exoplanets by NIR spectroscopy is widely applied e.g. Aronson & Waldén (2015);Benatti (2018); Shulyak *et al.* (2019).

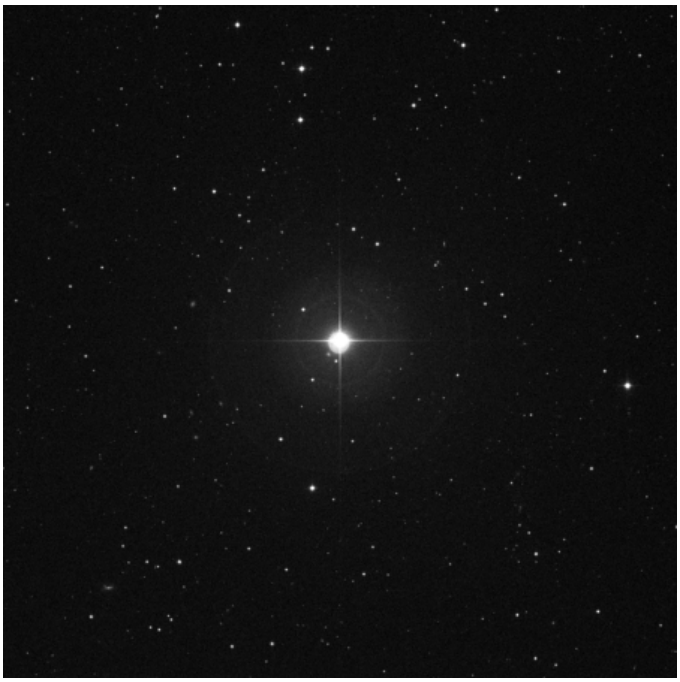

Figure 2: The star 10 Leo (picture from https://in-the-sky.org/data/object.php?id=TYC241-2399-1)

This work studies the high resolution NIR spectrum of 10 Leo (HD 83240) which is a typical representative of a cool giant with T_{eff} ≈4800 K. This star is amongst a representive set of stars that have been selected by the CRIRES (**CR**yogenic high resolution **I**nfrared**R**ed **E**chelle **S**pectrograph)-POP project (Lebzelter *et al.* (2012)) in an effort to establish a library of high resolution spectra for the NIR. The selected set of stars represents various spectral types and luminosity classes across the Hertzsprung-Russell diagram (HRD).

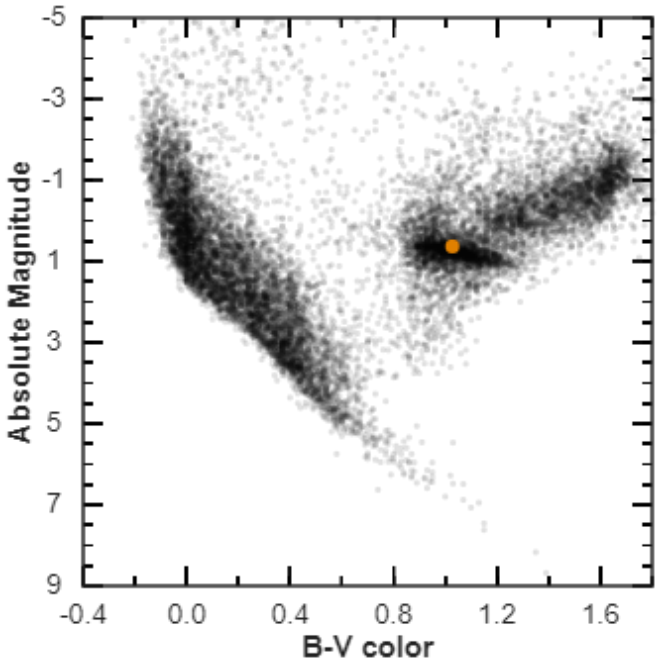

Figure 3: HR diagram of 10 Leo marked as an orange dot. (Taken from https://in-the-sky.org/data/object.php?id=TYC241-2399-1)

Table 1: Properties of 10 Leonis and Arcturus

Property	Leo 10	Reference	Arcturus	Reference.
SpT	K1 IIIVAR	1	K0 III	7
T_{eff}	4801±89 K	2	4286±30 K	8
L	59.35 $L_{\odot}$	2	170 ±8 $L_{\odot}$	9
R	14 $R_{\odot}$	2	25.4 ±0.2 $R_{\odot}$	8
M	2	3	1.08 ±0.06 $M_{\odot}$	8
log g	2.83 ±0.23	2	1.66 ±0.05	8
Distance	77.3 ±1.5 pc	4	11.26 ±0.07 pc	10
Age	4.51 ±1.8 Gyr	5	$7.1^{+1.5}_{-1.3}$ Gyr	8
$[Fe/H]$	-0.03 ±0.08	2	-0.52 ±0.04	8
v_{mic}	1.3 km s^{-1}	6	1.2 ±0.11 km s^{-1}	11

References:(1) Roman, 1952; (2) da Silva *et al.*, 2011; (3) Mishenina *et al.*, 2006; (4) Bailer-Jones *et al.*, 2021; (5) Soubiran *et al.*, 2008; (6) Tan *et al.*, 2016; (7) Gray *et al.*, 2003; (8) Ramírez & Allende Prieto, 2011; (9) Schröder & Cuntz, M., 2007; (10) van Leeuwen, 2007(11) Kondo *et al.*, 2019

The position of 10 Leo (red dot) within the HRD is given in Fig. 3. Table 1 lists selected properties of 10 Leo and Arcturus, which is another well studied cool star and used in this work for comparison.

The CRIRESPOP NIR-spectrum of 10 Leo, which is available from various open sources[1,2], provides high resolution in the order of R=100000 which enables the visible deconvolution of molecular bands, resolution of fine structures and the identification of possible line blends. The interpretation of the spectrum requires a solid knowledge of line wavelength, intensities and physical status of the contributing species. Laboratory - and computationally - produced atomic and molecular line lists, model stellar atmospheres and synthetic spectra are important tools in this endeavour. In practice, many gaps, uncertainties and discrepancies exist in the published data. It is important to improve the quality of data by identifying shortcomings and discrepancies in the existing data while searching for new signatures. The improvement of the evaluated results of observational data and predicted data, e.g. synthetic spectra, is an iterative process, which will hopefully enhance the present tool set.

The main emphasis of this work is on the **pratical** line identification within the high resolution NIR spectrum of the K-star 10 Leo (HD 83240: Figure 2) with the goal to find signatures of neutron capture process elements in cool stars in the NIR. Therefore, the work is focussed on the observed data whereas the derivation of radiation transport phenomena, description of detection systems and data reduction processes are not elaborated in detail. Instead, short summaries of the parameters that influence the main spectral features are described in a general and qualitative manner using free accessible on-line material[3].

[1] https://vizier.u-strasbg.fr/viz-bin/VizieR?-source=J/A%2BA/598/A79

[2] https://www.univie.ac.at/crirespop/data.htm

[3] e.g. https://phys.libretexts.org/Bookshelves/Astronomy__Cosmology/Book%3A_Stellar_Atmospheres_(Tatum)

2 Data Sources and Evaluation Tools

2.1 Data sources

High resolution, pipeline-corrected spectra (1μm-5μm) of 10 Leo are easily available via the CRIRES-POP project homepage[4] (Nicholls *et al.*, 2017). The NIR spectrum for 10 Leo shows the fraction of absorbed flux of photons as a function of wavelength between 1000 nm and 5000 nm. Observations have been obtained with the CRIRES high-resolution infrared echelle spectrograph (Kaeufl *et al.*, 2004) installed at the ESO-VLT (Very Large Telescope) at an altitude of 2648 m above sea level. The spectra are corrected for telluric lines, detector properties, velocities and provide wavelength-calibrated and normalized flux values for the YJ, H, K, L, M-bandpasses. The properties of the 10 Leo spectra are summarized in Table 2 (Nicholls *et al.*, 2017).

Table 2: Properties of 10 Leo NIR spectra

Property	Value
Data format	five ASCII files; YJ, H, K, L, M bandpass
Wavelength coverage & scale	962-5245 nm, vacuum
Observing time	$\approx$ 15 h
Observation period	2009 Dec-2010 Jan
Average precipitable water vapour	2-4 mm
Continuum	normalized
Echelle order	$\approx \lambda/70$
Slit width	0.2 arcsec
Number of detector chips	4
Instrument pixels scale	0.086 arcsec/pixel
Constant resolving power	90000
Two pixel Resolution	0.22 Å at 2000 nm
mean S/N	241 (M-bandpass)-330 (YJ-bandpass)
Wavelength calibration	<2500 nm ThAr,>2500 sky lines
Amplitude of radial velocity	12.66 km/s
Applied software	
Data reduction	ESO CRIRES pipeline version 2.3.2
Removal of telluric lines	Molecfit 1.0.2
Heliocentric corrections	ESO hourly airmass webtool

The data processing of the observational data is well described in detail (Nicholls *et al.*, 2017), including the discussion of the various correction steps, and is not further elaborated in this work.

Files for modelling stellar atmospheres have been requested from the Vienna Atomic Line Database (VALD3) (Ryabchikova *et al.*, 2015). Table 3 lists a set of respective parameters in accordance with Table 1 for a typical request. Data are then quickly available as a download link from VALD3. The files are converted to Excelfiles after the download. It has to be noted that the generated models use oscillator strengths scaled by solar isotopic ratios. The Arcturus IR spectra and line lists[5] (Hinkle *et al.*, 1995) were downloaded and individual Arcturus files were

[4] https://www.univie.ac.at/crirespop/data.htm
[5] ftp://ftp.noao.edu/catalogs/arcturusatlas

Table 3: Typical parameter for VALD3 request

wavelength interval (vacuum) Å	micro-turbulence km/sec	Teff K	log *g*	generated model
9600-50000	2	4801	2.83	castelli_ap00k2_T04750G30.krz
9600-50000	2	4301	1.67	castelli_ap00k2_T04250G15.krz

combined to match the bandpasses of 10 Leo. For comparison, the ratioed Arcturus spectrum after smoothing and continuum adjustment is used. The Arcturus line lists include transition data for atoms and molecules. Further data regarding the molecules CN, OH and CO were extracted from the Hitran Database (Gordon *et al.*, 2017) and from Brooke *et al.* (2014).
Table 4 shows the wavelength coverage of the studied spectra and the number of data points. Each bandpass features a distinct signature of atomic and molecular absorption lines.

Table 4: Wavelength coverage of 10 Leo and Arcturus spectra

Band	**wavelength range (nm)**		**number of records**	
	10 Leo	Arcturus	10 Leo	Arcturus
YJ	963 - 1344	912 - 1354	53095	96420
H	1412 - 1890	1497 - 1827	38100	60250
K	1950 - 2501	1958 - 2955	39645	56495
L	3366 - 4169	3367- 3639	36395	57115
M	4548 - 5228	4566 - 5221	19350	25600

The **YJ-band** comprises many molecular lines from CN (fundamental $\Delta v = 0,1$) and a rich variety of strong metal lines especially from Fe I, Mg I, Si I, Ti I, including some Sr II lines. There have been no CO-lines detected.
The **H-band** region features also many strong metal lines from Al I, Cr I, Fe I, Mg I, Mn I, Ni I, Si I and Ti I. It includes molecular bands from CN (fundamental Δv = -1, medium strong), CO (second overtone $\Delta v = 3$, weak) and OH (first overtone $\Delta v = 2$, weak).
The **K-band** is dominated again by strong metal lines (e.g. Al I, Fe I, Mg I, Na I, S I, Sc I, Si I and Ti I). In addition, CO molecular lines (first overtone $\Delta v = 2$, strong) and molecular lines from CN (first overtone Δv = -2, weak) are numerously present.
The **L-band** has no CO and CN molecular lines but has a number of weak SiO, CH and strong OH lines (fundamental $\Delta v = 1$) along with some metal lines from Al I, Ca I, Fe I, K I, Mg I, Na I, Ni I and Si I.
The **M-band** is dictated by molecular lines from CO (fundamental bands $\Delta v = 1$, very strong) and a few lines from Al I, Ca I, Fe I, Si I and Mg I.
The variety of lines in the 10 Leo spectrum is documented in Table 5. The table has been compiled from a VALD3 stellar request with the parameter set from Table 3 and gives an impression of the large number of lines across the observed wavelength region. About 1300 additional lines have been observed and classified as "unknowns", representing $\approx$ 5% of all lines observed in the 10 Leo spectrum. This high number includes lines which are not identified in VALD3, very small contributions within 3-sigma above the background and artifacts, which may have resulted from the various data reduction steps. The compilation and reduction of the number of unlisted lines is a major goal of this work.

Table 5: Distribution of absorption-lines from VALD3 stellar extraction

Element/	# of lines (≥0.005 central depth)					
molecule	YJ	H	K	L	M	Sum
Al1	21	26	21	18	9	95
Ba1	1	1	0	0	0	2
C1	36	131	22	30	1	220
Ca1	105	75	87	34	27	328
Ca2	6	4	5	2	0	17
Ce2	7	1	0	0	0	8
CH	0	0	0	314	69	383
CN	2261	1874	1244	0	0	5379
CO	0	918	1500	0	3494	5912
Co1	27	27	6	0	0	60
Cr1	102	67	39	11	8	227
Cu1	0	12	0	4	0	16
Dy2	2	0	0	0	0	2
Er2	1	0	0	0	0	1
Eu2	2	0	0	0	0	2
Fe1	973	2276	907	733	96	4985
Fe2	6	18	2	0	0	26
Ga1	2	0	0	0	0	2
Ge1	3	2	0	0	0	5
H1	3	10	2	2	3	20
HF	0	0	0	0	0	0
K1	10	9	2	9	0	30
La2	1	0	0	0	0	1
Lu1	0	0	1	0	0	1
Mg1	55	185	131	161	65	597
Mg2	2	3	3	0	0	8
Mn1	22	66	35	29	3	155
N	0	0	0	0	0	0
Na1	30	12	22	18	13	95
Ni1	102	276	93	63	6	540
NH	0	0	0	4	0	4
O1	0	10	0	0	0	10
OH	0	306	63	182	36	587
P1	10	17	0	0	0	27
Rb1	0	0	0	0	0	0
S1	27	55	51	12	0	145
Sc1	3	1	18	0	0	22
Sc2	0	0	2	0	0	2
Si1	217	257	254	186	79	993
SiO	0	0	0	0	0	0
Sm2	0	0	0	0	0	0
Sr2	3	0	0	0	0	3

Continued on next page

Table 5 – *Continued from previous page*

Element/ molecule	# of lines (>0.005 central depth) YJ	H	K	L	M	Sum
Ti1	200	176	70	15	8	469
Ti2	7	9	0	0	0	16
V1	27	34	20	0	0	81
V2	0	0	0	0	0	0
Y1	0	9	9	0	0	18
Y2	4	0	0	0	0	4
Yb1	0	0	1	0	0	1
Yb2	0	1	0	0	0	1
Zn1	4	0	2	0	0	6
Zr1	2	0	0	0	0	2
Sum:	4284	6868	4612	1827	3917	21508

VALD3 stellar request with v_{mic}=2km/s, model castelli_ap00k2_T04750G30.krz

2.2 Evaluation tools

The downloaded data files for the 10 Leo spectrum from Nicholls *et al.* (2017) provide two columns with wavenumber (cm^{-1}) and normalized flux. The data for each bandpass is saved as a separate Excel file. The wavelength (nm) is calculated in a separate column by :

$$\text{wavelength (nm)} = \frac{10^7}{wavenumber(cm^{-1})}$$

A simple, automated calculation of the wavelength difference between two subsequent records provides the pixelsize and unveils a large number of gaps in the spectra (Figure 4), e.g. the YJ bandpass data has 226 gaps with sizes ranging from 0.04 nm to 2.1 nm. The nature of the gaps is mainly due to the opaqueness of the atmosphere (blue color) and the performance of the collector chips. More details regarding the performance of collector chips, ghosts and artefacts and their correction for the 10 Leo spectrum are given in Nicholls *et al.* (2017).

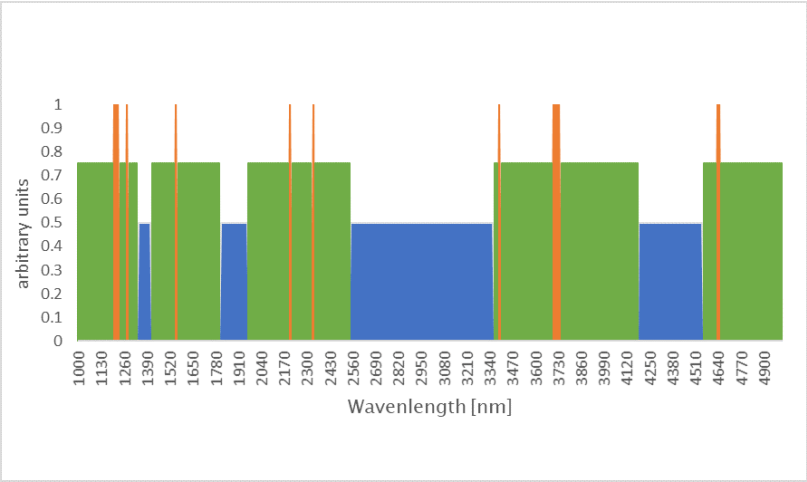

Figure 4: Major gaps (blue and orange) in observed wavelength coverage (arbitrary units for distinction only) for 10 Leo in the range of 1000-5000 nm.

The pixelsize corresponds to the wavelength interval between adjacent records in the original measurement data file. It increases with wavelength in a strict linear correlation from ≈0.0056 nm (at 1000 nm) to ≈0.028 nm (at 5000 nm). Figure 5 shows the correlation for the YJ band.

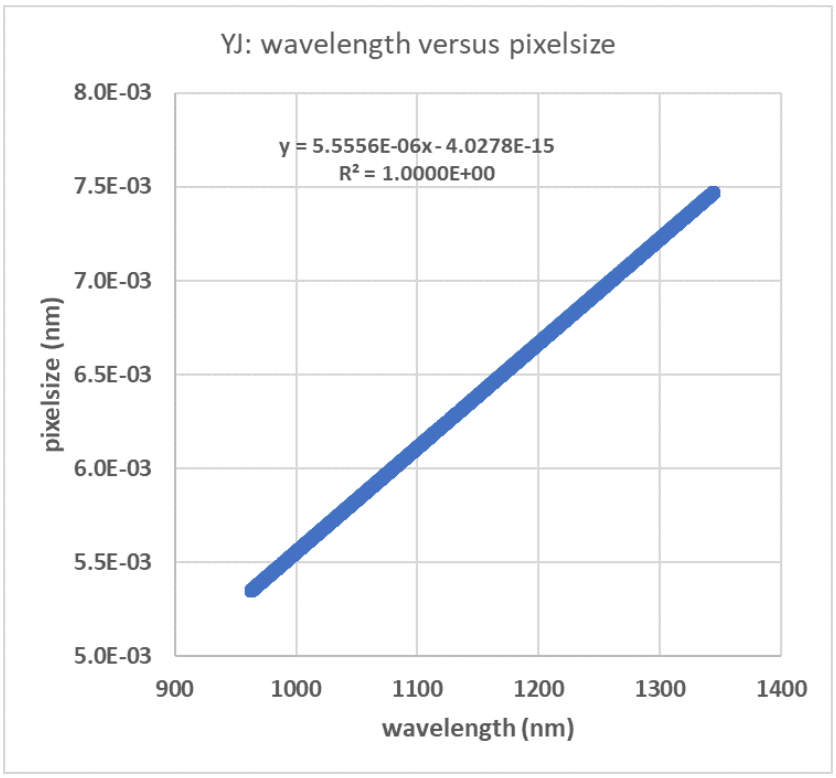

Figure 5: Pixelsize as a function of wavelength in the YJ band

Additional columns have been inserted in the Excel files to accomodate data from the requested VALD3 extracted stellar model (Ryabchikova *et al.*, 2015), the Arcturus lists (Hinkle *et al.*, 1995) and HITRAN (Gordon *et al.*, 2017). Each spreadsheet has a column for gap, wavenumber, wavelength (observed), flux, 1-flux, sum, equivalent width, wavelength (VALD3), identified element/molecule from VALD3 stellar extraction, log *gf*, cdepth, quality and number of line

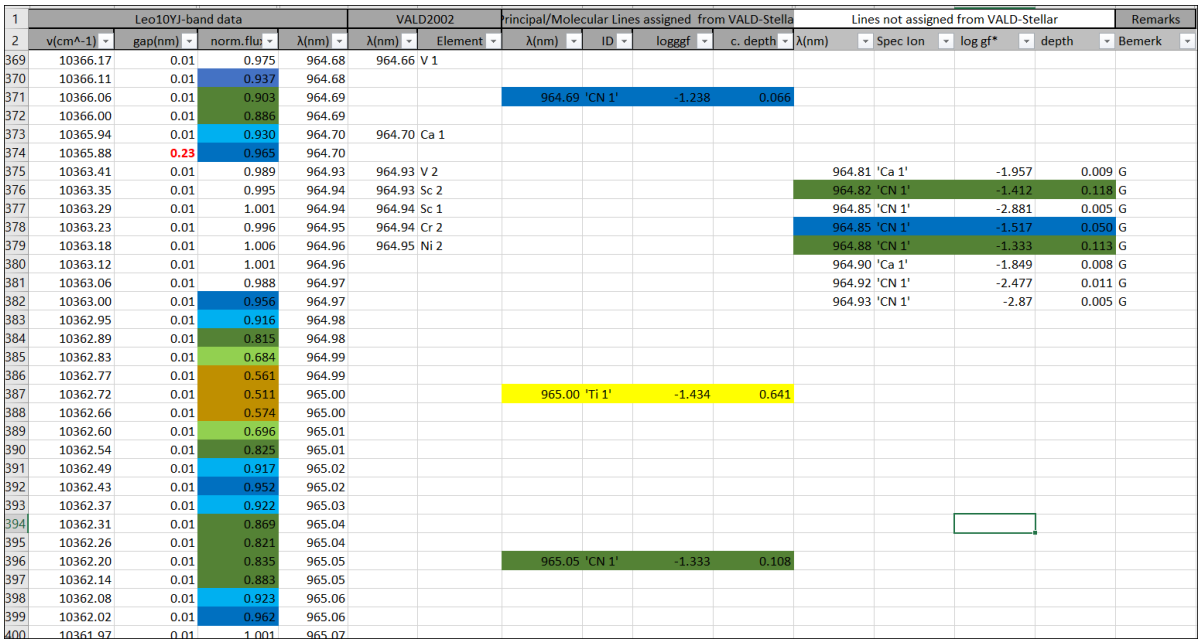

	Leo10YJ-band data				VALD2002		Principal/Molecular Lines assigned from VALD-Stella				Lines not assigned from VALD-Stellar				Remarks
2	ν(cm^-1)	gap(nm)	norm.flux	λ(nm)	λ(nm)	Element	λ(nm)	ID	loggf	c. depth	λ(nm)	Spec Ion	log gf*	depth	Bemerk
369	10366.17	0.01	0.975	964.68	964.66	V 1									
370	10366.11	0.01	0.937	964.68											
371	10366.06	0.01	0.903	964.69			964.69	'CN 1'	-1.238	0.066					
372	10366.00	0.01	0.886	964.69											
373	10365.94	0.01	0.930	964.70	964.70	Ca 1									
374	10365.88	0.23	0.965	964.70											
375	10363.41	0.01	0.989	964.93	964.93	V 2					964.81	'Ca 1'	-1.957	0.009	G
376	10363.35	0.01	0.995	964.94	964.93	Sc 2					964.82	'CN 1'	-1.412	0.118	G
377	10363.29	0.01	1.001	964.94	964.94	Sc 1					964.85	'CN 1'	-2.881	0.005	G
378	10363.23	0.01	0.996	964.95	964.94	Cr 2					964.85	'CN 1'	-1.517	0.050	G
379	10363.18	0.01	1.006	964.96	964.95	Ni 2					964.88	'CN 1'	-1.333	0.113	G
380	10363.12	0.01	1.001	964.96							964.90	'Ca 1'	-1.849	0.008	G
381	10363.06	0.01	0.988	964.97							964.92	'CN 1'	-2.477	0.011	G
382	10363.00	0.01	0.956	964.97							964.93	'CN 1'	-2.87	0.005	G
383	10362.95	0.01	0.916	964.98											
384	10362.89	0.01	0.815	964.98											
385	10362.83	0.01	0.684	964.99											
386	10362.77	0.01	0.561	964.99											
387	10362.72	0.01	0.511	965.00			965.00	'Ti 1'	-1.434	0.641					
388	10362.66	0.01	0.574	965.00											
389	10362.60	0.01	0.696	965.01											
390	10362.54	0.01	0.825	965.01											
391	10362.49	0.01	0.917	965.02											
392	10362.43	0.01	0.952	965.02											
393	10362.37	0.01	0.922	965.03											
394	10362.31	0.01	0.869	965.04											
395	10362.26	0.01	0.821	965.04											
396	10362.20	0.01	0.835	965.05			965.05	'CN 1'	-1.333	0.108					
397	10362.14	0.01	0.883	965.05											
398	10362.08	0.01	0.923	965.06											
399	10362.02	0.01	0.962	965.06											
400	10361.97	0.01	1.001	965.07											

Figure 6: View of customized Excel spreadsheet for line identification

components, unidentified lines, Arcturus data assignments including transition identification for molecules and a match category (see Section 4.1). The Excel file is sorted by flux and organized in flux intervals to facilitate the line identification. Then cells within a selected flux interval are coloured with the same colour. A re-sorting of data on wavelength, results in a spreadsheet which visualizes the line shapes of the individual lines by the different colours of the flux intervals. In a similar manner, elements/molecules are coloured according to their central depth interval. By scrolling the spreadsheet it is easy to visually identify the various lines and central depths. A typical section of a customized spreadsheet is given in Figure 6. A major part of the transition identifiers is deduced from a separate analysis (see 4.3.1). The data is organized line by line, matching the observed, normalized flux minima with the reported wavelengths of absorption lines. This alignment is a simple tool to compare observed wavelength with the literature values from VALD3 and Arcturus atlas by automating the calculation between these differences. Figure 7 (a) - (e) provide plots of these differences versus wavelength for the various bands using isolated lines only. A very good correspondence is observed and most lines are within a difference of 0.1 Å, except for a small region in the beginning of the M band from 45482 Å to 45700 Å. This region shows a shift in wavelengths towards a larger wavelength of up to 1.3 Å. The plots are also useful to spot outliers (see Section 4) in the data which are mostly due to uncertainties in the literature value or an indication of a contribution of lines yet unknown/unidentified.
Another useful feature of the spreadsheet is its database capability providing filters, which enable quick extraction of selected records for further evaluations and to perform statistics by the number of filtered records.
A python program (Annex 7.3.1) has been developed to plot a spectrum in comparison to other observed spectra or synthetic spectra using the normalized flux values at the corresponding wavelength. The plotting range is entered in the input parameter section as lower and upper boundaries. In the same section, a shift of wavelengths and flux by a fixed amount can be specified if needed. The names of the source data files are entered in the respective filename1-3 within the red quotation marks. The program delivers “overlay” plots of the selected spectra.
A small phython program (Annex 7.3.1) has been written which scales the normalized flux data of Arcturus by replacing all data with a negative flux and flux>1.10 by 0 and 1 accordingly.

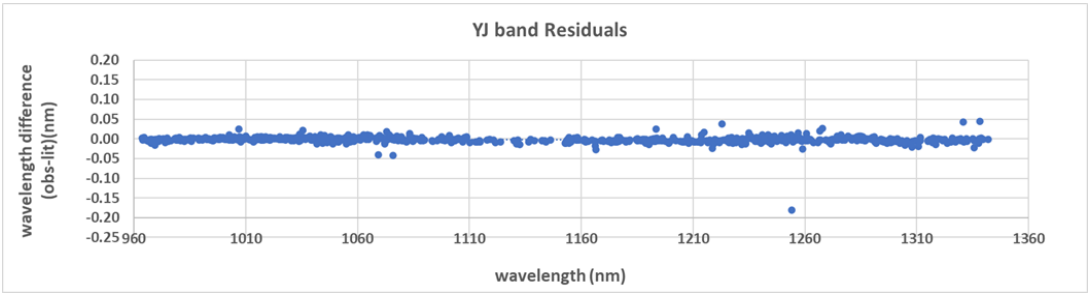

(a)

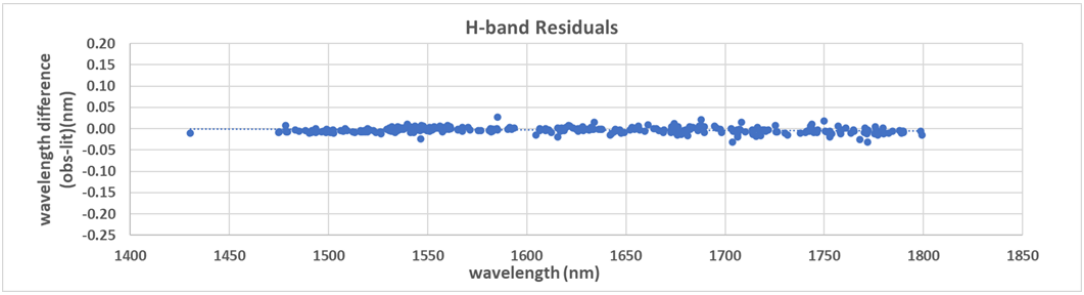

(b)

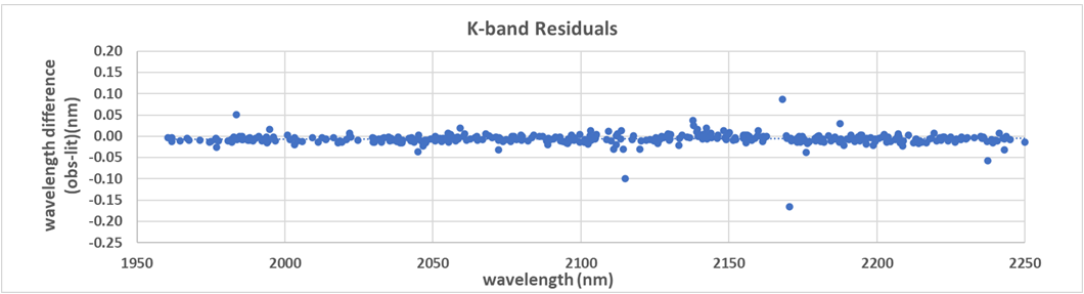

(c)

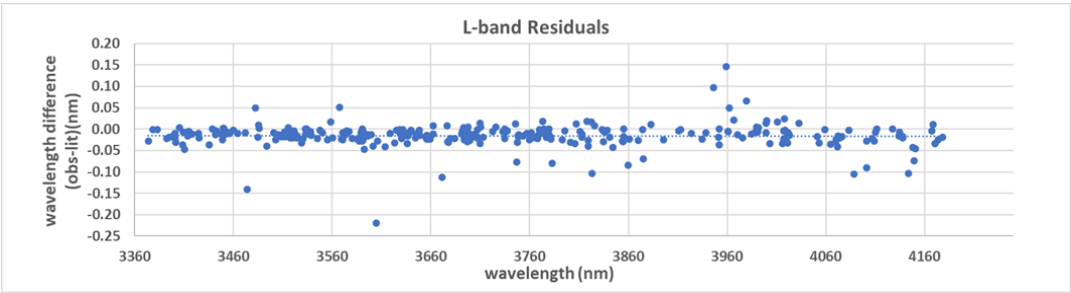

(d)

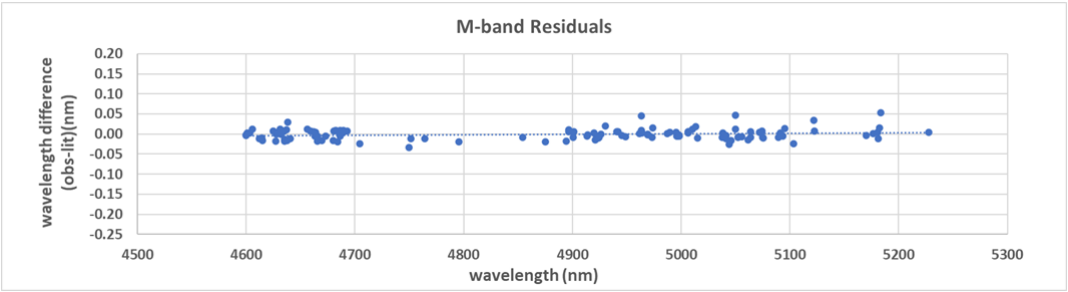

(e)

Figure 7: Calibration checks for 10 Leo IR-bands

In addition, the program standardizes and extracts only two columns of data: wavelength and normalized flux. The resulting .txt-file can be used as an input file fur further applications, e.g. Excel or python.
Different software applications based on Linux are used to generate and evaluate synthetic spectra together with the observed spectra. These applications are described in the Annex 7.3.4, 7.3.3.

3 Near Infrared Spectroscopy

3.1 IR spectroscopy for atoms and ions

The observed atomic spectral lines are the result of the interaction occuring during the absorption process of a photon with an electron of the atom/ion. According to the quantum theory only photons with an energy that exactly matches the energy-difference of two electronic states can be absorbed :

E (initial state) + $h\nu$ (photon) → E(excited state)

These photons with the right amount of energy are selectively taken from the continous flux of photons and enable the change in the respective electronic state of the species. The process is called photoexcitation and an absorption line is formed. Although the transition results in a change of electron configuration, the energy levels concerned are those of the atom, and it is the atom that makes a transition between energy levels and not the electron.
Various line lists exist (Goorvitch (1994), Hinkle *et al.* (1995), Piskunov *et al.* (1995), Ryabchikova *et al.* (2015), Gordon *et al.* (2017), Kondo *et al.* (2019), Kramida *et al.* (2019)) to use this quantified energy difference to identify the species by their specific electronic transitions. The line lists provide additional information on spectral features such as log gf values, energies of lower and upper level, Einstein coefficients etc.

3.2 Molecular spectra

In general, the spectra of molecules are more complex than the atomic spectra due to the additional effects caused by vibrational and rotational excitation of the molecule. The excitation causes changes in the shape of molecules such as stretching of bonds, bending of bonds, or internal rotation around bonds.
A given energy state of a molecule is characterized by additional quantitized vibrational levels which are further split into quantitized rotational states. The observed molecular lines are the combined result of rotational and vibrational interaction occuring simultanously during the absorption process of a photon with the molecule.
Not all molecular vibrations lead to observable infrared absorptions. A vibration must cause a change in the charge distribution (dipole momentum) within a molecule to absorb infrared light. Molecules such as N_2 or O_2 have no dipole momentum and hence do not have lines in the IR. The greater the change in charge distribution, the stronger the absorption. Ro-vibrational spectra are only observed in the gas phase.
Vibrational transitions within a molecule can be described using the anharmonic oscillator model which assumes that the two masses m_1 and m_2 are connected with a spring (with known strength). Quantum mechanical calculations (Schroedinger equation) provide the frequencies of basic stretching and bending modes.
The quantum mechanical solution of a harmonic oscillator is remarkably simple and can be compared to the relationship of balls and springs obtained from considering the classical model :

$$E = \frac{1}{2\pi^2 c} * \sqrt{k\mu} * (\nu + \frac{1}{2}) \tag{1}$$

with k=force constant, ν=vibrational quantum number, μ=reduced mass=$m_1 m_2/(m_1+m_2)$
The energy of vibration associated with a molecule in its lowest level of vibration (zero point

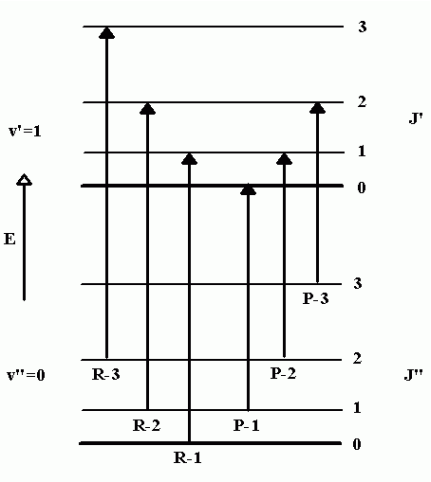

Figure 8: Rovibrational levels of CO

energy) is given by:

$$E = \frac{1}{4\pi^2 c} * \sqrt{k\mu} \tag{2}$$

The different rotational levels are described by the rotational quantum number J and the vibrational level by the vibrational quantum number ν. Not all transitions between the levels are allowed and selection rules, e.g. $\Delta J = \pm 1$ and $\Delta\nu = \pm 1$, apply. Figure 8 shows a number of ro-vibrational energy levels for CO. By convention, ground state parameters are identified with a double prime “, and excited state parameters with a single prime ’. Transitions that can occur between $\Delta\nu$” and $\Delta\nu$’ level, will increase the rotational quantum number ($\Delta J = -1$) or decrease ($\Delta J = +1$) the rotational number.The difference in energy between the J+1 transitions and J-1 transitions causes splitting of vibrational spectra into two branches. The lines that result from $\Delta J = -1$ transitions are called P-branch transitions and the $\Delta J = +1$ transitions are called R-branch transitions. As energy increases, the R-branch lines move closer together and the P-branch lines move farther apart. This is attributable to the rotational-vibrational coupling and centrifugal distortion.

The combined rotational-vibrational energy can be calculated by a combination of a harmonic oscillator and a rotator. Energy differences within a series of rotational levels are very small compared to the energy differences within vibrational levels. This allows to simplify the calculation (Born-Oppenheimer approximation) of the rovibrational lines by adding the multiple rotational transitions to a single vibrational transition.

A wide range of rotational states and a number of vibrational states are occupied at the temparature of a K-star and can be subject to a transition. Detailed data of rotational and vibrational states for the observed CO-bands and CN-bands are tabulated in Section 4.3.1 (Table 23), Section 4.3.2 (Tables 24, 25, 26), Section 5.1 (Tables 38, 39, 40) and Section 5.2 (Tables 41, 42, 43, 45, 48).

The strongest (fundamental) IR bands are due to the excitation from the ground state with vibrational quantum number ν=0 to the first excited state with vibrational quantum number ν=1. Overtone bands are observed arising from direct transitions from the ground state to the excited state with $\Delta\nu$=2 (first overtone) and $\Delta\nu$=3 (second overtone). They are weaker than the fundamental lines and do not occur at the exact multiple of the frequency of the fundamental transition, but at a lower frequency due to anharmonicity of the oscillator. A detailed analysis including the determination of basic parameter such as rotation constant B_e, harmonic wavenumber ω_e,

centrifugal distortion constant D_e, and vibration-rotation interaction constant α_e are covered in Section 5.

3.3 Spectral and physical parameters

This section describes in short summeries main spectral and physical parameters of NIR spectroscopy that influence the main spectral features. The summaries of the parameters are mainly based on free accessible on-line material, e.g.Tatum, J. (2015), Scholz, M. (2009).

3.3.1 Flux and continuum

The **flux** of photons is the observed quantity to be evaluated. It is usually normalized to the **continuum**, e.g. a flux value of 1 would correspond to a zero depression of the line, whereas 0.6 would stand for a 40% reduction. Values greater than 1 would indicate emission lines. However, due to the data reduction steps, e.g. telluric correction by subtracting a calculated spectrum, continuum values could fluctuate and impair the normalization. In the worst case some of the weak lines can disappear or the shape of the absorption line is distorted. Other possible sources for continuum deviations are of instrumental nature (Nicholls *et al.*, 2017).

3.3.2 Resolution and resolving power

The **resolution** is defined as the wavenumber, wavelength or frequency difference of two still distinguishable lines in a spectrum (McNaught & Wilkinson, 1997).The **resolving power R** is defined as the wavenumber (or wavelength or frequency) divided by the resolution (McNaught & Wilkinson, 1997). This can be expressed as:

$$R = \frac{\lambda}{n * \Delta\lambda} \tag{3}$$

with n = number of pixels per resolution element, $\Delta\lambda$ = pixelsize
The final 10 Leo spectrum has a constant resolving power of 90000 equivalent to a two-pixel resolution of $0.2\overline{2}$ Å at 2 μm.

3.3.3 Frequency, wavenumber, wavelength

The position of an absorption line along the wavelength axis is a measure of the energy difference that is used to excite specific energy states in atoms and molecules. The photon energy due to an electron transition between an upper atomic level k (of energy E_k) and a lower level i is:

$$\Delta E = E_k - E_i = h\nu = hc\tilde{\nu} = \frac{hc}{\lambda_{vac}} \tag{4}$$

where ν is the **frequency**, $\tilde{\nu}$ the **wavenumber** in vacuum, and λ_{vac} the **wavelength** in vacuum.
The SI unit for frequency is Hz and in most cases commonly noted as a multiple of Hz, e.g. MHz (1MHz=10^6 Hz).
The most common wavelength units are nanometer (nm), Ångström (1 Å = 10^{-1} nm) and micrometer (µm). The SI unit for wavenumber $\tilde{\nu}$ is the inverse meter, but in practice wavenumbers are expressed in inverse centimeters equivalent to $\approx 2.998 \times 10^4$ MHz.

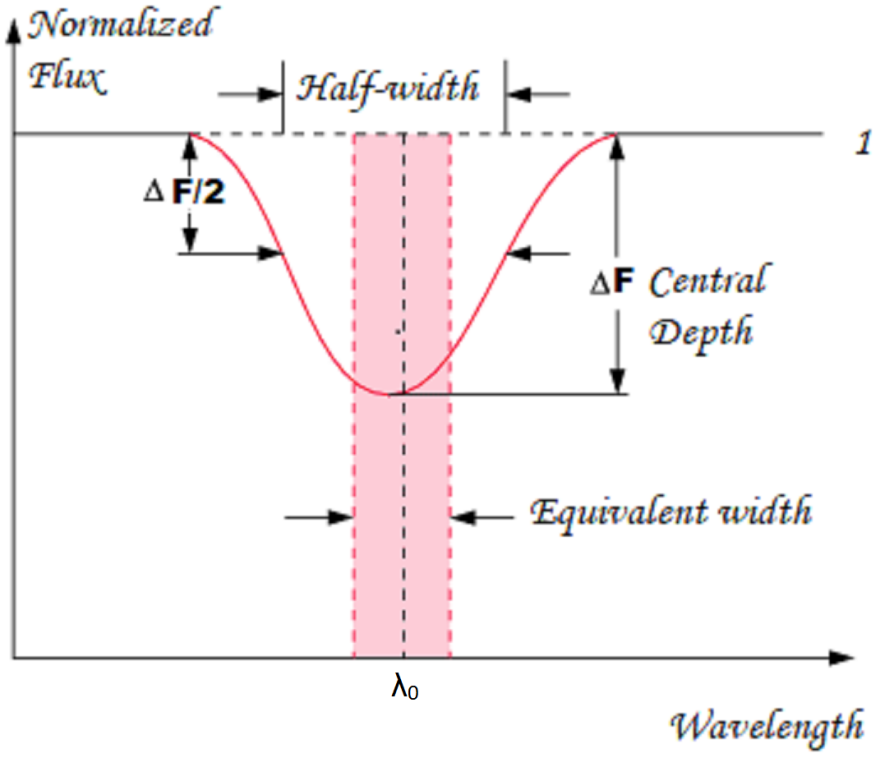

Figure 9: Absorption line profile (adapted from Karttunnen *et al.*, 2016)

The wavenumber $\tilde{\nu}$ is customarily used in IR-spectroscopy as it is a measure for the absorbed energy and proportional to the wavelength(λ):

$$\tilde{\nu}(cm^{-1}) = \frac{10^7}{\lambda(nm)} \tag{5}$$

In addition to frequency and wavenumber units, atomic energies are often expressed in electron volts (eV). One eV corresponds $\approx 2.418 \times 10^4$ Hz or $\approx 8\,065.54$ cm^{-1}.

3.3.4 Line profile

Most of the observed spectral lines in the NIR spectrum of 10 Leo have a **gaussian profile**. The profile can be described by **Equivalent Width (EW)**, **Central Depth** and **Full Width at Half Maximum (FWHM)**, Figure 9. Unlike in liquids, gases show discrete and sharp excitation lines of rotational levels. The shape of an absorption line depends on the line width of an atomic/molecular transition and the resolving power of the detection system. The observed line width in spectroscopy is significantly broader than the natural width of a spectroscopic line which is caused by the Heisenberg's uncertainty principle and is typically in the order of 10^{-2} pm. The natural line width is further broadened by the motion of the atom/molecules caused by temperature, gravity, pressure, magnetic forces and turbulences. The most important broadening mechanisms are Doppler broading and collision broadening. The Doppler broadening stems from the thermal motion of molecules/atoms and it results in a gaussian profile of a line. Collision broadening happens when molecules/atoms can interact during the radiaton process with other atoms/molecules. In this case a Lorentzian profile of the line is observed. The general equation for a gaussian profile is:

$$y = a * exp(-\frac{(x-b)^2}{2c^2})$$

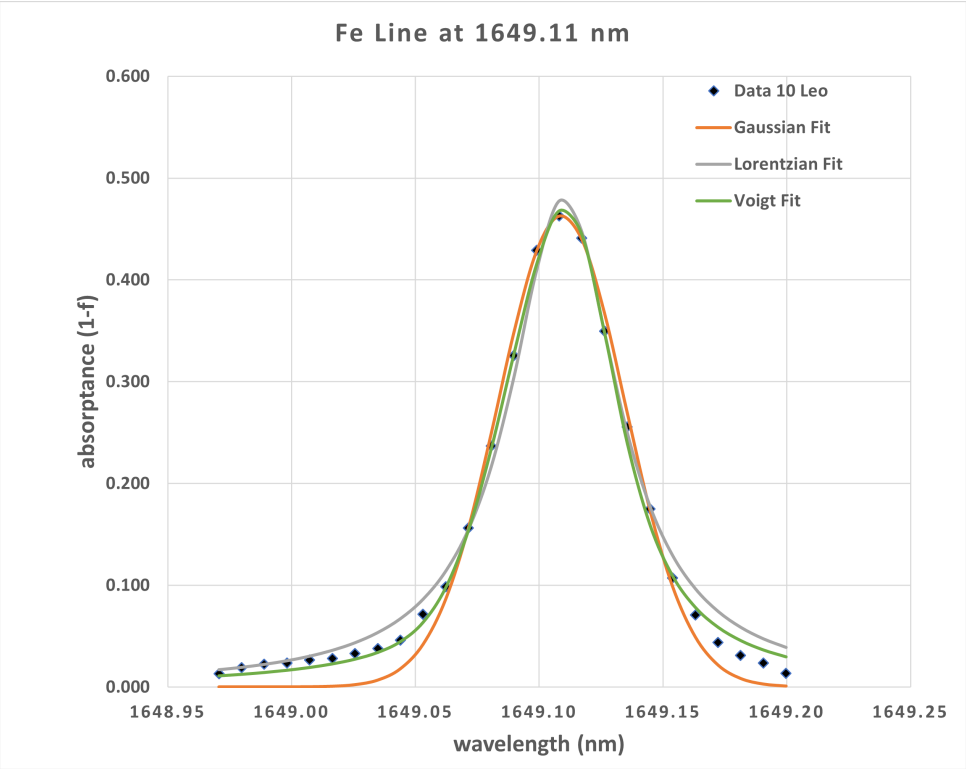

Figure 10: Gaussian, Lorentzian and Voigt profile for the strong 1649.11 nm line of Fe I

with f=normalized flux, y=(1-f), x=wavelength at (1-f), a=central depth, b=wavelength at cdepth, and c=FWHM.
Very strong lines show "wings" on both sides and are better approximated by a Lorentzian profile or by a Voigt-profile. The Lorentzian profile looks pointy in the centre and decreases slower than a Gaussian curve.The Lorentzian profile can be described by the equation:

$$y = \frac{I}{(1+(\frac{x-a}{\gamma})^2)}$$

with y=(1-f), x=wavelength at (1-f), a=wavelength at cdepth, I=cdepth, γ=scaling factor
The Voigt profile is a convolution of a Gaussian and a Lorentzian profile. This profile enhances the lower intensity parts of the line und reproduces the wings. Fig 10 shows the differences of the various profiles for the observed strong Fe I line at 1649.11 nm.

3.3.5 Equivalent width

The **equivalent width** (EW) of a spectral line is a quantitative measure of its strength. The EW is defined as the width of a rectangle with a height equal to that of the continuum emission (e.g. normalized flux=1), whereby the area of the rectangle has the same area as the spectral line. The units of equivalent width are the units of wavelength and most often EW is measured in mÅ or pm (1mÅ=0.1pm).
In many conditions, EW yields the number of absorbing or emitting atoms regardless of the shape of an absorption/emission line as long as the line is optically thin. The equivalent width of a spectral line changes differently with temperature, microturbulence, log g and magnetic field. For an optically thin line with multiple components, the EW is equal to the sum of EWs of its

Table 6: Equivalent width (EW0) derived from the sum of (1-normalized flux) compared to fitted equivalent width (EW1) by BinMag2

Element	λ(nm)	sum(1-F_λ)	gap	EW0(mÅ)	EW1(mÅ)	EW1/EW0
Sr	1003.94	2.125	0.0056	118.5	118.4	0.999
Fe	1034.37	2.010	0.0057	115.5	115.2	0.997
Ti	1049.90	2.414	0.0058	140.8	141.1	1.002
CN	1058.23	0.185	0.0059	10.9	10.9	1.005
Fe	1483.05	2.084	0.0082	171.7	171.1	0.996
Mg	1973.93	1.92	0.0110	211.0	210.5	0.997
Fe	1992.88	1.17	0.0111	129.6	129.4	0.998
Si	2038.40	1.49	0.0113	168.2	168.5	1.002
Ca	2265.98	1.05	0.0126	132.7	132.3	0.997
Fe	3382.95	0.347	0.0188	65.2	64.6	0.991
OH	3394.93	0.863	0.0189	162.8	162.4	0.997
CO	4627.23	1.599	0.0257	411.1	409.6	0.997

components. This facilitates the evaluation of blended lines.
Equivalent widths have been determined partly via line fit with BinMag2 and by a direct summation with Excel across the line using Nissen & Gustafsson (2018):

$$\mathrm{EW(nm)} = \int_{i=1}^{n_{pix}} (1 - \frac{F_\lambda}{F_C}) d\lambda \tag{6}$$

$$\mathrm{EW(nm)} = \sum_{i=1}^{n_{pix}} (1 - \frac{F_\lambda}{F_c}) \delta\lambda_{pix} \tag{7}$$

$$\mathrm{EW0(mÅ)} = \mathrm{EW(nm)} * 10^4 \tag{8}$$

F_λ = Flux at λ, F_c = Flux at continuum =1, $\delta\lambda_{pix}$ = wavelength-difference of two adjacent records ("spectral pixel size"), n_{pix} = number of pixel covering the range of the line.
The equation has been verified across the spectrum and Table 6 provides some selected lines with various line strengths. The statistical error of the EW can be calculated by:

$$\sigma(EW) \approx \sqrt{n_{pix}} (S/N)^{-1} \delta\lambda_{pix} \tag{9}$$

With two pixel per spectral resolution, S/N = 330 (YJ bandpass) and $\delta\lambda_{pix}$ = 0.006 nm , σ would be in the order of 0.3 mÅ.

3.3.6 Central depth

The **central depth** gives the maximum height of a line below the continuum. It is a dimensionless number and equivalent to the absorptance at the line centre:

$$\mathrm{cdepth} = \frac{I_\lambda(c) - I_\lambda(\lambda_0)}{I_\lambda(c)} \tag{10}$$

with I_λ(c)= intensity of continuum, $I_\lambda(\lambda_0)$=intensity at line center λ_0
Using the normalized flux of the continuum I_λ(c)= f_λ = 1, the relation simplifies to:

$$\mathrm{cdepth} = 1 - f(\lambda_0) \tag{11}$$

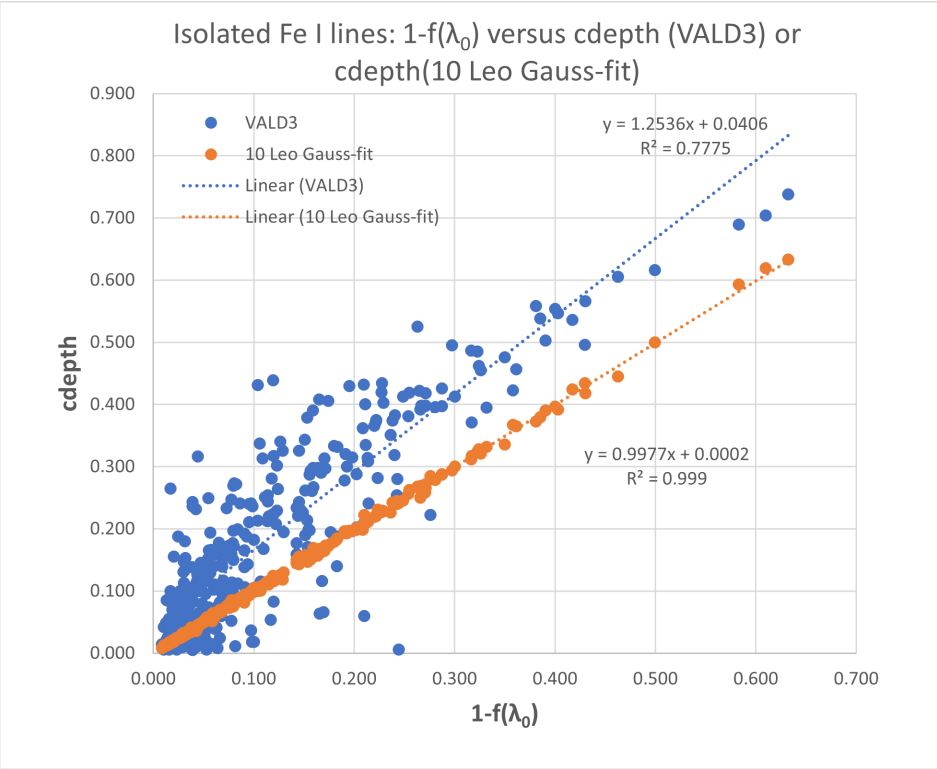

Figure 11: Fe I lines (1-f$_{(\lambda_0)}$) versus cdepth. The orange dots are from individual gaussian fits of isolated Fe-lines in the observed 10 Leo spectrum. The blue dots refer to cdepths from the VALD3 extracted stellar calculation for 10 Leo based on solar Fe-abundances.

The alignment of lines to the minima of the normalized flux in the customized Excel spreadsheets (see 2.2) quickly gives the central depth for a pure line. This is illustrated in Figure 11 for a large number of isolated Fe I lines (340) plotting 1-f(λ_0) versus cdepth. The orange curve represents the data set of individual Fe-line, each fitted by a gaussian curve using the Excel solver tool (see 7.3.2) to derive the respective position, cdepth, FWHM and the equivalent width. The second data set (blue dots) refers to the same Fe-lines and the plot shows 1-f(λ_0) versus the calculated cdepth values as listed in the VALD3 stellar extraction file (see Table 3). The scatter and shift of the blue dots is caused by the uncertainties in the line data and the default Fe abundances scaled to solar values used in the VALD3's stellar calculation.

3.3.7 Full width of the line at half height maximum (FWHM)/minimum(FWHm)

The width of an emission line is expressed as the **full width of the line at half maximum (FWHM)** and the width of an absorption line as the **width at half minimum (FWHm)**. Instead of the nomalized flux f, it is possible to use the absorptance (1-f) which graphically"converts" absorption lines to emission lines. The FWHM for a gaussian distribution it is calculated by:

$$\mathrm{FWHM} = 2\sigma\sqrt{2ln(2)} \approx 2.355\sigma \tag{12}$$

σ = standard deviation derived from signal to noise ratio.
Equivalent width, cdepth and FWHM are correlated via the equation:

$$\mathrm{EW} = m * cdepth * FWHM \tag{13}$$

$$m = \sqrt{2\pi} = 2.5066 \tag{14}$$

Table 7: Slope of relation EW=m*cdepth*FWHM

species	m	R	# lines evaluated
CO	2.4942E+00	9.9995E-01	190
Fe	2.5046E+00	9.9995E-01	275
Ni	2.5082E+00	9.9999E-01	17
Ca	2.5051E+00	9.9999E-01	21
Cr	2.5073E+00	9.9998E-01	15
Mg	2.5061E+00	9.9999E-01	14
Ti	2.5031E+00	9.9999E-01	14
Si	2.5082E+00	9.9999E-01	17

The reproduction of the constant m in Equ. (14) by the observed spectrum of 10 Leo has been checked for clean Fe I lines across the complete spectral range (Figure 12). Values for FWHM, cdepth and EW have been derived from the gaussian fits of the respective lines using the solver tool of Excel (see 7.3.2). Several other metals have been evaluated accordingly and are listed in Table 7.

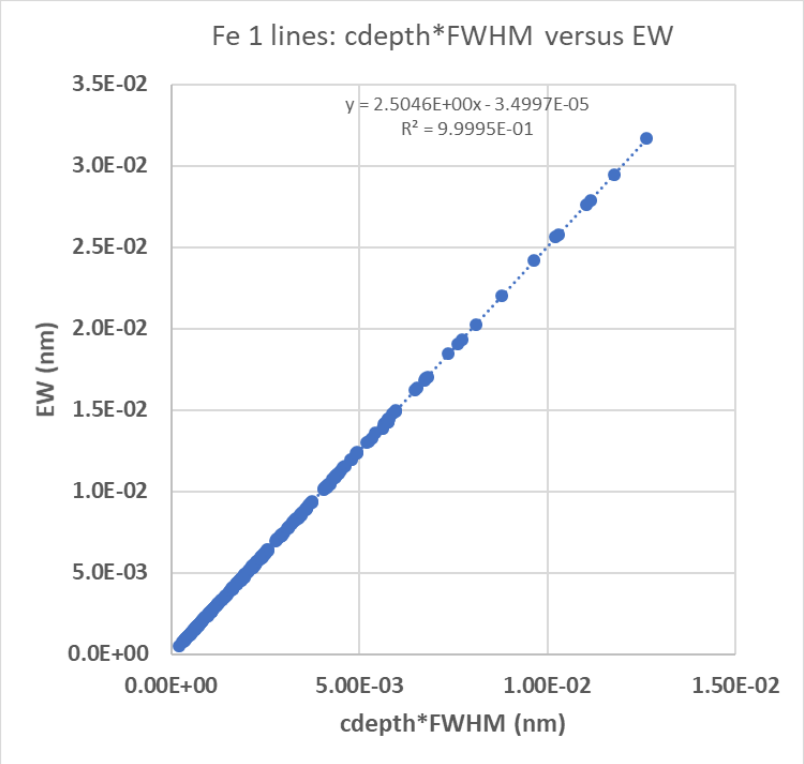

Figure 12: Cdepth*FWHM versus EW for Fe I lines

There is no significant difference in the slope. A deviation from the linear fit is a hint that the respective line is blended or that the peak shape is distorted, possibly caused by the data reduction process.

3.3.8 Temperature - T_{eff}

Temperature is the main factor affecting line strength as it determines the population of excited states and the degree of ionization/dissociation. The **temperature T_{eff}** is defined as the temperature at which a black body radiates the total flux F according to :

$$T_{eff} = (\frac{F}{\sigma})^{1/4} \tag{15}$$

$$F = \sigma T^4_{eff} \tag{16}$$

with the Stefan–Boltzmann constant σ= 5.67·10^{-8}Wm^{-2}K^{-4} = 5.67·10^{-5}ergs^{-1}cm^{-2}K^{-4}

The luminosity L of a star can be expressed by:

$$L = \text{Area*flux F} = 4\pi R^2 \sigma T^4_{eff} \tag{17}$$

with R=stellar radius.
At a high enough temperature and/or density, the thermal collisions of the atoms in a gas will ionize some of the atoms. In this process, the outer electron(s) dissociate(s) from the atom which becomes an ion with a completely different transition scheme than the original atom. The degree of ionization strongly depends on how strongly the outer electron(s) are bound to the atom, which is given by the ionization energy. The ionization energy is a specific physical property of an element. The Saha equation describes the degree of ionization for any gas in thermal equilibrium as a function of the temperature, density, and ionization energies of the atoms. For a gas composed of a single atomic species with one level of ionization, the Saha equation reads:

$$\frac{{n_e}^2}{n - n_e} = \frac{2}{\lambda^3}\frac{g_1}{g_0} exp\left[\frac{-\epsilon}{k_B T}\right] \tag{18}$$

with n= total density (n_0+$_1$), n_e = electron density, g_1,g_0 =degeneracy of state 1,0, ϵ = energy of ionization and λ, the thermal de Broglie wavelength of an electron which is defined by:

$$\lambda = \sqrt{\frac{h^2}{2\pi m_e k_B T}} \tag{19}$$

whereby m_e = mass of an electron, T = temperature of the gas, h=Planck constant and k_B=Boltzmann constant.

3.3.9 Dissociation energy

The stability of molecules and hence their presence in the stellar atmosphere depend on their **dissociation energy** and the temperature. Molecules will split into atoms when the excitation energy, e.g. thermal energy kT, exceeds the dissociation energy. Dissociation energies are given in Table 8 for a number of molecules. Most of the molecules are unstable at T_{eff} of 10 Leo ≈ 4800 K and dissociate into atoms. With increasing dissociation energy the fraction of "surviving" molecules increases. In particular large fractions of CO, CN, SiO and OH molecules are detected in the 10 Leo spectrum.

Table 8: Dissociation energies for selected molecules (Luo, Y.R., 2007)

Molecule	Dissociation Energy (eV)	± (eV)
CO	11.16	0.01
CN	7.77	0.03
OH	4.46	0.00
SiO	8.29	0.14
CH	3.51	0.01

Table 9: Ionization energies (eV), partition function Z1, Z2 and degree of ionization for selected atoms (calculated based on Saha equation with electron pressure of P=1.2 Pa)

Atom	Ionization energy(eV)	Z1, Z2 and degree of ionization (%) Arcturus (T=4301K) Z1	Z2	%	10 Leo (T=4801K) Z1	Z2	%
C	11.260	9.10	5.91	0.00	9.19	5.92	0.01
Na	5.139	1.95	1.00	97.65	2.00	1.00	99.57
Mg	7.646	1.00	2.00	12.86	1.00	2.00	62.49
Si	8.152	9.17	5.62	1.14	9.37	5.67	12.92
K	4.341	2.00	1.00	99.64	2.12	1.00	99.91
Ca	6.113	1.03	2.11	90.40	1.11	2.17	98.24
Sc	6.562	10.72	21.07	73.03	11.49	22.29	95.70
Ti	6.828	25.63	51.45	57.38	28.24	54.29	92.05
Fe	7.903	25.36	40.27	5.54	27.02	42.49	30.89
Rb	4.177	1.00	2.01	99.94	1.00	2.15	99.99
Sr	5.695	1.32	2.24	96.04	1.62	2.35	99.26
Y	6.217	10.34	14.16	82.68	11.27	15.35	97.29
Ce	5.539	145.47	151.39	95.77	178.05	179.32	99.27

3.3.10 Partition function

The **partition function** is the statistical sum over all the Boltzmann factors for all the bound levels. It determines how atoms and molecules in thermodynamic equilibrium are distributed among the various energy states at particular temperatures. In order to determine the total number of atoms (in all energy levels) in the source, it is necessary to know, in addition to the number of atoms in a particular level, how the atoms are distributed, or partitioned, among their numerous energy levels. The partition functions for atoms and molecules are calculated by respective computer codes (Barklem & Collet, 2016) and are available from the Strasbourg astronomical Data Center (CDS)[6]. A comparison of different approaches to calculate the partition function using different assumptions can be found in Popovas & Jørgensen (2016).
Table 9 provides the partion function at temperatures for Arcturus and 10 Leo and the ionization energies for some elements. The data is used to calculate the fraction of ionized to neutral atoms by the Saha equation.

[6] http://cdsweb.u-strasbg.fr/

3.3.11 Curve of growth (CoG)

The **curve of growth** is a graph that shows the equivalent width of an absorption line in relation to the number of atoms producing the line. For optical thin lines, the equivalent width increases linearly with the column density of absorbing species. A line is considered weak when the central depth does not exceed 0.4 (40%) (Hinkle *et al.*, 1976). Most of the lines observed are within this limits and the construction of a curve of growth is straightforward for weak lines. The weak line approach can be expressed as follows:

$$log(\frac{W_\lambda}{\lambda}) \propto N = logC + logA + loggf - \Theta_{ex}\chi + log\lambda - log\kappa_c \tag{20}$$

with N = column density, C = constant (for given star and species), A = abundance, gf statistical weigth times oscillator strength, $\Theta_{ex} = 5040K/T_{ex}$(excitation temperature), χ = excitation potential (lower level, (eV)), κ_c = continous opacity at line position.
With increasing column density N, the line gets saturated and additional atoms will not fully contribute to the reduced equivalent width. The reduced equivalent width increases only $\propto \sqrt{lnN}$. Finally, there will be a third stage in which the reduced equivalent width increases $\propto \sqrt{N}$. At this stage the line is forming broad wings on both sides.

3.3.12 Einstein coefficients

Three different processes can take place in the formation of a spectral line which are: spontaneous emission, stimulated emission and absorption. The probability that one of these processes occurs is given by the Einstein coefficients $\mathbf{A_{21}}$ **(spontaneous emission)**, $\mathbf{B_{21}}$ **(stimulated emission)** and $\mathbf{B_{12}}$ absorption. The Einstein coefficient B_{12} has the dimension $m^3J^{-1}s^{-1}$.
The three Einstein coefficients are interrelated by:

$$\frac{A_{21}}{B_{21}} = F(\nu) \tag{21}$$

$$\frac{B_{21}}{B_{12}} = \frac{g_1}{g_2} \tag{22}$$

$$F(\nu) = \frac{2h\nu^3}{c^3} \tag{23}$$

with h = Planck's constant, c=speed of light, g_1 = degeneracy of lower state 1, g_2 = degeneracy of upper state 2.

3.3.13 Oscillator strength and log *gf*

The absorption **oscillator strength** $\mathbf{f_{12}}$ of a line is defined as the ratio of its observed equivalent width to the equivalent width predicted on the basis of the classical oscillator model. The f_{12} value is a dimensionless quantity that is specific for each transition and is of order unity for the strongest transitions. It is related to the Einstein coefficients A_{21} , B_{21} and B_{12} and can be expressed by:

$$f_{12} = B_{12}\frac{4\epsilon_0 m_e h\nu}{e^2} \tag{24}$$

Alternatively, it can be written as:

$$f_{12} = A_{21} * 1.49919 * 10^{-16} * \frac{g_2}{g_1}\lambda^2 \tag{25}$$

with A_{ki} = transition probability (units of 10^8 sec^{-1}), λ = wavelength in Å.
The **log *gf*** value refers to a particular transition between two energy levels in an atom/ion or molecule and expresses the weighted oscillator strength (product of the oscillator strength f_{ik} of the atomic transition and the statistical weight g of the lower level):

$$log\ gf = log_{10}(g_i f_{ik}) \tag{26}$$

Calculated log *gf* values and A_{21} are usually available as part of a line list.

3.3.14 Intensity

The **intensity** of a transition line between two energy levels depends mainly on the population of the corresponding levels, that means on the number of atoms/molecules that can be excited and a linestrength factor. The probability of a transition taking place from an initial state is proportional to the population of the initial state involved in the transition. Within a given rotational or vibrational spectrum, the lower state populations are usually the dominant factor. Under thermal conditions, these are given by the Boltzmann distribution. The fraction N_J/N_0 can be calculated by:

$$\frac{N_J}{N_0} = (2J+1)exp(-\frac{\Delta E_{rot}}{kT}) \tag{27}$$

with

$$\Delta E_{rot} = BhcJ(J+1) \tag{28}$$

With rising temperature, higher rotational levels can be populated as shown in Figure 13. In general, the distribution is broadened with increasing temperature and the maximum of J moves with rising temperature towards larger J-values.

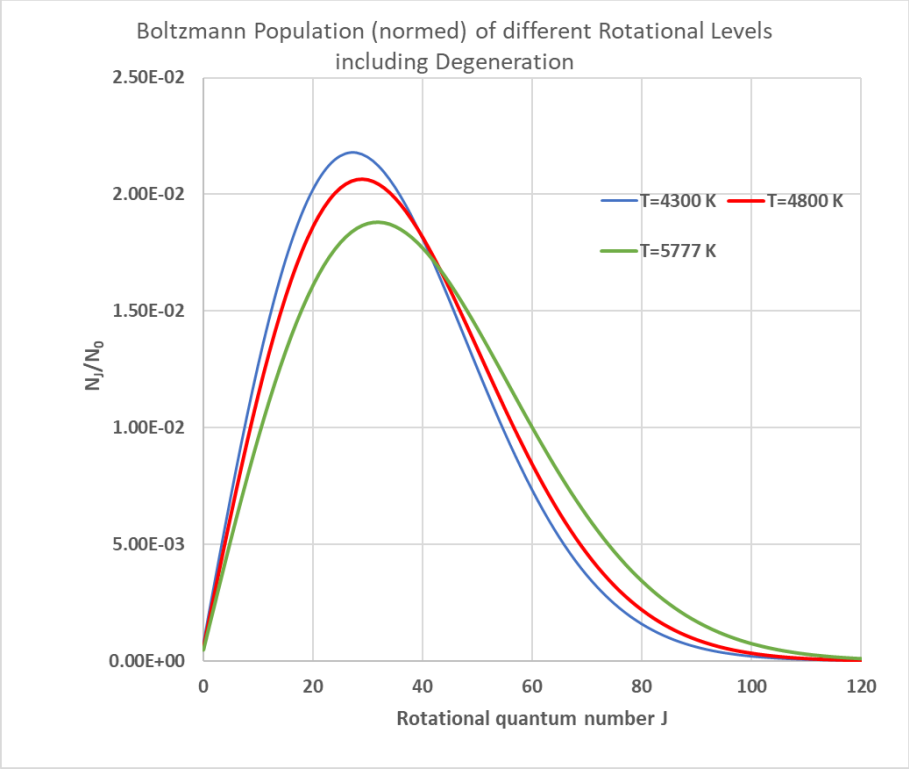

Figure 13: Boltzmann Population (normed) of rotational levels for different temperatures

.

Fig. 13 can be used to estimate the temperature T_{eff} by setting the first derivative equal to zero and solving for Jmax:

$$J_{max} = \sqrt{\frac{kT_{eff}}{2hcB}} - \frac{1}{2} \tag{29}$$

$$T_{eff} = \frac{2hcB}{k}(J_{max} + 0.5)^2 \tag{30}$$

As presented below, we derive B=1.931 cm^{-1} and J_{max}=29 from ^{12}CO bands in the 10 Leo spectrum (Table 36 in Section 5). Using Equ. (30) with these values we get T_{eff}=4835 K, which is close to the value of 4801 K given in Table 1 for 10 Leo. However, it should be noted that a Δ=1 of J_{max} already causes a difference of 300 K! Nethertheless, a calculation for J_{max} (eqtn 29), provides a good estimate for the expected J_{max} in the Arcturus spectrum to be at J=27.

3.3.15 Surface gravity - log *g*

The surface gravity of a star is usually given as **log *g***. It is calculated assuming that the atmosphere of the star is in hydrostatic equilibrium, i.e. the gravitational force is balanced by kinetic properties of plasma (with $r_{atmosphere} \ll R_{star}$):

$$g = \frac{GM_{star}}{R_{star}} \tag{31}$$

with G=gravitational constant=6.67*10^{-8} $cm^3g^{-1}s^{-2}$. The surface gravity is commonly expressed with its cgs units omitted.
Calculations for Arcturus, 10 Leo and the Sun using the values in Table 1 (Arcturus: M=1.08$M_\odot$, R=25.4$R_\odot$, 10 Leo: M=2$M_\odot$, R=14$R_\odot$, Sun:M=1.989*10^{33}g, R=6.96*10^{10}cm) gives log *g* values of 1.66, 2.48 and 4.44, respectively. The agreement for Arcturus and the Sun is perfect but the value for 10 Leo is significantly lower than reported in Table 1.This suggests that the quoted value for the radius is too high. Nicholls *et al.* (2017) have reported this discrepancy and have suggested a radius of 11.9 $R_\odot$. This value would give a log *g* of 2.62 which is still low but within the quoted uncertainty.

3.3.16 Optical depth, transparency and opacity

The **optical depth** τ gives the fraction of radiation which is absorbed during the passage of an absorbing medium, e.g. a stellar atmosphere. With the column density Σ (number of absorbing species per unit surface area) and the absorption cross-section σ (effective area that is needed to absorb the photon), the optical depth can be expressed as:

$$\tau = \Sigma\sigma \tag{32}$$

The loss of intensity follows an exponential law:

$$I_{out} = I_{in}e^{-\tau} \tag{33}$$

As optical depth gets large, the amount of light drops exponentially and the medium is called "optically thick". If $\tau \ll 1 \rightarrow e^{-\tau} \approx 1\text{-}\tau$ radiation passes easily which means that the medium is

"optically thin". The effect of the medium can be characterized by an attenuation coefficient κ, defined as the fraction of intensity lost per unit distance traveled. In general, the **opacity** κ or absorption coefficient describes the ability of stellar material to absorb radiation and is a parameter for the energy transport equation. A low opacity means high transparency; a high opacity means a low transparency. Apart from the fine-structure constant α (Sommerfeld constant), the optical depth also depends on the properties of the absorber, namely the ionic column density N_i, oscillator strength f and the velocity dispersion v.

3.3.17 Column number density

The **column density** is a projected number density along a specific line of sight. It is a measure of how many atoms/molecules are between the object and the observer. The column number density is important to derive the number of absorbing species. It is calculated in units of m^{-2}.

3.3.18 Force constant

The **force constant k** is a measure of stiffness of the vibrating bond between two atoms in a molecule and has its origin from the Hooke's law. It can be calculated from the equation (35):

$$\tilde{\nu} = \frac{1}{2\pi^2 c} * \sqrt{k\mu} \tag{34}$$

$$k = 4\pi^2 c \tilde{\nu}^2 \mu \tag{35}$$

$\tilde{\nu}$=wavenumber of vibration (transition energy), μ= reduced mass of both atoms, c=speed of light. The calculation for the $^{12}C^{16}O$ with $\tilde{\nu} \approx 2143.27$ cm^{-1}, μ= 1.1385*10^{-26}kg and c=2.9979*10^{10}cm yields a force constant of 1856 Nm^{-1}.

3.3.19 Rotational constant

The **rotational constant B** of a diatomic molecule is given by:

$$B = \frac{h}{8\pi^2 c I} \tag{36}$$

with

$$I = \left(\frac{m_1 m_2}{(m_1 + m_2)}\right) r^2 \tag{37}$$

I=moment of inertia of the molecule, r=distance of the mass points (bond-length), h is Planck's constant and c is the speed of light in vacuum.
B has the dimension of a wavenumber and decreases with increasing vibrational quantum number. The rotational constants for CO and CN differ very little since they have similar molecular weigths and bond lengths. Therefore, the spacing of rotational lines for CO and CN will be comparable. In contrast, the rotational constant for OH is much smaller and the spacing of wavelength between rotational lines for OH will be larger compared to CO and CN.

3.3.20 Microturbulence - v_{mic} (ζ)

Microturbulence is one of several mechanisms that can cause broadening of the absorption lines in the stellar spectrum. The microturbulent velocity is defined as the microscale non-thermal component of the gas velocity in the region of spectral line formation. The distribution of these

velocities along the line of sight produces the microturbulence broadening of the absorption lines due to the Doppler effect. Stellar microturbulence varies with the effective temperature and the surface gravity. Equivalenth widths are heavily changing with ζ. For the 10 Leo spectra a ζ-value of 2 km/s is adopted.

3.3.21 Macroturbulence - v_{mac}

Macroturbulence is another broadening mechanism for spectral lines. The broadening is caused by convection in the outer layers of the star. The wings of the lines get stretched outwards. It is important to note that v_{mac} does not alter the equivalent width. In this respect, v_{mac} and v_{sini} have a similar impact on the profile of the absorption line.

3.3.22 Radial velocity - v_{rad}

The **radial velocity** of a star is observable by the Doppler shift of its spectrum. It will shift the wavelength λ according to:

$$\Delta\lambda = \frac{v_{\mathrm{rad}}}{c}\lambda_0 \tag{38}$$

3.3.23 Stellar rotation - v_{sini}

The projected **rotational velocity** v_{sini} can be calculated using the FWHM value of an isolated and relatively unblended line and assuming a Gaussian profile for this line:

$$v_{\mathrm{sini}} = c\frac{FWHM}{2\lambda\sqrt{ln2}} \tag{39}$$

Equivalent widths are not changing with v_{sini}.

3.3.24 Abundances and metallicity - [Fe]

All chemical elements except H and He are considered metals. The **abundance** of a chemical element (X) is a measure of how often one can find it relative to all other chemical elements in a given environment (for practical reasons it is usually measured relative to the abundance of H only). It is mainly expressed in mass fractions. The relative abundance of an element X can be converted to the absolute abundance ϵ by:

$$\log\epsilon(\mathrm{X}) = \log(\frac{N_{\mathrm{X}}}{N_{\mathrm{H}}}) + 12 \tag{40}$$

Table 10: Abundances (log) for extracted VALD3 line catalogue scaled to solar values

H : 0.92	He: -1.11				
Li:-10.94	Be:-10.64	B : -9.49	C : -3.52	N : -4.12	O : -3.21
F : -7.48	Ne: -3.96	Na: -5.71	Mg: -4.46	Al: -5.57	Si: -4.49
P : -6.59	S : -4.71	Cl: -6.54	Ar: -5.64	K : -6.92	Ca: -5.68
Sc: -8.87	Ti: -7.02	V : -8.04	Cr: -6.37	Mn: -6.65	Fe: -4.54
Co: -7.12	Ni: -5.79	Cu: -7.83	Zn: -7.44	Ga: -9.16	Ge: -8.63
As: -9.67	Se: -8.63	Br: -9.41	Kr: -8.73	Rb: -9.44	Sr: -9.07
Y : -9.80	Zr: -9.44	Nb:-10.62	Mo:-10.12	Tc:-20.00	Ru:-10.20
Rh:-10.92	Pd:-10.35	Ag:-11.10	Cd:-10.27	In:-10.38	Sn:-10.04
Sb:-11.04	Te: -9.80	I :-10.53	Xe: -9.87	Cs:-10.91	Ba: -9.91
La:-10.87	Ce:-10.46	Pr:-11.33	Nd:-10.54	Pm:-20.00	Sm:-11.03
Eu:-11.53	Gd:-10.92	Tb:-11.69	Dy:-10.90	Ho:-11.78	Er:-11.11

Table 10 is extracted from a VALD3 stellar request and lists the log(abundances) in the Sun. **Metallicity** is the mass fraction of **all** metals and is usually expressed as the logarithm of the ratio of a star's iron abundance compared to that of the Sun.

$$[\text{Fe/H}] = log_{10}\left(\frac{N_{\text{Fe}}}{N_{\text{H}}}\right)_{star} - log_{10}\left(\frac{N_{\text{Fe}}}{N_{\text{H}}}\right)_{sun} \tag{41}$$

Absorption lines depend strongly on the kind and number of absorbing atoms present. Therefore, the metallicity is an important parameter for the interpretation of the spectrum.

4 Spectroscopic Results

The studied 10 Leo IR-spectrum features a complex mixture of lines with various line shapes, a wide range of line intensities and some discontinuities. The spectrum is subdivided according to the bandpasses YJ, H, K, L and M. The elimination of the telluric lines by a subtraction algorithm (*Molecfit software*, e.g. Kausch, W. *et al.* (2015), Smette *et al.* (2015)) and the applied corrections of various instrumental impacts (Nicholls *et al.*, 2017) create some artefacts and discontinuities in the background. This necessitates a visual inspection of the spectrum to properly identify the spectral lines (excluding gaps in 10 Leo/Arcturus).
Table 11 provides a summary of the overwhelming number of lines identified within the 10 Leo IR-spectrum sorted by bandpass and match category (see 4.1).

Table 11: Number of line matches between 10 Leo (observed), VALD3 (calculated), Arcturus (observed (Hinkle atlas))

Category	YJ	H	K	L	M	sum
A	1344	1398	687	357	1076	4862
B	1902	3022	2290	835	1493	9542
C	1441	2879	1717	808	1230	8075
D	77	134	31	10	106	358
E	65	73	8	97	1	244
F	712	316	200	418	70	1716
G	23	69	18	45	9	164
sum:	5564	7891	4951	2570	3985	24961
includes:						
U	367	286	153	407	69	1282

4.1 Matching of lines

The wavelength of an observed absorption line is matched with the reported value of the “stellar extraction” from VALD3 and the Arcturus atlas. The matches are categorized according to :
A - line observed in 10 Leo matches line listed in VALD3 and Arcturus-atlas
B - line observed in 10 Leo matches line listed in VALD3 but no match with Arcturus-atlas
C - line listed in VALD3 only but not observed in 10 Leo and not listed in Arcturus-atlas
D - line listed in VALD3 and listed in Arcturus-atlas but not identified in 10 Leo
E - line observed in 10 Leo matches Arcturus-atlas but not listed in VALD3
F - line observed in 10 Leo but not listed in VALD3 or in Arcturus-atlas
G - line listed in Arcturus-atlas but not observed and not listed in VALD3
U - unknown lines observed in 10 Leo with no matches.
Category C includes lines which are not observed due to the gaps and lines which are in conflict with the observation, e.g. they are not observed although their strength should allow their observation. Especially some strong Mg I and Fe I lines seem misplaced as no line strength is observed in 10 Leo and Arcturus. This indicates that some lines listed in VALD3 may not be correct. Unassigned items (category U) are included in category F. A number of lines matches the position but have larger equivalent widths than expected and are transfered to the unknown category. Items that are not referenced in VALD3 and Arcturus atlas but have been assigned to

molecular lines based on the analysis of individual rovibrational bands (see Section 4.3.1) are assigned to category F.
Some of the "no matches with Arcturus" are due to saturated regions and differences in the spectrometers wavelength coverage. A few of the observed unlisted lines may have been generated by the data reduction process itself, which is assumed "perfect" for this search.
Annex, Section 7.1.1 (Tables 54 - 58), lists absorption lines of species with VALD3 declared cdepth>0.05 which are not observed in the 10 Leo spectrum. These tables compare the (1-f) values of the 10 Leo spectrum at the declared wavelengths with the stated cdepth values provided by the VALD3 stellar extraction file. A large number of the normalized flux values in the 10 Leo spectrum is >1, which causes negative (1-f) values. These values may originate from possible emission lines, counting statistics or from corrections caused by the data reduction process itself.
A number of lines (category E), observed in the spectra of 10 Leo and Arcturus, are not listed in VALD3 and are summarized in the Annex, Section 7.1.3. These lines are mostly attributed to Fe I in the H-band.

Table 12: Outliers exceeding a wavelength difference of ±0.05 nm

	Wavelength (nm)		
Assignment	Observed	Listed (1)	Difference
'Si I'	1253.83	1254.01	-0.18
'Fe I'	1983.67	1983.62	0.05
'Si I'	2114.89	2114.99	-0.10
'Si I'	2168.12	2168.03	0.09
'Si I'	2170.31	2170.48	-0.17
'Si I'	2237.28	2237.33	-0.06
'Fe I'	3410.31	3410.36	-0.05
'Mn I'	3473.74	3473.88	-0.14
'Si I'	3592.62	3592.67	-0.05
'Ca I'	3604.58	3604.80	-0.22
'Si I'	3671.27	3671.38	-0.11
'Si I'	3746.54	3746.61	-0.08
'Fe I'	3782.91	3782.99	-0.08
'Si I'	3822.99	3823.09	-0.10
'Si I'	3859.65	3859.73	-0.08
'CH 1'	3874.67	3874.74	-0.07
'Ca I'	3946.07	3945.97	0.10
'Ca I'	3959.31	3959.17	0.15
'Ni I'	3979.27	3979.20	0.07
'Si I'	4088.33	4088.44	-0.10
'Cr 1'	4101.35	4101.44	-0.09
'Si I'	4143.58	4143.68	-0.10
'Si I'	4149.34	4149.41	-0.07
'Ni I'	4150.67	4150.72	-0.05
'CO'	5183.80	5183.75	0.05

References:(1) Ryabchikova *et al.*, 2015

Most of the expected lines could be found and are marked in the spreadsheet accordingly for

later retrieval using the filter options. Some lines, in particular Si I, Ca I and Fe I lines, seem to be shifted compared to the VALD3 values although the adjacent wavelengths for the CN and CO lines match within 0.1 Å. A list of lines with the most significant, absolute differences ≥ 0.5 Å is shown in Table 12.
Many more inconsistencies related to wavelength and cdepth have been spotted across the entire observed wavelength range, complicating quite severely the search for new lines. These inconsistencies will also add to the uncertainty in the synthetic spectra.

4.2 Identification of elements

The observed elements are grouped into Hydrogen, α-process elements (C, N, O, Ne, Mg, Si, S, Ar and Ca), odd-Z elements (Na, Al, P, K and Sc), iron peak elements (Ti, V, Cr, Mn, Fe, Co and Ni), and neutron capture elements (Cu, Zn, Rb, Sr, Y, Zr, Ce, Yb). It is noted that there is no clear separation for some of the elements due to the overlapping processes, e.g. Ti, Co and Fe can be formed by the α-process as well.
In addition, elements form ions at higher temperatures dependent on their ionization energy. The loss of an electron completely changes the energy level structure of the atom and hence the emitted/absorbed atomic spectrum. Although Na and Ca have very low ionization energies, no Na II or Ca II lines are detected. Sr, Y, Ce, Dy and Yb are observed in their first ionized form (Sr II, Y II, Ce II, Dy II and Yb II), all others species are neutral.
Spectral cutouts for identified elements are given in the Annex, Section 7.2.1 (Figures 41 - 68). The spectral cutouts include line information such as position, identification, log gf, EW (10 Leo), cdepth (solar values) and match status.

4.2.1 Hydrogen

Table 13: H I lines

Transition		10 Leo		Literature (Kramida *et al.*, 2019)		
Name	$v"\leftarrow v'$	$\lambda(nm)$	EW(mÅ)	$\lambda(nm)$[a]	Intensity	Remarks
Paschen	3 → 7	1005.21	75	1005.26	(13000)	very broad
Paschen	3 → 6	1094.10	97	1094.12	14000	very broad
Paschen	3 → 5	1282.16	377	1282.16	32000	very broad
Brackett	4 → 16	(1556.08)	6	1556.05	800	1556.09 Fe I
Brackett	4 → 15	(1570.49)	5	1570.50	(800)	1570.50 V I
Brackett	4 → 14	(1588.47)	7	1588.49	(1000)	1588.49 Ca I
Brackett	4 → 12	(1641.16)	30	1641.14	1400	1641.23 Fe I
Brackett	4 → 11	1681.10	61	1681.11	1600	1681.20 Fe I
Brackett	4 → 10	1736.68	55	1736.69	3100	very broad
Brackett	4 → 7	2166.11	601	2166.12	8000	very broad
Pfund	5 → 8	3740.55	26	3740.58	2500	very broad
Brackett	4 → 5	4052.29	625	4052.28	11000	very broad
Pfund	5 → 7	4653.77	17	4653.78	4200	4653.67 CO

[a] values converted from air to vacuum for λ <2000 nm

Hydrogen has been identified via several lines belonging to Paschen series (transitions from principal quantum number n=3 to n'=4,5,6..), Brackett series (transitions from principal quantum number n=4 to n'=5,6,7...) and Pfund series (transitions from principal quantum number n=5 to n'=6,7,8...). The observed lines are summarized in Table 13. The noted lines of the Brackett 4→11 to 16 transitions are weak and heavily blended by metal lines. In fact, their assignment in the 10 Leo spectrum is questionable and the quoted cdepth values should be taken as upper limits. The Pfund 5→7 transition at 4653.78 nm is only visible as a shoulder to the CO 7-6R97 line at 4653.67 nm. The remaining H I absorption lines are generally very broad and the derived EW-values are not corrected for possible metal/molecular line blending.

4.2.2 α-process elements

Table 14: Equivalent widths (EW) of individual lines to confirm the presence of α process elements

	clean - most intense		clean -weakest		
Element	λ(nm)	EW(mÅ)	λ(nm)	EW(mÅ)	# of all lines
N (CN)	1156.31	92	1240.40	2	3249
O(CO)	4949.01	1074	1558.97	2	4471
O(OH)	3460.20	190	1542.98	2	396
C I	1069.42	117	3777.32	2	142
Mg I	3677.19	271	1030.21	12	294
Ca I	1615.52	153	1079.44	14	140
Si I	1203.48	305	1080.02	2	534
S I	1547.40	55	2258.16	22	43

The α-process elements are: C, O, Ne, Mg, Si, S, Ar and Ca. Oxygen and Nitrogen are not directly observed as elements in the 10 Leo IR spectrum but show their strong presence in the molecules CO, OH and CN. Table 14 shows equivalent widths for unblended lines of C I, Mg I, Si I and Ca I across the spectrum.

Table 15: Comparison of Si I lines in part of YJ bandpass with Literature(Tan *et al.*, 2016)

10 Leo (HD83240)						Arcturus	
	This work			Reference		This work	Reference
λ(nm)	EW	cat	blends	λ(nm)	EW	EW	EW
1029.18	90	T	CN	1029.17	91.8	81	82.3
1037.41	173	Q4	Fe,CN	1037.41	169.1	168	160.9
1058.81	274	T	Fe,Ti	1058.81	279.5	255	257.1
1060.64	231	T	Si,CN	1060.64	233.0	211	216.8
1063.06	117	D	CN	1063.06	121.0	112	102.4
1066.39	238	Q4	Co,Ti,Fe	1066.39	241.2	222	226.8
1069.26	156	D	Ti	1069.27		143	126.5
1069.73	164	S		1069.72	162.6	144	135.0
1073.04	183	T	CN	1073.04	179.4	145	153.3
1075.23	268	T	Na,Unk	1075.23	263.1	245	237.0
1078.75	93	S		1078.75		72	68.4
1078.98	248	S		1078.98	236.6	229	223.0
1083.00	363	Q7	Ca,Si,Ti	1083.01	364.4	342	318.3
1084.68	163	S		1084.68	164.2	139	141.6
1088.58	79	S		1088.58	82.6	71	64.0
1098.23	191	D	Ni	1098.23	207.5	184	197.7

Figures 42 to 47 in the Annex, Section 7.2.1 provide views of spectral ranges to support the line identification of α-process elements.
16 Si I lines with line positions and EWs are reported by Tan *et al.* (2016) for 10 Leo and Arcturus. The comparison in Table 15 with the present work shows a very good match in the wavelength

and also the EWs are in reasonable agreement despite the noted blending. The blending has been taken into account for the 10 Leo but not for Arcturus. The mean percentage difference of the EWs is (-1 ± 2.5)% for 10 Leo and (2 ± 5)% for Arcturus.

4.2.3 Iron peak elements

The iron peak is a local maximum of the abundance distribution of chemical elements in the vicinity of Fe. The iron-peak elements include elements with atomic numbers in the range $22 \leq Z \leq 32$, from scandium to germanium. The iron peak group is mostly produced in supernovae due to explosive oxygen and silicon fusion, followed by radioactive decay of nuclei such as ^{56}Ni. Table 16 lists equivalent width of the most prominent and weakest undisturbed lines for Ti I, V I, Cr I, Mn I, Fe I, Co1 and Ni I across the spectrum.

Table 16: EW of individual lines to confirm the presence of iron group elements

	clean - most intense		clean -weakest		
Element	λ(nm)	EW(mÅ)	λ(nm)	EW(mÅ)	# of all lines
Ti I	964.09	192	998.40	2	227
V I	1290.47	21	1318.86	2	33
Cr I	1291.36	75	1295.06	4	79
Mn I	1332.26	322	1319.72	7	58
Fe I	1188.61	325	1071.29	2	2429
Co I	1676.22	82	2207.29	3	33
Ni I	1631.50	144	1240.51	3	213

Figures 48 to 54 in the Annex, 7.2.1 show spectral cutouts to support the line identification of iron group elements.

Andreasen *et al.* (2016) have published a catalogue with about 320 lines for Fe I and 13 lines for Fe II featuring line positions, log *gf* values and EWs for the **Sun** which is available from CDS. With a few exceptions, all lines could be identified in the 10 Leo spectrum. While the line positions match very well, some of the reported lines are not present in the 10 Leo spectrum and large differences between the log *gf* values reported in VALD3 and their log *gf* values (recalibrated for the Sun) are observed. Andreasen *et al.* (2016) claim that most of the Fe-lines taken from VALD3 have bad log *gf* values.The differences in the EW-values are not surprising due to the differences in temperature and log *g*. Table 17 summarizes the most obvious discrepancies ($|\Delta \log gf| > 1$ for Fe I).

The comparison for Fe II lines is compiled in Table 18. The majority of Fe II lines could not be confirmed in the 10 Leo spectrum. Likely, this can be attributed to the higher temperature of the Sun which enhances the formation of Fe II versus Fe I.

Table 17: Comparison of **discrepant** Fe I lines

Reference: Andreasen *et al.* (2016) Solar spectrum			This work[a] 10 Leo spectrum			
λ(nm[b])	log *gf*	EW (mÅ)	λ(nm)	log *gf*	EW (mÅ)	Comments
1033.02	0.504	134.4	1033.01		232	Blend (Sr II !)
1485.82	-1.059	24.3	1485.82		0	not found
1510.00	-0.148	72.8	1509.98	-1.985	4	
1520.57	-1.34	27.4	1520.57	-0.161	58	
1523.45	0.017	76	1523.45		0	not found
1558.33	-1.088	10.5	1558.34	-2.123	33	
1603.38	-0.754	22	1603.38	-2.102	66	Fe I+U+CN
1606.91	0.314	144.7	1606.91		0	not found
1661.22	-0.566	34	1661.22	-1.6	12	
1680.42	-0.672	59.3	1680.42	-2.544	117	
1689.98	-1.023	12.6	1689.96	-2.361	3	
1756.96	-0.76	48.1	1756.97		<3	not found

[a] log *gf* values from VALD3 file, [b] values converted from air to vacuum

Table 18: Comparison of **discrepant** Fe II lines

Reference: Andreasen *et al.* (2016) Solar spectrum			This work[a] 10 Leo spectrum			
λ(nm[b])	log *gf*	EW (mÅ)	(nm)	log *gf*	EW (mÅ)	Comments
1043.02	-1.662	12.4	1043.01		20	Not listed in VALD3
1050.44	-1.926	18.2	1050.44	-2.086	12	CN 2-1P_{1}66.5 at 1050.42 subtracted
1086.56	-2.043	14.8	1086.56	-2.199	13	
1112.86	-2.301	9.1	1112.85	-2.3	3	
1183.63	-3.379	81.7	1183.62		17	Not listed in VALD3
1291.74	0.045	97.7	(1291.74)		0	not found
1325.48	0.86	13	(1325.48)		0	not found
1328.09	-2.043	35.9	(1328.09)		0	not found
1329.85	-3.613	56.9	(1329.85)		0	not found
1342.28	-3.484	32.8	(1342.28)		0	not found
1525.13	-1.691	10.5	(1525.13)		0	not found
1535.44	0.602	29	(1535.44)		0	not found
2046.57	-5.758	36.5	2046.58	-7.779	5	

[a] log *gf* values from VALD3 file, [b] values converted from air to vacuum

4.2.4 Odd-Z elements

Table 19: EW of individual lines to confirm the presence of odd-Z elements

	clean - most intense		clean -weakest		
Element	λ(nm)	EW(mÅ)	λ(nm)	EW(mÅ)	# of all lines
Na I	2208.97	331	991.87	3	60
Al I	1312.70	479	3601.13	6	28
P I	1058.45	16	1068.43	6	16
K I	1177.61	158	3662.25	20	19
Sc I	2207.13	34	2173.64	2	9

Table 19 lists the most intensive and weakest detected lines from the odd-Z elements: Na, Al, P, K and Sc. Sc (Z=21) is a transition element between the α-process elements and the iron-peak elements. Annex, Section 7.2.1 (Figures 55 to 59) gives views of spectral ranges to support the line identification of odd Z elements.

4.2.5 neutron capture elements

Table 20: EW of individual lines to confirm the presence of neutron capture process elements

	clean - most intense		clean -weakest		
Element	λ(nm)	EW(mÅ)	λ(nm)	EW(mÅ)	# of all lines
Cu I	1601.09	4	1601.00		3
Zn I	1305.71	17			3
Sr II	1033.01	232	1003.94	119	3
Y I	2255.00	5			5
Y II	1024.80	11	1018.93	6	5
Zr I	982.53	3			2
Rb I	1529.37	6	1475.64		2
Ce II	1759.95	41	1258.57	5	50
Dy II	1052.63	3			1
Er II	1106.26	11			1
Yb II	1650.28	10			1

For the purpose of this survey, all identified elements with the atomic number Z >28 (Ni) have been attributed as neutron capture elements. This category includes the elements Cu, Zn, Sr, Y, Zr, Rb, Ce, Dy, Er and Yb. Table 20 lists equivalent widths of prominent, undisturbed lines (strongest and weakest) for the neutron capture elements. Annex, Section 7.2.1 (Figures 60 to 68) provides views of spectral ranges to support the line identification of neutron capture elements. The strongest lines stem from Sr II. Sr and Ba are highly ionized due to their low first ionization potentials, 5.69 and 5.21 eV, respectively. They exist mostly in form of Sr II and Ba II - even in the atmospheres of cool stars. There are no strong Ba II lines expected in the NIR range.
The majority of lines attributable to neutron capture elements is found for Ce II. About 50 lines from the line list published by Corliss (1973) are identifiable in the 10 Leo spectrum but are not reported in the VALD3 file. Cunha *et al.* (2017) report the identification and

Table 21: Comparison of Ce II lines

Reference: Cunha *et al.* (2017)			This work		
λ(nm[a])	log *gf*	Intensity	λ(nm)	EW (mÅ)	Comments
1528.18	-1.94	5	1528.17	12	
1578.91	-1.54	7	1578.90	42	C I:1578.92
1583.42	-1.80	6	1583.41	30	
1596.28	-1.71	6	1596.27	52	Fe I:1596.25
1598.15	-2.10	6	1598.15	30	
1633.18	-2.40	4	1633.18	4	
1638.10	-1.79	7	1638.10	67	
1659.97	-2.19	7	1659.97	36	
1672.71	-1.65	7	1672.72	47	

[a]values converted from air to vacuum

characterization of nine Ce II lines in the H-band spectral window which have been studied in the spectra of a sample of red giants observed by the Apache Point Observatory Galactic Evolution Experiment(APOGEE) which includes Arcturus. Table 21 compares these lines with the 10 Leo observation. The line positions are in good agreement. The lines for Zn, Sr and Y could be definitely identified. The presence of Cu, Zr, Rb, Yb, Dy, Er and Yb lines is close to the background. Further studies, varying the abundance for these elements in the synthetic spectra may give location and a value of the lower limit of detection in the observed spectrum.

Table 22: Comparison of Nd II lines

Reference: Hasselquist *et al.* (2016)			This work		
λ(nm[a])	log *gf*	Intensity	λ(nm)	EW (mÅ)	Comments
1528.86	-2.13	6	1528.88	104	CN 0-1Q_{1}56.5
1537.23	-1.55	5	1537.26	11	Fe I
1591.66	-2.39	5	1591.67	2	Mg I
1598.23	-2.47	5	1598.23	12	CO 5-2R32
1605.80	-2.2	5	1605.80	5	OH 3-1P_{1*e*}9.5
1626.65	-1.99	5	1626.68	12	CO 6-3R10
1630.82	-2.11	5	1630.81	8	Fe I
1638.74	-1.48	4	1638.74	13	CN 2-3P_{1}46.5
1656.27	-2.4	3	1656.27	6	Fe I
1663.92	-2.37	3	1663.92	26	Ti I

[a]values converted from air to vacuum

The identification of Nd failed in the 10 Leo spectrum. Table 22 lists Nd II lines previously reported by Hasselquist *et al.* (2016) in comparison with the observed 10 Leo spectrum. The authors present the detection of 10 lines of Nd II in H-band spectra using observations from the APOGEE survey. These lines are very weak and should be heavily blended. None of the lines could be identified in the spectrum of 10 Leo despite its superior spectral resolution as compared to the APOGEE survey.

4.3 Identification of molecules

Molecular lines provide an excellent tool for wavelength calibration. However, due to the large number of lines they will blend with most of the metal lines and will even "bury" weak and moderate metal lines to the extent that they will become undetectable.
The abundant molecular lines stem from CO, CN and OH molecules. In addition some weak lines from CH and SiO are found. Annex, Section 7.2.2 (Figures 69 to 72) shows several specific cutouts to illustrate the variety of the rovibrational molecular lines. The selection of cutouts includes also molecular lines from the isotopes ^{13}CO, ^{12}C^{17}O and ^{12}C^{18}O.
This veritable mixture of lines is difficult to analyse, especially for identification of unknown lines, unless the lines are properly assigned to their covibrational band. A major effort was spent to organize this "jungle" of lines by attributing molecular lines to their transition within each band. Lines belonging to a specific band, have been identified by the Arcturus/HITRAN data and their wavelengths are fitted versus the rotational quantum number J with a 4th order polynomial to find missing members which are not attributed to a specific transition.

4.3.1 CO molecule

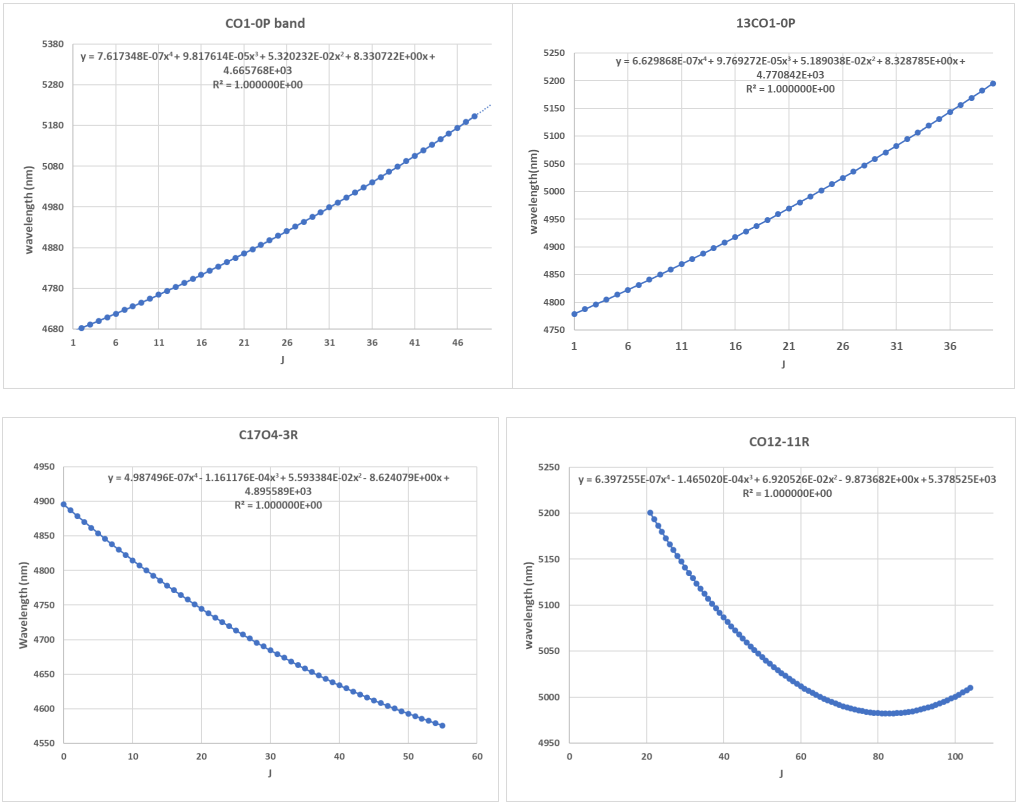

Figure 14: Examples of polynomial fits for transition identification

A large number of CO lines is found in the H, K and M region. The covibrational lines are grouped in bands that are distinguished by the P and R branch, vibrational transition and isotopic differences. The Arcturus spectrum identifies only half of the CO-lines that are present in the 10 Leo spectrum. There is an almost complete match with the VALD3 atlas, however no transition information is given in VALD3 extracted stellar data. To overcome this problem, CO lines with available transition information are separated into the individual bands by sorting them in a

dedicated Excel spreadsheet. In a next step, all lines belonging to the same branch with the same vibrational transition and same isotopics are grouped together and sorted in ascending order by their rotational number J. Gaps in the sequence of J show that lines are missing. The wavelength of all lines are calculated by 4th order polynomial fits J versus wavelength. Typical examples are given in Figure 14 for the ^{12}CO1-0P, ^{13}CO1-0P, ^{12}CO11-12R and $^{12}C^{17}$O5-4R bands.

Table 23: Rovibrational CO-bands evaluated

Filter	P=P-branch, R=R-branch					
M	CO1-0P	CO2-1P	CO3-2P	CO4-3P	CO5-4P	CO6-5P
M	CO7-6P	CO8-7P	CO9-8P			
M	^{13}CO1-0P	^{13}CO2-1P	^{13}CO3-2P	^{13}CO4-3P	^{13}CO5-4P	^{13}CO6-5P
M	^{13}CO7-6P					
M	C^{18}O1-0P	C^{18}O2-1P	C^{18}O3-2P	C^{18}O4-3P	C^{18}O5-4P	
M	C^{17}O1-0P	C^{17}O2-1P	C^{17}O3-2P	C^{17}O4-3P		
M	CO1-0R	CO2-1R	CO3-2R	CO4-3R	CO5-4R	CO6-5R
M	CO7-6R	CO8-7R	CO9-8R	CO10-9R	CO11-10R	CO12-11R
M	CO13-12R	CO14-13R				
M	^{13}CO1-0R	^{13}CO2-1R	^{13}CO3-2R	^{13}CO4-3R	^{13}CO5-4R	^{13}CO6-5R
M	^{13}CO7-6R	^{13}CO8-7R	^{13}CO9-8R	^{13}CO10-11R	^{13}CO12-11R	
M	C^{18}O1-0R	C^{18}O2-1R	C^{18}O3-2R	C^{18}O4-3R	C^{18}O5-4R	C^{18}O6-5R
M	C^{18}O7-6R	C^{18}O8-7R				
M	C^{17}O1-0R	C^{17}O2-1R	C^{17}O3-2R	C^{17}O4-3R	C^{17}O5-4R	C^{17}O6-5R
K	CO2-0P	CO3-1P	CO4-2P	CO5-3P	CO6-4P	CO7-5P
K	^{13}CO2-0P	^{13}CO3-1P	^{13}CO4-2P	^{13}CO5-3P		
K	CO2-0R	CO3-1R	CO4-2R	CO5-3R	CO6-4R	CO7-5R
K	CO8-6R	CO9-7R				
K	^{13}CO2-0R	^{13}CO3-1R	^{13}CO4-2R	^{13}CO5-3R	^{13}CO6-4R	^{13}CO7-5R
H	CO3-0P	CO4-1P	CO5-2P	CO6-3P	CO7-4P	CO8-5P
H	CO9-6P	CO10-7P	CO11-8P			
H	CO3-0R	CO4-1R	CO5-2R	CO6-3R	CO7-4R	CO8-5P
H	CO9-6R	CO10-7R	CO11-8R	CO12-9R	CO13-10R	

Using this method about 99.7 % of all CO-lines listed in VALD3 stellar request (Table 3) could be attributed to their respective band including transition information. Graphical plots showing cdepth versus wavelength and log *gf* versus wavelength are used to confirm the line assignments for a specific band. This is demonstrated in Figure 15 for several bands. In general, very good agreement within 0.1 Å is achieved and lines can be unambigously attributed. The identification of molecular lines is important as they often blend with metal lines and "unknown lines" might be discovered knowing the strength of the respective blending contribution. A total of 105 CO-bands (64 in M, 23 in K and 18 in H) are evaluated including about 4500 CO lines (Table 23).

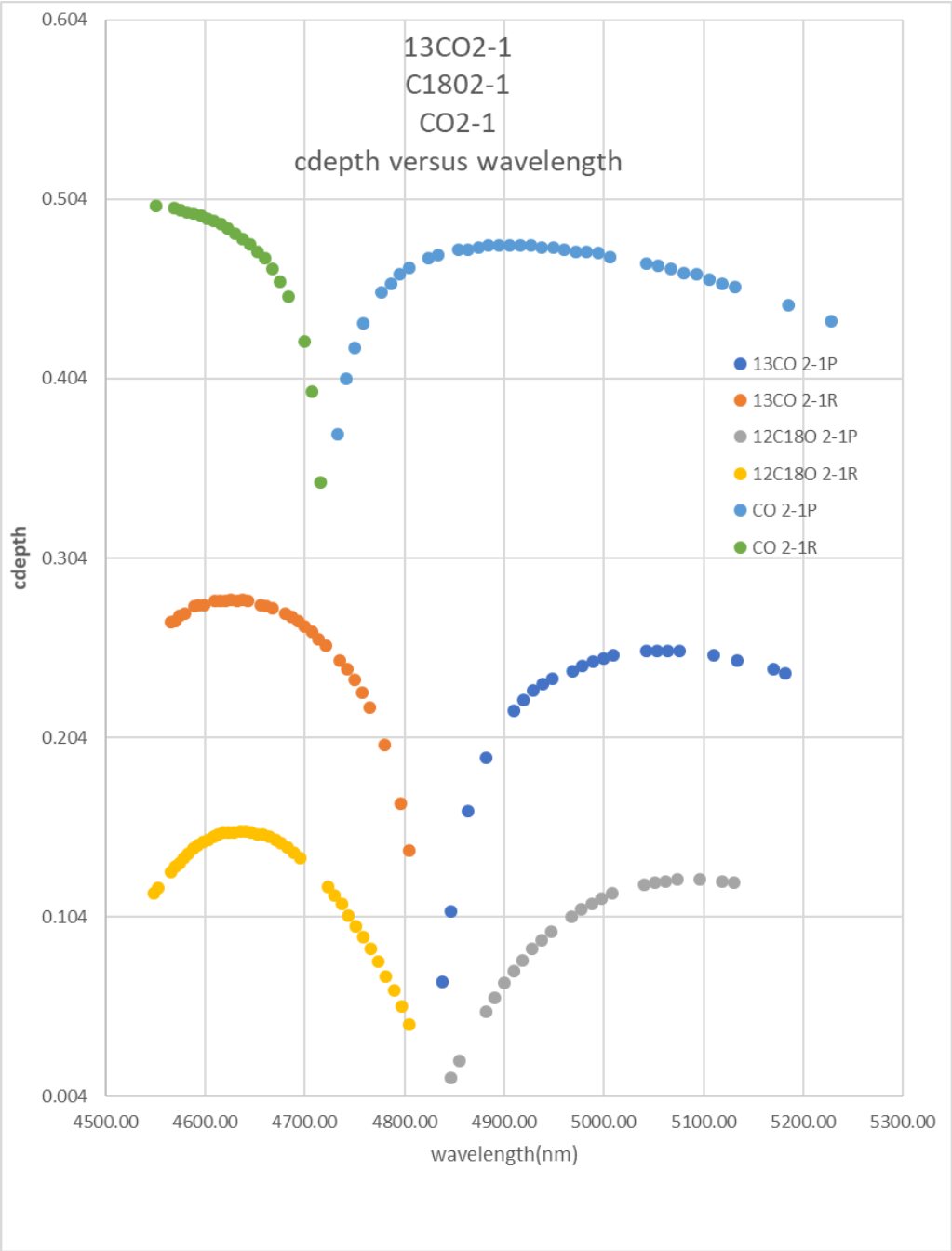

Figure 15: Wavelength versus cdepth for various CO-bands

The observed strength of the CO lines differs systematically within the band as well as between the bands. The strongest bands (fundamental bands) are found in the M region with decreasing strength from the CO1-0 (max cdepth=0.501) to the CO14-13 (max cdepth=0.074).
A plot of the reduced equivalent widths versus cdepth (1-f) shows a linear behaviour (Figure 16). The graph represents only data from unblended lines with stable background conditions and (1-f) < 0.4 ("optically thin"). In addition an outlier test on a 2 σ-level is applied and data points are binned by averaging ten (1-f)-values. The obvious correlation is valuable to correct for the CO share of blended lines.

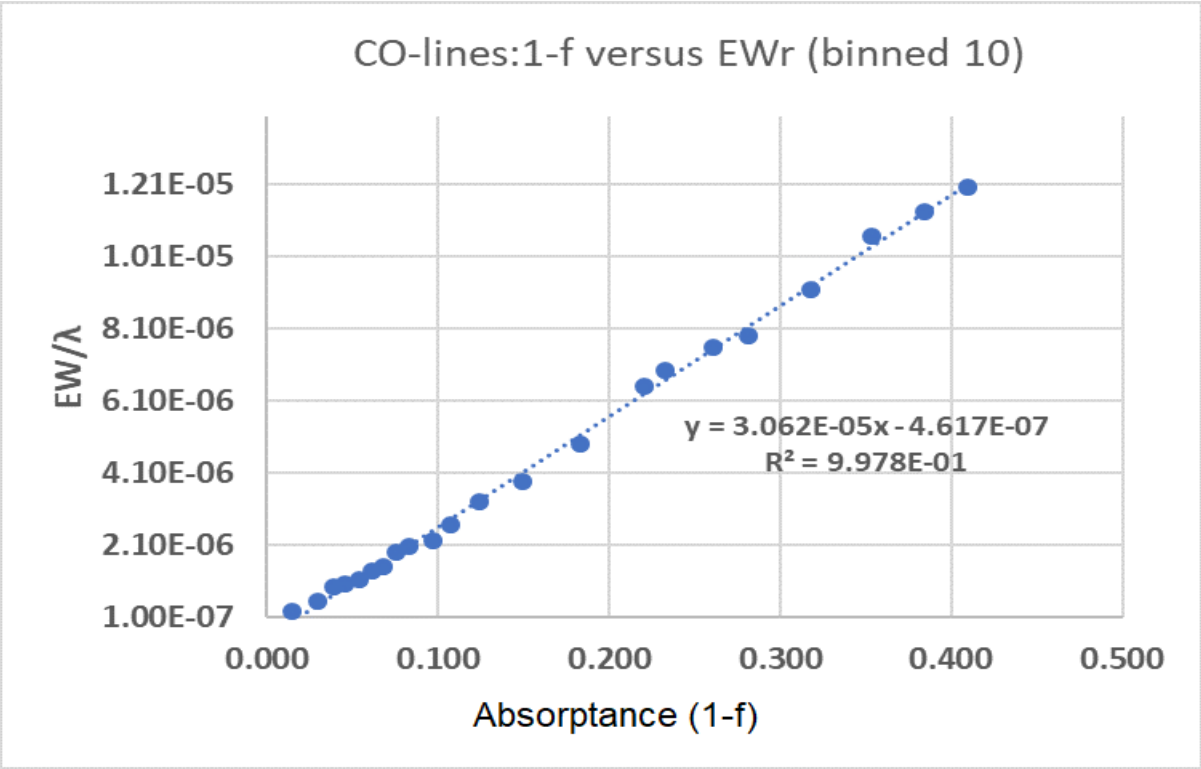

Figure 16: Reduced equivalent width versus (1-f(norm) at λ) for CO lines

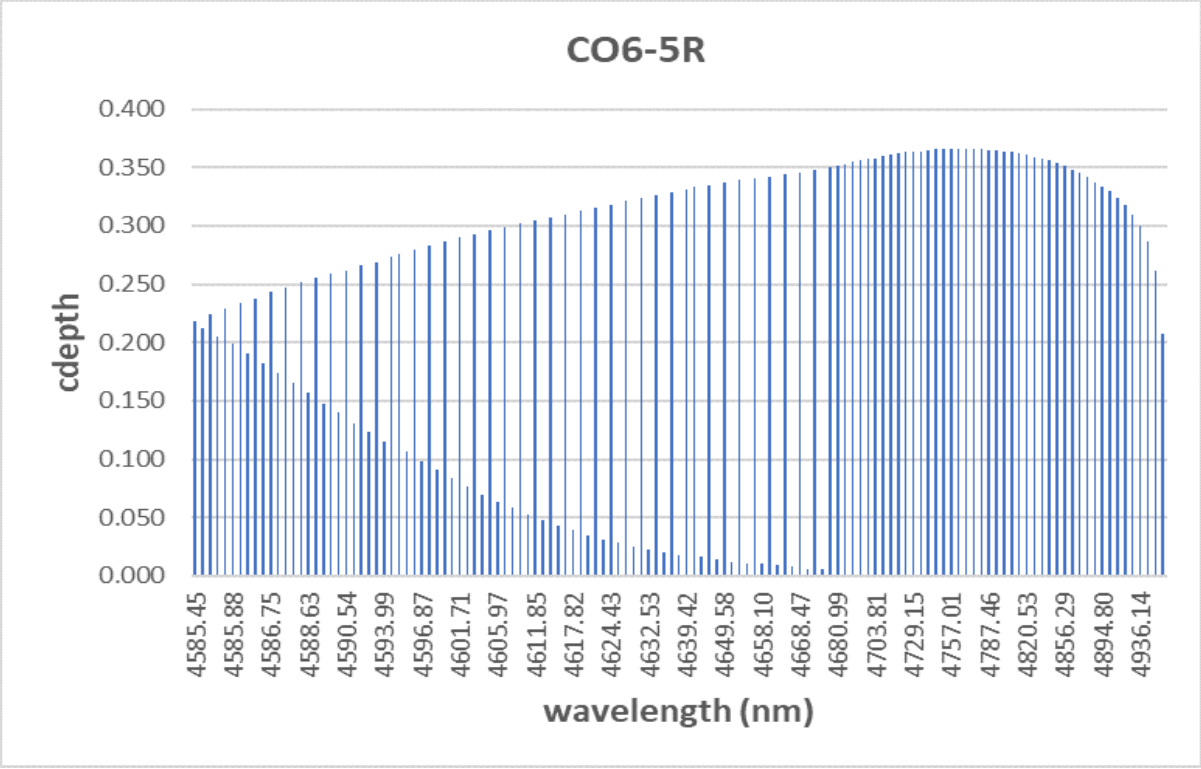

Figure 17: Variation of cdepth (VALD3 values) within the CO6-5R band

Figure 17 shows the expected variation (calculated VALD3 values) within the CO6-5R band which covers the full range of rotational transitions (J = 0 to J = 128) and is completely observable

within the M region. The cdepth increases sharply from J = 0 (λ=4962.33 nm, cdepth = 0.208) to J = 10 (λ=4879.06 nm, cdepth = 0.342) followed by a moderate increase until a flat region around J = 28 (λ=4757.01 nm, cdepth = 0.366) is reached. The cdepth drops very slowly (e.g. cdepth = 0.316 at J = 60, 4621.72 nm) and than drops faster until the last observed transition at J = 128 (cdepth = 0.006, λ=4675.42.33 nm). The bend in the wavelength at about J = 87 (λ=4585.42 nm, cdepth = 0.218) is also clearly visible. The level spacing around this point becomes very small. The turning point is called the **bandhead**. This pattern is only observed for the R-branch and can be explained by the centrifugal distortion expressed by the centrifugal constant D. The calculation of the level spacing constant k is given by:

$$k = G(v) + B_v J(J+1) - D_v(J(J+1))^2 + ... \tag{42}$$

Although D_v is several orders of magnitude smaller than the rotational constant B_v that describes the "normal" spacing between the levels J and J+1, the contribution of D_v increases quadratically in the term (J+1)J and at the bandhead both terms are equal. It is to be noted that in most branches only part of the full range of J-values is observable within the respective bandpass region.

4.3.2 CN molecule

The CN molecule has a more complicated IR spectrum than CO caused by the splitting of levels (quantum number S) in half. This results in additional branches **R{2}, P{2}, Q{1}** and **Q{2}**. The same data analysis as described in the previous Section 4.3.1 has been applied and branches have been reconstructed. A typical example is given in Figure 18 for the CN 0-1P1 band. The black dots denote datapoints with available transition information, whereas the red data points are "newly" identified. In some cases only 5 original datapoints from a branch are available but the stepwise fit can successfully reconstruct the missing data for the whole branch. The correlation coefficient R = 1 indicates that the fit of the data over the whole branch is valid. In addition to the "newly" assigned lines, the fit could also identify possible mistakes in the dataset, e.g. wrong wavelength assignment for a particular transition.

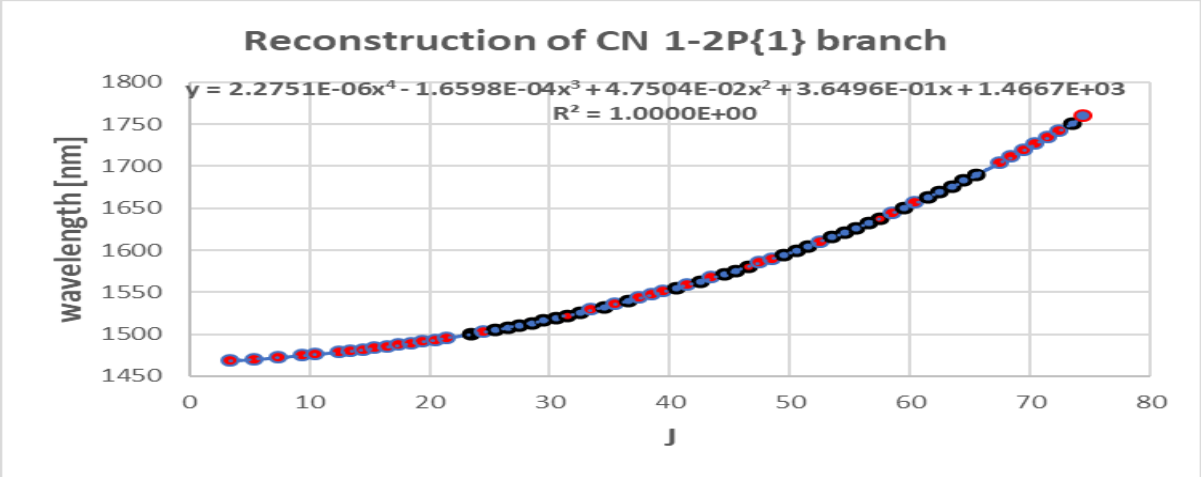

Figure 18: Reconstruction of CN 0-1P1 branch (black dots=original data, red dots=fitted data)

With this method most of the CN-lines with cdepth>0.01 could be attributed to their respective band. In a subsequent exercise, the catalogue of CN-lines from Brooke *et al.* (2014) has been matched with the 10 Leo spectrum and 99.5% of the CN lines listed in the VALD3 extraction file have been assigned. In total, 5158 out of 5186 reported lines (cdepth >0.005, gaps excluded)

have been assigned to their individual bands. A total of 138 bands (61 in YJ, 41 in H, 36 in K) are evaluated resulting in assignments of about 5158 individual CN lines matched with the VALD3 stellar extraction and/or Arcturus atlas. The strongest CN lines are found in the Q, R, P branches within the vibrational transitions of 0-0 (YJ), 1-0 (YJ) and 0-1 (H) states. The transitions of 2-1 (YJ), 1-2 (H) and 2-3 (H) have a medium strength while P,R, Q-bands for 0-2, 1-3, 2-4 and 3-5 are observed with weak intensities in the K-band.

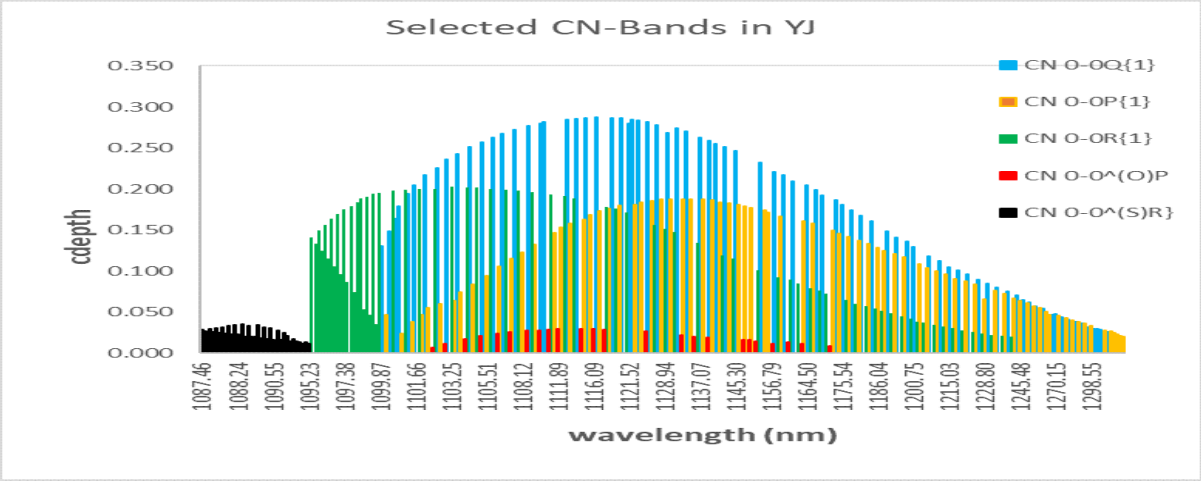

Figure 19: Selected CN 0-0 bands in YJ region

The majority of the transitions for CN are only partly identified in the Arcturus atlas (<50%). No transition information regarding the ^{13}CN is given in VALD3 extracted stellar data. Figure 19 compares the branches for the 0-0 vibrations.

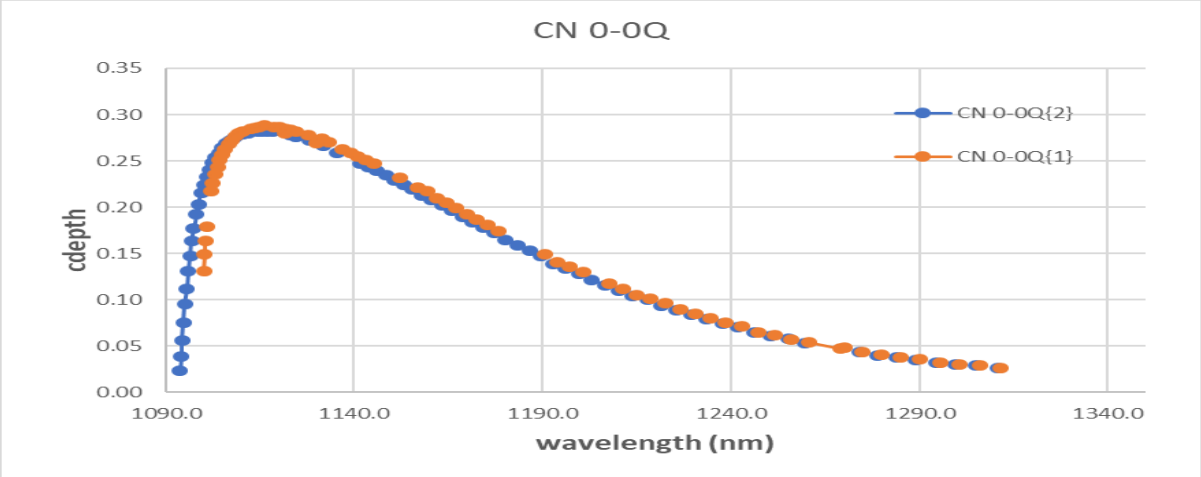

Figure 20: CN 0-0Q1 and CN 0-0Q2 in the YJ region

The CN 0-0Q1 and CN 0-0Q2 branches in Figure 20 show very small differences in their wavelength and cdepth. In addition, there are two weak satellite bands for each P, Q and R branch, namely **P{12}, P{21}, Q{12}, Q{21}, R{12}** and **R{12}**. The satellite bands are about 10 times weaker than the main bands and show a distinctly different behaviour as compared to the main bands. While the maximum intensity for a transition within a main band occurs at J ≈31, the maximum for the satellite band is shifted to J ≈10 (see Figure 21). Furthermore, the

log *gf* values for transitions of the satellite bands as a function of J show a distinct maximum, whereas the log *gf* values for the main bands are steadily increasing (see Figure 22).

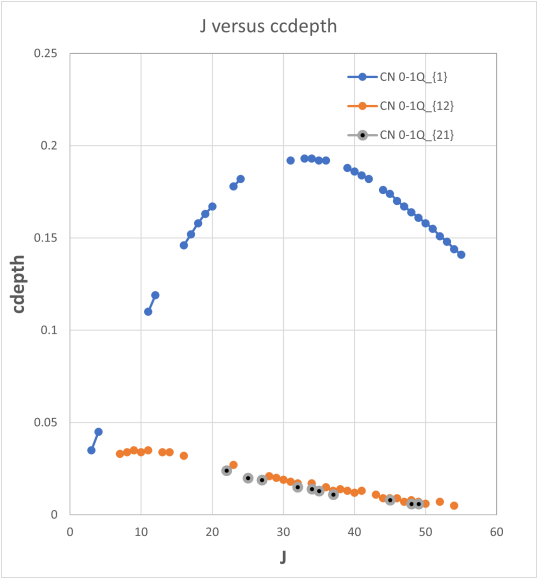

Figure 21: Rotational quantum number versus cdepth of transition line for CN 0-1Q_{1}, CN 0-1Q_{12} and CN 0-1Q_{21}

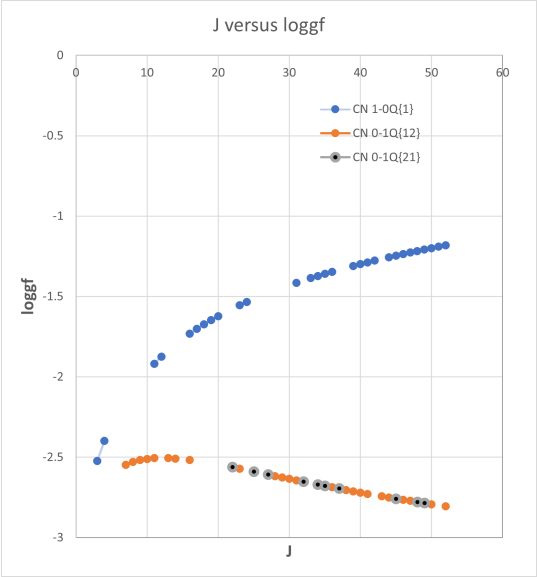

Figure 22: Rotational quantum number versus log *gf* value of transition line for CN 0-1Q_{1}, CN 0-1Q_{12} and CN 0-1Q_{21}

Table 24 - 26 provide an overview of all observed CN-bands in the 10 Leo spectrum. From the remarkable strength of the ^{13}CO lines (see 4.3.1), one would expect ^{13}CN lines to be clearly visible, too. However, only weak lines from ^{13}CN0-0Q1,^{13}CN0-0Q2, ^{13}CN0-0P1, ^{13}CN0-0P2, ^{13}CN0-0R1 and ^{13}CN0-0R2 have been identified in the 10 Leo spectrum. No lines of C^{15}N could be identified in the 10 Leo spectrum, using the catalogue of CN lines from Brooke *et al.* (2014). The central depths for unblended CN lines as given by the (1-norm flux)-value at the line center is plotted versus the **reduced equivalent width** (**EW$_r$**, Figure 23). The linear plot represents

Table 24: CN-lines: number of assigned lines to various bands, cdepths(max) compared with VALD3 and equivalent widths (EW) in the YJ-band

Main band	Sub bands	#lines assigned	cdepth (max)		EW (mA)
			VALD3	10 Leo	10 Leo
13CN 0-0	R{1}, R{2}	47	-	0.021	5
	P{1}, P{2}	42	-	0.023	
	Q{1}, Q{2}	44	-	0.032	6
CN 0-0	R{1}, R{2}	167	0.202	0.260	87
	R{12}, R{21}	92	0.047		17
	P{1}, P{2}	156	0.188	0.258	81
	P{12}, P{21}	79	0.040		19
	Q{1}, Q{2}	168	0.285	0.333	111
	Q{12}, Q{21}	96	0.070		32
CN 1-0[a]	R{1}, R{2}	53	>0.070	>0.200	>53
	P{1}, P{2}	85	>0.123	>0.170	>40
	Q{1}, Q{2}	75	>0.174	>0.190	>60
	Q{12}	11	>0.011	>0.015	>4
CN 1-1	R{1},R{2}	65	0.014	0.025	6
	P{1}, P{2}	93	0.013	0.027	9
	Q{1}, Q{2}	104	0.025	0.040	12
CN 2-1	R{1}, R{2}	74	0.053	0.102	27
	P{1}, P{2}	116	0.062	0.112	29
	Q{1}, Q{2}	98	0.114	0.178	41
CN 2-2	R{1}, R{2}	5	-	0.016	4
	P{1}, P{2}	5	-	0.014	4
	Q{1}, Q{2}	11	-		
CN 3-2	R{1}, R{2}	109	0.015	0.035	8
	P{1}, P{2}	108	0.014	0.024	7
	Q{1}, Q{2}	138	0.028	0.041	10
CN 3-3	R{1},R{2}	74	0.009	0.018	5
	P{1}, P{2}	76	0.008	0.016	4
	Q{1}, Q{2}	111	0.015	0.030	8
CN 4-4	R{1}, R{2}	44	0.007	0.014	4
	P{1}, P{2}	48	0.007	0.015	4
	Q{1}, Q{2}	98	0.013	0.020	9

[a]maximum outside wavelength interval

Table 25: CN-lines: number of assigned lines to various bands, cdepths(max) compared with VALD3 and equivalent widths (EW) in the H-band

Main band	Sub bands	#lines assigned	cdepth max		EW (mA)
			VALD3	10 Leo	
CN 0-1	R{1}, R{2}	113	0.110	0.190	55
	R{12}, R{21}	17	0.020	0.022	10
	P{1}, P{2}	126	0.116	0.210	62
	P{12}, P{21}	37	0.016	0.020	9
	Q{1}, Q{2}	117	0.192	0.231	99
	Q{12}, Q{21}	41	0.034	0.024	18
CN 1-2	R{1}, R{2}	154	0.068	0.118	36
	R{12}, R{21}	29	0.013	0.012	5
	P{1}, P{2}	130	0.075	0.135	46
	P{12}, P{21}	39	0.012	0.007	4
	Q{1}, Q{2}	136	0.123	0.180	68
	Q{12}, Q{21}	59	0.017	0.020	10
CN 2-3	R{1}, R{2}	111	0.028	0.050	14
	R{12}	9	0.005	0.005	3
	P{1}, P{2}	113	0.028	0.040	16
	P{12}, P{21}	4	0.005	0.005	3
	Q{1}, Q{2}	123	0.053	0.115	30
	Q{12}, Q{21}	38	0.009	0.007	4
CN 3-4	R{1}, R{2}	47	0.007	0.022	4
	P{1}, P{2}	35	0.007	0.030	4
	Q{1}, Q{2}	80	0.013	0.031	8

Table 26: CN-lines: number of assigned lines to various bands, cdepths(max) compared with VALD3 and equivalent widths (EW) in the K-band

Main band	Sub bands	#lines assigned	cdepth max		EW (mA)
CN 0-2	R{1}, R{2}	119	0.025	0.044	20
	P{1}, P{2}	104	0.021	0.036	17
	Q{1}, Q{2}	126	0.045	0.078	37
	Q{12}, Q{21}	22	0.006		5
CN 1-3	R{1}, R{2}	116	0.022	0.038	18
	P{1}, P{2}	94	0.020	0.032	18
	Q{1}, Q{2}	106	0.042	0.069	35
	Q{12}, Q{21}	29	0.006		5
CN 2-4	R{1}, R{2}	97	0.014	0.025	13
	P{1}, P{2}	77	0.013	0.022	8
	Q{1}, Q{2}	103	0.027	0.043	22
CN 3-5	R{1},R{2}	9	-	0.010	4
	P{1}, P{2}	9	-	0.018	6
	Q{1}, Q{2}	34	-	0.020	8

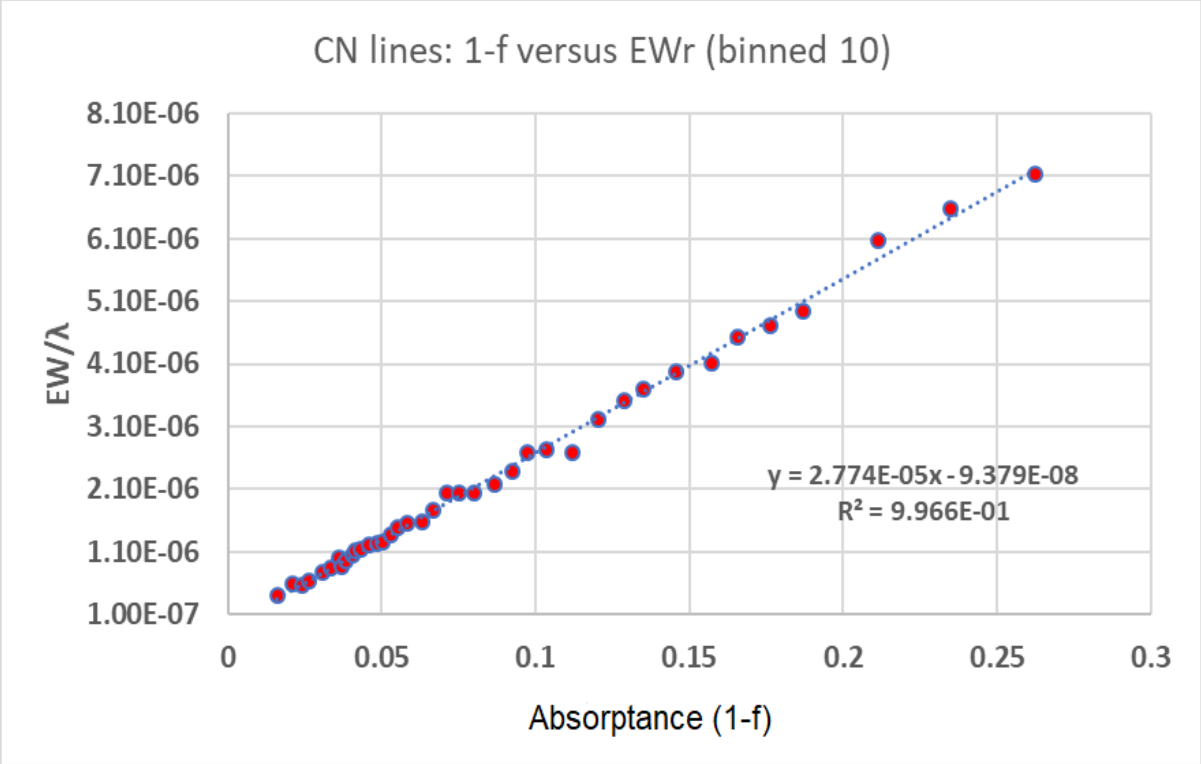

Figure 23: Reduced equivalent width versus (1-f) for CN lines

only data from unblended lines (390) with stable background conditions. The data is binned by averaging ten (1-f)-values and removing outliers that differ by more than two standard deviations from the average value. With this linear correlation it is possible to correct for the CN share of blended lines and to decide on the line assignment due to different contributors.

4.3.3 OH molecule

32 bands for the OH-molecule have been identified and evaluated. Table 27 summarizes the observed bands for OH.

Table 27: Rovibrational OH-bands evaluated

Filter	P=P-branch					
H	OH2-0P1e	OH2-0P1f	OH2-0P2e	OH2-0P2f	OH3-1P1e	OH3-1P1f
H	OH3-1P2e	OH3-1P2f	OH4-2P1e	OH4-2P1f	OH4-2P2e	OH4-2P2f
H	OH5-3P1e	OH5-3P1f	OH5-3P2e	OH5-3P2f		
L	OH1-0P1e	OH1-0P1f	OH1-0P2e	OH1-0P2f	OH2-1P1e	OH2-1P1f
L	OH2-1P2e	OH2-1P2f	OH3-2P1e	OH3-2P1f	OH3-2P2e	OH3-2P2f
L	OH4-3P1e	OH4-3P1f	OH4-3P2e	OH4-3P2f		

Figure 24 shows a region in the L-band of the 10 Leo spectrum with strong OH-lines which are even more prominent in the Arcturus spectrum.

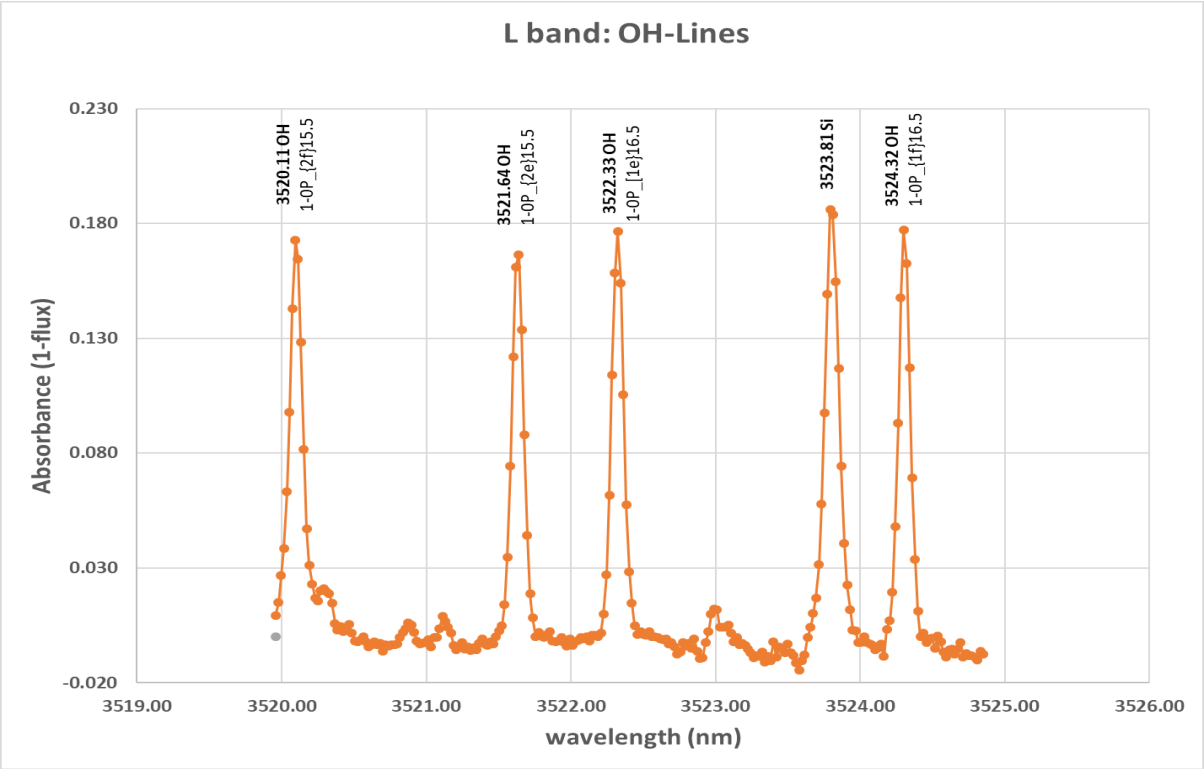

Figure 24: OH-lines in a region of the L-band

4.3.4 Other molecules

Weak signatures of CH and SiO are found but no lines from TiO or hydrides. A cutout featuring CH is attached in the Annex to proof its presence. The NH molecule is identified in the Arcturus spectrum in a region from 2891.00 nm to 3397.94 nm. This region is not covered by the 10 Leo spectrum except a small part starting at 3367.02 nm. Only two lines of the NH molecule at 3373.06 nm and 3397.94 nm could be identified in the 10 Leo spectrum.

4.4 Identification of unknown lines

Table 28: Number of unknown lines

	Band					
EW-Interval	YJ	H	K	L	M	All
≤10 mÅ	194	92	64	138	0	488
>10 mÅ ≤50 mÅ	156	118	67	215	23	579
>50 mÅ ≤100 mÅ	17	42	11	42	19	131
> 100mÅ	0	34	11	12	27	84
Total	367	286	153	407	69	1282

A large effort has been spent to identify lines, which are not reported in literature. The number of possible candidates exceeds 1200 lines which could not be attributed (cdepth >0.005). Table 28 shows the number of lines for each band sorted in intervals of equivalent widths of ≤ 10, >10 ≤ 50, >50 ≤ 100 and >100.

Values of the EWs are often only of qualitative nature due to noisy background, blending by other lines, etc.. The 10 Leo spectrum has a calibration error in the wavelength of less than 0.2 Å. All lines which are not matched within 1 Å of their reported wavelength are considered as "unknown" lines. A detailed line list of "unknowns" (EW ≥50 mÅ) has been compiled for each bandpass which includes position, EW and possible contributors. The lists are included in the Annex, Section 7.1.1, Tables 49-53. In addition several spectral cutouts with unknown lines are presented in the Annex, Section 7.2.3, Figures 77-86 as well.

4.5 Comparison between 10 Leo and Arcturus spectra

10 Leo and Arcturus are both K-stars. Arcturus is ≈ 500 K cooler than 10 Leo and has a lower metallicity than 10 Leo. They also differ in their age, log g value, radius and luminosity (see Table 1). From the differences in the stellar atmospheres, e.g. Arcturus has a lower log g value and a lower pressure due to its extended radius, it is expected that the Arcturus spectrum should feature more pronounced and stronger molecular lines and less metallic lines due to the lower metallicity than the 10 Leo spectrum. The data files for the IR-spectrum of Arcturus (Hinkle *et al.*, 1995)[7], cover two observation periods (summer and winter). The individual Arcturus files are combined to match the bandpasses of 10 Leo.

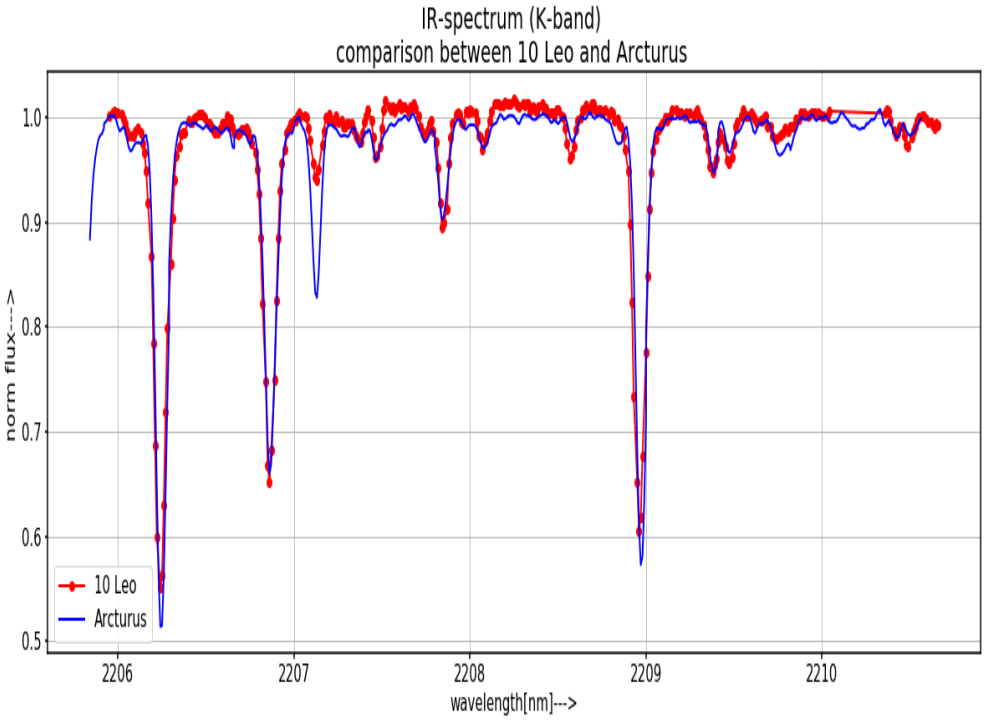

Figure 25: Overlay spectra 10 Leo and Arcturus for 5 major lines

Figure 25 shows a typical spectral section with 5 major lines at 2206.24 nm (Na I), 2206.87 nm (Si I), 2207.13 nm (Sc I), 2207.86 nm (Si I) and 2208.97 nm (Na I) in the overlay mode. The most obvious difference between both spectra is the line for Sc I (2207.13 nm), which is significantly enhanced in Arcturus. Only a small enhancement is observed for Na I lines (2206.24 nm, 2208.97 nm) and a minor reduction can be noted for the Si lines (2206.87nm, 2207.86 nm).

[7]downloaded from ftp://ftp.noao.edu/catalogs/arcturusatlas/ir/

Table 29: Ratios of equivalent widths (Arcturus/10 Leo)

species	Ratio (Arcturus/10 Leo)	# evaluated lines
CO	1.73 ± 0.23	35
CH	1.37 ± 0.31	10
C I	0.76 ± 0.15	9
CN	0.83 ± 0.13	171
OH	3.26 ± 0.43	37
Na I	0.94 ± 0.03	3
Mg I	1.10 ± 0.14	20
Al I	1.12 ± 0.02	10
Si I	0.94 ± 0.10	51
K I	1.13 ± 0.13	4
Ca I	1.01 ± 0.11	22
Sc I	1.90 ± 0.68	3
Ti I	1.54 ± 0.12	27
V I	1.69 ± 0.30	4
Cr I	0.95 ± 0.10	17
Mn I	1.03 ± 0.01	7
Fe I	0.96 ± 0.11	164
Ni I	0.97 ± 0.10	10
Sr II	1.04 ± 0.06	3

Annex, Section 7.2.4 (Figures 87-108), offers further spectral cutouts of overlay spectra between 10 Leo and Arcturus for a number of elements and molecules. These spectral cutouts are shown as absorptance versus wavelength and are combined with line information such as line position, identification, log gf, cdepth(solar), EW(Leo) and match status. The largest differences in central depth are noted for Ti I (Fig. 93), Sc I (Fig. 100), V I (Fig. 104), OH (Fig. 109) and CO (Fig. 105), which are reduced in 10 Leo. Higher values for 10 Leo are found for Fe I (Fig. 94), S I (Fig. 92), C I (Fig. 88) and CN (Fig. 108). Some differences between the isotopologues of CO are observed. 10 Leo is enhanced in $^{12}C^{17}O$ (Fig. 111) compared to Arcturus, whereas $^{13}C^{16}O$ is weaker in 10 Leo than in Arcturus (note the difference in the bandheads as shown by Fig. 107 and Fig. 105) for both isotopes.

In general, it is noted that the spectra from 10 Leo and Arcturus are very similar and only small differences are observed. From the observed differences in the 10 Leo and Arcturus spectra, there is little hope to see metal lines in Leo which are not present in Arcturus or at least reduced in Arcturus. The Sr II - lines (10039.4 Å, 10330.2 Å, 10917.9 Å, see also Fig. 101) are prominent lines in both spectra.

A later analysis using synthetic spectra with the respective temperatures (10 Leo=4800 K, Arcturus=4300 K) and log g values (10 Leo=2.83, Arcturus=1.67) revealed more differences in the various element abundances.

Table 29 lists the ratios of observed EWs for Arcturus and 10 Leo. The respective EWs have been obtained with the spectrum analysis tool BinMag2 (Kochukhov, 2018) . Most of the ratios are close to 1, which stresses that a comparison between 10 Leo and Arcturus spectrum may not help to identify new lines of higher Z elements. However, the direct comparison helps to identify contributions/assignments of lines for OH, CO, Sc I, V I and Ti I.

It is quite surprising that most of the ratios are close to 1 as both stars differ significantly in

Table 30: Properties of models used for simulation

Star	Parameter:	T_{eff} (K)	log g	v_{mic} (km/s)	Model
Arturus		4250	1.5	1.5	castelli_ap00k2_T04250G15.krz
10 Leo		4750	3	2	castelli_ap00k2_T04750G30.krz
Sun		5750	4.5	0	castelli_ap00k2_T05750G45.krz

T_{eff} and log g value. Apparently, the impact of both parameters paired with the differences in abundances are cancelling. Several simulations, varying temperature, v_{mic} and log g values in the VALD3 stellar extraction requests have been performed to investigate their impact on the calculated central depth values of various absorption lines. The simulations use the same scaled solar abundances which means that the simulation should show how the same number of respective atoms influence cdepth at different conditions.
The range of temperatures start at 4250 K (Arcturus) and ends at 5750 K (Sun). In between there is the temperature of 4750 K (10 Leo). Table 30 shows the main models used in the simulations for Arcturus, 10 Leo and the Sun. Temperature can be varied only stepwise by 250 K and log g by 0.5 steps. The variation of v_{mic} is not reflected as part of the name of the model and its input value is used in the calculations. Table 31 summarizes properties of the selected Fe-line used in the simulations.

Table 31: Properties of selected Fe I lines used for simulation

This work				VALD3-data		Andreasen *et al.* (2016)	
λ (nm)	1-f	EW(mÅ) 10 Leo	EW(mÅ) Arcturus	EP(eV)	log gf	log gf	EW(mÅ) Sun
1034.37	0.391	116	127	2.20	-3.577	-3.672	46.7
1035.08	0.190	55	37	5.39	-0.551	-0.754	36.9
1042.66	0.271	84	87	3.07	-2.918	-3.121	29.7
1205.63	0.240	75	63	4.56	-1.543	-1.645	39.6
1212.27	0.167	49	73	4.59	-1.635	-1.809	29.5
1256.04	0.323	117	118	2.28	-3.626	-4.023	33.4
1281.07	0.280	111	98	3.64	-2.452	-2.664	36.0
1315.15	0.223	87	72	5.39	-0.814	-0.777	55.6
1335.58	0.317	125	129	5.31	-0.521	-0.479	91.4
1339.58	0.358	145	137	5.35	-0.125	-0.210	117.9

Figure 26(a), 26(b) and 26(c) show the calculated cdepth versus T_{eff} for various Fe-I lines at fixed v_{mic}=2 km/s for log g=1.5 (a), log g=3 (b) and log g=4.5 (c).
It is noted that the Fe I-lines show differences within the same set of selected parameters. For the log g=1.5 set, the lines at 1034.37 nm and 1256.04 nm start with a high value of cdepth at Arcturus (T=4250 K), stay almost constant until 10 Leo (T=4750 K) and then drop sharply towards the Sun (T=5750 K). Both lines have the the lowest excitation energy of 2.2 eV and 2.3 eV of the set which ranges from 2.2 eV to 5.4 eV. The other lines start with a lower value of cdepth and show a small increase from Arcturus towards 10 Leo and a slow decline towards the Sun.
With increasing log g values (set (b), (c)), the maximum of cdepth is shifted towards higher temperatures and the decrease of cdepth towards the Sun levels off. The ratios of cdepth increase

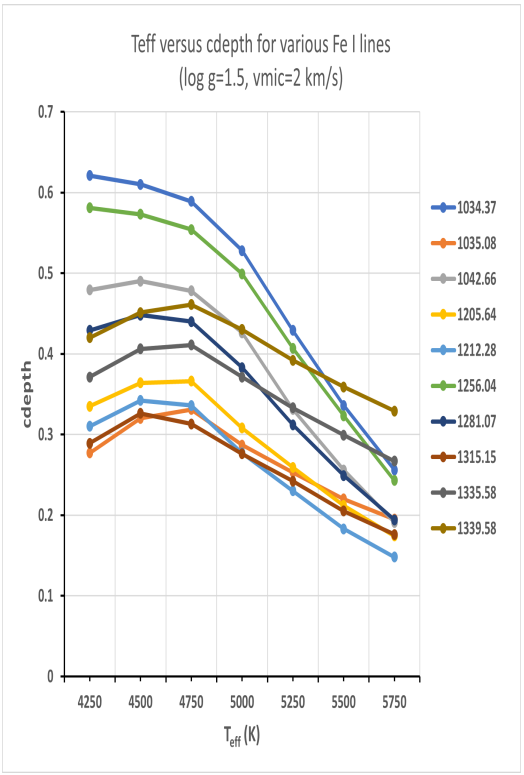

(a) **log g=1.5**

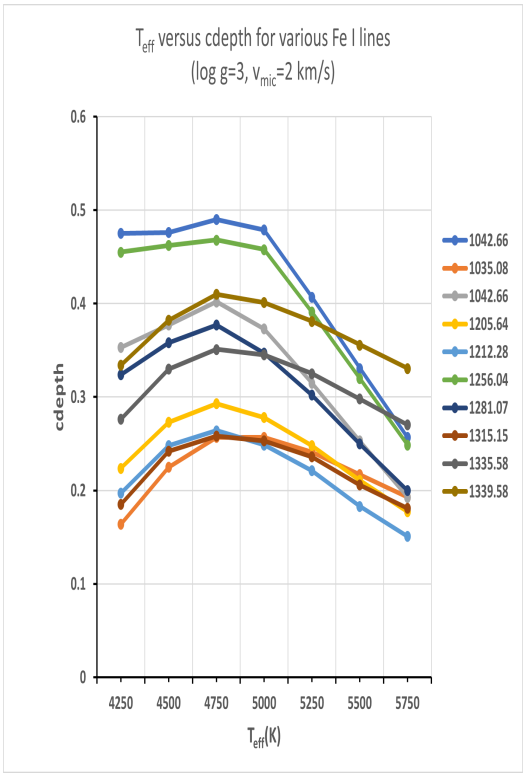

(b) **log g=3.0**

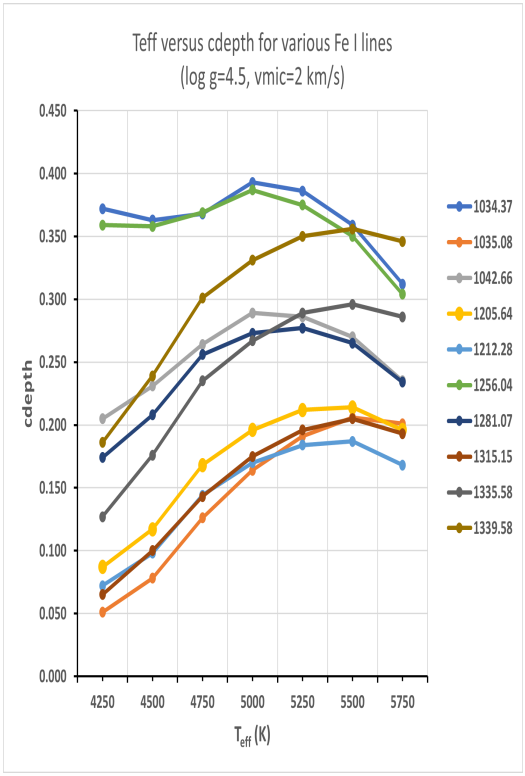

c) **log g=4.5**

Figure 26: Simulation of cdepth of Fe I lines in YJ band as a function of T_{eff} at fixed v_{mic} = 2 km/s

between 10 Leo and Arcturus up to a ratio of 2, except for the two lines with the lowest excitation energy, which remain at a ratio close to 1.
A different picture is observed changing the log g value at a given T_{eff} (Figure 27). The cdepth values for all lines seem to drop almost linear with increasing log g value. With higher temperatures (set 27(c)), the decrease levels off and an almost constant cdepth at different log g values is noted. In particular, the lines at 1034.37 nm and 1256.04 nm for the series (a) (T_{eff} = 4250 K) have the highest cdepth values in set 27(a), (b). These two lines become weaker than the lines at 1335.58 and 1339.58 nm in the third set (Figure 27(c), T_{eff} = 5750 K). Finally increasing v_{mic} values will also increase the cdepth at fixed temperatures and at fixed log g values. Figures 28(a-c) show plots of cdepth as a function of v_{mic} at three different temperature/log g combinations. The values for cdepth decrease with increasing v_{mic}. The differences within set 28 (a) and 28(b), representing Arcturus and 10 Leo are marginal. For the Sun (set 28 (c)) the line at 1339.58 nm is stronger than the lines at 1335.58 and 1256.04 nm.
The review of the simulation data for other element/molecule lines has been restricted to three models with characteristic conditions of Arcturus, 10 Leo and the Sun. Figures 29(a1), (a2) show several metals at v_{mic}=0 km/s compared to v_{mic}=2 km/s for figures 29(b1), (b2). In general, there seems little differences in the cdepth "distribution" of both scenarios, except for a decrease of cdepth with higher v_{mic} and a disproportional decrease for La II with increasing v_{mic}.
The differences become more obvious within the sets. The cdepths for C I, S I and Fe II absorption lines are increasing from Arcturus to Sun whereas those for Ti I, Cr I, V I, Ni I and Ca I are decreasing. V I lines exhibit the largest decrease in cdepth from Arcturus to the Sun (factor ≈25), followed by Ti I (factor ≈10), Y II and La II (factor ≈10).
The steepest drop in cdepth of absorption lines between 10 Leo and Sun is calculated for CN, which can be explained by the destruction of the CN molecule by the high temperature of the Sun. This also explains the rise of C I with higher temperature. The cdepths of Si I lines seem rather constant across the selected cases.
The results of these calculations are consistent with the observed spectra for 10 Leo and Arcturus, e.g. higher cdepth values for Ti I lines in Arcturus and weaker cdepth values for C I lines.

4.6 Synthetic spectra

Synthetic spectra are a valuable tool to determine element abundances. In principle, a computer code builds a stellar atmosphere based on physical parameters such as T_{eff}, log g and microturbulence. Once the stellar atmosphere is produced, its impact on the formation of lines for a given mixture of atoms/molecules is calculated by using atomic and molecular spectral line data and software for radiative transfer. The resulting synthetic spectrum can now be compared to the observed spectrum. Differences between observed and synthetic spectrum will be minimized by adjusting the parameters, e.g. abundances, of the synthetic spectrum. The process is repeated until synthetic spectrum and observed spectrum are in agreement. Assuming that the synthetic spectrum properly corrects for the individual line properties (e.g. differences in line strength due to various excitation energies/temperatures/log g) then the element abundances can be directly taken from the section of scaled abundances of the VALD3 file used for the generation of the synthetic spectrum.

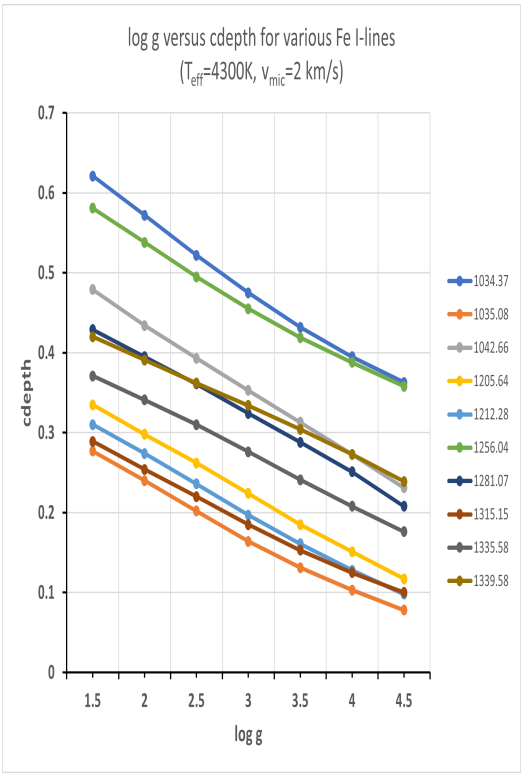

(a) $\mathbf{T_{eff} = 4250\ K}$

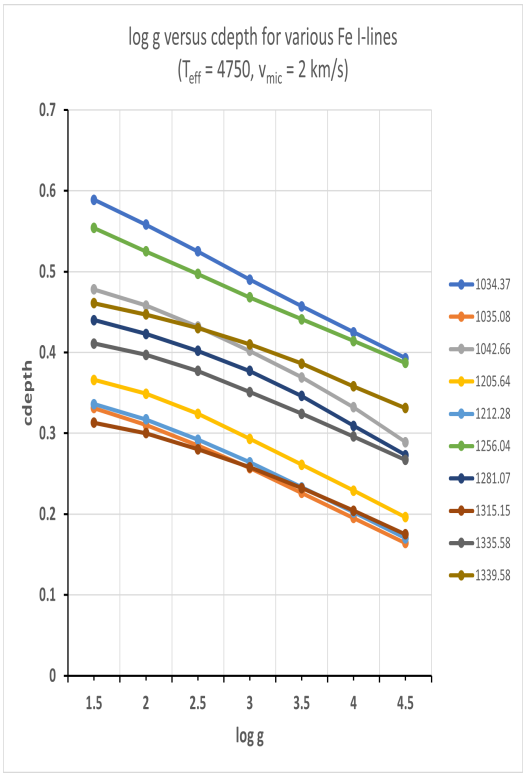

(b) $\mathbf{T_{eff} = 4750\ K}$

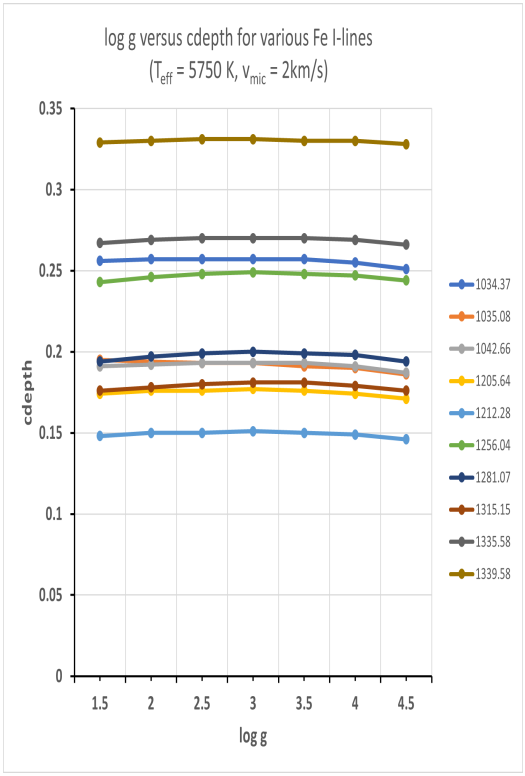

(c) $\mathbf{T_{eff} = 5750\ K}$

Figure 27: Simulation of cdepth of Fe I lines in YJ band as a function of log g at three different T_{eff} (4250 K, 4750 K and 5750 K) and fixed v_{mic}=2 km/s

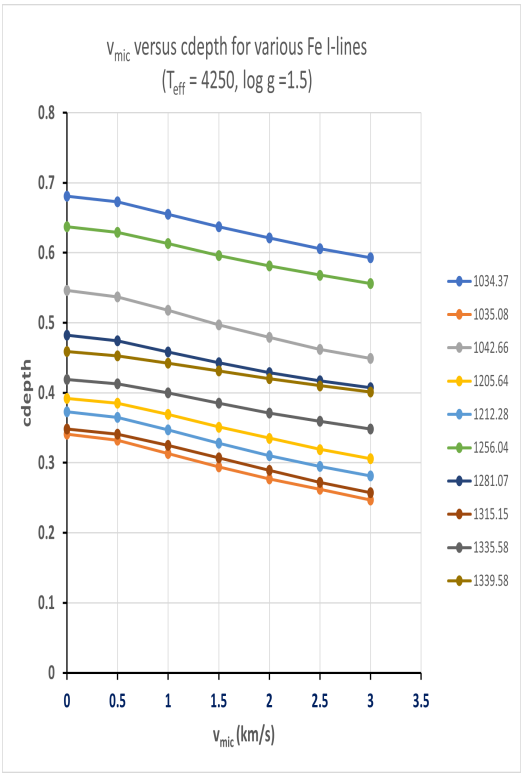

(a) $\mathbf{T_{eff} = 4250\ K,\ \log g{=}1.5}$

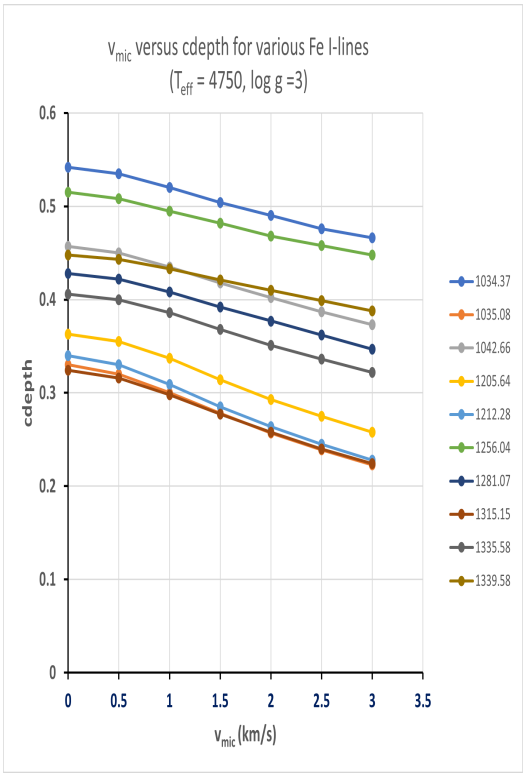

(b) $\mathbf{T_{eff} = 4750\ K,\ \log g{=}3.0}$

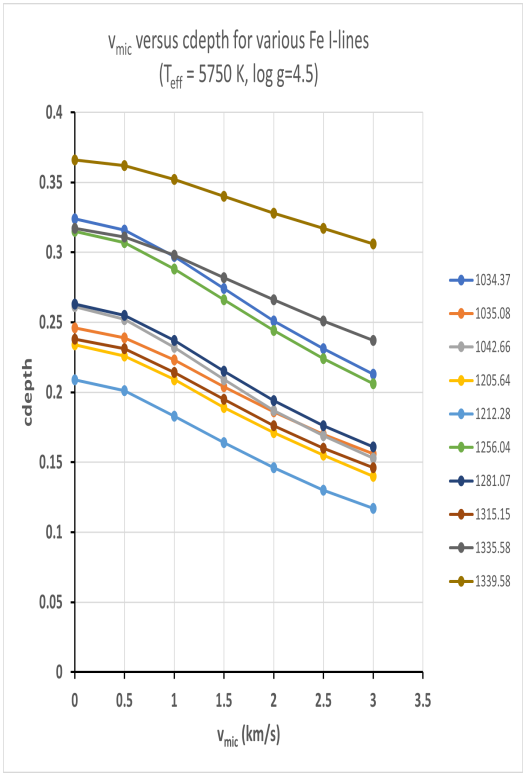

(c) $\mathbf{T_{eff} = 5750\ K,\ \log g{=}4.5}$

Figure 28: Simulation of cdepth of Fe I lines in YJ band as a function of v_{mic} for three different T_{eff}&log g conditions.

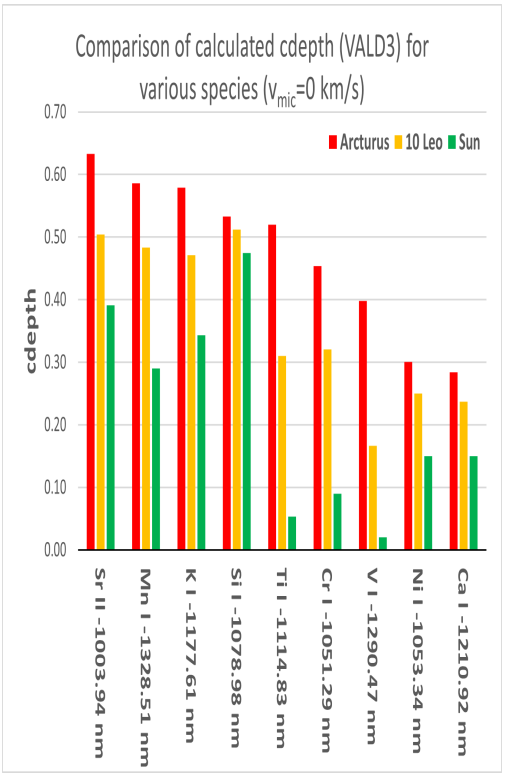

a1) $\mathbf{v_{mic}=0}$ **km/s**

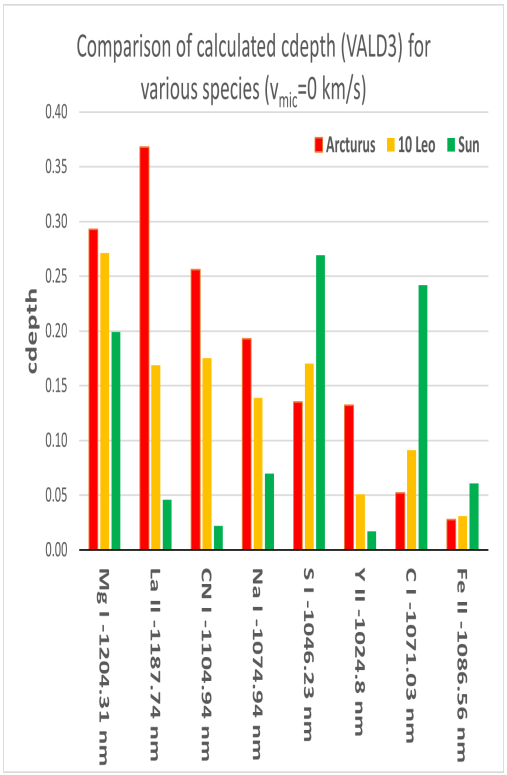

a2) $\mathbf{v_{mic}=0}$ **km/s**

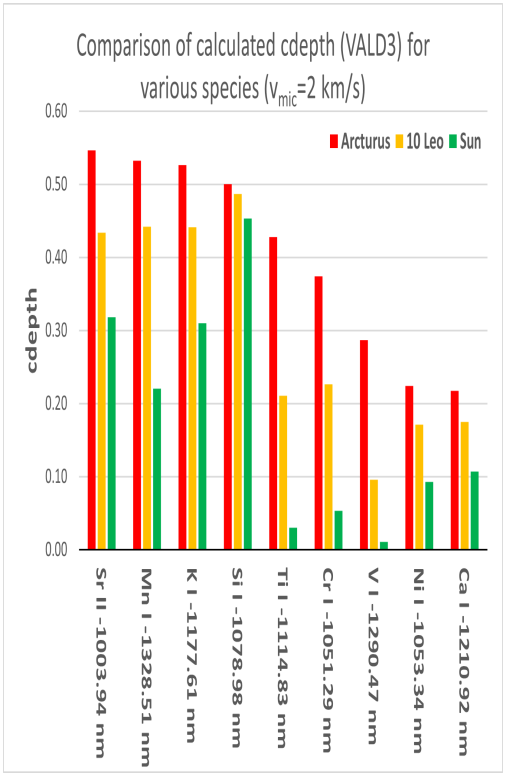

b1) $\mathbf{v_{mic}=2}$ **km/s**

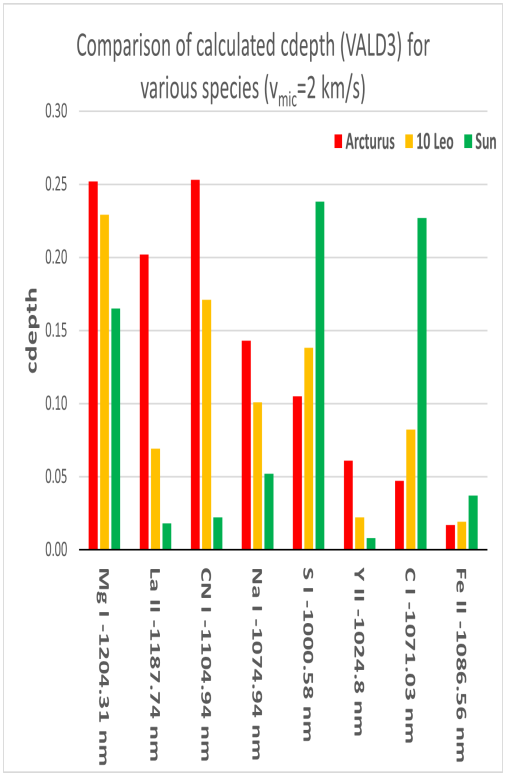

b2) $\mathbf{v_{mic}=2}$ **km/s**

Figure 29: Simulation of cdepth (scaled solar abundances) of various species in YJ band at v_{mic}=0 km/s and v_{mic}=2 km/s for Arcturus, 10 Leo and Sun

4.6.1 Model Atmospheres in Radiative and Convective Scheme (MARCS)

About 52000 stellar atmospheric models for stars within the range of 2500 K ≤ Teff ≤ 8000 K are available from the **MARCS** homepage[8] (Gustafsson *et al.*, 2008). The models cover not only different temperatures but also different geometries, log g, v_{mic}, masses and chemical compositions.
The stellar models are chosen using the search form. The first input screen of the search form allows the selection of the chemical composition class and model geometry. Once selected, the search form expands for the input of effective temperature, log g, overall metallicity, microturbulence and mass. It is possible to select a range of values. The available models are displayed in the "Search results" on the right panel and can be put in a basket for download. The download basket screen has four format options for the selected models: **opa** (basic model structures and continuous opacities as a function of wavelength and optical depth),**mod** (model structure and thermodynamical quantities) **krz**(retrieves the MARCS models in the .krz format) and **flx** (statistical samples of the model surface fluxes). After pressing the "Download models" tab and confirming the start of download, a tar file is sent to the requestor. This .tar file and its components need to be extracted before further use. The .krz file is renamed (e.g. *s4750.krz*) for convenience and further processed as described below in Section 4.6.2.
The chosen parameter set for the calculation used for 10 Leo model is displayed in Figure 30 as part of a screenshot from a MARCS request. The model file generated for Arcturus uses T=4250 K (closest available options: 4000 K, 4250 K, 4500 K), log g=1.5 (closest available options: 1, 1.5, 2) and v_{mic}=2 km/s (options: 1,2 and 5). This work uses these two MARCS models in .krz format for all synthetic 10 Leo spectra and Arcturus spectra. The metal abundance is the **only** parameter that is modified.

Figure 30: Parameters for 10 Leo to generate MARCS atmospherical model

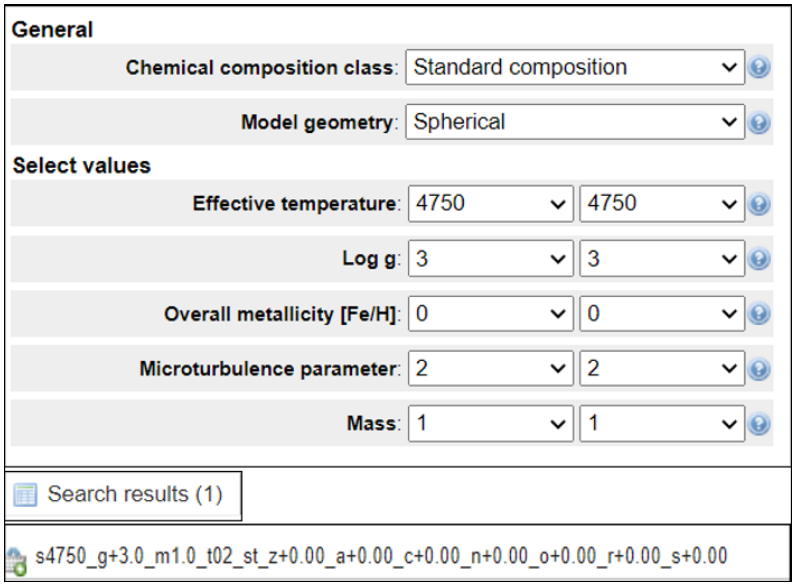

4.6.2 Generation of synthetic spectra

The generation of a synthetic spectrum is a multistep process. The different data processing steps are illustrated in Figure 31.

[8] https://marcs.astro.uu.se/index.php

Figure 31: Data flow for the comparison of observed and synthetic spectra

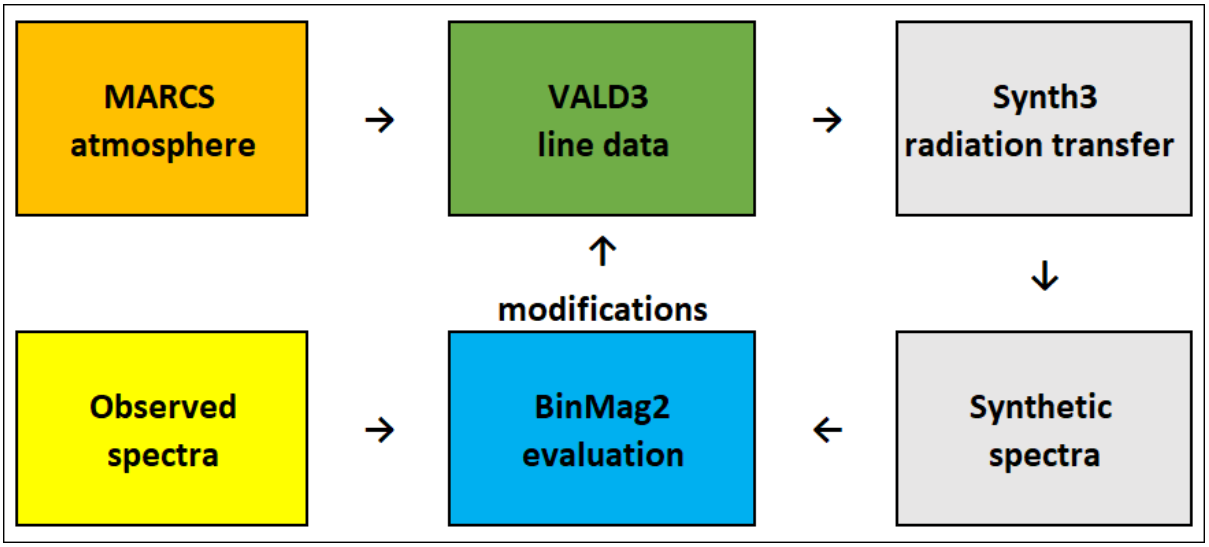

In a first step a line catalogue with respective temperature, log *g* and microturbulence is requested from VALD3 (see 2.1). The line catalogue is using solar abundances and a specific atmospheric model (e.g. castelli_ap00k2_T04750G30.krz) and provides various parameters, e.g. damping constants, log *gf*, line positions, that are needed to build the synthetic spectrum. In the next step the VALD3 file is edited and and the file name of the respective castelli file in the VALD3 file is replaced by the MARCS-model filename , e.g. **castelli_ap00k2_T04750G30.krz→s4750.krz**. The third step uses the tool **Synth3** (Kochukhov, 2012) to process the modified VALD3 file with the matching MARCS model file (same T_{eff}, microturbulence and log *g* values as for the VALD3 file) to create the synthetic spectrum (datatype: **".out file"**). The out-file is transferred to the Linux working directory of IDL for subsequent data analysis using **BinMag2** (Kochukhov, 2018).

In practice, the first synthetic spectrum (based on solar abundances), compared to the observed spectrum, will show a number of differences in the atomic/molecular line intensities. The original "solar abundances" (" Kurucz abundance values", see Table 10) are replaced in the VALD3 file with new abundance values that should closer fit the observed spectrum. Subsequently, a new synthetic spectrum is created by **Synth3** using the modified VALD3 file. This is an iterative process and will require a renewed generation of the synthetic spectrum with updated abundance values. The iteration continues until a consistent set of abundances for the synthetic spectrum is obtained. The quality of the synthetic spectrum is visually checked by overlaying synthetic spectrum and observed spectrum using BinMag2. Furthermore, the equivalent widths of selected lines are compared for both spectra.

Figure 32: Improved match between synthetic and observed 10 Leo spectrum by abundance variation

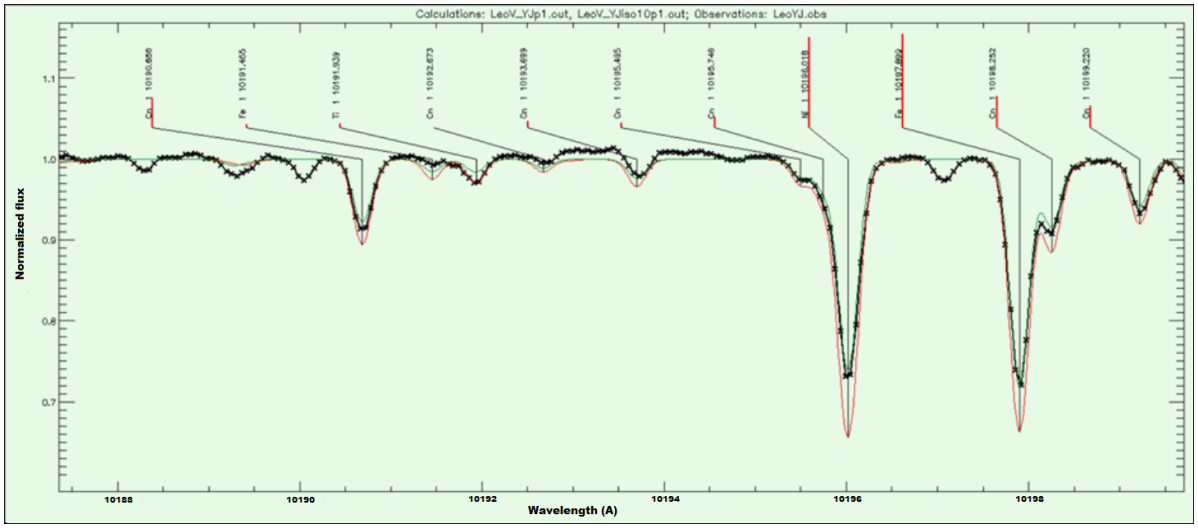

observation spectrum (black *), synthetic spectrum based on solar abundance values (red) and synthetic spectrum with modified abundances (green) for CN, Fe and Ni

Figure 32 shows a comparison for 10 Leo between observed spectrum and two synthetic spectra. The “red “ synthetic spectrum is based on solar scaled abundances and the green one on modified abundances. Obviously, the green graph matches the observation much better than the red graph.

Table 32 provides the ratios of EWs for several elements and molecules. A perfect match would yield a ratio of 1 between Syn/10 Leo. However, deviations are expected due to the differences of available model parameters and observed parameters, e.g. 4750 K instead of 4800 K and log g=3.0 instead of 2.67 for 10 Leo.

Figure 33: Comparison of 10 Leo and Arcturus spectrum

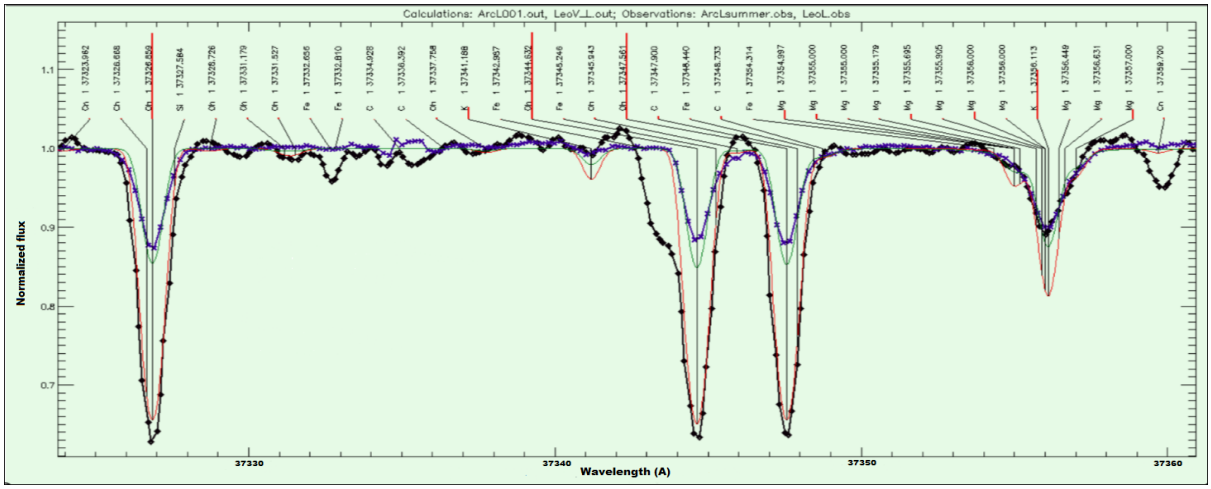

Category A match, L-band, OH-lines (black with diamonds = observed Arcturus, blue with *=observed 10 Leo, red=synthetic spectrum Arcturus, green=synthetic spectrum 10 Leo)

Figure 33 shows a section of the L-Band for Arcturus and 10 Leo (two synthetic spectra, two observed spectra). The synthetic spectra have been broadened by a macroturbulence value of 3.5

Table 32: Comparison of ratios of between synthetic and observed equivalent widths

species	Ratios			
	Sol/10 Leo	Syn/10 Leo	Sol/Syn	ArcSol/Arcsyn
CO	1.23 ± 0.09	0.98 ± 0.05	1.26 ± 0.13	0.98 ± 0.05
CH	1.74 ± 0.28	1.16 ± 0.15	1.51 ± 0.09	1.16 ± 0.15
CN	1.35 ± 0.12	1.02 ± 0.09	1.34 ± 0.05	1.02 ± 0.09
OH	1.03 ± 0.09	1.04 ± 0.09	0.99 ± 0.02	1.04 ± 0.09
Na I	1.05 ± 0.03	1.01 ± 0.02	1.04 ± 0.01	1.01 ± 0.02
Mg I	1.07 ± 0.14	1.09 ± 0.17	0.99 ± 0.04	1.09 ± 0.17
Al I	1.01 ± 0.08	1.09 ± 0.08	0.92 ± 0.02	1.09 ± 0.08
Si I	1.16 ± 0.07	0.97 ± 0.07	1.20 ± 0.05	0.97 ± 0.07
K I	1.12 ± 0.11	1.05 ± 0.09	1.07 ± 0.04	1.05 ± 0.09
Ca I	1.26 ± 0.09	0.97 ± 0.06	1.31 ± 0.04	0.97 ± 0.06
Sc I	1.75 ± 0.74	1.21 ± 0.52	1.46 ± 0.04	1.21 ± 0.52
Ti I	1.13 ± 0.06	0.88 ± 0.13	1.31 ± 0.14	0.88 ± 0.13
V I	1.91 ± 0.63	1.11 ± 0.31	1.69 ± 0.12	1.11 ± 0.31
Cr I	1.30 ± 0.05	1.02 ± 0.07	1.28 ± 0.12	1.02 ± 0.07
Mn	0.78 ± 0.10	1.05 ± 0.10	0.74 ± 0.03	1.05 ± 0.10
Fe I	1.19 ± 0.18	0.96 ± 0.17	1.27 ± 0.10	0.96 ± 0.17
Ni I	1.33 ± 0.12	0.91 ± 0.08	1.47 ± 0.08	0.91 ± 0.08
Sr II	0.89 ± 0.03	0.99 ± 0.05	0.89 ± 0.01	0.99 ± 0.05

Sol = synthetic VALD3 spectrum (T=4801 K, log g=2.83, v_{mic}=2km/s) with solar scaled abundances Syn = synthetic VALD3 spectrum (Sol) with modified abundances to match 10 Leo spectrum
ArcSol = synthetic VALD3 spectrum (T=4301 K, log g=1.67, v_{mic}=2km/s) with solar scaled abundances
Arcsyn = synthetic VALD3 spectrum (ArcSol) with modified abundances to match Arcturus spectrum

km/s. The observed spectra of Arcturus summer have been shifted using v_r=-14.5 km/s. The synthetic spectrum for Arcturus predicts very well the increased strength of the OH-lines versus the 10 Leo spectrum. The green graph follows the observation for 10 Leo.

Table 33: Abundances for synthetic spectra

species	Abundances			
	Solar	Syn_10 Leo	Syn_Arc	Leo-Arc
C I	-3.52	-3.85	-4.14	0.29
N I	-4.12	-4.05	-4.37	0.32
O I	-3.21	-3.35	-3.27	-0.08
Na I	-5.71	-5.80	-5.89	0.09
Mg I	-4.46	-4.46	-4.48	0.02
Al I	-5.57	-5.40	-5.41	0.01
Si I	-4.49	-4.80	-4.83	0.03
K I	-6.92	-7.00	-7.09	0.09
Ca I	-5.68	-6.00	-6.08	0.08
Sc I	-8.87	-9.00	-9.10	0.10
Ti I	-7.02	-7.30	-7.39	0.09
V I	-8.04	-8.30	-8.74	0.44
Cr I	-6.37	-6.55	-6.67	0.12
Mn	-6.65	-6.00	-6.18	0.18
Fe I	-4.54	-4.80	-4.96	0.16
Ni I	-5.79	-6.25	-6.40	0.15
Sr II	-9.07	-9.00	-9.09	0.09

Solar = original Kurucz solar scaled abundances, Syn_10 Leo = modified abundances for synthetic 10 Leo spectrum, Syn_Arc = modified abundances for synthetic Arcturus spectrum

Table 33 lists the abundance values as modified in the VALD3 line catalogue (see Section 4.6.2) used to generate the respective synthetic spectra.
The "Solar" column refers to the original solar scaled abundances (see Table 10), "Syn_10 Leo" = modified abundances for synthetic 10 Leo spectrum and "Syn_Arc = modified abundances for synthetic Arcturus spectrum". These modified abundances have been derived iteratively by comparing the observational spectra with the generated synthetic spectra. The best match has been considered if the ratios of equivalent widths of the absorption lines between observed and synthetic spectra are closest to 1. Several iterations have been performed as the variation of the abundance value for a single element will influence the line signature of the other elements.
The match of the molecular lines for CO, CN and OH have been achieved by varying the abundances for C, N and O.The differences between solar abundance and the synthetic abundances for 10 Leo and Arcturus are all positive except for Mn and Al. This is consistent with a lower metallicity for 10 Leo and Arcturus as reported by da Silva *et al.* (2011) and Ramírez & Allende Prieto (2011), respectively. The deviation for Mn and Al requires further analysis.
The differences in element abundances between 10 Leo and Arcturus become apparent by the comparison of the synthetic spectra. All elements are more abundant in 10 Leo spectrum with some element specific differences: e.g. Na, Mg, Al, Si, K, Ca, Ti and Sr show small differences of < 0.1 dex, whereas Sc, Cr, Mn, Fe and Ni show larger differences between 0.1 and 0.2 dex. V shows the most significant difference in abundance with 0.44 dex.

Figure 34: Lines present in synthetic spectra but not in observed spectra (match category C)

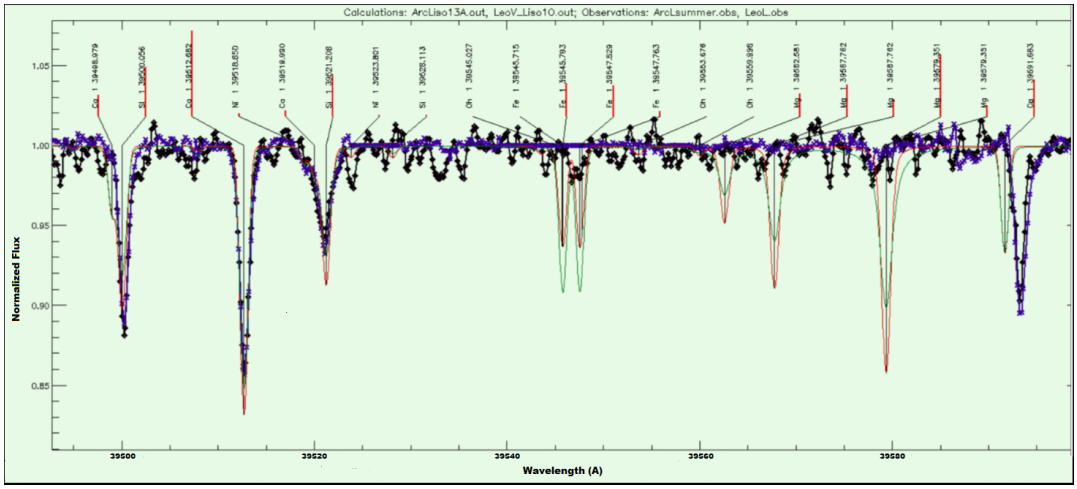

Category C match, L-band, OH-lines (black with diamonds = observed Arcturus, blue with * = observed 10 Leo, red = synthetic spectrum Arcturus, green = synthetic spectrum 10 Leo

It has been noted that some of the synthetic lines are not present in the observed spectrum and vice versa. This indicates some flaws in the VALD3 catalogue values. Typical examples are shown in Figure 34, which shows a doublett of Fe I lines at 39545.8 Å and 39547.5 Å together with three prominent Mg I lines at 39552.8 Å, 39567.8 Å and 39579.4 Å in the synthetic spectra. These lines are not present in the observed spectra of 10 Leo and Arcturus. The Ca I line at 39591.7 Å in the synthetic spectra can be attributed to a line at 39593.1 Å observed in 10 Leo and Arcturus.

Figure 35: Lines present in observed spectra but not in synthetic spectra

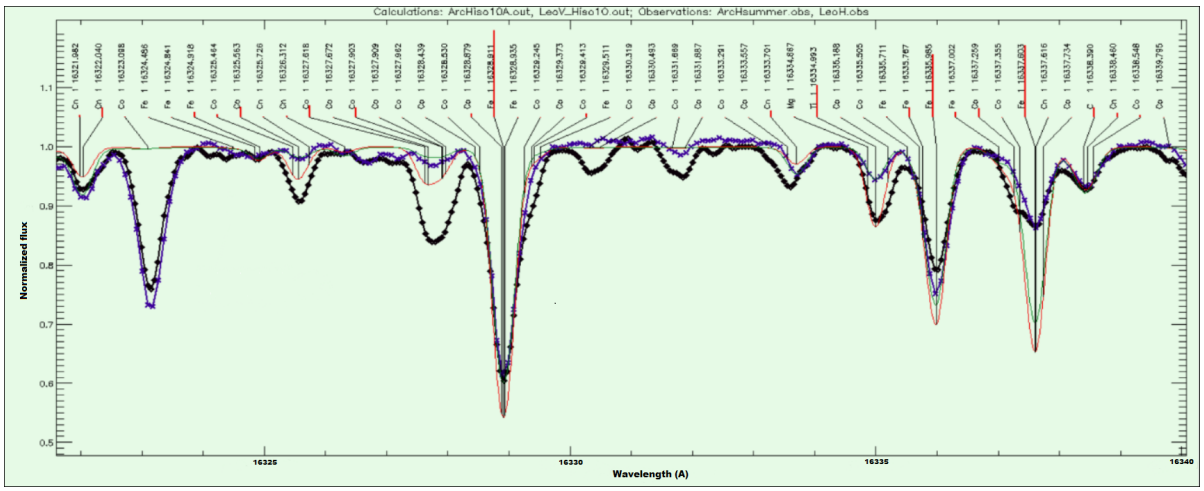

H-band, Fe I-lines (black with diamonds = observed Arcturus, blue with * = observed 10 Leo, red = synthetic spectrum Arcturus, green = synthetic spectrum 10 Leo

Another example is shown in Figure 35 which shows a strong line at 16323.2 Å (left side of the plotted range, attributed to Fe I in the Arcturus atlas). The line is present in the 10 Leo spectrum (blue x) and in the Arcturus spectrum (black diamond) but not in any of the synthetic spectra. It is also noticeable that the observed Fe I line at 16337.6 Å do not match the intensity of the

synthetic spectra, although there is agreement between 10 Leo and Arcturus. The Fe I lines at 16328.9 Å and 16336.0 Å are reasonably in agreement between observed and synthetic spectra.

Table 34: K-band: Lines present in synthesis (> 50mÅ) but not in observation (10 Leo/Arcturus)

Line properties			Observed Equivalent width (mÅ)			
X	λ(Å)	Ex(cm^{-1})	Synthesis	10 Leo	Arcturus	Remarks
Fe I	19986.98	51692.0	53	-9	15	
Fe I	21495.41	47960.9	178	50	39	
Fe I	21826.62	54683.3	146	45	43	Si contr.
Fe I	22145.86	51692.0	78	4	4	
Fe I	22184.25	46720.8	75	18	14	
Fe I	22615.51	48531.9	89	3	18	OH contr.
Fe I	22878.66	50008.5	107	24	25	
Fe I	23690.14	42784.4	137	-12	110	OH contr.
Mg I	20527.44	56308.4	274	5	54	
Mg I	20838.99	56308.4	261	58	87	
Mg I	20872.78	54250.1	64	4	29	
Mg I	21239.26	56308.4	228	1	31	
Mg I	21767.02	56308.4	196	14	23	

Table 34 and Table 35 list some lines with EWs above 50 mÅ not matched in the K-band. Additional lines and more details regarding the other bands are summarized in Annex, Section 7.1.2, Tables 49 - 58.

Table 35: K-band: Lines present (>50mÅ) in observation (10 Leo/Arcturus) but not in synthesis

	Observed Equivalent width (mÅ)			
λ(Å)	Synthesis	10 Leo	Arcturus	Remarks
19600.09	2	87	13	Unknown
19676.14	18	63	76	Arcturus: 19676.22 Fe I
19799.17	14	163	36	VALD3: 19798.96 Mn I, cdepth:0.039
20085.78	10	90	77	Unknown
20095.27	3	213	193	Unknown
20589.67	4	119	115	VALD3: 20589.81 Fe I, cdepth 0.018 Arcturus: 20589.81 Fe I
20810.70	15	156	166	Arcturus: 20810.77 Fe I
21065.45	54	265	243	VALD3: 21066.00 Mg I, cdepth 0.288 Arcturus: 21065.51 Mg I
21213.78	25	162	146	VALD3: 21213.93 Mg I, cdepth 0.064 Arcturus: 21213.96 Al I
21631.74	9	111	71	Unknown

5 Further Studies

Apart from the specific line information such as presence of metals/molecules and their abundances in the atmosphere of 10 Leo, a large variety of general information is contained in the IR-spectrum. The following Section 5.1 is limited to determine a few spectral parameter for the ro-vibrational spectra of CO and its isotopologues. The results should prove the overall consistency of the spectroscopic NIR data for 10 Leo with published data.

5.1 Determination of spectral parameters

The underlying model to calculate the wavenumber and respectively the wavelength of transition lines uses the parameters α_e (rovibrational coupling constant), ω_e, χ_e(anharmonicity constant), ω_0 (wavenumber for v=0), $\mathbf{B_e}$ (rotational constant at equilibrium), $\mathbf{D_e}$ (centrifugal distortion constant), **J** (rotational quantum number) and v (vibrational quantum number).
These parameter can be easily determined with the help of an Excel spreadsheet by comparing the corresponding fundamental and the first overtone transitions. The wavenumbers of the P-branch and R-Branch of a specific vibrational transition are organized in rows sorted by J. The row for the R-branch starts with J=0, whereas the P-branch starts at J=1. The rows are fitted by a 3rd order polynomial against J+1 (R-Branch) and -J (P-Branch). The following formulae are the basis of the calculation (Mina-Camilde *et al.*, 1996):
(m ≡**-J"** on the P branch and m ≡**J"+1** on the R branch, for the fundamental band v=1 and for the overtone band v=2)

$$\omega(v,m) = \omega_v + (B_v + B_0)m + (B_v - B_0)m^2 - 4D_e m^3 \tag{43}$$

$$\omega(v,m) = c_0 + c_1 m + c_2 m^2 + c_3 m^3 \tag{44}$$

$$\omega(v+1,m) = c'_0 + c'_1 m + c'_2 m^2 + c'_3 m^3 \tag{45}$$

The coefficients from the polynomials provide the respective parameter:

$$\omega_1 = c_0; \omega_2 = c'_0 \tag{46}$$

$$B_0 = \frac{1}{2}(c_1 - c_2); B_1 = \frac{1}{2}(c_1 + c_2) \tag{47}$$

$$D_e(2) = -\frac{1}{4}c_3 \tag{48}$$

$$\tag{49}$$

From the parameter B_0, B_1, c_0 further parameter can be obtained:

$$\omega_e = 3c_0 - c'_0 \tag{50}$$

$$\alpha_e = B_0 - B_1 \tag{51}$$

$$B_e = B_0 - 0.5\alpha_e \tag{52}$$

$$\chi = \frac{(2\omega_1 - \omega_2)}{2\omega_e} \tag{53}$$

$$D_e = \frac{4{B_e}^3}{{\omega_e}^2} \tag{54}$$

Figure 36 displays a typical screenshot of a customized Excel sheet. This example combines the graphical results of the 2-1 fundamental and the corresponding first overtone (3-1) for ^{12}CO and the evaluation routines of the various parameters. The values for c_0-c_3 are taken from the

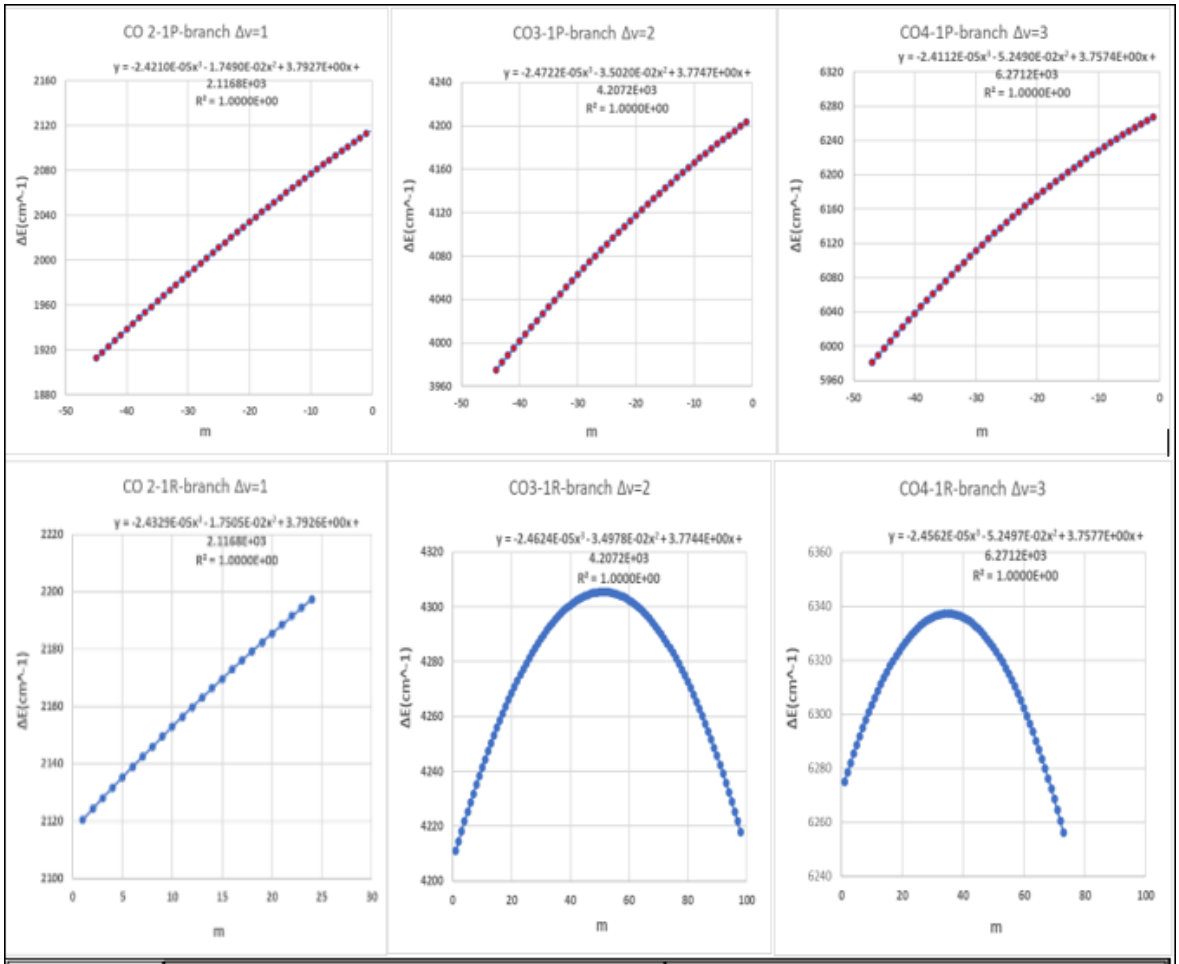

Parameter	P			R		
	2-1	3-1	4-1	2-1	3-1	4-1
$c_0=\omega_1,\omega_2,...$	2116.79	4207.17	6271.20	2116.79	4207.17	6271.20
c_1	3.793	3.775	3.757	3.793	3.774	3.758
c_2	-0.0175	-0.0350	-0.0525	-0.0175	-0.0350	-0.0525
c_3	-2.421E-05	-2.472E-05	-2.411E-05	-2.433E-05	-2.462E-05	-2.456E-05
B_0	1.9051	1.9049	1.9050	1.9050	1.9047	1.9051
B_1	1.8876			1.8875		
B_2		1.870			1.870	
B_3			1.852			1.853
B_v	1.9051	1.9049	1.9050	1.9050	1.9047	1.9051
v	1	1	1	1	1	1
ω_e	2143.21	2143.21	2143.23	2143.20	2143.21	2143.23
x_e	6.16E-03			6.16E-03		
α_e	1.749E-02	1.751E-02	1.750E-02	1.751E-02	1.749E-02	1.750E-02
B_e	1.9313	1.9311	1.9312	1.9313	1.9309	1.9313
D_e	6.2733E-06			6.2732E-06		
D_e (2)	6.0525E-06	6.1804E-06	6.0279E-06	6.0822E-06	6.1559E-06	6.1405E-06

Figure 36: Customized Excel spreadsheet for ^{12}CO 2-1, ^{12}CO 3-1 and ^{12}CO 4-1 bands

Table 36: Overview of derived molecular constants for ^{12}CO and ^{13}CO (all quantities are in units of cm^{-1})

	^{12}CO		^{13}CO	
Parameter	This work	Literature [ref]	This work	Literature [ref]
ω_e	2169.76	2169.756 [1]	2121.37	2141.41 [2]
ω_0(1-0)	2143.27	2143.27 [3]	2096.07	2096.07 [3]
ω_0(2-0)	4260.07	4260.06 [3]	4166.83	4166.82 [3]
ω_0(3-0)	6350.43	6350.44 [3]		6212.32 [3]
ω_0(3-1)	4207.17	4207.17 [3]	4116.25	4116.25 [3]
ω_0(4-2)	4154.41	4154.41 [3]	4065.81	4065.81 [3]
B_e	1.9309	1.9316 [1]	1.8461	
B_0	1.9222	1.9225 [3]	1.8372	1.8380 [3]
B_1	1.9049	1.9050 [3]	1.8215	1.8216 [3]
B_2	1.8872	1.8875 [3]	1.8055	1.8053 [3]
B_3	1.8700	1.8700 [3]	1.7890	1.7890 [3]
$\omega_e\chi_e$	13.236	13.288 [1]	13.236	12.67 [2]
α_e	1.7490E-02	1.7505E-02 [1]	1.6351E-02	
D_e	6.120E-06	6.122E-06 [1]	5.592E-06	5.593E-06 [3]
r_e(Å)	1.1242	1.1282 [1]		

References: [1]Le Floch, 1991; [2]Gendriesch *et al.*, 2009; [3]Coxon & Hajigeorgiou, 2004
Parameters: ω_e= harmonic wavenumber; ω_0= ΔE (v:1←0); B_e= equilibrium rotational constant, B_0= rotational constant (v=0); $\omega_e\chi_e$= anharmonicity term; α_e= vibration-rotation interaction constant; D_e= centrifugal distortion constant

Table 37: Overview of derived molecular constants for $^{12}C^{17}O$ and $^{12}C^{18}O$ (all quantities are in units of cm^{-1})

	$^{12}C^{17}O$		$^{12}C^{18}O$	
Parameter	This work	Literature[a],[b]	This work	Literature[a],[b]
ω_0(1-0)	2116.29	2116.29	2092.12	2092.12
ω_0(2-1)	2090.48	2090.48	2066.91	2066.90
ω_0(3-2)	2064.74	2064.74	2041.75	2041.75
ω_0(4-3)	2039.05	2039.05	2016.65	2016.65
ω_0(5-4)		2013.44	1991.62	1991.62
B_e	1.8825		1.83902	
B_0	1.8743	1.8740	1.8311	1.8310
B_1	1.8573	1.8571	1.8149	1.8147
B_2	1.8404	1.8403	1.7984	1.7985
B_3	1.8238	1.8234	1.7824	1.7822
α_e	1.6830 E-02		1.6221E-02	
D_e	5.63E-06	5.81E-06	5.50E-06	5.55E-06

References: [a]Coxon & Hajigeorgiou, 2004; [b]Velichko & Mikhailenko, 2015
Parameters: see Table 36

polynomials as listed in the graphs and are entered in the corresponding cells. The remaining parameters are automatically calculated by the customized spreadsheet.
Table 36 and Table 37 provide derived molecular constants for $^{12}C^{16}O$, $^{13}C^{16}O$,$^{12}C^{17}O$ and $^{12}C^{18}O$ in comparison to literature values.
The transition energy ΔE between the vibrational levels (see also Figure 37), are listed in Table 38 and compared to calculated values from Korek & El-Kork (2018) and Coxon & Hajigeorgiou (2004). A graphical display (Figure 37) of the vibrational levels versus the transition energy allows to estimate the transition energy for bands not yet observed and described in the current spectra.

Table 38: Transition energy (ΔE) of vibrational levels of ^{12}CO

	Transition energy ΔE(cm $^{-1}$) of ν'- ν"		
Transition	This work	Coxon & Hajigeorgiou (2004)	Korek & El-Kork (2018)[a]
1-0	2143.27	2143.27	2143.27
2-1	2116.79	2116.79	2116.79
3-2	2090.38	2090.38	2090.38
4-3	2064.03	2064.03	2064.03
5-4	2037.75	2037.75	2037.78
6-5	2011.55	2011.55	2011.58
7-6	1985.42	1985.41	1985.51
8-7	1959.35	1959.35	1959.54
9-8	1933.38	1933.37	1933.73
10-9	1907.47	1907.46	1908.09
11-10	1881.62	1881.64	1863.00
12-11	1855.84	1855.89	1850.89
13-12	1830.25	1830.22	1824.32

[a]from the differences of the energy eigenvalues of the pure vibrational energy levels of the Morse potential using Volterrra Integral Equation

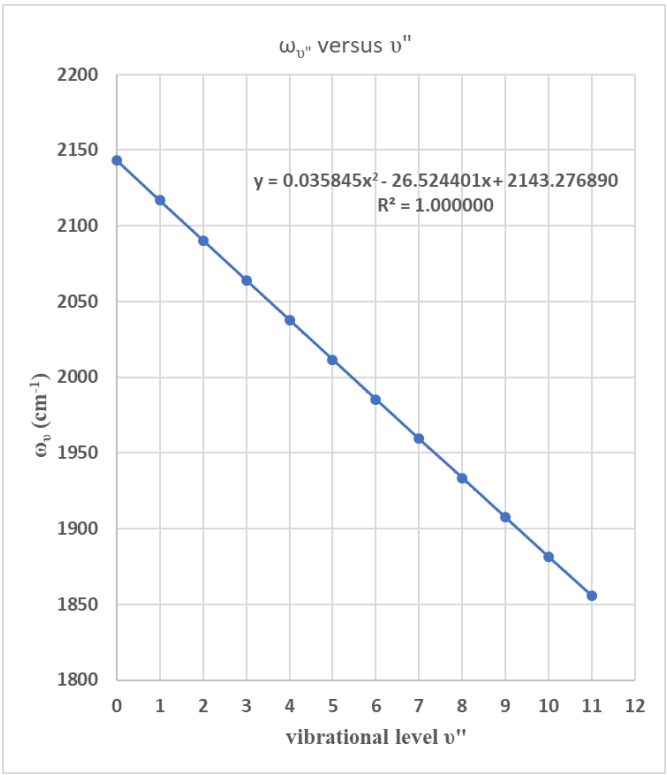

Figure 37: Vibrational quantum number ν" versus transition energy

With the estimated transition energy, the covibrational lines of the respective band can be calculated and compared with the observed spectra. However, as the line strength decreases with higher vibration number, it will be increasingly difficult to identify such lines in the spectrum. The linear dependency of the rotational constant B_ν on the vibrational quantum number ν" (ν"

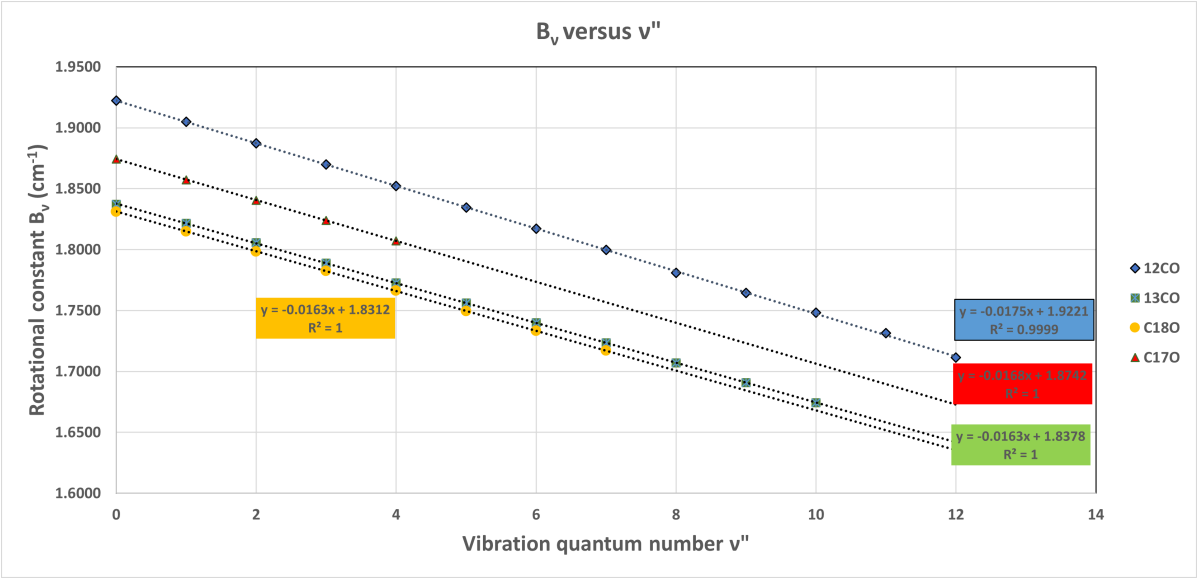

Figure 38: Vibrational quantum number v" versus rotational constant in fundamental transitions for ^{12}CO (blue) and ^{13}CO(red)

refers to the lower level of the transition) is illustrated in Figure 38. Slope and intercept can be used to derive the rovibrational coupling constant α_e and the rotational constant at equilibrium B_e. The differences for the isotopes of the rotational constants, α_e and D_v are mainly due to the differences of their reduced masses. The observed differences for the rotational constants are further studied in Section 5.3 and are compared to literature.

$$B_v = B_e - \alpha_e(v + 1/2) = (B_e - 1/2\alpha_e) - \alpha_e v$$

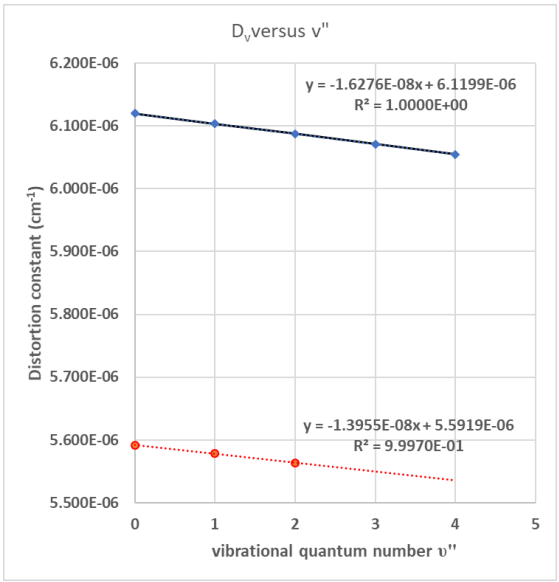

Figure 39: Vibrational quantum number v" versus distortion constant in fundamental transitions for ^{12}CO (blue) and ^{13}CO(red)

The linear dependency of the distortion constant D_v on the vibrational quantum number can be

seen in Figure 39.

Table 39: Fundamental CO-bands (^{12}CO, ^{13}CO, C^{17}O, C^{18}O) observed in 10 Leo spectrum

	R-branch			P-branch		
Band-ID	λ nm (at R0)[c]	cdepth[a] (max)	EW mÅ(max)[b]	λ nm (at P1)[c]	cdepth[a] (max)	EW mÅ(max)[b]
CO 1-0	4657.47	0.501	560	4674.15	0.493	920
CO 2-1	4715.72	0.500	772	4732.65	0.478	1030
CO 3-2	4775.28	0.475	592	4792.48	0.452	844
CO 4-3	4836.21	0.442	691	4853.69	0.417	665
CO 5-4	4898.54	0.404	509	4916.30	0.379	511
CO 6-5	4962.33	0.366	417	4980.39	0.342	485
CO 7-6	5027.62	0.333	367	5045.98	0.305	354
CO 8-7	5094.45	0.302	371	5113.12	0.256	308
CO 9-8	5162.90	0.272	305			
CO 10-9	5232.99	0.242	270			
CO 11-10	5304.84	0.210	255			
CO 12-11	5378.46	0.171	164			
CO 13-12	5453.62	0.121	146			
CO 14-13	5531.54	0.074	145			
^{13}CO 1-0	4762.56	0.294	392	4779.22	0.266	468
^{13}CO 2-1	4820.76	0.281	405	4837.67	0.252	431
^{13}CO 3-2	4880.25	0.251	375	4897.42	0.221	307
^{13}CO 4-3	4941.07	0.217	280	4958.52	0.171	428
^{13}CO 5-4	5003.26	0.175	229	5021.13	0.084	229
^{13}CO 6-5	5066.87	0.123	216	5084.89	0.073	108
^{13}CO 7-6	5131.95	0.079	174			
^{13}CO 8-7	5198.49	0.049	134			
^{13}CO 9-8	5266.54	0.029	92			
^{13}CO 10-9	5336.81	0.016	32			
^{13}CO 11-10	5407.79	0.009	13			
C^{18}O 1-0	4771.56	0.163	157	4788.22	0.135	127
C^{18}O 2-1	4829.92	0.152	143	4846.71	0.124	148
C^{18}O 3-2	4889.24	0.114	104	4906.41	0.092	123
C^{18}O 4-3	4950.05	0.079	76	4967.49	0.061	78
C^{18}O 5-4	5012.23	0.051	48	5029.94	0.034	50
C^{18}O 6-5	5075.83	0.030	42			
C^{18}O 7-6	5140.86	0.018	25			
C^{18}O 8-7	5207.42	0.010	10			
C^{17}O 1-0	4716.98	0.042	49	4733.66	0.034	74
C^{17}O 2-1	4775.19	0.039	62	4792.09	0.030	55
C^{17}O 3-2	4834.70	0.028	42	4851.88	0.021	33
C^{17}O 4-3	4895.59	0.017	25	4913.02	0.013	21
C^{17}O 5-4	4957.81	0.010	16			
C^{17}O 6-4	5051.58	0.006	9			

[a]value from VALD stellar extraction;[b]EW derived from the strongest line observed;[c]Fit value

Table 39 and Table 40 summarize wavelengths for R0, P1, cdepth and EW of the various vibrational bands of CO that have been observed in the 10 Leo spectrum. The values for cdepth are from the VALD3 stellar extraction request (see Table 3) whereas the EW-values are from the observed 10 Leo spectrum.

Table 40: First and second overtone ^{12}CO,^{13}CO - bands

	R-branch			P-branch		
Band-ID	λ nm (at R0)	cdepth (max)	EW mÅ(max)	λ nm (at P1)	cdepth (max)	EW mÅ(max)
CO 2-0	2345.33	0.454	290	2349.50	0.398	222
CO 3-1	2374.82	0.469	313	2379.05	0.430	264
CO 4-2	2404.98	0.459	290	2409.27	0.419	231
CO 5-3	2435.82	0.438	260	2440.19	0.388	207
CO 6-4	2467.38	0.405	235	2471.85	0.283	134
CO 7-5	2499.67	0.357	180	2504.20	0.204	112
CO 8-6	2532.73	0.304	130			
CO 9-7	2566.63	0.284	109			
^{13}CO 2-0	2397.84	0.018	22	2402.03	0.013	9
^{13}CO 3-1	2427.29	0.026	41	2431.55	0.018	27
^{13}CO 4-2	2457.39	0.026	36	2461.69	0.012	9
^{13}CO 5-3	2488.18	0.021	33	2492.56	0.010	6
^{13}CO 6-4	2519.66	0.016	20			
^{13}CO 7-5	2551.87	0.012	10			
CO 3-0	1573.77	0.011	3	1575.65	0.006	2
CO 4-1	1593.65	0.022	8	1595.56	0.010	4
CO 5-2	1613.98	0.027	13	1615.94	0.014	6
CO 6-3	1634.80	0.027	12	1636.77	0.014	5
CO 7-4	1656.09	0.021	8	1658.10	0.013	5
CO 8-5	1677.89	0.021	10	1679.93	0.011	5
CO 9-6	1700.20	0.017	7	1702.28	0.010	4
CO 10-7	1723.05	0.012	4	1725.15	0.008	2
CO 11-8	1746.45	0.010	4	1748.59	0.006	2
CO 12-9	1770.35	0.008	3			

[a]value from VALD3 stellar extraction;[b]EW of strongest line observed;[c]Fit value

5.2 Determination of CO-bandheads

The plots of the rotational quantum number J versus wavenumber $\tilde{\nu}$ show a maximum for the R-branch caused by the rotational distortion. The maximum defines the bandhead. The location of bandheads for fundamental, first overtone and second overtone has been derived from the derivatives of 3rd order polynomials for J versus wavenumber. The resulting polynomial of 2nd order is then solved for J. The calculated maximum is re-inserted in the 3rd order polynomial to receive the correspondig wavenumber of the bandhead which is converted to wavelength. Table 41 and 42 summarize the results for the calculations. Bandheads for the fundamental transitions are in the range of J≈88 whereas the bandheads for the 1st overtone and 2nd overtone can be

Table 41: ^{12}CO - bandhead properties

Transition	J[a]	λ(nm)	cdepth	EW (mÅ)
13-12	83	5054.33	0.019	33
12-11	84	4982.35	0.030	31
11-10	84	4912.14	0.049	50
10-9	85	4843.63	0.072	gap
9-8	86	4776.76	0.102	strong blend
8-7	87	4711.47	0.138	69
7-6	87	4647.71	0.184	144
6-5	88	4585.45	0.218	138
5-4	89	4524.60		outside
4-3	90	4465.23		outside
3-2	90	4407.50		outside
2-1	91	4350.43		outside
1-0	92	4294.52		outside
9-7	48	2512.22	0.195	58
8-6	49	2478.76	0.255	86
7-5	49	2446.06	0.343	gap
6-4	50	2414.14	0.361	100
5-3	50	2382.94	0.401	142
4-2	51	2352.46	0.425	174
3-1	51	2322.65	0.434	181
2-0	52	2293.52	0.395	156
11-8	33	1729.99	0.010	4
10-7	33	1706.71	0.013	8
9-6	33	1683.97	0.018	8
8-5	34	1661.77	0.023	strong blend
7-4	34	1640.08	0.027	strong blend
6-3	34	1618.89	0.028	19
5-2	35	1598.18	0.029	12
4-1	35	1577.95	0.022	8
3-0	35	1558.16	0.011	5

[a]rounded value

Table 42: ^{13}CO - bandhead properties

Transition	J[a]	λ(nm)	cdepth	EW (mÅ)
10-9	87	4938.64	too weak	
9-8	88	4872.11	too weak	
8-7	89	4807.13	strong blend	
7-6	89	4743.66	0.006	10
6-5	90	4681.60	0.008	13
5-4	91	4620.95	0.013	20
4-3	92	4561.67	0.017	34
3-2	93	4503.32	outside	
2-1	93	4446.82	outside	
1-0	94	4391.56	outside	
6-4	50	2465.24	0.011	25
5-3	50	2434.12	0.014	46
4-2	52	2403.69	0.016	45
3-1	52	2373.94	0.017	20
2-0	53	2344.85	0.012	11

[a]rounded value

found at J≈50 and J≈34. Some of the calculated bandheads are not within the spectral windows of the 10 Leo spectrum and could not be confirmed visually, e.g. bandheads for the 1-0, 2-1, 3-2, 4-3 and 5-4 bands. The shift of the bandheads towards lower J-values for the 1st and 2nd overtone enhances the line intensity of the bandhead region as compared to the fundamental transitions at J≈88.
Table 43 shows the results for the fundamental and first overtone CO-bandheads in comparison to literature values. Bandheads for C^{17}O and C^{18}O are either too weak or outside the spectral window.

Table 43: Wavelength (nm) of ^{12}CO and ^{13}CO - bandheads compared to literature

	^{12}CO			^{13}CO		
Band	10 Leo	Literature[a]	difference	10 Leo	Literature[b]	difference
fundamental						
4-3	outside	4465.21		4561.67		
5-4	outside	4524.63		4620.95		
6-5	4585.45	4585.45	0.00	4681.60		
7-6	4647.71	4647.72	-0.01	4743.66		
8-7	4711.47	4711.47	0.00			
9-8	4776.76	4776.75	0.01			
10-9	gap	4843.62				
11-10	4912.14	4912.14	0.00			
12-11	4982.35	4982.36	-0.01			
13-12	5054.33	5054.33	0.00			
1st overtone						
2-0	2293.52	2293.52	0.00	2344.85	2344.80	0.05
3-1	2322.65	2322.66	-0.01	2373.94	2373.90	0.04
4-2	2352.46	2352.46	0.00	2403.69	2403.70	-0.01
5-3	2382.94	2382.95	-0.01	2434.12	2434.10	0.02
6-4	2414.14	2414.14	0.00	2465.24	2465.20	0.04
7-5	2446.06	2446.08	-0.02	2497.08	2497.10	0.02
8-6	2478.76	2478.76	0.00			
9-7	2512.22	2512.23	-0.01			
10-8						
2nd overtone						
3-0	1558.16	1558.16	0.00			
4-1	1577.95	1577.95	0.00			
5-2	1598.18	1598.19	-0.01			
6-3	1618.89	1618.89	0.00			
7-4	1640.08	1640.08	0.00			
8-5	1661.77	1661.77	0.00			
9-6	1683.97	1683.97	0.00			

[a] Goorvitch (1994)

[b] http://www.not.iac.es/instruments/notcam/ReferenceInfo/co.html

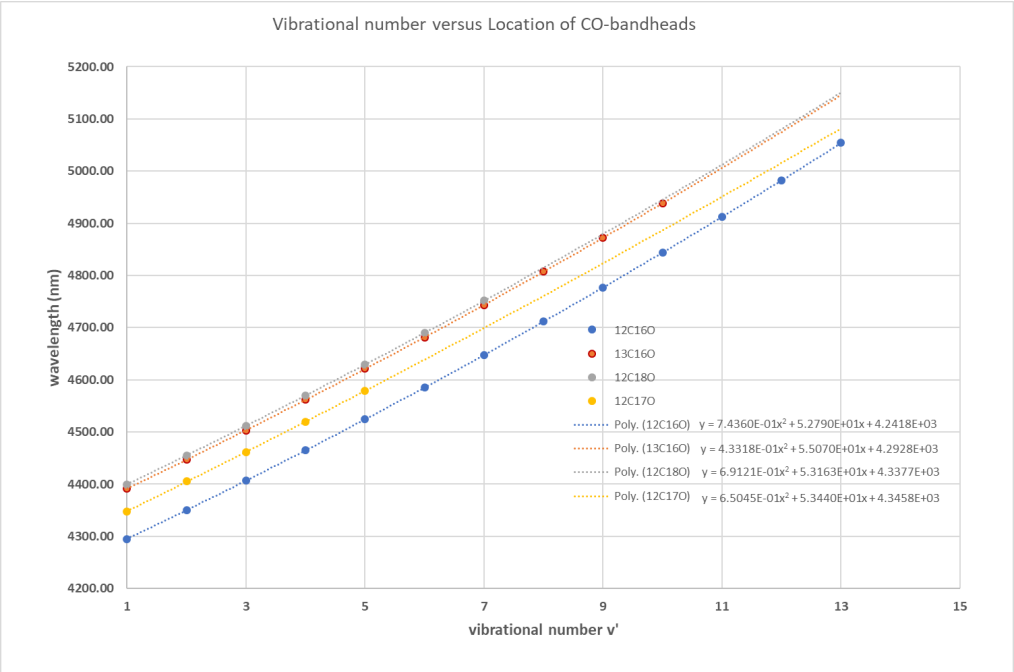

Figure 40: Location of fundamental CO bandheads as a function of vibrational number v'

The location of the bandheads as a function of the vibrational number v'(v'refers to the upper level of a transition) is a 2nd order polynomial. Figure 40 shows the calculated fundamental bandheads for$^{12}C^{16}O$, $^{13}C^{16}O$, $^{12}C^{17}O$ and $^{12}C^{18}O$.

5.3 Isotopic effects

The same element can have atoms with different atomic mass (A), namely isotopes. The effect on metal transition lines is very small and consists of two parts: normal mass shift (NMS) and specific mass shift (SMS). The NMS for a transition can be calculated (Aspect *et al.*, 1991) quickly:

$$\mathrm{NMS}(cm^{-1}) = \frac{\tilde{\nu}}{1822.9}\frac{(A^* - A)}{A^* A} \tag{55}$$

with A=Mass number of isotope 1, A^*= Mass number of isotope 2, A^*>A, $\tilde{\nu}$= wavenumber of observed transition.
The SMS shift is based on a momentum correlation between the electrons and can be positive or negative. It cannot be calculated accurately for moderate-mass and heavy atoms. Rosberg *et al.* (1993) have measured a total split of ≈104 mÅ for a Fe II (^{56}Fe/^{54}Fe) line at 999.966 nm. The calculated NMS (eqn (55)) for this line and isotope pair is 3.6 mÅ which would result in a SMS shift of ≈100 mÅ.
For molecules, the isotopic effect on the molecular transition lines is much larger since the rotational constant is mass dependent via the momentum of inertia. This causes additional complexity to the molecular transition lines. The isotopic effect can be quantified using the ratio of the reduced masses μ_1 and μ_2. For the pair $^{12}C^{16}O$ and $^{13}C^{16}O$ (m_1=mass of ^{16}O, m_2=mass

of ^{12}C, m$_3$=mass of ^{13}C):

$$\mu_1 = \frac{m_1 m_2}{m_1 + m_2} \tag{56}$$

$$\mu_2 = \frac{m_1 m_3}{m_1 + m_3} \tag{57}$$

$$f_{\text{iso}} = \frac{\mu_1}{\mu_2} \tag{58}$$

Table 44 lists f$_{\text{iso}}$-values for the observed isotopes of CO.

Table 44: f$_{\text{iso}}$ for different CO isotopes

X	^{12}C^{16}O	^{13}C^{16}O	^{12}C^{17}O	^{12}C^{18}O
f$_{\text{iso}}$	1.000	0.9559	0.9747	0.9523
$\sqrt{f_{\text{iso}}}$	1.000	0.9777	0.9873	0.9758

The rotational constant B can be calculated :

$$B_{(2)} = f_{\text{iso}} B_{(1)} \tag{59}$$

with (B$_{(1)}$ = ^{12}C^{16}O, B $_{(2)}$ = ^{13}C^{16}O, ^{12}C^{17}O, ^{12}C^{18}O), f$_{\text{iso}}$ according to Table 44.
The plot of B$_{(2)}$ from eqn. (59) versus the vibration number (v") shows a bias - calculated values of B$_{(2)}$ are systematically lower than the observed values:

$$B_{(2)\text{observed}} - B_{(2)} = mv'' + b \tag{60}$$

Combining eqn.(59) and eqn. (60):

$$B_{(2)} = a * B_{(1)} + mv'' + b \tag{61}$$

with B$_{(2)}$= rotational constant of ^{13}C^{16}O,^{12}C^{17}O or ^{12}C^{18}O, B $_{(1)}$= rotational constant ^{12}C^{16}O, a=f$_{\text{iso}}$, m=slope of residual correction, b=intercept, v"=lower vibrational quantum number. Table 45 provides the respective constants a, b, m for ^{13}C^{16}O, ^{12}C^{17}O, ^{12}C^{18}O.

Table 45: Bias correction parameter for the calculation of rotational constant B$_v$, eqn. (63), and vibrational transition energies ΔE, eqn. (61), for ^{13}C^{16}O, ^{12}C^{18}O, ^{12}C^{17}O based on observed values of ^{12}C^{16}O

	ΔE			B$_v$		
Parameter	^{13}C^{16}O	^{12}C^{18}O	^{12}C^{17}O	^{13}C^{16}O	^{12}C^{18}O	^{12}C^{17}O
a	0.97771	0.97584	0.98726	0.95591	0.95227	0.97468
m	0.5622	0.6142	0.3293	4.15*10^{-4}	3.73*10^{-4}	2.50*10^{-4}
b	0.5897	0.6403	0.3294	5.88*10^{-4}	6.36*10^{-4}	5.88*10^{-4}

Table 46 compares the results for the rotational constant B$_e$ as observed in the 10 Leo spectrum (see Section 5.1) for ^{13}C^{16}O and calculated from equation (59) as well as from (61) with the parameter given in Table 45.

Table 46: Comparison of rotational constant B_ν for ^{13}CO based on observed values of ^{12}CO

Transition ν'- ν''	observed B_ν		calculated B_ν(eq.(59))		bias corr. B_ν (eq.(61))	
	$^{12}C^{16}O$	$^{13}C^{16}O$	$^{13}C^{16}O$	%Difference	$^{13}C^{16}O$	%Difference
1-0	1.9222	1.8462	1.8462	5.95E-05	1.8461	7.10E-03
2-1	1.9049	1.8298	1.8294	2.20E-02	1.8298	1.67E-03
3-2	1.8872	1.8135	1.8126	4.76E-02	1.8135	-5.97E-04
4-3	1.8700	1.7972	1.796	6.75E-02	1.7973	-9.09E-03
5-4	1.8523	1.7808	1.7793	8.10E-02	1.7812	-2.45E-02
6-5	1.8345	1.7643	1.7614	1.64E-01	1.7638	2.90E-02
7-6	1.8170	1.7480	1.7453	1.52E-01	1.7482	-1.25E-02
8-7	1.7997	1.7316	1.7279	2.11E-01	1.7313	1.59E-02
9-8	1.7808	1.7152	1.7115	2.19E-01	1.7154	-7.29E-03
10-9	1.7644	1.6989	1.6945	2.59E-01	1.6989	3.07E-04
11-10	1.7481		1.6692		1.6773	
12-11	1.7316		1.6511		1.6592	
13-12	1.7114		1.6334		1.6416	

The vibrational frequencies for atoms/molecules are downshifted for higher mass isotopes. Since the frequency is proportional to the square root of μ, the $\sqrt{f_{\text{iso}}}$ can be used to estimate the isotopic shift in the wavenumbers. $\sqrt{f_{\text{iso}}}$ values are given in Table 44 as well (isotope(1)=$^{12}C^{16}O$).

$$\nu_{\text{isotope (2)}} = \sqrt{f_{\text{iso}}}\,\nu_{\text{isotope (1)}} \tag{62}$$

Equation (62) allows a calculation of vibrational levels and bands of isotopes which may not be observable due to their low abundance. The simplified calculation using equation (62) with the factors of Table 44 does not provide acceptable results for the isotope as shown in Table 47. However, a second correction can be applied as the residuals show a systematic behaviour. The final fit equation can be expressed analogous to eqn. (61) by:

$$\Delta E_{(2)} = a * \Delta E_{(1)} + m\nu'' + b \tag{63}$$

with $\Delta E_{(2)}$= transition energy of $^{13}C^{16}O$,$^{12}C^{17}O$ or $^{12}C^{18}O$, $\Delta E_{(1)}$= transition energy of reference isotope $^{12}C^{16}O$, a=$\sqrt{f_{\text{iso}}}$, m=slope of residual correction, b=intercept, ν''=lower vibrational quantum number. Table 45 provides the respective constants a, b, m for $^{13}C^{16}O$, $^{12}C^{17}O$, $^{12}C^{18}O$. The observed transition energies (ΔE) for ν'- ν'' for fundamental vibrational transitions for $^{12}C^{16}O$ and $^{13}C^{16}O$ are listed in Table 47 and compared with the calculated ΔE values using equation (62) and (63).

Table 47: Calculation of ΔE(cm^{-1}) for vibrational levels of ^{13}CO using observed values of ^{12}CO

Transition	ΔE observed		ΔE calculated (eq. 62)		ΔE bias corr. (eq. 63)	
v'- v''	$^{12}C^{16}O$	$^{13}C^{16}O$	$^{13}C^{16}O$	Residual	$^{13}C^{16}O$	Residual
1-0	2143.27	2096.07	2095.50	0.57	2096.09	-0.02
2-1	2116.79	2070.75	2069.61	1.14	2070.76	-0.01
3-2	2090.38	2045.50	2043.78	1.72	2045.50	0.00
4-3	2064.03	2020.31	2018.02	2.29	2020.30	0.01
5-4	2037.75	1995.18	1992.33	2.85	1995.17	0.01
6-5	2011.55	1970.13	1966.71	3.41	1970.11	0.01
7-6	1985.42	1945.13	1941.16	3.97	1945.12	0.01
8-7	1959.35	1920.21	1915.68	4.53	1920.20	0.01
9-8	1933.38	1895.36	1890.28	5.08	1895.37	-0.01
10-9	1907.47	1870.58	1864.95	5.63	1870.60	-0.02
11-10	1881.62	1845.84	1839.67	6.16	1845.88	-0.05
12-11	1855.84	1821.18	1814.48	6.70	1821.25	-0.07
13-12	1830.25	1796.58	1789.46	7.12	1796.79	-0.21

The observed and bias corrected ΔE-values for $^{13}C^{16}O$ (eqtn 63) in Table 47 agree remarkably well. The bias corrected results of the transition energies ΔE for the isotopologues $^{13}C^{16}O$, $^{12}C^{18}O$ and the observed $^{12}C^{17}O$ are summarized in Table 48.

Table 48: Comparison of calculated vibrational transition energies for CO isotopologues ($^{13}C^{16}O$, $^{12}C^{18}O$ and $^{12}C^{17}O$) with literature

Transition	ΔE (cm^{-1})					
v'- v''	$^{13}C^{16}O$		$^{12}C^{18}O$		$^{12}C^{17}O$	
	This work	Literature[a]	This work	Literature[a]	This work	Literature[b]
1-0	2096.09	2096.07	2092.13	2092.12	2116.29	2116.29
2-1	2070.76	2070.75	2066.90	2066.90	2090.48	2090.48
3-2	2045.50	2045.50	2041.74	2041.75	2064.73	2064.74
4-3	2020.30	2020.31	2016.65	2016.65	2039.05	2039.05
5-4	1995.17	1995.18	1991.62	1991.62	2013.44	2013.44
6-5	1970.11	1970.12	1966.66	1966.66	1987.90	1987.89
7-6	1945.12	1945.13	1941.77	1941.76	1962.43	1962.41
8-7	1920.20	1920.21	1916.95	1916.93	1937.03	1937.01
9-8	1895.37	1895.36	1892.22	1892.17	1911.71	1911.67
10-9	1870.60	1870.58	1867.55	1867.48	1886.47	1886.41
11-10	1845.88	1845.87	1842.93	1842.87	1861.27	1861.23
12-11	1821.25	1821.24	1818.40	1818.33	1836.16	1836.12
13-12	1796.79	1796.69	1794.04	1793.87	1811.22	1811.10

[a]values from the differences of vibrational energy levels calculated with RKR potentials Velichko & Mikhailenko (2015) and [b]Velichko(private communication)

Table 48 extends Table 47 and provides additional data for the isotopologues $^{13}C^{16}O$, $^{12}C^{18}O$ and $^{12}C^{17}O$ and a comparison with published data. It is emphasized, that the bias corrected results of the transition energies ΔE for the isotopologues are directly derived from the observed $^{12}C^{16}O$.

The differences of the calculated vibrational energy levels by Velichko & Mikhailenko (2015) and the calculated, bias corrected ΔE agree very well for the lower transitions but degrades for ν >10. Data in the red cells refers to bands which could not be detected in the 10 Leo spectrum due to their low intensity.

6 Conclusions and summary

This work takes advantage of the pipeline reduced and fully corrected high resolution NIR spectrum of the cool star 10 Leo. The datafile has about 186000 records of normalized flux values and corresponding wavenumbers. The spectrum reaches from 962 nm to 5225 nm covering the bandpasses YJ, H, K, L and M. The wavelength calibration error for the complete spectral range has been confirmed to be within 0.1 Å, except for a small region (45482 Å to 45700 Å) in the M-band showing wavelength shifts towards higher wavelengths of up to 1.3 Å. The average resolving power is equivalent to a two-pixel resolution of $0.2\overline{2}$ Å at 2 μm.
The 10 Leo spectrum features a multitude of absorption lines stemming from atoms and molecules. More than 23000 absorption lines were sorted in Excel spreadsheets with their line properties such as wavelength, normalized flux, identification, log gf, cdepth, transition identifier, equivalent width and respective published data. The spreadsheet unveils many gaps in the spectrum across the wavelength range of various sizes caused by atmospheric absorption and instrumental properties.
The identification of absorption lines is done visually with the help of various line lists,"stellar extraction" from VALD3 and relevant published articles. Hydrogen and metal lines from the various elements are identified. They include the elements C, Na, Mg, Al, Si, P, S, K, Ca, Sc, Ti, V, Cr, Mn, Fe, Co, Ni, Cu, Zn, Rb, Sr, Y, Zr, Ce and Dy. Some of the element, e.g. Sr, Y, Ce and Dy are only detectable in ionized form.
Fe I and Fe II lines are compared with recent published data. While line positions fit, loggf values show significant differences. A set of Si I lines shows reasonable agreement for wavelength and equivalent width for 10 Leo and Arcturus. Lines for Ce II are compared to published data.
Molecules such as CO, CN and OH dominate the spectrum. 99.7% (cdepth level > 0.005) of the CO and CN lines are assigned to their specific transition. More than 100 CO-bands from the P and R branch of the CO covibrational spectrum and about 140 CN-bands stemming from the P, R, Q and their satellite branches were evaluated. Each band is fitted with a 4th order polynomial to locate the transition lines and ensure consistency in transition assignment. Fundamental bands ($\Delta\nu$=1) of CO are observed in the M-band, first overtone bands ($\Delta\nu$=2) in the K-Band and second overtone bands ($\Delta\nu$=3) in the H-band. Fundamental bands ($\Delta\nu = \pm1,0$) for CN are located in the YJ and H regions, whereas the first overtone bands are found in the K band. The maximum cdepth for all observed molecular lines within a band is recorded at J ≈31 with the exception of the satellite bands of CN which have the maximum at J ≈10. Absorption lines from ^{13}CO, C^{17}O and C^{18} are easily identified in several bands and remarkably strong. In contrast, absorption lines from ^{13}CN are very weak and only identified for the 0-0 bands. The presence of C^{15}N is not detectable in the spectrum at all.
Spectral cutouts with identification information are attached for each element and molecule in the Annex 7.2.1, 7.2.2.
About 1300 lines are not attributed to any species, representing ≈ 6% of all observed lines in the 10 Leo spectrum. Those exceeding an equivalent width of >50 mÅ are listed in a separate table for each bandpass in the Annex 7.1.1. Lines that have been categorized as unknown lines include lines that are partly due to the use of calculated wavelengths based on insufficient physical data.

A large potential of lines remains to find lines from neutron capture elements. A selection of spectral cutouts is provided in the Annex 7.2.3 as well.
The 10 Leo spectrum is compared to the Arcturus spectrum and several spectral ranges from 10 Leo are overlayed with the respective parts of the Arcturus spectrum (Annex 7.2.4). Distinct differences in the line strength of Sc I, Ti I, CO and OH are clearly visible and show an increased strength for Arcturus. On the other hand, lines for C I, S I, Fe I and CN seem stronger for 10 Leo. However, the majority of metal lines are very similar in strength for 10 Leo and Arcturus. Some differences are observed for the lines of the CO-isotopologues. The lines for the isotope $^{12}C^{17}O$ are stronger for 10 Leo whereas the lines for $^{13}C^{16}O$ are enhanced in the Arcturus spectrum.
The impact of T_{eff}, log g and v_{mic} on the cdepth was modelled for Arcturus, 10 Leo and the Sun. The results are consistent with the observed similarity between Arcturus and 10 Leo.
Synthetic spectra for 10 Leo and Arcturus are generated with MARCS models that are modified by the metal abundance values to match the observations. The differences between solar abundance and the synthetic abundances for 10 Leo and Arcturus are all positive except for Mn and Al. The differences in abundances based on synthetic spectra between Leo and Arcturus are also all positive. Na, Mg, Al, Si, K, Ca, Ti and Sr seem only slightly more abundant ($\leq$ 0.1 dex) in the 10 Leo spectrum. Sc, Cr, Mn, Fe and Ni show greater differences in their abundance between 0.1 and 0.2 dex. V shows the most significant difference (0.4 dex) in abundance between 10 Leo and Arcturus. The findings are consistent with a lower metallicity for Arcturus compared to 10 Leo and a lower metallicity for 10 Leo compared to the Sun. The significant differences for the molecules CO and CN with about 0.3 dex may be an indication that oxygen and nitrogen are more abundant in 10 Leo.
The comparison between observed and synthetic spectra identified a large number of lines which are present in the synthetic spectra but are not observed and lines which are observed and identified but not present in the synthetic spectra. Tables for the most prominent "discrepancies" with cdepth >0.05 are given for each bandpass in the Annex 7.1.2. The high number of discrepancies reveals the need to improve the spectroscopic data for metals, e.g. for Mg and Fe. This is of utmost importance in order to to assess their interference with possible lines originating from neutron capture elements. This work tries to identify lines belonging to molecules, Fe and less massive elements as complete as possible since these interfering lines can completely mask or mimic lines of possible neutron capture elements. Therefore, search for absorption lines for neutron capture elements in the NIR is critically dependent on the quality of data for molecules and the "known" metals such as Fe and less massive elements.
The quality of the spectrum allows the determination of various spectral parameter for CO such as rotational constant, vibrational coupling constant, distortion constant and transition energies of the vibrational states. Linear relations between rotational constant and vibrational quantum number v" show a decrease of the rotational constant with rising v". A similar dependency is noted for the distortion constant.
Special attention is given to the identification of CO-bandheads. Bandheads for the fundamental transitions are in the range of J$\approx$88 whereas the bandheads for the 1st overtone and 2nd overtone can be found at J$\approx$50 and J$\approx$34. The relation between the wavelengths of bandheads of a given isotop and the vibrational quantum number v' is almost linear but can be better fitted with a quadratic polynomial. CO-bandheads are identified for the R-branches at J $\approx$88 (fundamental bands), J$\approx$50 (1st overtone) and J$\approx$34 (2nd overtone).
Finally, the spectral parameter of the CO isotopologues are calculated from the observed $^{12}C^{16}O$ spectra. A simple bias correction is applied and a very good agreement with available observed values of the isotopologues as well as with published data is achieved.

Bibliography

Andreasen, D. T., Sousa, S. G., Delgado Mena, E., Santos, N. C., Tsantaki, M., Rojas-Ayala, B., & Neves, V. 2016. Near-infrared spectroscopy of the Sun and HD 20010. Compiling a new line list in the near-infrared. *A&A*, **585**(Jan.), A143.

Arnould, M., & Goriely, S. 2020. Astronuclear Physics: A tale of the atomic nuclei in the skies. *Progress in Particle and Nuclear Physics*, **112**(May), 103766.

Aronson, E., & Waldén, P. 2015. Using near-infrared spectroscopy for characterization of transiting exoplanets. *A&A*, **578**(June), A133.

Aspect, A, Bauche, J, Godefroid, M, Grangier, P, Hansen, J E, & Vaeck, N. 1991. Experimental and MCHF isotope shifts of strongly perturbed levels in Ca I and Sr I. *Journal of Physics B: Atomic, Molecular and Optical Physics*, **24**(18), 4077–4099.

Bailer-Jones, C. A. L., Rybizki, J., Fouesneau, M., Demleitner, M., & Andrae, R. 2021. Estimating Distances from Parallaxes. V. Geometric and Photogeometric Distances to 1.47 Billion Stars in Gaia Early Data Release 3. *AJ*, **161**(3), 147.

Barklem, P. S., & Collet, R. 2016. Partition functions and equilibrium constants for diatomic molecules and atoms of astrophysical interest. *A&A*, **588**(Apr.), A96.

Benatti, S. 2018. Multi-Wavelength High-Resolution Spectroscopy for Exoplanet Detection: Motivation, Instrumentation and First Results. *Geosciences*, **8**(8), 289.

Brooke, J. S. A., Ram, R. S., Western, C. M., Li, G., Schwenke, D. W., & Bernath, P. F. 2014. Einstein A Coefficients and Oscillator Strengths for the A $^2\Pi$-X $^2\Sigma^+$ (Red) and B$^2\Sigma^+$-X$^2\Sigma^+$ (Violet) Systems and Rovibrational Transitions in the X $^2\Sigma^+$ State of CN. *ApJS*, **210**(2), 23.

Burbidge, E. M., Burbidge, G. R., Fowler, W. A., & Hoyle, F. 1957. Synthesis of the Elements in Stars. *Reviews of Modern Physics*, **29**(4), 547.

Busso, M., Gallino, R., & Wasserburg, G. J. 1999. Nucleosynthesis in Asymptotic Giant Branch Stars: Relevance for Galactic Enrichment and Solar System Formation. *Annual Review of Astronomy and Astrophysics*, **37**(1), 239.

Corliss, C. H. 1973. Wavelengths and Energy Levels of the Second Spectrum of Cerium (Ce II). *Journal of research of the National Bureau of Standards. Section A, Physics and chemistry*, **77A**(4), 419.

Coxon, J. A., & Hajigeorgiou, P. G. 2004. Direct potential fit analysis of the X $^1\Sigma^+$ ground state of CO. *The Journal of chemical physics*, **121**(7), 2992–3008.

Cunha, K., Smith, V. V., Hasselquist, S., Souto, D., Shetrone, M. D., Allende Prieto, C., Bizyaev, D., Frinchaboy, P., García-Hernández, D. A., Holtzman, J., Johnson, J. A., Jőnsson, H., Majewski, S. R., Mészáros, S., Nidever, D., Pinsonneault, M., Schiavon, R. P., Sobeck, J., Skrutskie, M. F., Zamora, O., Zasowski, G., & Fernández-Trincado, J. G. 2017. Adding the s-Process Element Cerium to the APOGEE Survey: Identification and Characterization of Ce II Lines in the H-band Spectral Window. *ApJ*, **844**(2), 145.

da Silva, R., Milone, A. C., & Reddy, B. E. 2011. Homogeneous photospheric parameters and C abundances in G and K nearby stars with and without planets. *A&A*, **526**(Feb.), A71.

Gendriesch, R., Lewen, F., Klapper, G., Menten, K. M., Winnewisser, G., Coxon, J. A., & Müller, H. S. P. 2009. Accurate laboratory rest frequencies of vibrationally excited CO up to v = 3 and up to 2 THz. *A&A*, **497**(3), 927–930.

Goorvitch, D. 1994. Infrared CO Line List for the X 1 Sigma + State. *ApJS*, **95**(Dec.), 535.

Gordon, I. E., Rothman, L. S., Tan, Y., Kochanov, R. V., & Hill, C. 2017 (June). HITRAN2016: Part I. Line lists for H_2O, CO_2, O_3, N_2O, CO, CH_4, and O_2. *Page TJ08 of: 72nd International Symposium on Molecular Spectroscopy*.

Gray, R. O., Corbally, C. J., Garrison, R. F., McFadden, M. T., & Robinson, P. E. 2003. Contributions to the Nearby Stars (NStars) Project: Spectroscopy of Stars Earlier than M0 within 40 Parsecs: The Northern Sample. I. *The Astronomical Journal*, **126**(4), 2048.

Gustafsson, B., Edvardsson, B., Eriksson, K., Jørgensen, U. G., Nordlund, Å., & Plez, B. 2008. A grid of MARCS model atmospheres for late-type stars. I. Methods and general properties. *A&A*, **486**(3), 951.

Hasselquist, S., Shetrone, M., Cunha, K., Smith, V. V., Holtzman, J., Lawler, J. E., Allende Prieto, C., Beers, T. C., Chojnowski, D., Fernández-Trincado, J. G., García-Hernández, D. A., Hearty, F. R., Majewski, S. R., Pereira, C. B., Placco, V. M., Villanova, S., & Zamora, O. 2016. Identification of Neodymium in the Apogee H-Band Spectra. *ApJ*, **833**(1), 81.

Hinkle, K. H., Lambert, D. L., & Snell, R. L. 1976. The $^{12}C/^{13}C$ ratio in stellar atmospheres. VI. Five luminous cool stars. *ApJ*, **210**(Dec.), 684.

Hinkle, K. H., Wallace, L., & Livingston, W. 1995. Infrared Atlas of the Arcturus Spectrum, 0.9-5.3 microns. *Publications of the Astronomical Society of the Pacific*, **107**(nov), 1042.

Kaeufl, H. U., Ballester, P., Biereichel, P., Delabre, B., Donaldson, R., Dorn, R., Fedrigo, E., Finger, G., Fischer, G., Franza, F., Gojak, D., Huster, G., Jung, Y., Lizon, J. L., Mehrgan, L., Meyer, M., Moorwood, A., Pirard, J. F., Paufique, J., Pozna, E., Siebenmorgen, R., Silber, A., Stegmeier, J., & Wegerer, S. 2004 (Sept.). CRIRES: a high-resolution infrared spectrograph for ESO's VLT. *Pages 1218–1227 of:* Moorwood, Alan F. M., & Iye, Masanori (eds), *Ground-based Instrumentation for Astronomy*. Society of Photo-Optical Instrumentation Engineers (SPIE) Conference Series, vol. 5492.

Käppeler, F., Beer, H., & Wisshak, K. 1989. s-process nucleosynthesis-nuclear physics and the classical model. *Reports on Progress in Physics*, **52**(8), 945.

Karakas, A. I., & Lattanzio, J. C. 2014. The Dawes Review 2: Nucleosynthesis and Stellar Yields of Low- and Intermediate-Mass Single Stars. *PASA*, **31**(July), e030.

Karttunnen, H., Kröger, P., Oja, H., Poutanen, M., & Donner, K. J. 2016. *Fundamental Astronomy*. Springer.

Kausch, W., Noll, S., Smette, A., Kimeswenger, S., Barden, M., Szyszka, C., Jones, A. M., Sana, H., Horst, H., & Kerber, F. 2015. Molecfit: A general tool for telluric absorption correction - II. Quantitative evaluation on ESO-VLT/X-Shooterspectra. *A&A*, **576**, A78.

Kochukhov, O. 2012. Synth3: Non-magnetic spectrum synthesis code. Dec., ascl:1212.010.

Kochukhov, O. 2018 (May). *BinMag: Widget for comparing stellar observed with theoretical spectra*. Available at http://www.astro.uu.se/ oleg/binmag.html, (ascl:1805.015).

Kondo, S., Fukue, K., Matsunaga, N., Ikeda, Y., Taniguchi, D., Kobayashi, N., Sameshima, H., Hamano, S., Arai, A., Kawakita, H., Yasui, C., Izumi, N., Mizumoto, M., Otsubo, S., Takenaka, K., Watase, A., Asano, A., Yoshikawa, T., & Tsujimoto, T. 2019. Fe I Lines in 0.91-1.33 μm Spectra of Red Giants for Measuring the Microturbulence and Metallicities. *ApJ*, **875**(2), 129.

Korek, M., & El-Kork, N. 2018. Solution of the Rovibrational Schrödinger Equation of a Molecule Using the Volterra Integral Equation. *Advances in Physical Chemistry*, **2018**(10), 1.

Kramida, A., Ralchenko, Y., Reader, J., & and NIST ASD Team. 2019. NIST Atomic Spectra Database (ver. 5.7.1), [Online]. Available: `https://physics.nist.gov/asd` [2020, October 2]. National Institute of Standards and Technology, Gaithersburg, MD.

Le Floch, A. 1991. Revised molecular constants for the ground state of CO. *Molecular Physics*, **72**(1), 133–144.

Lebzelter, T., Seifahrt, A., Uttenthaler, S., Ramsay, S., Hartman, H., Nieva, M. F., Przybilla, N., Smette, A., Wahlgren, G. M., Wolff, B., Hussain, G. A. J., Käufl, H. U., & Seemann, U. 2012. CRIRES-POP. A library of high resolution spectra in the near-infrared. *A&A*, **539**(Mar.), A109.

Luo, Y.R. 2007. Comprehensive Handbook of Chemical Bond Energies. *Boca Raton: CRC Press*, Mar.

McNaught, A. D., & Wilkinson, A. 1997. *Compendium of Chemical Terminology,(the "Gold Book")*. Vol. 2nd ed. Blackwell Scientific Publications, Oxford.

Mina-Camilde, N., Manzanares I., C., & Caballero, J. F. 1996. Molecular Constants of Carbon Monoxide at v = 0, 1, 2, and 3: A Vibrational Spectroscopy Experiment in Physical Chemistry. *Journal of Chemical Education*, **73**(8), 804.

Mishenina, T. V., Bienaymé, O., Gorbaneva, T. I., Charbonnel, C., Soubiran, C., Korotin, S. A., & Kovtyukh, V. V. 2006. Elemental abundances in the atmosphere of clump giants. *A&A*, **456**(3), 1109.

Nicholls, C. P., Lebzelter, T., Smette, A., Wolff, B., Hartman, H., Käufl, H. U., Przybilla, N., Ramsay, S., Uttenthaler, S., Wahlgren, G. M., Bagnulo, S., Hussain, G. A. J., Nieva, M. F., Seemann, U., & Seifahrt, A. 2017. CRIRES-POP: a library of high resolution spectra in the near-infrared. II. Data reduction and the spectrum of the K giant 10 Leonis. *A&A*, **598**(Feb.), A79.

Nissen, P. E., & Gustafsson, B. 2018. High-precision stellar abundances of the elements: methods and applications. *The Astronomy and Astrophysics Review*, **26**(1).

Piskunov, N. E., Kupka, F., Ryabchikova, T. A., Weiss, W. W., & Jeffery, C. S. 1995. VALD: The Vienna Atomic Line Data Base. *A&AS*, **112**(Sept.), 525.

Popovas, A., & Jørgensen, U. G. 2016. Partition functions. I. Improved partition functions and thermodynamic quantities for normal, equilibrium, and ortho and para molecular hydrogen. *A&A*, **595**(Nov.), A130.

Ramírez, I., & Allende Prieto, C. 2011. Fundamental Parameters and Chemical Composition of Arcturus. *ApJ*, **743**(2), 135.

Roman, N. G. 1952. The Spectra of the Bright Stars of Types F5-K5. *A&A*, **116**(July), 122.

Rosberg, M., Litzen, U., & Johansson, S. 1993. Experimental isotopic shifts in Ni II and Fe II. *MNRAS*, **262**(1), L1–L5.

Ryabchikova, T., Piskunov, N., Kurucz, R. L., Stempels, H. C., Heiter, U., Pakhomov, Y., & Barklem, P. S. 2015. A major upgrade of the VALD database. *Phys. Scr.*, **90**(5), 054005.

Scholz, M. 2009. Kleines Lehrbuch der Astronomie und Astrophysik, Band 15, Grundlagen der Sternspektroskopie. https://www.astronomie.de/bibliothek/kleines-lehrbuch-der-astronomie/.

Schröder, K.-P., & Cuntz, M. 2007. A critical test of empirical mass loss formulas applied to individual giants and supergiants. *Astronomy & Astrophysics*, **465**(2), 593.

Shulyak, D., Rengel, M., Reiners, A., Seemann, U., & Yan, F. 2019. Remote sensing of exoplanetary atmospheres with ground-based high-resolution near-infrared spectroscopy. *A&A*, **629**(Sept.), A109.

Smette, A., Sana, H., Noll, S., Horst, H., Kausch, W., Kimeswenger, S., Barden, M., Szyszka, C., Jones, A. M., Gallenne, A., Vinther, J., Ballester, P., & Taylor, J. 2015. Molecfit: A general tool for telluric absorption correction. I. Method and application to ESO instruments. *A&A*, **576**(Apr.), A77.

Sneden, C., Cowan, J. J., & Gallino, R. 2008. Neutron-Capture Elements in the Early Galaxy. *Annual Review of Astronomy and Astrophysics*, **46**(1), 241.

Soubiran, C., Bienaymé, O., Mishenina, T. V., & Kovtyukh, V. V. 2008. Vertical distribution of Galactic disk stars. IV. AMR and AVR from clump giants. *A&A*, **480**(1), 91.

Tan, K., Shi, J., Takada-Hidai, M., Takeda, Y., & Zhao, G. 2016. A non-LTE study of silicon abundances in giant stars from the Si I infrared lines in the ZJ-band. *The Astrophysical journal*, **823**(1), 36.

Tatum, J. 2015. *Stellar Atmospheres*. https://phys.libretexts.org/Bookshelves/Astronomy__Cosmology/Book%3A_Stellar_Atmospheres_(Tatum).

Truran, J. W. 1984. Nucleosynthesis. *Annual Review of Nuclear and Particle Science*, **34**(Jan.), 53.

van Leeuwen, F. 2007. *VizieR Online Data Catalog: Hipparcos, the New Reduction*.

Velichko, T. I., & Mikhailenko, S. N. 2015. RKR potentials of isotopologues of the CO molecule. *Optics and Spectroscopy*, **118**(1), 6–10.

7 Annex

7.1 Tables

7.1.1 Tables of unknowns with EW>50 mÅ

Possible blending lines are noted in the subsequent tables which have similar wavelength but are too weak to account for the observed EW.

Table 49: Unassigned lines with EW>50 mÅ in YJ-band

λ (nm)	EW (mÅ)	Possible blending lines	[a]Reference
1113.69	63	Co I 1113.68, Fe I 1113.69, V I 1113.70, Ca I 1113.70	(1)
1120.30	64	V II 1120.43, Fe II 1121.41	(1)
1121.40	55	Fe I 1121.39, Fe II 1121.41	(1)
1127.28	67	Fe II 1127.29	(1)
1131.46	72	Sc I 1131.45, Ti I 1131.47, Cr I 1131.45, Fe I 1131.44, Si2 1131.43	(1)
1132.25	58	doublet Fe II 1132.24, 1132.25	(1)
1132.40	66	Fe II 1132.39	(1)
1139.26	56	Co I 1139.27, Cr I 1139.28, (CN1 (cdepth 0.022) at 1139.27 subtracted)	(1)
1141.54	81	Cr II 1141.52	(1)
1144.07	55	Ti I 1144.05, Mn II 1144.04	(1)
1146.27	59		
1146.84	59	Si I 1146.85, 1146.85 Ca I	(1)(2)
1147.86	97	Fe II 1147.85, Sc1 1147.85, Co I 1147.88	(1)(2)
1150.19	78		
1165.18	61	Fe II 1165.18, Al I 1165.22, Mn II 1165.24	(1)
1261.72	77	Fe II 1261.69, C1 1261.75	(1)
1263.17	53	Ti I123.17, Cr II 1263.18	(1)
1266.23	55	Cr II 1266.20, 1266.29	(1)
1308.06	73	Fe II 1308.09, Fe I 1308.09, Ti I 1308.08 (cdepth 0.253) subtracted	(1)(2)

[a]Reference: (1) Ryabchikova *et al.* (2015), (2): Hinkle *et al.* (1995)

Table 50: Unassigned lines with EW>50 mÅ in H-band

λ (nm)	EW (mÅ)	Possible blending lines	[a]Reference
1415.75	122	Fe II 1415.74, Ti II 1415.75, Ni II 1415.76, Cs I 1415.78, 1415.81 Cr I	(1)
1416.53	75	C I 1416.52	(1)
1416.90	161	Co I 1416.90, Mn II 1416.94, V I 1416.92	(1)
1418.00	186		
1418.07	81	1418.06 CN 0-1R(1)0.5, Fe II 1418.05, Ti I 1418.11	(1)
1418.18	246	1418.18 CN 0-1Q(2)13.5, Fe II 1418.17, Ni I 1418.17, Mn I 1418.18, V I 1418.18, Sc II 1418.18	(1)
1420.10	65	Cr I 1420.11, V I 1420.07	(1)
1421.09	102	Fe II 1420.06	(1)
1421.12	87	Fe I 1421.12 (cdepth 0.020)	
1421.54	146	Fe II 1421.52, Sc I 1421.51, Mn II 1421.55, Cr I 1421.56	(1)
1424.87	177	Fe I 1421.90	(1)
1425.29	316	Fe I 1425.30 (CN0-1R(2)31.5 subtracted)	
1426.16	58	Fe I 1426.11, As I 1426.18	(1)
1426.37	185	Fe I 1426.39, Ca I 1426.34	(1)
1426.81	134	Ti I 1426.81, Fe I 1426.89	(1)
1427.08	62	Fe II 1427.10	(1)
1427.25	74	Ni I 1427.24	(1)
1427.29	98	Co I 1427.31	(1)
1427.65	258	Fe II 1427.68, P I 1427.67, C I 1427.64, Ni I 1427.65	(1)
1427.75	114	Mn I 1427.74, Fe I 1427.74	(1)
1428.02	68	Ti I 1428.04, Fe II 1428.04, Fe I 1428.35	(1)
1428.38	222	V I 1428.75, (CN 0-1RQ(1)35.5 subtracted)	(1)
1428.60	80	Fe II 1428.60	(1)
1428.76	66	V I 1428.75, (CN 0-1RQ(1)20.5 subtracted)	(1)
1429.56	142	Mn II 1429.51, (CN 0-1R(1)35.5 subtracted)	(1)
1429.88	103	Mn I 1429.87	(1)
1429.90	146	Sc II 1429.90, V II 1429.91	(1)
1429.93	93	V II 1429.91, Ti I 1429.94, V I 1429.94	(1)
1432.89	102	Mn I 1432.88, Fe I 1432.84, Fe II 1432.85	(1)
1434.09	143	Fe II 1434.09, Ti I 1434.09, Si I 1434.07	(1)
1449.79	258	Ti I 1449.79, Fe II 1449.78, Mn1 1449.74,V I 1449.76, C I 1449.77, V I 1449.83	(1)
1452.93	230	Fe I 1452.93, Mn I 1452.92, Sc I 1452.94	(1)
1463.56	93	Ti II 1463.55, Fe II 1463.53, H I 1463.60	(1)
1478.08	76	Ni I 1478.08 (CN 1-2Q(1) 20.5 at 1478.12 subtracted)	(1)
1486.44	61	Fe II 1486.46, C I 1486.43	(1)
1486.66	158	Fe II 1486.61, Si I 1486.69	(1)
1487.90	151	Mn I doublet 1487.92 and 1487.93 (cdepth 0.26), (CN 0-1P(2)36.5 subtracted)	(1)
1518.24	93	Cr I 1518.27 (cdepth 0.146)	(1),(2)

Continued on next page

Table 50 – *Continued from previous page*

λ (nm)	EW (mÅ)	Possible blending lines	[a]Reference
1551.32	70	Ti I 1551.26	(1)
1554.44	51	C I 1554.44	(1)
1573.39	82	Ti II 1573.39, Fe I 1573.39, Fe II 1573.42	(1),(2)
1581.45	181	Fe I 1581.45(cdepth 0.037)	(1),(2)
1594.82	51	Fe I 1594.82 (cdepth 0.015)	(1),(2)
1594.96	77	Fe I 1594.96 (CN1 1594.96 subtracted)	(1),(2)
1596.27	52	Fe I 1596.26, Sc I 1596.26	(1)
1597.20	251	Fe I 1597.20, Al I triplet 1597.27 (cdepth 0.288)	(1),(2)
1597.73	129	V I 1597.77	(1)
1600.21	94	Fe II 1600.22, Fe I,2 1600.19, (CN1 1600.20 subtracted)	(1),(2)
1602.10	81	Ni I 1602.11, Cr I 1602.12, Ca I 1602.13	(1),(2)
1603.38	66	Ti I 1603.46	(1)
1604.98	146	Co I 1 1605.01	(1)
1608.03	187	Ti I 1 1607.98, Fe I 1608.03 (cdepth 0.048)	(1),(2)
1609.31	113	Fe I 1609.31	(2)
1612.32	53	Fe II 1612.28, Mn II 1612.28, Fe I 1612.31, Fe II 1612.33	(1)
1625.03	61	Fe I 1625.02(cdpeth 0.041)	
1630.40	62	Ni I 1630.38, Ti I 1630.38, P I 1630.38, Fe I 1630.39, Ti I 1630.41, Ca I 1630.42	(1),(2)
1638.10	67	V I 1638.09, (Fe I 1638.12(cdepth 0.082) subtracted)	(1)
1640.78	89	Mn II 1640.79	(1)
1643.34	135	Ni I 1643.34, Fe II 1643.30	(1)
1645.93	112	CO 3-0P45 1645.91, Fe I 1645.94	(1),(2)
1680.42	117	Fe I 1680.43, Ni II 1680.43	(1),(2)
1686.03	64	Cr I 1684.04	(1)
1688.94	76	Ti II 1688.94, Fe I 1688.94 (cdepth 0.087)	(1)
1693.45	51	Mn I 1693.45, Fe II 1693.41, Si I 1693.41, V I 1643.41	(1)
1696.57	70	Fe II 1696.57	(1)
1696.63	158	Fe I 1696.65 (cdepth 0.090), Cr I 1696.66, Ti I 1696.97	(1)
1704.24	107	Fe I 1704.26 (cdepth 0.176), V I 1704.24, Mn II 1704.25, Fe II 1704.22	(1),(2)
1707.21	127	Fe I 1707.22 (cdepth 0.055), Fe II 1707.22	(1),(2)
1707.97	87	Fe I 1707.98 (cdepth 0.041), Co I 1707.93(cdepth 0.085)	(1),(2)
1708.13	53	Ti I 1708.12, CN 0-1P(1)76.5 1708.16 subtracted	(1),(2)
1708.20	56	Ti I 1708.16, Si I 1708.18	(1)
1727.91	53	Cr I 1727.91, Ti I 1727.92, Fe II 1727.95	(1)
1732.63	57	Fe II 1732.63, C I 1732.63 (cdepth 0.055), Ca I 1732.63(cdepth 0.068)	(1)
1733.03	117	V I 1733.02 Fe II 1733.05, Cr II 1733.05, (Fe I 1733.06 (cdepth 0.176) subtracted)	(1)
1735.44	94	Mn I 1735.46 (cdepth 0.076), Ti I 1736.53	(1)

Continued on next page

Table 50 – *Continued from previous page*

λ (nm)	EW (mÅ)	Possible blending lines	[a]Reference
1736.53	89	Ni I 1736.54 (cdepth 0.076),Ti I 1736.53	(1),(2)
1751.63	60	Mn II 1751.63, Fe I 1751.63(cdepth 0.057)	(1)
1752.74	53	Fe I 1752.76(cdepth 0.083), Fe II 1754.19	(1)
1754.16	82	Cr I 1754.16, Fe II 1754.19	(1)
1758.51	183	Co I 1758.47, Cr II 1758.46, Fe I 1758.53	(1),(2)
1770.57	54	Fe I 1770.57 (cdepth 0.018), Co II 1770.60, Fe II 1770.61	(1),(2)
1774.35	79	Fe II 1774.35, Cr II 1774.34	(1)
1774.44	189		
1775.22	110	Fe I 1775.22 (cdepth 0.060), Co II 1770.60,Fe II 1770.61	(1)
1777.00	84	Fe I 1777.02 (cdepth 0.064), Fe II 1776.98, Cr II 1777.03, Fe II 1777.04	(1),(2)
1779.28	80	Fe I 1779.28, V I 1779.27, Ti I 1779.27, 1779.31, V II 1779.30	(1)
1785.25	76	C I 1785.26 (cdepth 0.032) subtracted	
1788.50	59	Sc I 1788.50, V I 1788.51, Fe I 1788.53, Ni II 1788.53	(1)
1788.55	56		
1794.36	113	Cr II 1794.33, P I 1794.34, Si I 1794.38, K I 1794.40	(1)
1807.84	67	Fe I doublet 1807.86 (cdepth 0.413) subtracted	

[a]Reference: (1) Ryabchikova *et al.* (2015), (2): Hinkle *et al.* (1995)

Table 51: Unassigned lines with EW>50 mÅ in K-band

λ (nm)	EW (mÅ)	Possible blending lines	[a]Reference
1960.01	87	Mn II 1960.02, Fe II 1960.03	(1)
1967.61	62	Fe I 1967.02, cdepth 0.054	(1),(2)
1969.91	68	Fe I 1969.93, cdepth 0.014	
1972.32	61	V I 1972.27	(1)
1979.92	169	Mn I 1979.90, cdepth 0.039	(1)
2008.58	105	Cr II 2008.58, Co I 2008.57, CN 0-2P1-12.5	(1)
2009.53	213	Co II 2009.55, Fe II 2009.58, Mn1 2009.48	(1)
2085.64	71	Fe I 2085.68, cdepth0.034; Fe I 2085.64, cdepth 0.039	
2106.54	265	Cr I 2106.56	(1)
2121.39	163	Mg I 1212.39, cdepth 0.064	(1),(2)
2163.17	112	Ti I 2163.24, Fe II 2163.25, V I 2163.12, Ca I 2163.11	(1)
2308.13	55	Fe II 2308.15	(1)
2366.07	74	Sc I 2366.09 13CO 2-0R19, cdepth 0.019	(1)
2366.97	53	H I 2366.94, Cr II 2366.96	(1)
2379.37	74	Fe II 2379.37, 2379.27 CO, cdepth 0.025,	(1)
2395.49	63	Fe II 2395.46	(1)
2398.13	52	Si I 2398.13	(1)
2405.34	80	13CO 4-2R42, cdepth 0.023	(1)
2417.39	75	Mn II 417.39	(1)
2478.67	157		
2499.27	157	Al I 2499.28, cdepth 0.073	(1)
2508.83	224	Ni II 2508.82	(1)

[a]Reference: (1) Ryabchikova *et al.* (2015), (2): Hinkle *et al.* (1995)

Table 52: Unassigned lines with EW>50 mÅ in L-band

λ (nm)	EW (mÅ)	Possible blending lines	[a]Reference
3383.33	88	Ti I 3383.41	(2)
3415.38	381	Ti I 3415.36, Cr I 3415.41	(1)
3416.00	410	Cr I 3416.04	(1)
3491.21	69		
3499.43	79	Fe I 3499.44	(1)
3515.33	85	Fe II 3515.28	(1)
3527.71	70	Fe II 3527.69	(1)
3532.32	72		
3540.20	99	Mg I 3540.10, 3540.15	(2)
3541.46	88	Fe I 3541.46	(1)
3542.12	104	Fe II 3542.11	(1)
3543.32	79	Mn I 3543.30	(1)
3544.45	103	V I 3544.45	(1)
3546.79	168	Fe II 3546.77	(1)
3559.19	55	P1 3559.19	(1)
3582.16	59	Dublett (+ 3582.30)	
3582.30	57	Dublett (+ 3582.16)	
3582.82	63	Dublett (+ 3582.85)	
3583.21	55	Fe II 3583.25	(1)
3591.48	57	OH 3591.46 + Ti I 3591.50	(1)
3663.06	68	Sc II 3663.08	(1)
3664.61	111		
3673.90	56		
3696.77	53	V II 3696.75	(1)
3715.01	364	V I 3715.08	(1)
3866.50	662	Mg I 3866.49	(2)
3880.63	56		
3911.76	89	Dublett (+ Al I 3911.82 subtracted)	(2)
3934.73	104	Fe I 3934.71	(2)
3941.98	75	Sc II 3942.71	(1)
3959.31	149	Ca I 3959.17 (VALD) Ca I 3959.32 (Hinkle)	(2)
3966.05	51	Fe I 3966.07	(1)
3979.47	78	Cr II 3979.56	(1)
3979.91	88	Dublett (+ OH 3979.84 subtracted)	
3981.15	57	Fe I 3981.18 contribution	
3983.61	100	Ni I 3983.50 contribution	
3986.55	65	Cr II 3979.56, Cs1 3986.53	(1)
3986.97	66	Quartett C I 3986.97 (Fe I 3987.06/Fe II 3986.54/Ti I 3987.22)	(1)
3987.06	81	Quartett Fe I 3987.06 (C I 3986.97/Fe II 3986.54/Ti I 3987.22)	(1)
3988.83	88	C I 3988.83	(2)
3990.12	63	V II 3990.12	(1)

Continued on next page

Table 52 – *Continued from previous page*

λ (nm)	EW (mÅ)	Possible blending lines	Lit
3996.26	103	Dublett (3996.13 /Co I 3996.23)	
3997.13	55	Ti I 3997.06, 3997.18	(1)
3998.44	152	C I 3998.45	(2)
3999.95	127	C I 3999.94, Cr II 4000.00	(1)
4000.42	63	Fe II 4000.38, Sc I 4000.45	(1)
4001.04	133	C I 4001.04	(2)
4003.46	74	Fe II 4003.44	(1)
4006.27	103		
4015.96	97		
4025.63	74	Cr I 4025.68	(1)
4038.38	75	Dublett C I 4038.42 (+ Ti I 4038.40)	(1)
4038.67	82	Fe I 4038.67	(2)
4079.96	69	C I 4079.95	(1)
4083.97	55		
4101.89	156	Fe I 4101.93. Fe II 4101.89 (VALD2002)	(2)
4123.90	70	Si I 4123.97 subtracted	
4134.36	94	Fe II 4134.35	(1)
4138.08	84	Ni II 4138.10	(1)
4160.42	104	Fe I 4160.31	(2)
4167.66	127		
4173.52	51		

[a]Reference: (1) Ryabchikova *et al.* (2015), (2): Hinkle *et al.* (1995)

Table 53: Unassigned lines with EW>50 mÅ in M-band

λ (nm)	EW (mÅ)	Possible blending lines	[a]Reference
4565.45	307	13CO 2-1R40, C18O 2-1R42, C18O 3-2R27 subtracted	
4569.91	426	13CO 2-1R39, C17O 2-1R80 subtracted	
4572.17	453	C17O 3-2R71, C18O 4-3R85 subtracted	
4574.46	449	CO 2-1R38 subtracted	
4576.77	449	Co I 4576.76 13CO 4-3R74, 13CO 2-1R38 subtracted	(1)
4579.11	356		
4580.28	472	Fe II 4580.31, Quartett: CO 1-0R10,13CO 3-2R50, C18O 4-3R76, CO 4-3R39 subtracted	(1)
4581.43	190	Fe I 4581.53, 13CO 4-3R70, CO subtracted	(1)
4583.80	109		
4595.01	168	Ti I 4594.94	(1)
4595.86	146	CO 3-2R25, CO 3-2R46 subtracted	
4625.85	640		

Continued on next page

Table 53 – *Continued from previous page*

λ (nm)	EW (mÅ)	Possible blending lines	[a]Reference
4678.84	416	13CO 4-3R40 subtracted	
4682.45	446	13CO 6-5R85 subtracted	
4702.32	84		
4704.75	58		
4705.95	299		
4726.57	721	CO 1-0P7 subtracted	
4748.62	211		
4751.71	72		
4794.91	210	C18O 3-2R12 subtracted	
4798.53	273	Fe I 4798.55 subtracted	
4822.08	177	13CO 6-5R35 subtracted	
4829.56	56	Co II 4829.50	(1)
4835.46	70		
4867.13	65		
4874.71	110	13CO 9-8R80 contribution subtracted	
4881.51	55	Cr II 4881.48, Ti I 4881.53, Si I 4882.54	(1)
4882.62	230	17CO 1-0P17, CO 10-9R110, 13CO 8-7R49 subtracted	
4883.87	500	CO 10-9R57, 13CO 7-6R35, 13CO 9-8R72 subtracted	
4888.46	52	CO 9-8R39 subtracted	
5023.28	59		
5023.58	95		
5024.90	50	Co I 5024.80	(1)
5025.04	50		
5025.26	62		
5087.31	133		
5168.21	50		
5168.36	57		
5180.40	86	'CO' at 5180.397 nm, cdepth 0.008	
5185.84	63	Ti I 5185.82	(1)
5186.19	122	Mn1 5186.29	(1)

[a]Reference: (1) Ryabchikova *et al.* (2015), (2): Hinkle *et al.* (1995)

7.1.2 Synthetic lines not present in 10 Leo spectrum

Table 54: Lines with cdepth>0.050 not present in observed YJ-band

λ (nm)	species	10 Leo Spectrum 1-f	Synthetic Spectrum cdepth
964.20	'Fe I'	0.016	0.176
965.50	'Ti I'	-0.018	0.079
966.63	'Ca I'	0.002	0.058
969.90	'Ca I'	-0.022	0.148
974.16	'Fe I'	0.018	0.107
976.57	'Fe I'	-0.008	0.063
979.58	'Fe I'	-0.008	0.055
981.62	'Ti I'	0.005	0.058
982.43	'Mg I'	-0.009	0.213
982.53	'Zr I'	0.016	0.088
983.08	'Mg I'	0.005	0.102
1000.27	'Fe I'	0.003	0.068
1006.40	'Ni I'	0.014	0.069
1038.78	'Si I'	0.007	0.102
1062.08	'Fe I'	0.012	0.107
1072.07	'Fe I'	0.017	0.265
1082.80	'Ca I'	-0.001	0.050
1083.49	'Ca I'	-0.005	0.152
1142.47	'Fe I'	-0.002	0.078
1166.59	'Fe I'	-0.015	0.141
1181.48	'Mg I'	0.017	0.325
1182.42	'Mg I'	0.004	0.212
1187.74	'La II'	0.007	0.110
1189.82	'Co I'	0.020	0.177
1207.25	'Ge I'	0.004	0.059
1211.91	'Fe I'	0.012	0.071
1227.64	'Fe I'	0.000	0.063
1243.95	'Ni I'	0.007	0.070
1265.88	'Ni I'	0.001	0.055
1270.25	'Ni I'	0.007	0.050
1273.94	'Mg I'	-0.003	0.071
1274.37	'Mg I'	-0.003	0.160
1312.07	'Mg I'	0.000	0.106
1337.26	'Si I'	0.005	0.056

Table 55: Lines with cdepth>0.050 not present in observed H-band

λ (nm)	species	10 Leo Spectrum 1-f	Synthetic Spectrum cdepth
1424.28	'Fe I'	0.004	0.277
1429.42	'Fe I'	0.001	0.268
1432.78	'Fe I'	-0.006	0.156
1449.58	'Fe I'	0.008	0.283
1452.71	'Si I'	-0.013	0.053
1454.80	'Fe I'	-0.007	0.060
1457.84	'Fe I'	-0.021	0.056
1458.38	'Fe I'	-0.002	0.063
1460.77	'Fe I'	0.006	0.140
1461.02	'Mg I'	-0.030	0.120
1465.35	'Mg I'	-0.014	0.119
1465.36	'Mg I'	-0.025	0.099
1467.61	'Fe I'	-0.006	0.070
1468.45	'Fe I'	-0.030	0.095
1472.95	'Fe I'	-0.011	0.071
1481.13	'Mg I'	0.012	0.123
1481.93	'Fe I'	0.001	0.071
1486.77	'Fe I'	0.015	0.129
1487.07	'Fe I'	-0.024	0.203
1487.84	'Mn I'	-0.004	0.080
1487.84	'Cr 1'	-0.011	0.076
1494.12	'Fe I'	-0.001	0.227
1495.65	'Co I'	-0.003	0.080
1500.41	'Fe I'	-0.008	0.094
1501.35	'Fe I'	-0.001	0.261
1501.96	'Fe I'	0.020	0.106
1502.23	'Fe I'	0.003	0.064
1504.06	'Fe I'	-0.013	0.061
1510.18	'Ni I'	0.028	0.146
1515.94	'Fe I'	-0.013	0.242
1518.76	'Fe I'	-0.006	0.094
1519.09	'Ti I'	-0.018	0.156
1519.94	'Ni I'	-0.017	0.142
1521.83	'Fe I'	-0.015	0.103
1523.45	'Fe I'	-0.002	0.063
1526.35	'Fe I'	0.031	0.180
1527.57	'Fe I'	-0.008	0.173
1528.35	'Fe I'	-0.004	0.054
1530.83	'Fe I'	0.008	0.060
1535.26	'Fe I'	0.020	0.217
1540.27	'Fe I'	0.014	0.350
1541.02	'S I'	0.009	0.066

Continued on next page

Table 55 – *Continued from previous page*

λ (nm)	species	10 Leo Spectrum 1-f	Synthetic Spectrum cdepth
1544.86	'Fe I'	-0.004	0.366
1544.86	'Fe I'	0.000	0.285
1548.86	'Fe I'	-0.002	0.146
1549.03	'Fe I'	0.008	0.274
1551.49	'Fe I'	-0.004	0.344
1555.20	'Fe I'	-0.014	0.097
1555.63	'Fe I'	0.000	0.060
1557.43	'Mg I'	-0.012	0.056
1559.12	'Fe I'	0.005	0.201
1560.16	'Mg I'	-0.010	0.051
1562.20	'Fe I'	0.026	0.186
1565.01	'Si I'	-0.003	0.091
1565.48	'Si I'	-0.007	0.100
1568.26	'Fe I'	0.015	0.146
1573.71	'Fe I'	-0.011	0.091
1573.82	'Mg I'	-0.003	0.061
1576.03	'Fe I'	-0.006	0.081
1578.60	'Fe I'	0.016	0.142
1579.38	'Fe I'	0.028	0.424
1580.38	'Mg I'	-0.006	0.082
1580.53	'Si I'	0.012	0.140
1580.80	'Fe I'	0.000	0.084
1581.21	'Fe I'	0.001	0.058
1581.24	'Si I'	0.001	0.189
1585.84	'Fe I'	0.037	0.246
1587.62	'Co I'	0.008	0.056
1590.09	'Fe I'	0.082	0.459
1590.13	'Fe I'	0.016	0.146
1590.32	'Fe I'	0.057	0.293
1590.70	'Mg I'	-0.007	0.098
1591.95	'Mg I'	-0.014	0.064
1592.98	'Fe I'	-0.002	0.110
1593.30	'Fe I'	0.027	0.327
1593.42	'Fe I'	0.042	0.357
1593.65	'Fe I'	0.003	0.405
1595.30	'Mn I'	-0.004	0.052
1596.80	'Fe I'	0.012	0.174
1597.44	'Ni I'	0.005	0.097
1599.55	'Mg I'	-0.042	0.057
1600.66	'Fe I'	0.019	0.213
1600.78	'Fe I'	0.022	0.171
1602.24	'Fe I'	-0.008	0.080
1603.01	'Fe I'	0.017	0.277
1603.92	'Ca I'	-0.018	0.055

Continued on next page

Table 55 – *Continued from previous page*

λ (nm)	species	10 Leo Spectrum 1-f	Synthetic Spectrum cdepth
1605.42	'Fe I'	-0.014	0.074
1606.18	'Fe I'	0.019	0.160
1606.91	'Fe I'	0.015	0.261
1608.12	'Fe I'	-0.002	0.133
1609.06	'Fe I'	0.006	0.071
1609.26	'Si I'	0.002	0.055
1609.53	'Fe I'	-0.006	0.100
1609.76	'Fe I'	0.009	0.090
1610.29	'Mg I'	-0.016	0.089
1611.37	'H 1'	0.009	0.069
1611.55	'Fe I'	0.016	0.101
1613.18	'Fe I'	-0.007	0.091
1620.68	'Fe I'	-0.001	0.229
1623.70	'Fe I'	0.035	0.210
1624.34	'Fe I'	-0.008	0.255
1631.74	'Fe I'	0.015	0.074
1638.95	'Co I'	-0.003	0.067
1639.06	'Fe I'	-0.004	0.052
1641.40	'Fe I'	0.013	0.076
1642.02	'C I'	-0.007	0.056
1646.89	'S I'	-0.006	0.063
1649.43	'Fe I'	0.001	0.295
1649.45	'Mn I'	-0.004	0.273
1650.86	'Fe I'	0.015	0.293
1652.02	'Fe I'	-0.004	0.075
1652.53	'Fe I'	0.015	0.078
1655.23	'Fe I'	-0.008	0.115
1657.98	'Fe I'	0.036	0.238
1658.26	'Fe I'	0.016	0.272
1658.59	'Fe I'	0.015	0.392
1659.43	'Si I'	0.007	0.133
1659.46	'P I'	0.005	0.058
1659.78	'S I'	0.013	0.108
1663.44	'Fe I'	0.016	0.247
1664.52	'Fe I'	0.025	0.162
1664.54	'Fe I'	-0.007	0.063
1664.55	'Cu 1'	0.001	0.055
1664.98	'Fe I'	0.000	0.115
1665.16	'Fe I'	0.015	0.091
1665.18	'Fe I'	-0.002	0.233
1667.13	'Fe I'	0.048	0.254
1671.06	'Ni I'	-0.011	0.054
1674.18	'Fe I'	0.012	0.129
1681.52	'Fe I'	-0.005	0.103

Continued on next page

Table 55 – *Continued from previous page*

λ (nm)	species	10 Leo Spectrum 1-f	Synthetic Spectrum cdepth
1682.26	'Fe I'	0.035	0.180
1682.62	'Fe I'	-0.013	0.106
1684.99	'Fe I'	-0.015	0.084
1685.77	'Ni I'	0.008	0.189
1685.81	'Fe I'	-0.015	0.179
1686.10	'Fe I'	0.064	0.409
1686.17	'Fe I'	0.081	0.474
1686.31	'Fe I'	0.011	0.455
1687.10	'Fe I'	-0.005	0.092
1687.59	'Ni I'	0.000	0.071
1688.23	'Ti I'	-0.003	0.071
1688.32	'Fe I'	0.016	0.225
1688.54	'Fe I'	-0.011	0.079
1688.82	'Fe I'	0.004	0.175
1689.41	'Fe I'	0.025	0.188
1696.36	'Fe I'	-0.007	0.059
1697.39	'Fe I'	0.008	0.076
1699.16	'Fe I'	0.012	0.059
1700.93	'Fe I'	-0.034	0.143
1701.50	'Mg I'	0.018	0.120
1701.74	'Fe I'	-0.010	0.289
1702.01	'Fe I'	-0.011	0.091
1702.98	'Fe I'	0.009	0.244
1703.75	'Fe I'	0.021	0.151
1704.48	'Fe I'	-0.004	0.219
1705.23	'Fe I'	0.017	0.115
1705.23	'Fe I'	0.021	0.440
1705.75	'Fe I'	-0.010	0.184
1710.36	'Fe I'	-0.008	0.096
1712.63	'Fe I'	0.015	0.115
1715.64	'Fe I'	0.044	0.316
1715.74	'Si I'	0.011	0.065
1717.19	'Fe I'	-0.012	0.130
1720.32	'Fe I'	-0.001	0.097
1720.38	'Fe I'	0.012	0.125
1723.44	'Fe I'	0.014	0.104
1724.41	'Fe I'	0.010	0.054
1725.90	'Fe I'	0.013	0.144
1725.97	'Fe I'	0.018	0.134
1728.55	'Fe I'	-0.002	0.138
1728.87	'Fe I'	-0.010	0.098
1730.19	'Fe I'	0.010	0.077
1732.95	'Mn I'	0.013	0.175
1733.75	'Fe I'	0.019	0.108

Continued on next page

Table 55 – *Continued from previous page*

λ (nm)	species	10 Leo Spectrum 1-f	Synthetic Spectrum cdepth
1737.19	'Fe I'	0.010	0.053
1737.59	'Fe I'	-0.003	0.254
1739.67	'Fe I'	-0.009	0.074
1740.02	'Fe I'	-0.015	0.079
1745.73	'Ca I'	-0.003	0.143
1746.39	'Fe I'	-0.004	0.236
1747.37	'Fe I'	-0.010	0.060
1750.52	'Fe I'	0.019	0.229
1752.68	'Fe I'	-0.002	0.081
1756.47	'Fe I'	0.010	0.098
1756.84	'Fe I'	-0.033	0.142
1757.68	'Fe I'	0.001	0.066
1758.94	'Fe I'	0.007	0.294
1759.29	'Fe I'	0.006	0.069
1760.30	'Fe I'	0.010	0.113
1760.59	'Fe I'	-0.016	0.100
1761.14	'Mn I'	0.031	0.284
1761.93	'Fe I'	0.047	0.340
1763.06	'Fe I'	-0.052	0.054
1763.07	'Fe I'	-0.057	0.233
1764.50	'Fe I'	0.031	0.257
1766.29	'Fe I'	0.015	0.126
1766.40	'Fe I'	0.003	0.066
1769.83	'Fe I'	0.006	0.096
1769.93	'Fe I'	-0.005	0.379
1771.42	'Fe I'	0.006	0.373
1772.80	'Fe I'	0.028	0.204
1773.75	'Fe I'	-0.014	0.062
1774.17	'Fe I'	-0.013	0.076
1774.71	'Fe I'	-0.023	0.085
1775.37	'Co I'	-0.002	0.118
1776.00	'Fe I'	0.042	0.232
1776.47	'Fe I'	-0.001	0.062
1776.51	'Fe I'	-0.028	0.312
1780.08	'Fe I'	-0.014	0.066
1781.67	'Fe I'	-0.024	0.133
1781.75	'Fe I'	0.013	0.225
1783.24	'Fe I'	0.008	0.176
1783.61	'Fe I'	0.021	0.202
1784.41	'Fe I'	-0.007	0.054
1785.53	'Fe I'	0.010	0.268
1786.53	'Fe I'	-0.020	0.410
1786.56	'Fe I'	0.010	0.132
1786.92	'Fe I'	0.035	0.193

Continued on next page

Table 55 – *Continued from previous page*

λ (nm)	species	10 Leo Spectrum 1-f	Synthetic Spectrum cdepth
1787.47	'Ni I'	-0.039	0.080
1794.69	'Ni I'	-0.015	0.095
1795.42	'Ni I'	-0.018	0.124
1795.49	'Si I'	-0.038	0.051
1804.32	'Fe I'	0.047	0.270
1805.47	'Y I'	-0.059	0.155
1807.11	'Fe I'	0.006	0.136
1809.54	'C I'	-0.027	0.052
1809.54	'Fe I'	0.007	0.077

Table 56: Lines with cdepth>0.050 not present in observed K-band

λ (nm)	species	10 Leo Spectrum 1-f	Synthetic Spectrum cdepth
1960.15	'Fe I'	0.001	0.068
1960.19	'Ni I'	0.005	0.111
1963.07	'Si I'	-0.001	0.062
1971.72	'V I'	-0.011	0.080
1971.87	'Mn I'	-0.007	0.091
1979.05	'Fe I'	-0.001	0.066
1981.58	'Fe I'	-0.005	0.064
1986.03	'Fe I'	0.009	0.072
1986.14	'Fe I'	0.010	0.119
1998.69	'Fe I'	0.013	0.230
2000.46	'Fe I'	-0.001	0.087
2007.77	'Fe I'	-0.006	0.223
2009.19	'Fe I'	-0.005	0.118
2011.34	'Fe I'	0.039	0.236
2019.20	'Fe I'	0.020	0.155
2031.47	'Ni I'	-0.004	0.052
2034.51	'Fe I'	0.000	0.102
2048.42	'Fe I'	-0.008	0.077
2050.11	'Ca I'	-0.006	0.168
2052.72	'Mg I'	0.000	0.082
2052.72	'Mg I'	-0.005	0.356
2052.72	'Mg I'	-0.003	0.107
2055.31	'Fe I'	0.015	0.104
2059.15	'Fe I'	0.024	0.144
2067.77	'Fe I'	0.011	0.089
2067.82	'Fe I'	-0.005	0.083

Continued on next page

Table 56 – *Continued from previous page*

λ (nm)	species	10 Leo Spectrum 1-f	Synthetic Spectrum cdepth
2083.06	'Fe I'	0.004	0.113
2087.28	'Mg I'	0.000	0.202
2088.43	'Mg I'	0.001	0.095
2093.97	'Fe I'	0.020	0.166
2117.64	'Fe I'	0.014	0.147
2123.24	'Fe I'	0.001	0.086
2123.95	'Mg I'	-0.002	0.071
2123.95	'Mg I'	0.001	0.087
2123.95	'Mg I'	0.001	0.323
2154.09	'Mg I'	0.000	0.076
2155.12	'Fe I'	-0.005	0.086
2155.72	'Fe I'	0.011	0.072
2156.99	'V I'	0.023	0.155
2176.70	'Mg I'	0.007	0.072
2176.70	'Mg I'	0.006	0.081
2176.70	'Mg I'	0.010	0.310
2182.66	'Fe I'	0.036	0.262
2186.21	'Fe I'	-0.001	0.087
2195.21	'Fe I'	0.000	0.056
2195.73	'Fe I'	0.000	0.157
2207.29	Co I	0.008	0.124
2214.57	'Fe I'	0.012	0.248
2218.42	'Fe I'	0.039	0.243
2249.39	'V I'	0.009	0.088
2257.78	'Fe I'	-0.006	0.148
2261.54	'Fe I'	0.015	0.264
2287.87	'Si I'	0.008	0.050
2287.88	'Fe I'	0.004	0.225
2296.43	'Si I'	0.010	0.108
2308.35	'Si I'	0.008	0.055
2316.04	'Fe I'	-0.011	0.085
2318.32	'Ti I'	0.010	0.089
2318.66	'Fe I'	-0.031	0.057
2329.29	'Fe I'	0.013	0.200
2344.56	'Fe I'	-0.038	0.069
2346.56	'Ca I'	-0.006	0.061
2347.96	'Ca I'	-0.010	0.083
2350.28	'Fe I'	-0.020	0.050
2350.50	'Mg I'	-0.016	0.080
2350.59	'Mg I'	0.015	0.137
2351.67	'Fe I'	0.040	0.247
2369.02	'Fe I'	-0.011	0.335
2381.59	'Sc 1'	-0.003	0.072
2394.56	'Mn I'	0.003	0.121

Continued on next page

Table 56 – *Continued from previous page*

λ (nm)	species	10 Leo Spectrum 1-f	Synthetic Spectrum cdepth
2415.14	'Fe I'	0.028	0.151
2425.13	'Si I'	-0.008	0.178
2438.50	'Fe I'	0.015	0.124
2442.25	'S I'	0.010	0.073
2453.29	'Fe I'	0.023	0.263
2453.93	'Si I'	-0.064	0.221
2471.82	'CO 1'	-0.023	0.074
2473.80	'Si I'	-0.008	0.050
2477.87	'Fe I'	-0.014	0.110
2485.05	'Fe I'	-0.034	0.090
2508.40	'Mg I'	0.035	0.205
2509.22	'Mg I'	0.022	0.109
2509.22	'Mg I'	0.024	0.289

Table 57: Lines with cdepth>0.050 not present in observed L-band

λ (nm)	species	10 Leo Spectrum 1-f	Synthetic Spectrum cdepth
3372.41	'Fe I'	-0.004	0.071
3376.07	'Fe I'	-0.006	0.093
3382.26	'Fe I'	0.003	0.053
3408.28	'Fe I'	-0.006	0.055
3408.29	'Fe I'	-0.004	0.072
3421.24	'Fe I'	0.000	0.058
3423.42	'Fe I'	0.004	0.051
3455.51	'Fe I'	0.026	0.169
3469.62	'Fe I'	-0.009	0.054
3473.12	'Mg I'	-0.005	0.134
3473.12	'Mg I'	-0.005	0.067
3501.64	'Fe I'	0.000	0.052
3515.84	'Fe I'	0.011	0.086
3551.22	'Ca I'	0.001	0.053
3551.58	'Ca I'	0.000	0.066
3571.92	'Fe I'	-0.006	0.061
3628.14	'Fe I'	0.006	0.060
3653.47	'Mg I'	0.021	0.216
3653.48	'Mg I'	0.018	0.161
3653.48	'Mg I'	0.012	0.074
3653.48	'Mg I'	0.010	0.052
3653.51	'Mg I'	0.006	0.173
3678.18	'Fe I'	0.009	0.111
3682.04	'Fe I'	0.005	0.242
3694.39	'Fe I'	-0.002	0.052
3703.07	'Fe I'	0.005	0.081
3744.54	'Si I'	-0.006	0.082
3753.46	'Mg I'	0.007	0.202
3753.48	'Mg I'	0.002	0.146
3753.48	'Mg I'	0.003	0.066
3753.51	'Mg I'	0.005	0.158
3767.36	'Fe I'	0.003	0.084
3816.43	'Mg I'	-0.001	0.112
3816.43	'Mg I'	0.000	0.073
3817.51	'Mg I'	0.002	0.176
3817.51	'Mg I'	-0.001	0.055
3872.42	'Si I'	0.006	0.053
3883.31	'Fe I'	0.011	0.132
3885.37	'Mg I'	-0.003	0.191
3885.39	'Mg I'	0.008	0.135
3885.39	'Mg I'	0.002	0.060
3885.42	'Mg I'	-0.002	0.147

Continued on next page

Table 57 – *Continued from previous page*

λ (nm)	species	10 Leo Spectrum 1-f	Synthetic Spectrum cdepth
3886.01	'Fe I'	0.000	0.157
3886.58	'Fe I'	-0.004	0.096
3888.49	'Fe I'	0.000	0.071
3891.67	'Fe I'	0.007	0.138
3892.55	'Fe I'	0.020	0.103
3895.44	'Fe I'	-0.009	0.123
3897.32	'Fe I'	-0.004	0.079
3898.44	'Fe I'	-0.007	0.064
3901.47	'Fe I'	-0.013	0.079
3901.60	'Fe I'	-0.012	0.094
3902.03	'Fe I'	-0.011	0.068
3902.38	'Fe I'	-0.013	0.055
3903.97	'Fe I'	-0.006	0.066
3904.38	'Fe I'	0.025	0.164
3904.66	'Fe I'	0.003	0.053
3915.43	'Fe I'	0.004	0.084
3928.05	'Ni I'	0.005	0.074
3956.26	'Mg I'	-0.001	0.081
3956.78	'Mg I'	0.003	0.103
3956.78	'Mg I'	0.002	0.067
3957.94	'Mg I'	0.001	0.166
3965.50	'Mg I'	-0.005	0.063
4065.61	'Mg I'	0.019	0.182
4065.62	'Mg I'	0.014	0.125
4065.62	'Mg I'	0.008	0.058
4065.66	'Mg I'	-0.004	0.138
4086.35	'Ca I'	-0.001	0.056
4092.01	'Ni I'	0.001	0.054
4093.97	'Fe I'	0.000	0.161
4114.68	'Fe I'	0.003	0.190
4117.24	'Mg I'	0.007	0.058
4120.60	'Fe I'	-0.001	0.132
4149.13	'Mg I'	-0.001	0.076
4149.70	'Mg I'	0.000	0.098
4149.70	'Mg I'	0.003	0.062
4150.98	'Mg I'	0.014	0.156

Table 58: Lines with cdepth>0.050 not present in observed M-band

λ (nm)	species	10 Leo Spectrum 1-f	Synthetic Spectrum cdepth
4632.90	'Fe I'	-0.048	0.053
4649.31	'CO'	-0.053	0.417
4649.32	'CO'	0.044	0.279
4708.99	'CO'	-0.012	0.094
4709.30	'CO'	0.020	0.113
4717.06	'CO'	0.003	0.076
4825.88	'CO'	-0.019	0.065
4864.63	'Mg I'	-0.030	0.107
4979.54	'CO'	0.005	0.058
5097.05	'CO'	-0.013	0.081
5101.43	'Fe I'	-0.013	0.102
5101.43	'Fe I'	-0.013	0.102

7.1.3 Line matches between 10 Leo and Arcturus

The following Table 59 summarizes lines (EW≥50 mÅ) observed in 10 Leo that match the Arcturus atlas but are not listed in VALD3.

Table 59: lines with EW>50 mÅ observed in 10 Leo matches Arcturus atlas but not listed in VALD3 - match category E

10 Leo		Arcturus atlas[a]	
λ (nm)	EW (mÅ)	λ (nm)	Element
1045.56	69	1045.56	Fe I
1146.84	59	1146.85	Fe I
1147.86	101	1147.89	Fe I
1192.64	52	1192.65	Fe I
1291.98	50	1291.98	Fe I
1310.24	61	1310.25	Fe I
1546.36	109	1546.35	Fe I
1550.36	93	1550.36	Fe I
1552.36	52	1552.36	Fe I
1561.84	66	1561.84	Fe I
1595.70	55	1595.70	Fe I
1600.21	94	1600.21	Fe I
1602.10	81	1602.11	Fe I
1609.31	113	1609.31	Fe I
1628.20	78	1628.19	Fe I

Continued on next page

Table 59 – *Continued from previous page*

10 Leo		Arcturus atlas[a]	
λ (nm)	EW (mÅ)	λ (nm)	Element
1630.40	62	1630.40	Ni I
1632.32	148	1632.32	Fe I
1669.01	125	1669.01	Fe I
1672.78	125	1672.78	Fe I
1676.46	122	1676.47	Fe I
1680.42	117	1680.42	Fe I
1682.51	119	1682.51	Fe I
1703.22	55	1703.23	Fe I
1706.35	75	1706.37	Fe I
1709.35	71	1709.34	Fe I
1710.17	68	1710.18	Fe I
1732.29	51	1732.31	Fe I
1754.81	71	1754.82	Fe I
1755.32	106	1755.33	Fe I
1759.72	63	1759.73	Fe I
1761.72	101	1761.73	Fe I
1763.56	121	1763.57	Fe I
1764.90	76	1764.91	Fe I
1789.42	140	1789.42	Fe I
1798.43	153	1798.43	Fe I
1964.05	180	1964.07	Fe I
2081.07	156	2081.08	Fe I
2121.38	163	2121.40	Al I
3664.61	111	3664.61	Al I
3866.50	662	3866.49	Mg I
3911.80	87	3911.82	Al I
3998.44	152	3998.45	C1
4702.47	96	4702.47	CO

[a]Hinkle *et al.* (1995)

7.2 Line Identifications

7.2.1 Identification of Elements

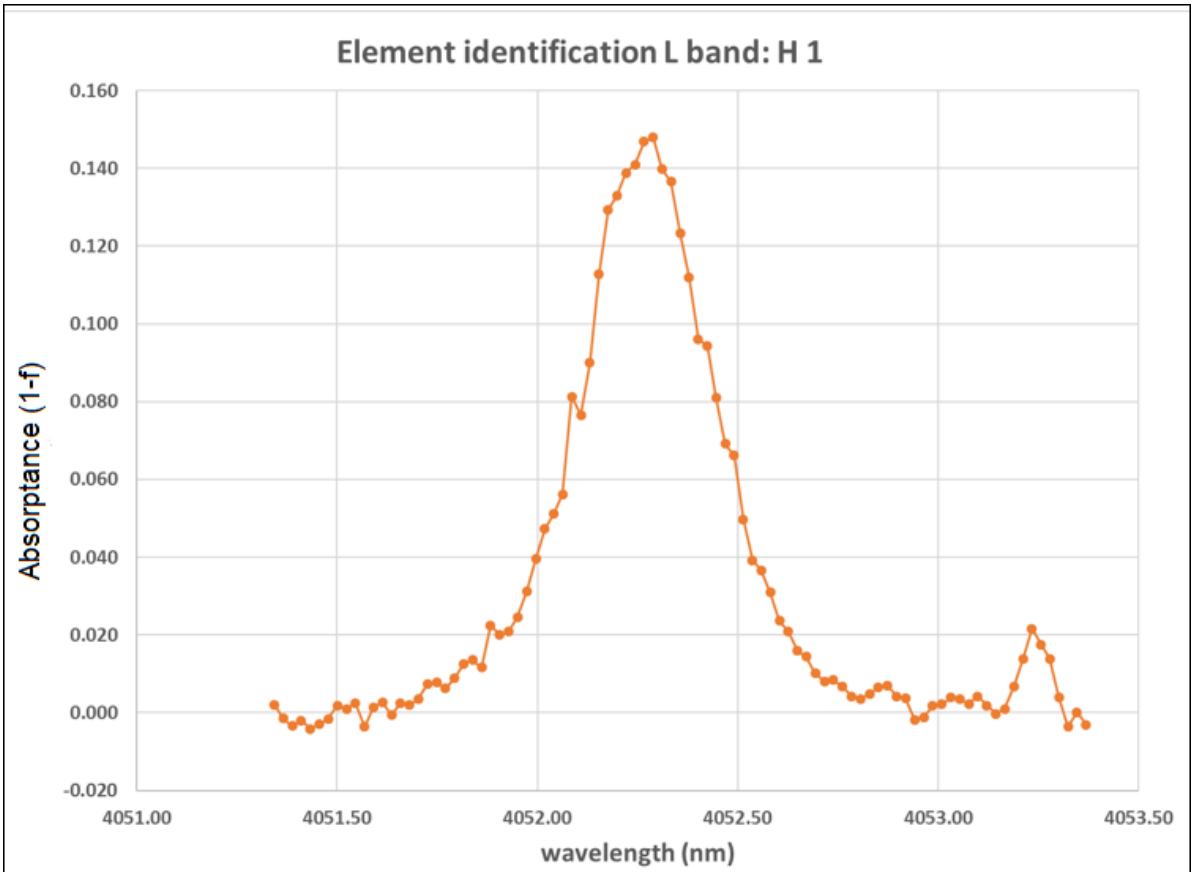

λ(nm)	Description	log gf	cdepth	EW (mA)	Match
4051.38	'Fe 1'	-0.405	0.028	0	C
4051.71	SiO 3-1R46			6	E
4052.01	'Si 1'	-1.115	0.011	7	B
4052.26	'H 1'	1.521	0.099	625	A
4052.48	SiO 3-1R45			0	G
4053.27	OH 4-3P_{2f}14.5	-3.751	0.010	18	A

Figure 41: Identification of H I

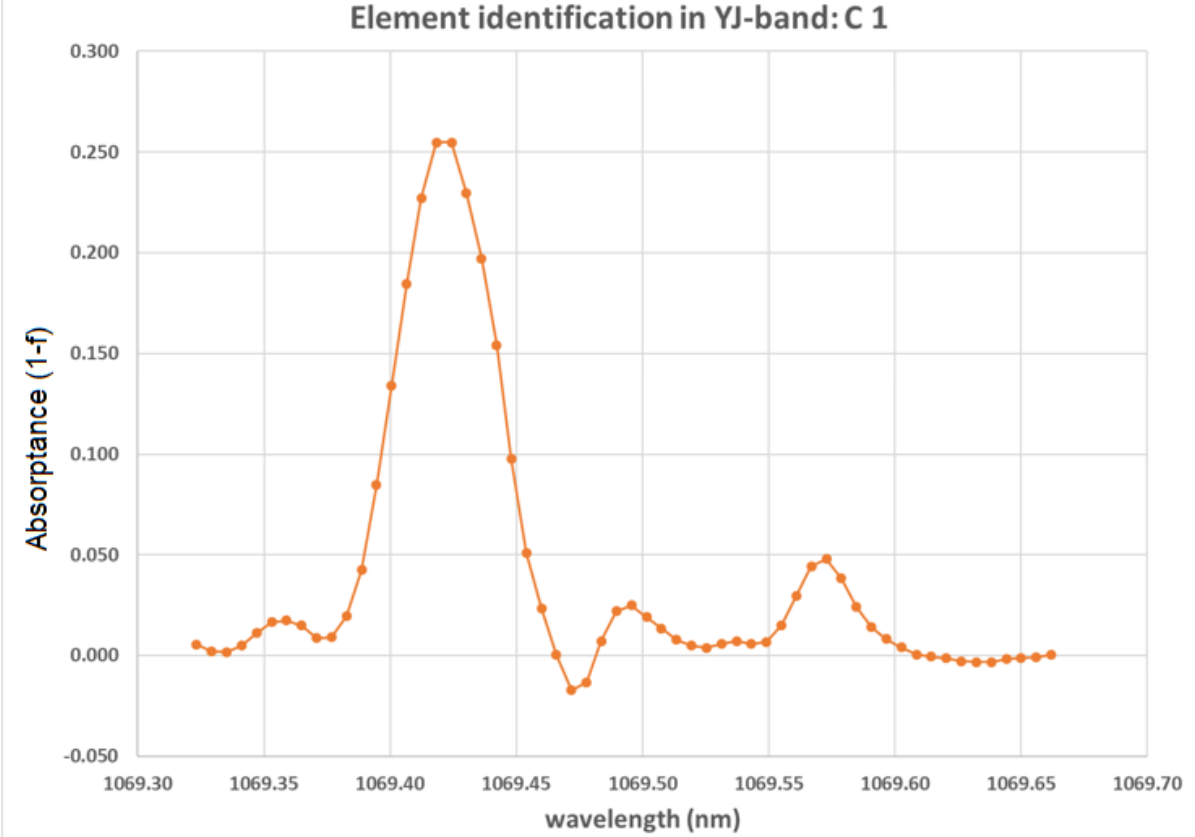

λ(nm)	Description	log gf	cdepth	EW (mA)	Match
1069.39	'Ti 1'	-3.22	0.024	5	B
1069.42	'C 1'	0.344	0.187	117	A
1069.50	U+'Mn 1'	-2.183	0.007	6	F
1069.57	'Fe 1'	-4.905	0.023	14	E

Figure 42: Identification of C I

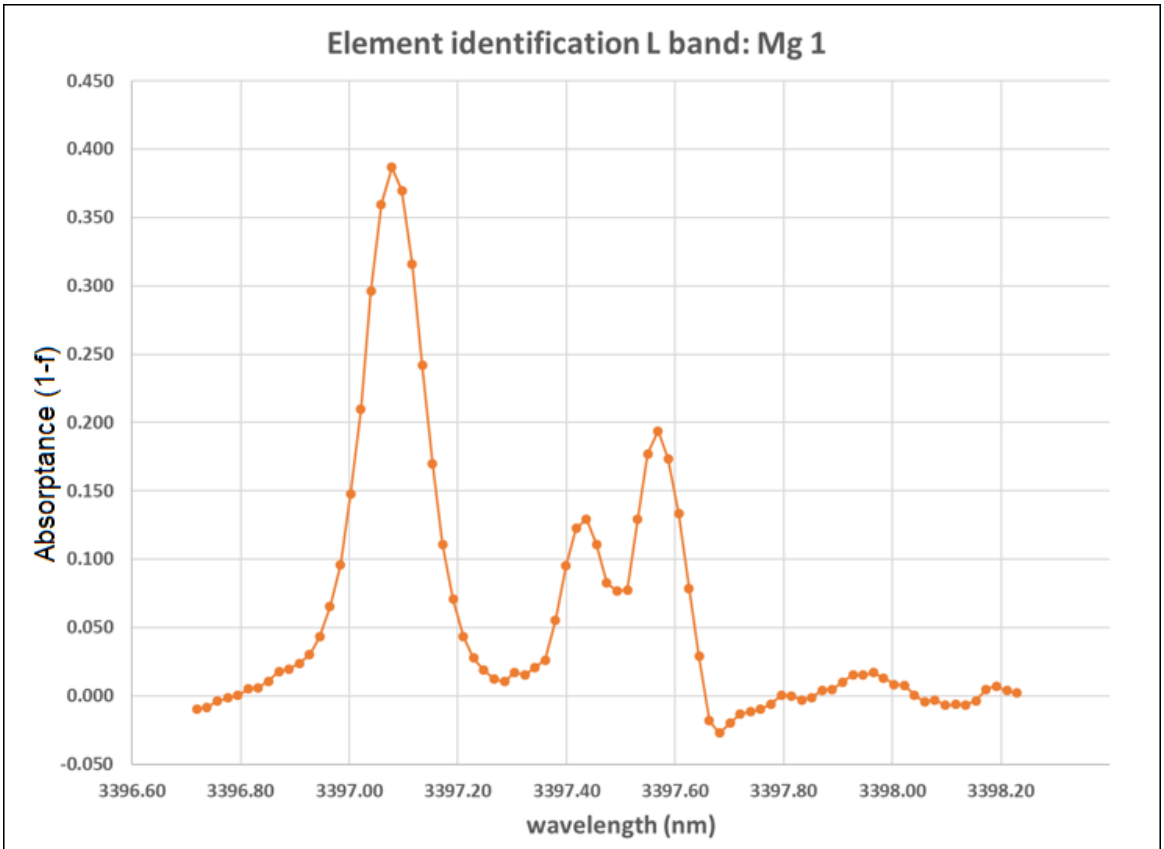

λ(nm)	Description	log gf	cdepth	EW (mA)	Match
3397.08	'Mg 1'	-0.137	0.375	300	A
3397.13	'Mg 1'	-0.51	0.355	284	B
3397.27	'Ni 1'	-1.002	0.012	0	C
3397.36	'Si 1'	-1.295	0.016	8	B
3397.44	OH 2-1P_{1f}11.5	-4.032	0.088	116	A
3397.45	'Fe 1'	-1.556	0.008	0	C
3397.58	OH 1-0P_{1e}14.5	-4.075	0.138	181	A
3397.94	NH 3-2R4			17	E

Figure 43: Identification of Mg I

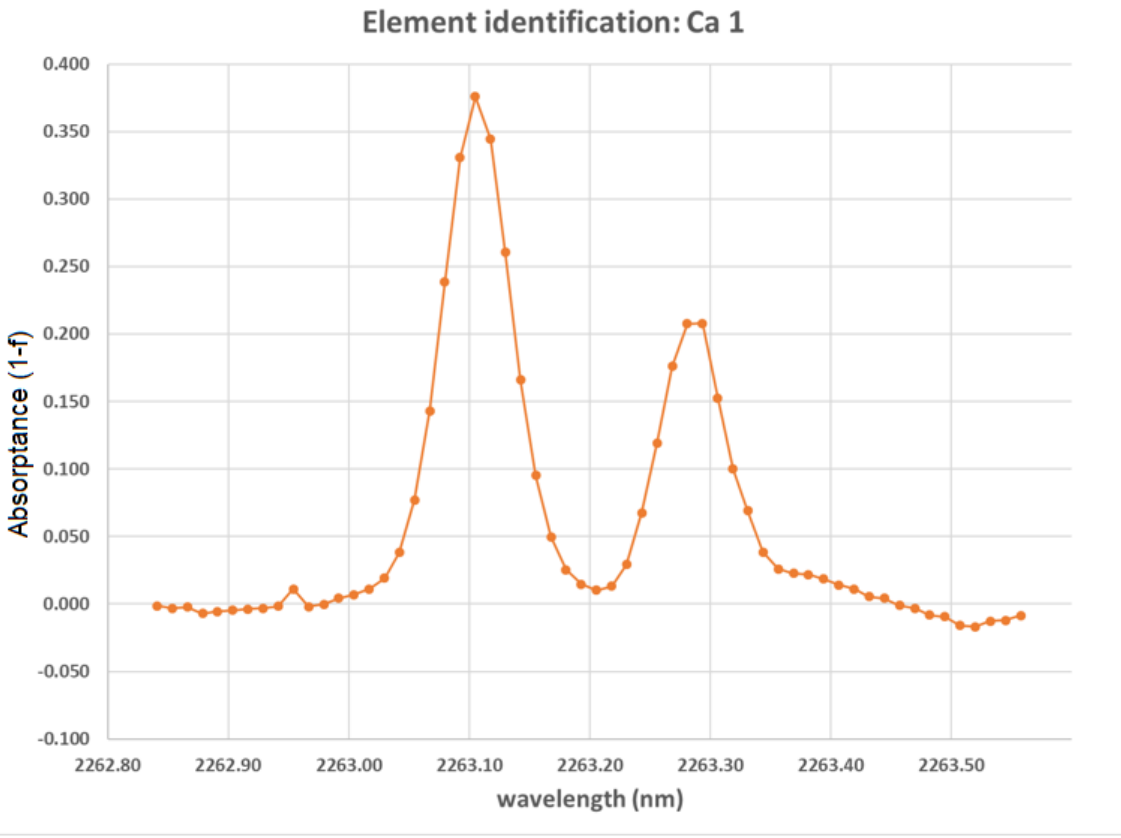

λ(nm)	Description	log gf	cdepth	EW (mA)	Match
2263.11	'Ca 1'	0.687	0.459	278	A
2263.29	'Ca 1'	-0.216	0.337	121	A
2263.29	'Si 1'	-1.221	0.078	25	B
2263.40	'Ni 1'	-1.522	0.047	19	B
2263.45	'Si 1'	-1.994	0.012	0	C

Figure 44: Identification of Ca I

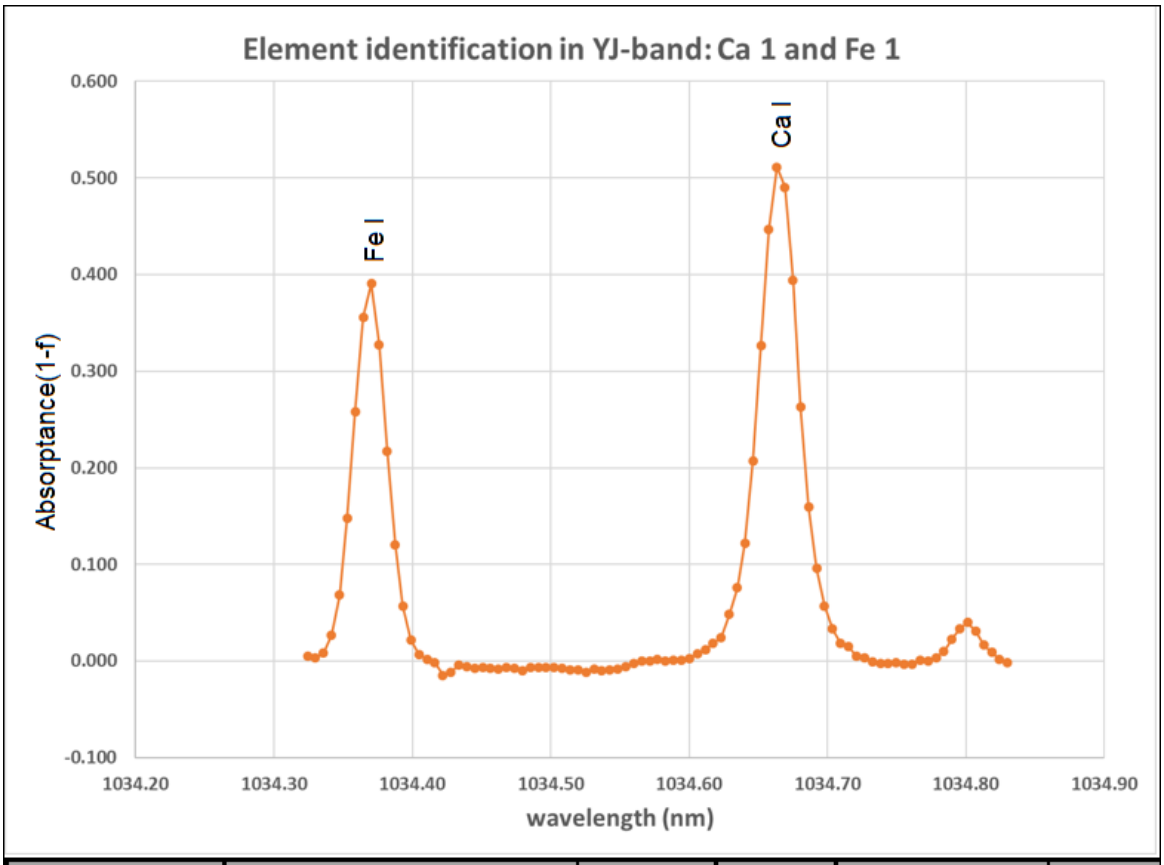

(nm)	Description	log gf	cdepth	EW (mA)	Match
1034.37	'Fe 1'	-3.577	0.503	116	A
1034.67	'Ca 1'	-0.300	0.564	187	A
1034.69	CN 3-2P_{1}50.5	-1.893	0.009	5	B
1034.77	'Fe 1'	-1.592	0.008		C
1034.80	'Fe 1'			10	E

Figure 45: Identification of Ca I and Fe I

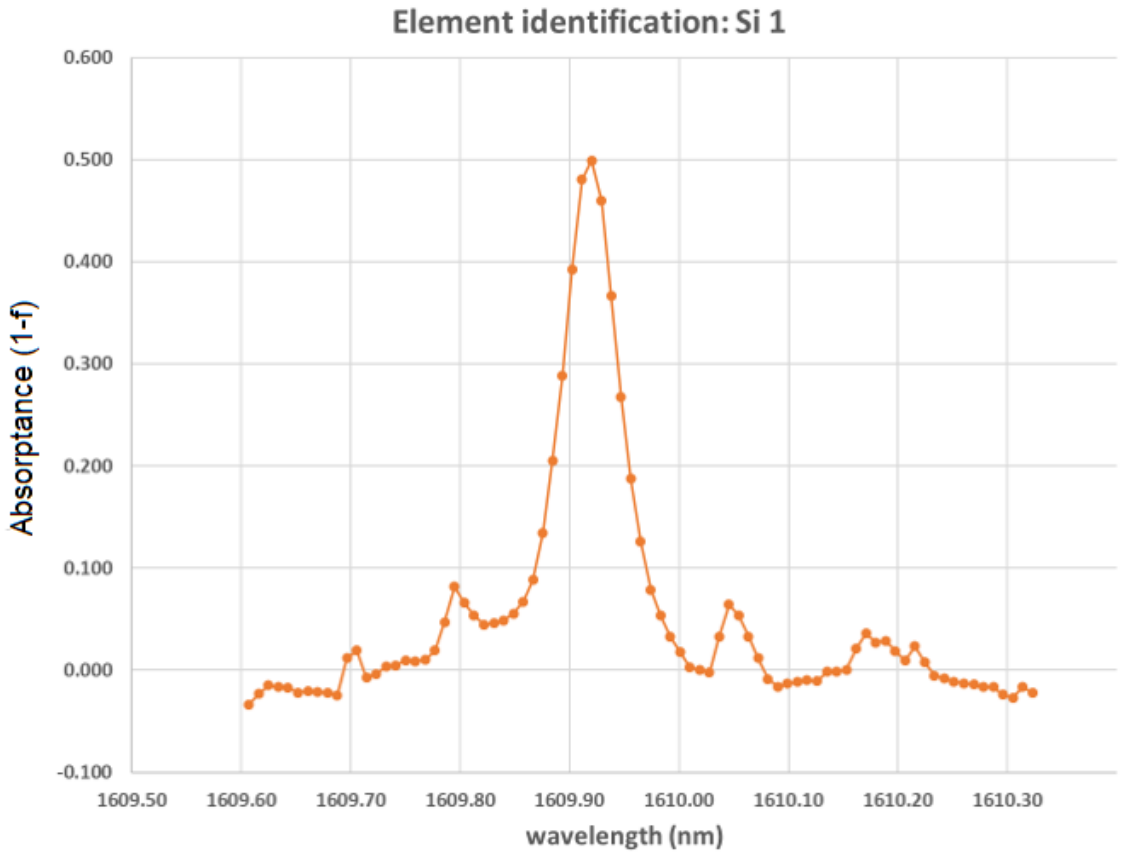

λ(nm)	Description	log gf	cdepth	EW (mA)	Match
1609.74	CO 5-2R62	-6.173	0.013	2	A
1609.76	'Fe 1'	-1.244	0.090	0	C
1609.81	Ni1+U			30	E
1609.90	CN 3-4Q_{2}32.5	-2.122	0.012	7	B
1609.92	'Si 1'	-0.144	0.555	342	A
1610.05	CN 1-2P_{1}52.5	-1.544	0.059	18	A
1610.18	'Fe 1'	-2.173	0.029	1	B
1610.18	CN 1-2R_{1}72.5	-1.376	0.020	12	A
1610.20	'Mg 1'	-2.33	0.040	0	C
1610.20	'Mg 1'	-3.24	0.006	0	C
1610.24	CO 3-0P27			0	G
1610.26	'Mg 1'	-2.27	0.045	0	C
1610.26	'Mg 1'	-3.17	0.007	0	C
1610.27	'Mg 1'	-2.97	0.010	0	C
1610.29	'Mg 1'	-1.94	0.089	0	C

Figure 46: Identification of Si I

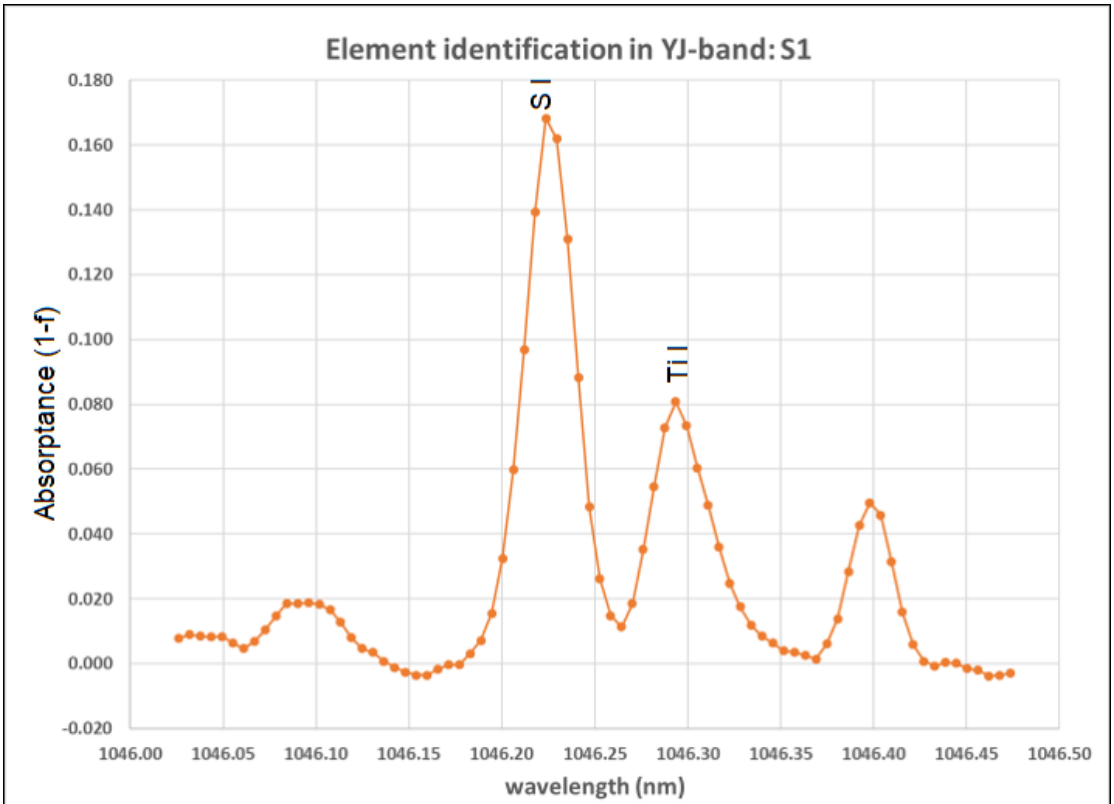

λ(nm)	Description	log gf	cdepth	EW (mA)	Match
1046.08	CN 3-2Q_{1}62.5	-1.482	0.011	6	B
1046.10	'Fe 1'	-1.752	0.033	2	B
1046.14	'V 1'	-2.388	0.006		C
1046.23	'S 1'	0.030	0.187	58	A
1046.29	'Ti 1'	-1.399	0.146	21	A
1046.31	CN 2-1P_{2}64.5	-1.373	0.019	11	B
1046.34	'Si 1'	-1.62	0.017		C
1046.40	CN 1-0P_{2}73.5	-1.172	0.026	14	A

Figure 47: Identification of S I

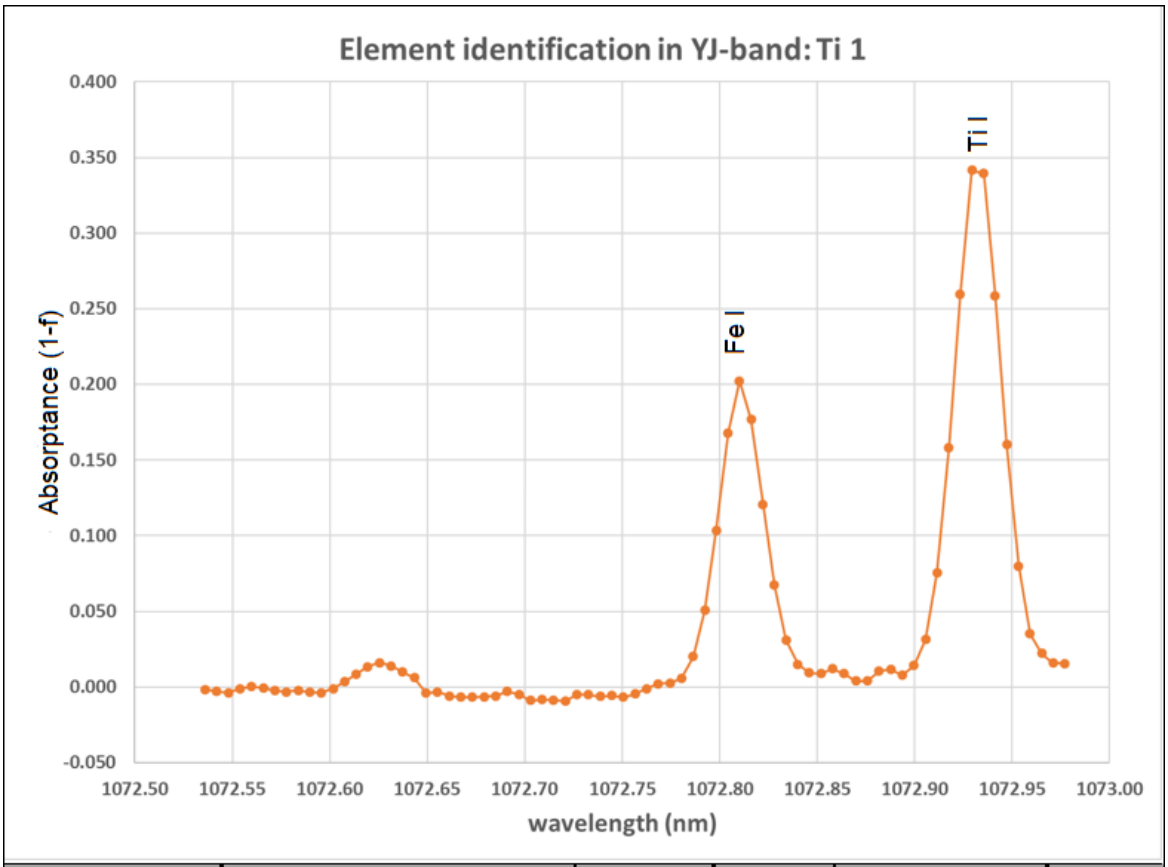

λ(nm)	Description	log gf	cdepth	EW (mA)	Match
1072.64	U+Mn 1			4	F
1072.56	'Fe 1'	-5.113	0.037	0	C
1072.81	'Fe 1'	-2.763	0.288	58	A
1072.93	'Ti 1'	-2.064	0.503	107	A
1072.97	'Ca 1'	-2.154	0.007	0	C

Figure 48: Identification of Ti I

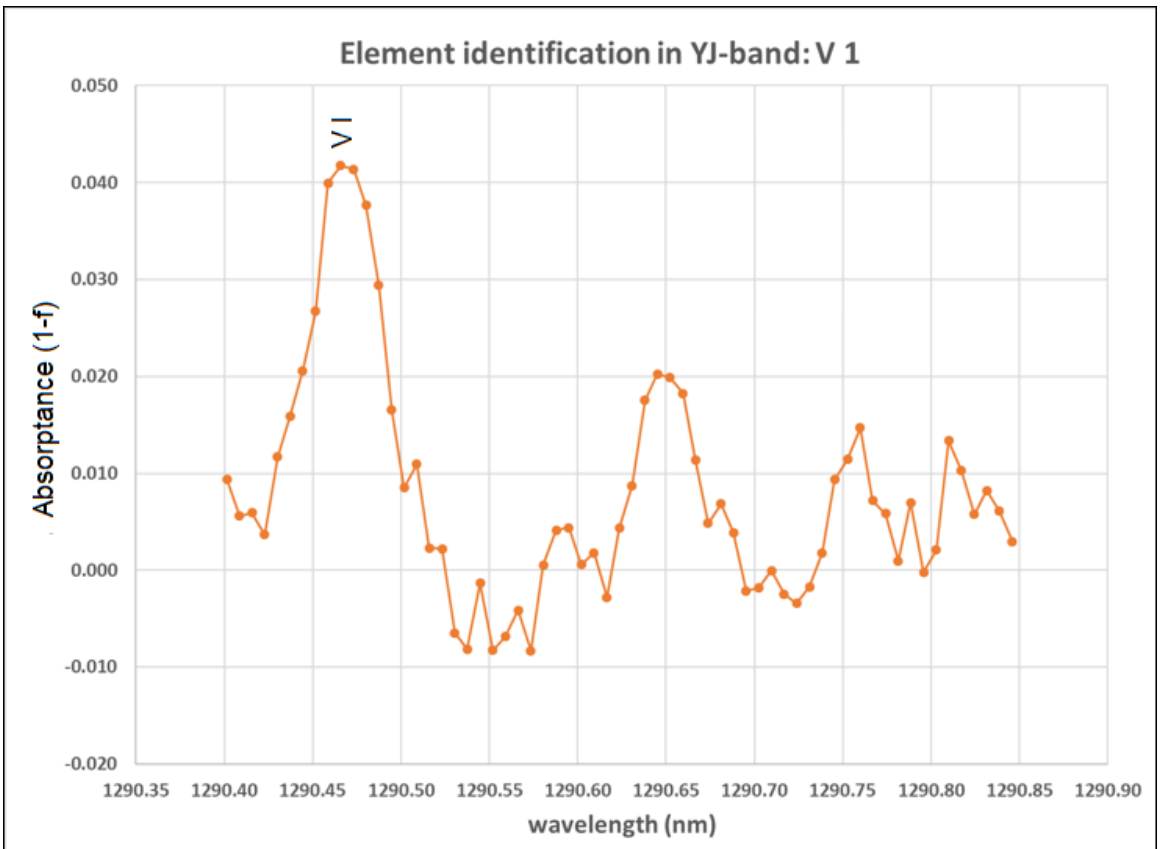

λ(nm)	Description	log gf	cdepth	EW (mA)	Match
1290.47	'V 1'	-1.052	0.111	22	A
1290.65	U			8	F
1290.77	CN 4-4P_{1}35.5	-1.996	0.007	4	B

Figure 49: Identification of V I

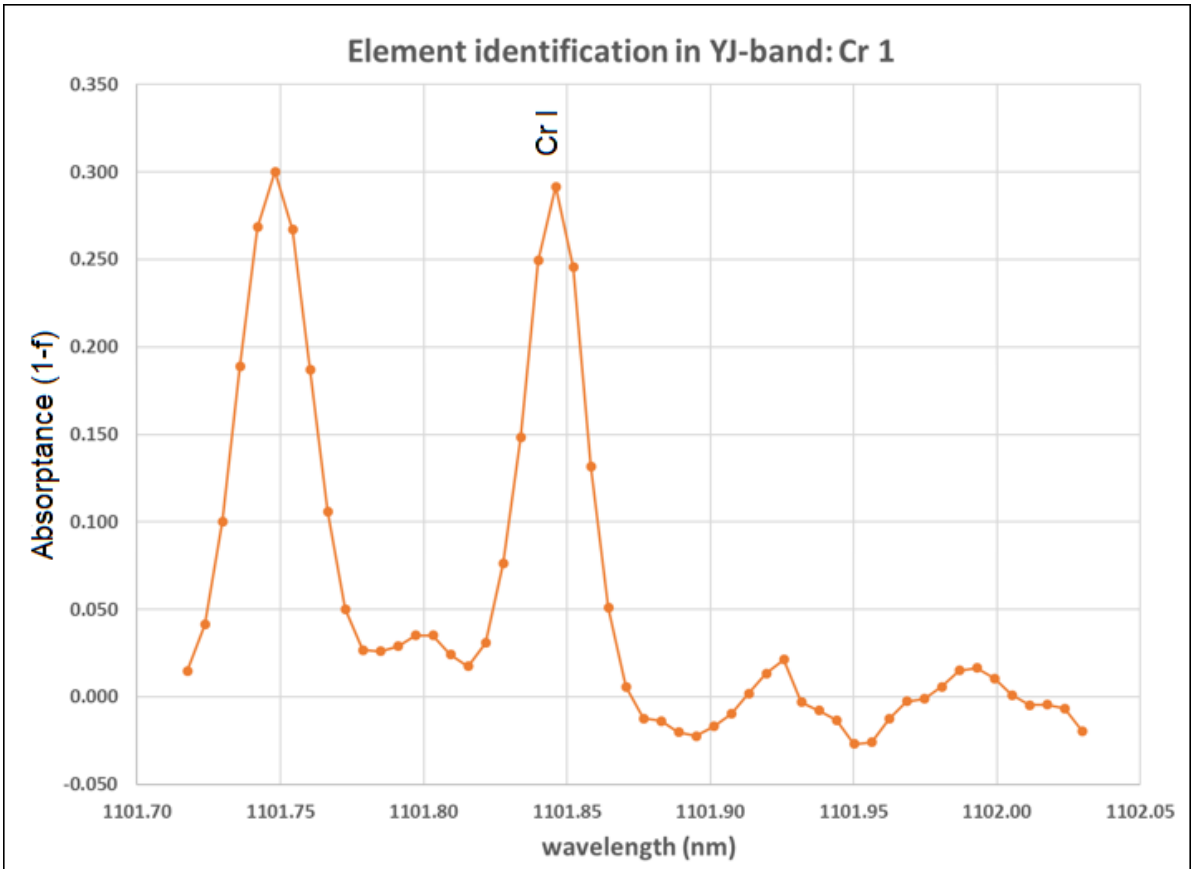

λ(nm)	Description	log gf	cdepth	EW (mA)	Match
1101.75	CN 0-0R_{1}25.5	-1.523	0.200	71	A
1101.76	CN 0-0P_{1}5.5	-2.470	0.047	17	B
1101.76	CN 0-0Q_{12}3.5	-2.693	0.029	10	B
1101.81	^{13}CN 0-0Q_{2}16.5			8	F
1101.85	'Cr 1'	-0.429	0.416	77	A
1101.98	'Fe 1'	-1.592	0.010	3	B

Figure 50: Identification of Cr I

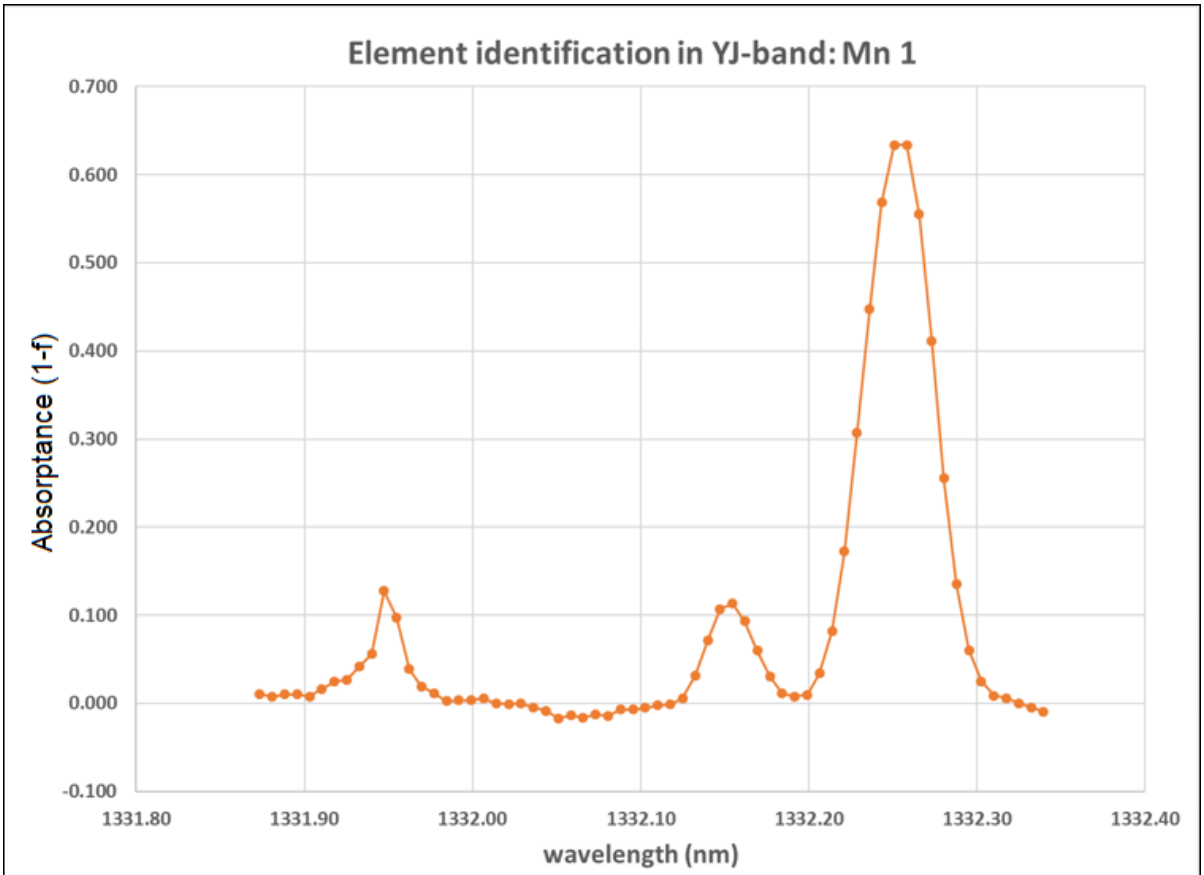

λ(nm)	Description	log gf	cdepth	EW (mA)	Match
1331.95	U			35	F
1332.11	'Ti 1'	-0.989	0.020		C
1332.16	'Ca 1'	-0.480	0.177	39	A
1332.26	'Mn 1'	-1.370	0.606	322	A

Figure 51: Identification of Mn I

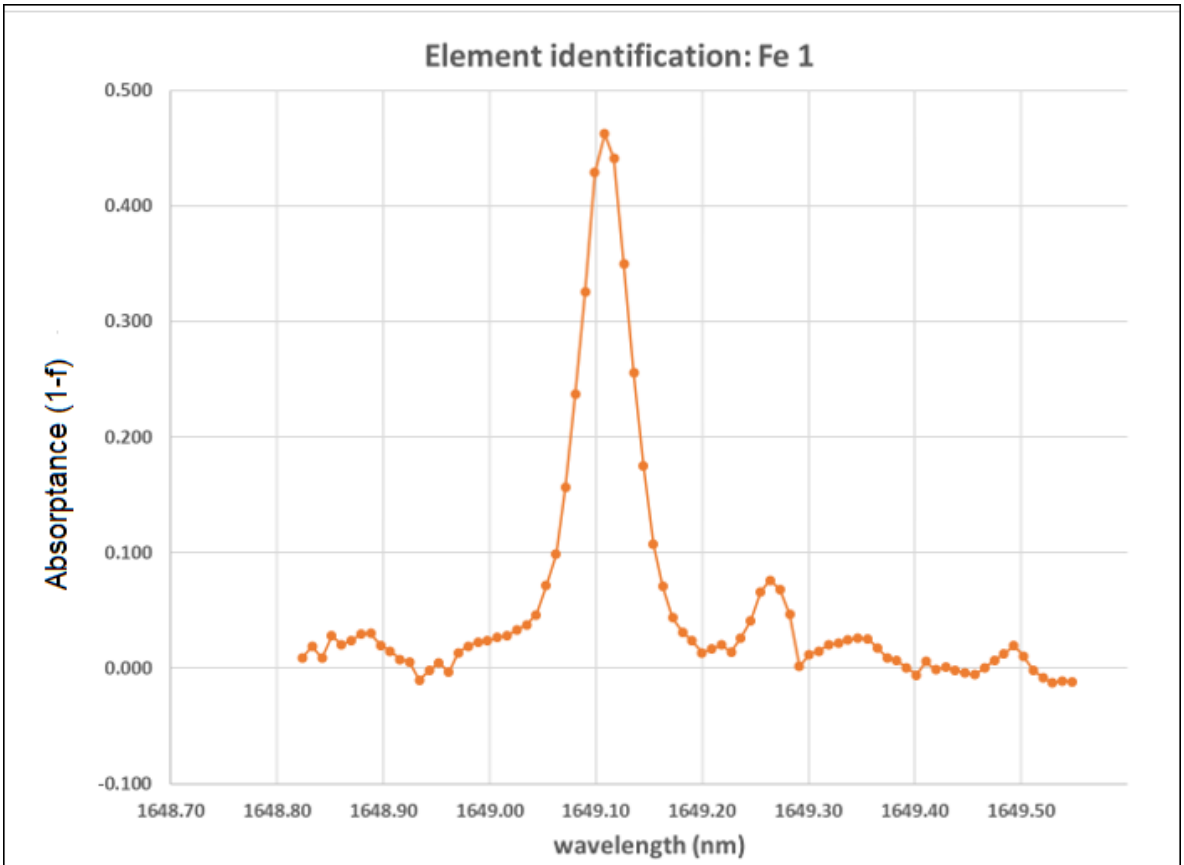

λ(nm)	Description	log gf	cdepth	EW (mA)	Match
1648.84	CO 6-3R78	-5.657	0.007	8	B
1648.89	CN 2-3P_{1}48.5	-1.825	0.024	14	B
1648.93	'Si 1'	-2.7	0.005	0	C
1648.96	'Co 1'	-0.13	0.024	0	C
1649.12	'Fe 1'	0.783	0.605	329	A
1649.20	'Fe 1'	-2.299	0.007	0	C
1649.25	Fe 1'+U	-2.593	0.007	27	F
1649.26	CO 7-4R8	-6.759	0.010	4	A
1649.43	'Fe 1'	-0.506	0.295	0	C
1649.45	'Mn 1'	-0.166	0.273	0	C
1649.47	'Fe 1'	-2.209	0.013	0	C
1649.50	CO 7-4R58	-5.652	0.016	4	A

Figure 52: Identification of Fe I

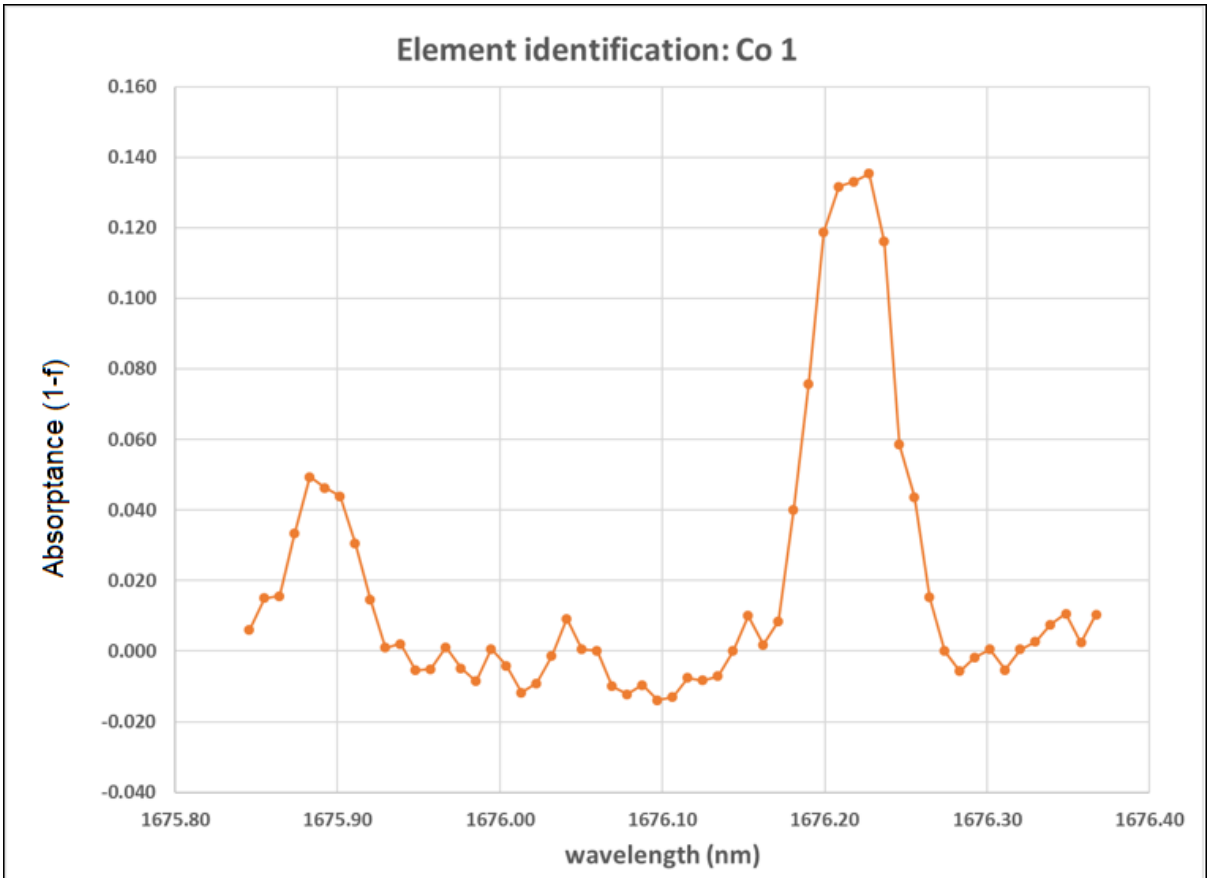

λ(nm)	Description	log gf	cdepth	EW (mA)	Match
1675.87	'Fe 1'	-1.521	0.051	0	C
1675.90	CN 1-2P_{1}63.5	-1.456	0.036	24	A
1676.05	CO 8-5R63	-5.372	0.009	0	D
1676.22	'Co 1'	-0.923	0.440	82	B

Figure 53: Identification of Co I

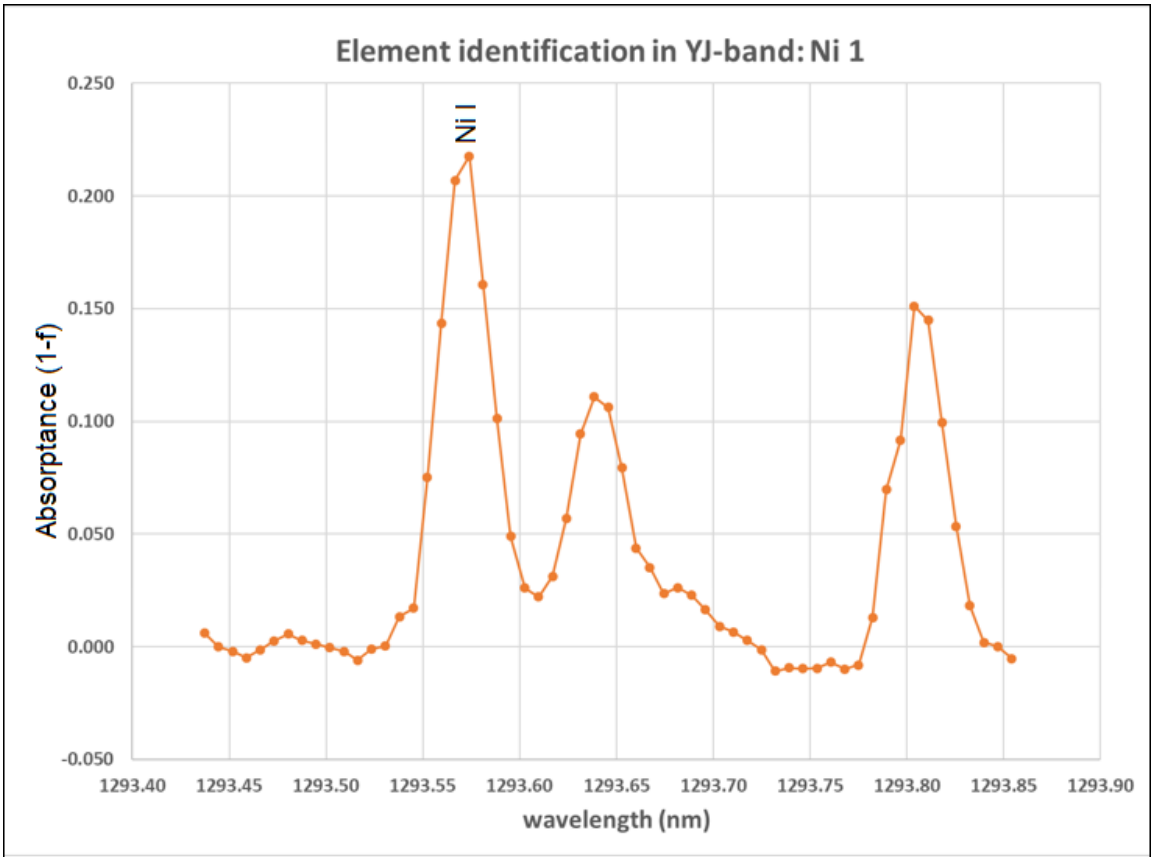

λ(nm)	Description	log gf	cdepth	EW (mA)	Match
1293.58	CN 4-4P_{2}36.5	-1.983	0.006	4	B
1293.59	'Ni 1'	-2.523	0.414	70	A
1293.65	'Fe 1'	-1.548	0.206	43	A
1293.70	CN 3-3P_{2}49.5	-2.037	0.006	4	B
1293.82	'Fe 1'	-0.948	0.243	46	A

Figure 54: Identification of Ni I

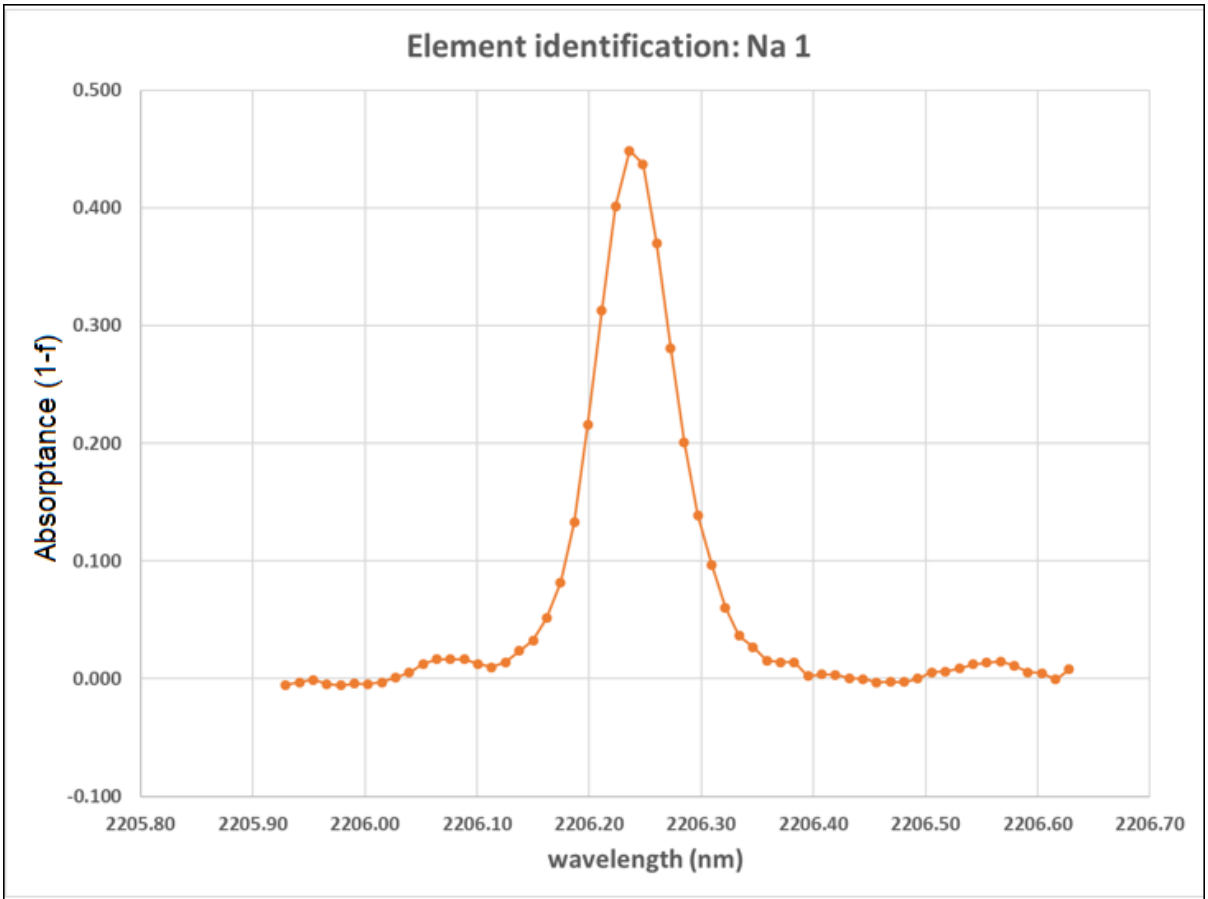

λ(nm)	Description	log gf	cdepth	EW (mA)	Match
2206.07	CN 1-3R_{2}58.5	-1.846	0.009	11	B
2206.24	'Na 1'	0.287	0.505	395	A
2206.29	CN 2-4Q_{2}29.5	-1.8	0.026	25	B
2206.53	'Na 1'	-1.674	0.014	0	C
2206.55	'Fe 1'	-2.775	0.024	2	B
2206.59	CN 2-4P {1}18.5	-2.363	0.009	8	B

Figure 55: Identification of Na I

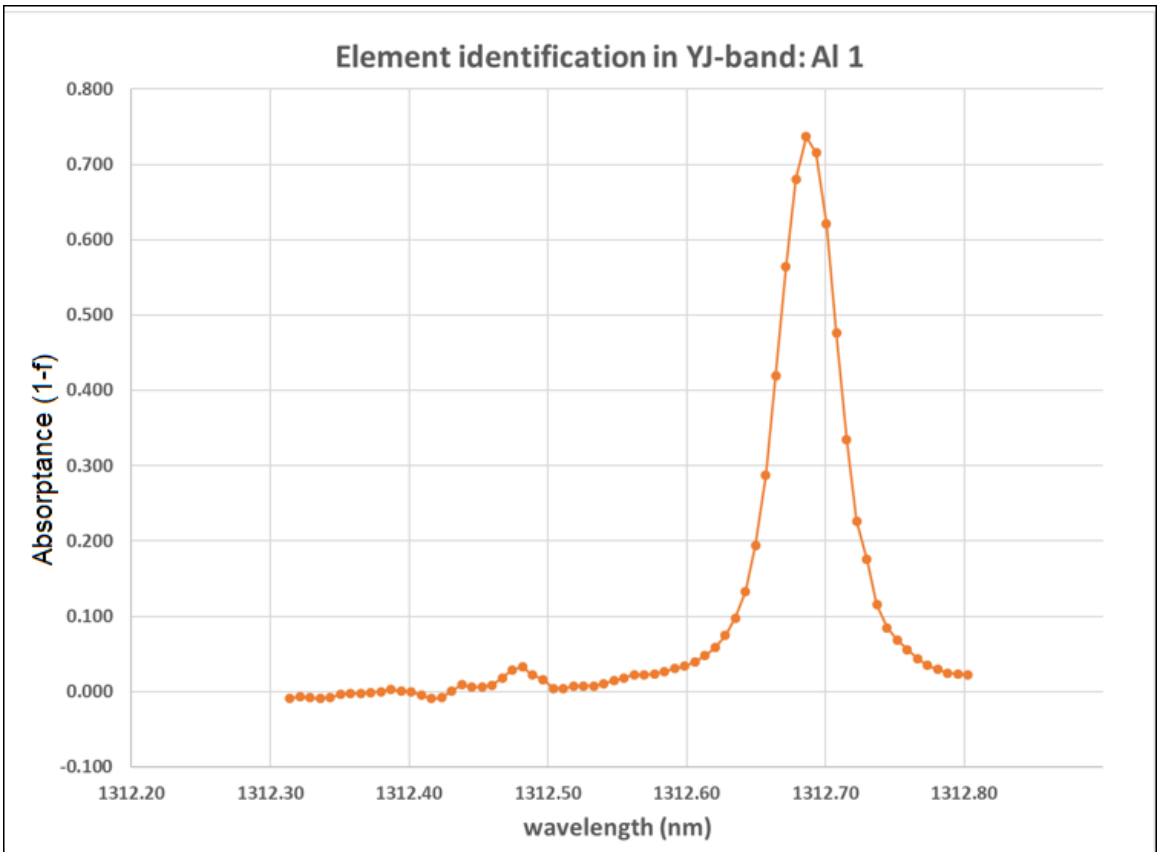

λ(nm)	Description	log gf	cdepth	EW (mA)	Match
1312.49	U(Fe 2, Sc 2)			10	F
1312.55	'Sr 2'	0.692	0.006	0	C
1312.59	'Al 1'	-1.642	0.019	14	B
1312.70	'Al 1'	0.270	0.608	461	B
1312.78	'Si 1'	-2.725	0.012	0	C

Figure 56: Identification of Al I

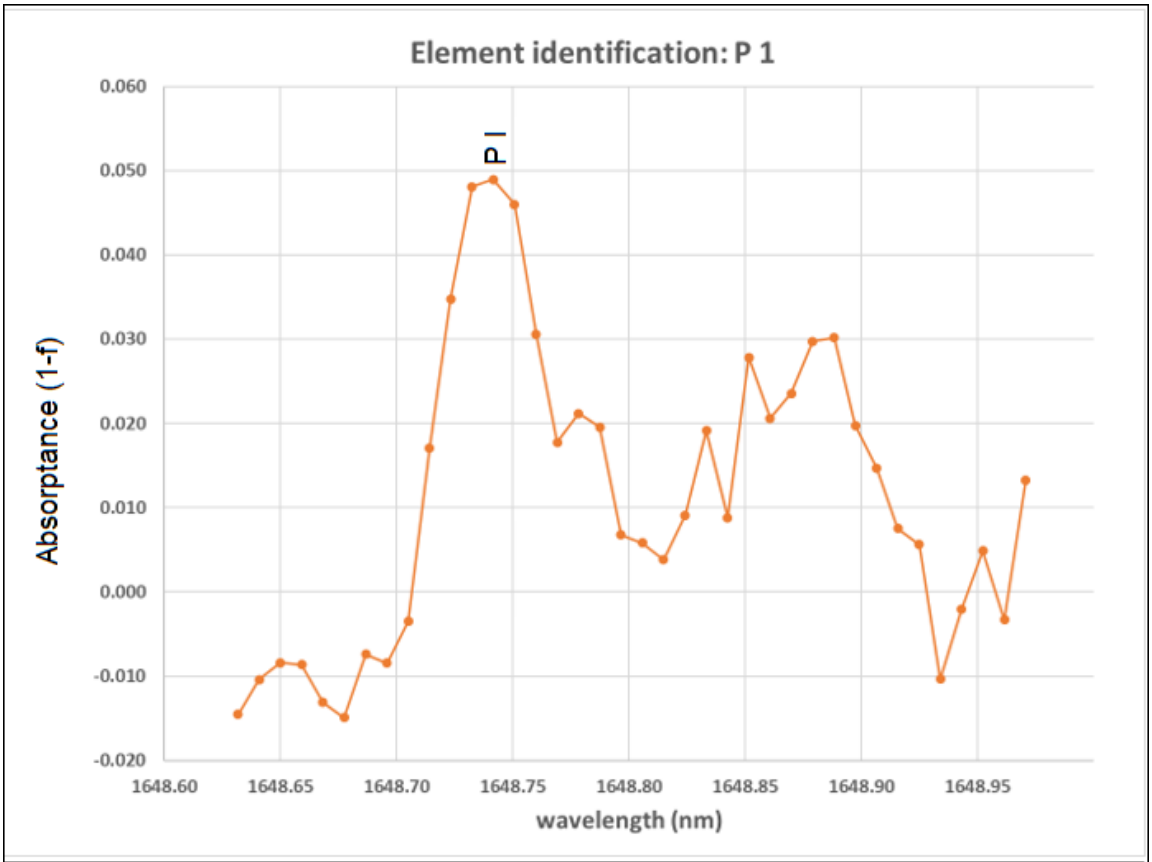

λ(nm)	Description	log gf	cdepth	EW (mA)	Match
1648.74	'P 1'	-0.29	0.079	15	B
1648.75	CO 7-4R57	-5.666	0.017	8	A
1648.84	CO 6-3R78	-5.657	0.007	8	B
1648.89	CN 2-3P_{1}48.5	-1.825	0.024	14	B
1648.93	'Si 1'	-2.7	0.005	0	C

Figure 57: Identification of P I

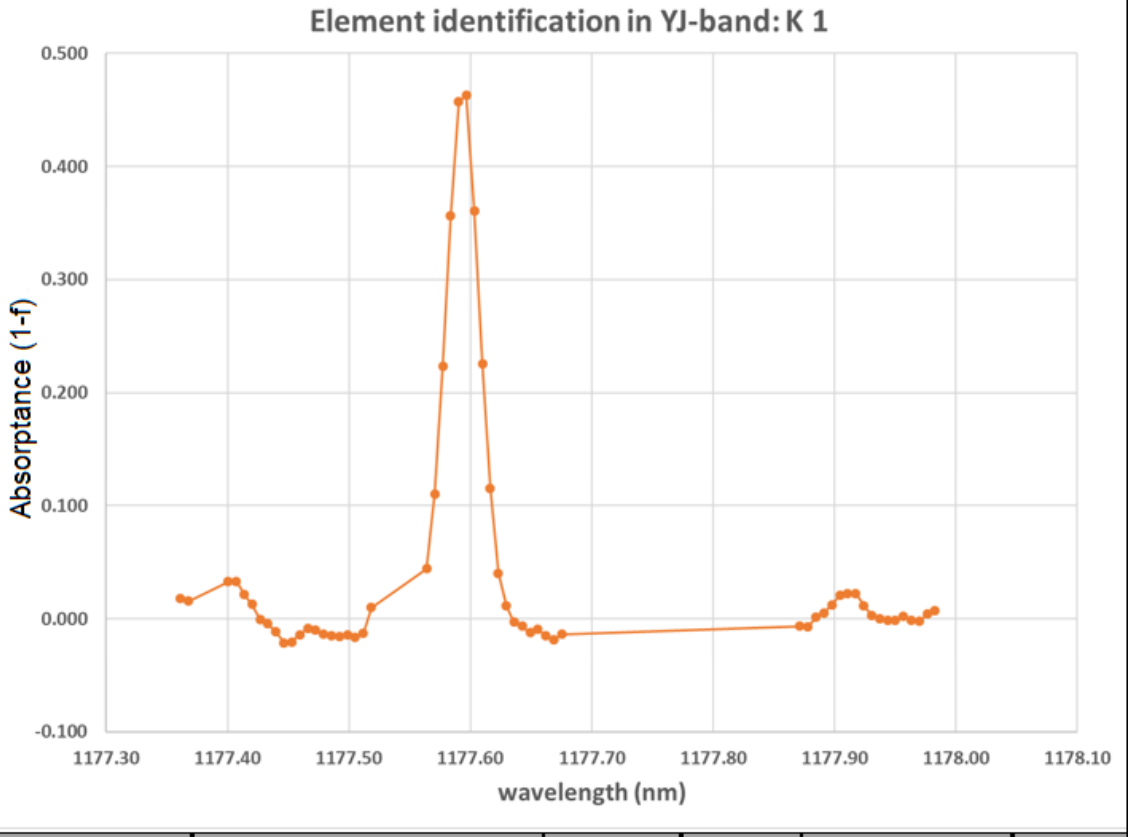

λ(nm)	Description	log gf	cdepth	EW (mA)	Match
1177.41	CN 1-1Q_{1}44.5	-2.066	0.020	9	B
1177.58	'Fe 1'	-1.722	0.007	0	C
1177.61	'K 1'	0.510	0.478	158	A
1177.71	'Co 1'	-4.408	0.006	gap	C
1177.93	CN 1-1P_{1}36.5	-2.479	0.012	6	B

Figure 58: Identification of K I

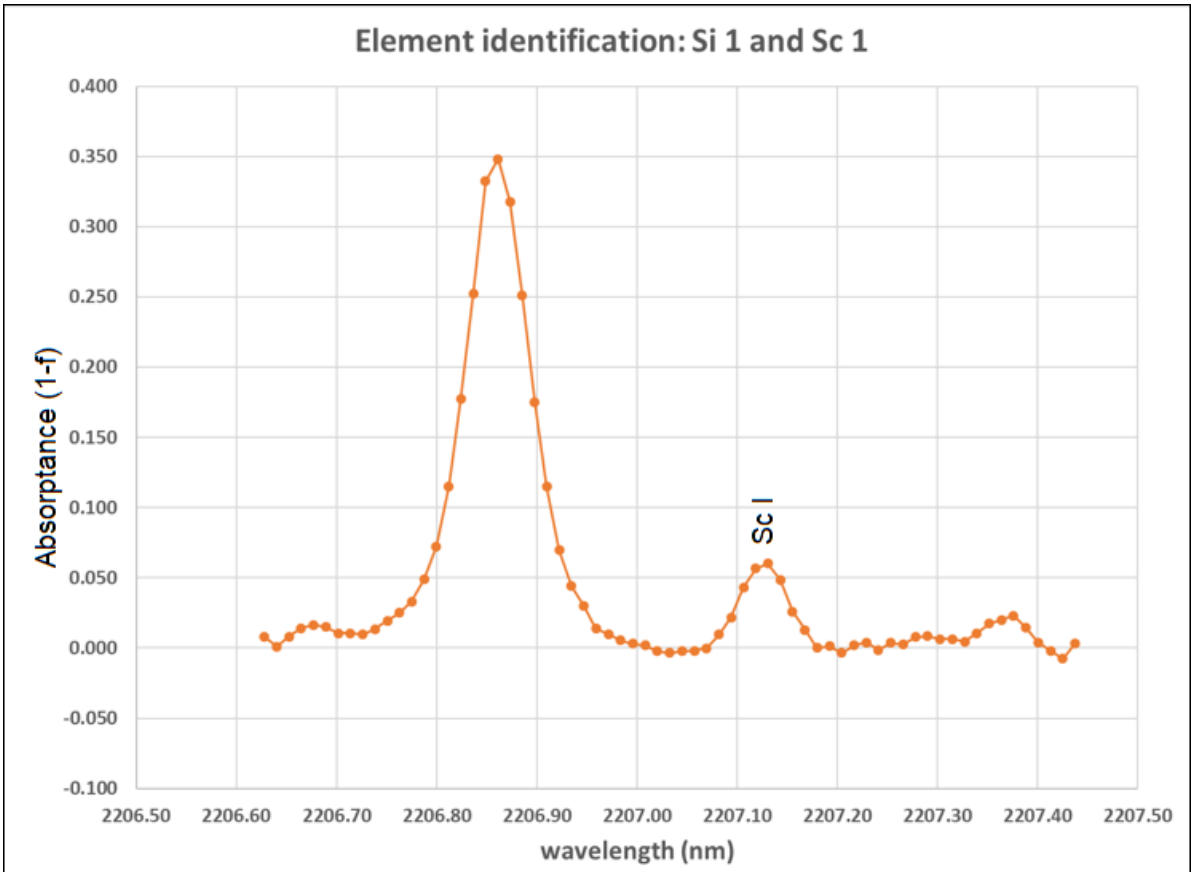

λ(nm)	Description	log gf	cdepth	EW (mA)	Match
2206.68	CN 2-4R_{1}41.5	-1.908	0.012	8	B
2206.87	'Si 1'	0.538	0.424	305	A
2207.13	'Sc 1'	-1.058	0.168	34	A
2207.29	Co 1	-1.75	0.124	3	B
2207.31	'Fe 1'	-1.015	0.042	0	C
2207.38	CN 1-3P_{1}36.5	-2.091	0.020	12	B

Figure 59: Identification of Si I and Sc I

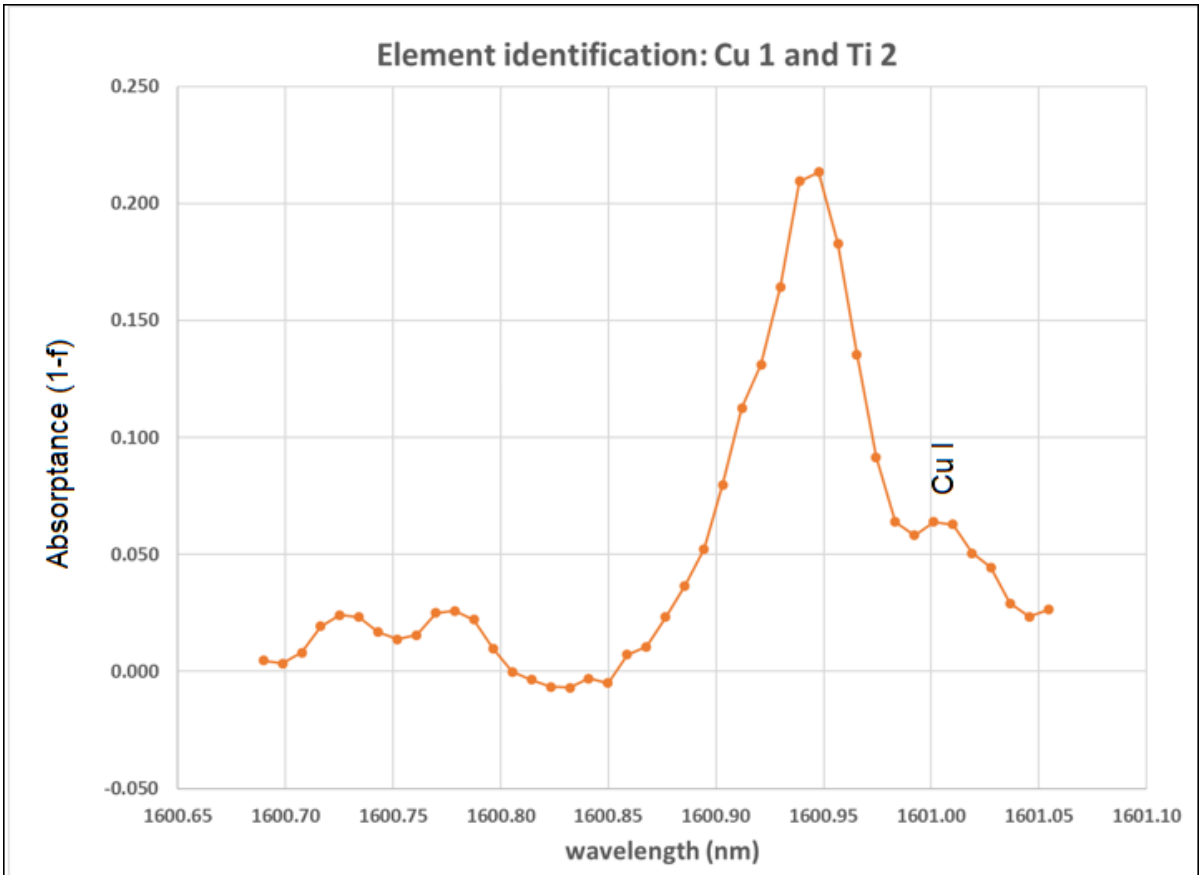

λ(nm)	Description	log gf	cdepth	EW (mA)	Match
1600.72	CO 5-2R47	-6.388	0.022	8	A
1600.75	CN 3-4R_{1}40.5	-2.302	0.005	3	B
1600.78	CO 5-2R20	-6.916	0.022	8	A
1600.78	'Fe 1'	-0.863	0.171	0	C
1600.92	'C 1'	0.234	0.171	47	A
1600.94	'Ti 2'	-2.07	0.269	79	B
1600.95	'Fe 1'	-0.645	0.281	83	B
1601.01	'Cu 1'	-0.045	0.161	27	B

Figure 60: Identification of Ti II and Cu I

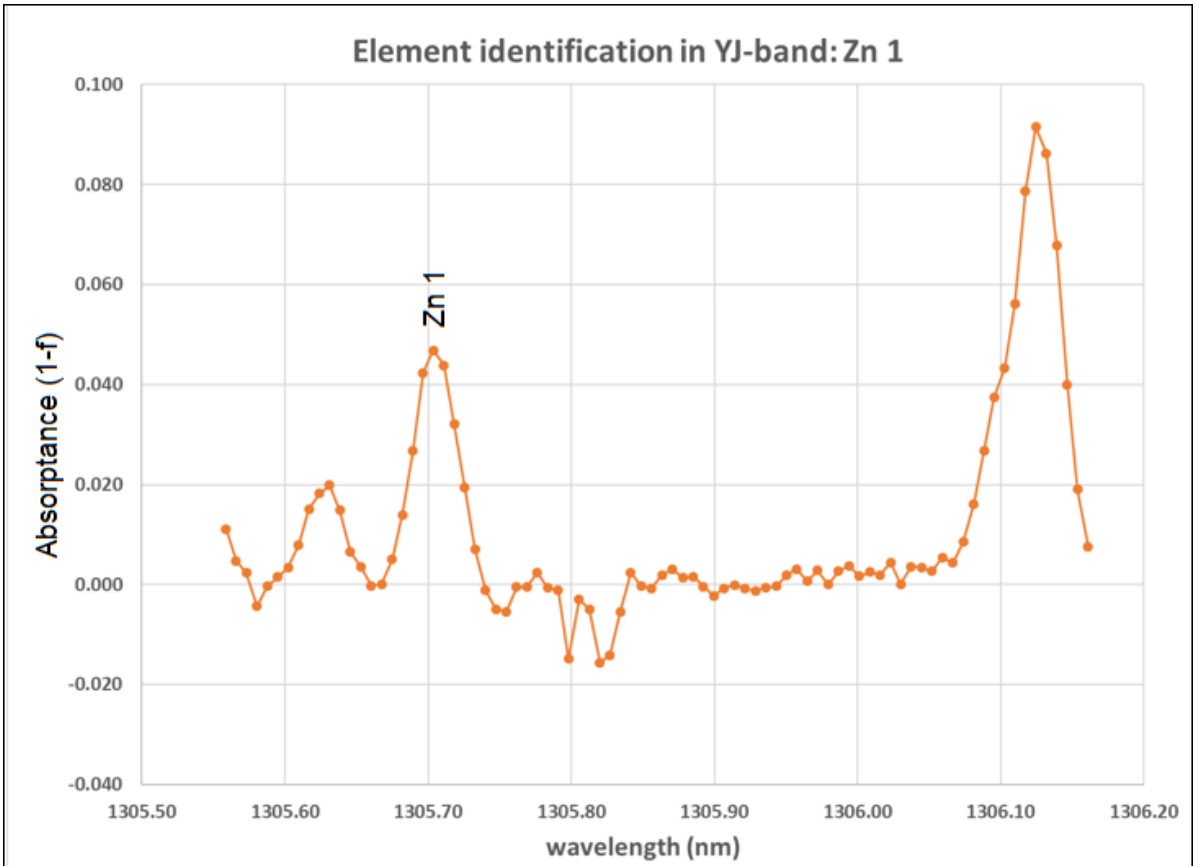

λ(nm)	Description	log gf	cdepth	EW (mA)	Match
1305.64	CN 4-4Q_{2}48.5	-1.536	0.009	7	B
1305.72	'Zn 1'	0.340	0.072	17	A
1305.90	'Si 1'	-1.882	0.010	0	C
1306.01	'Ni 1'	-1.791	0.007	0	C
1306.14	'Ga 1'	0.5	0.007	0	C
1306.14	CN 0-0Q_{1}89.5	-0.682	0.029	21	B
1306.15	'Ca 1'	-1.092	0.086	21	A
1306.16	'Ba 2'	0.34	0.006	0	C

Figure 61: Identification of Zn I and Ca I

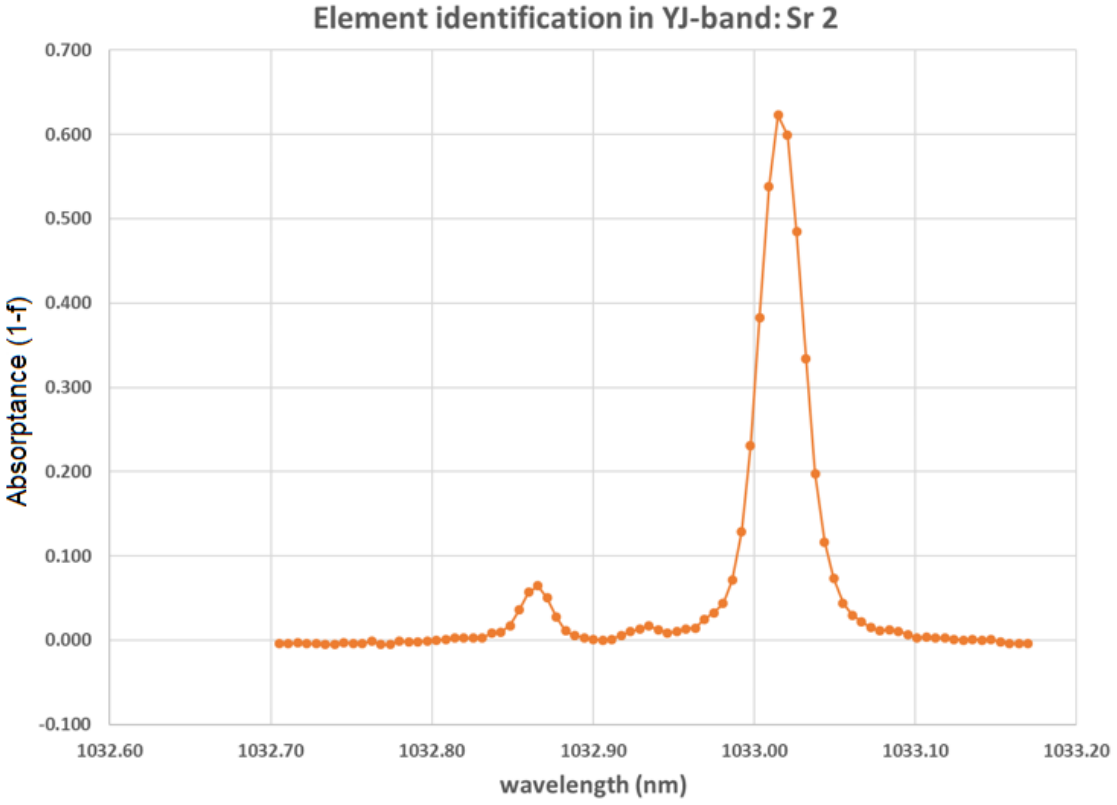

λ(nm)	Description	log gf	cdepth	EW (mA)	Match
1032.80	'Cr 1'	-1.375	0.014		C
1032.86	CN 2-1Q_{1}68.5	-1.036	0.032	17	A
1032.93	'Fe 1'	-2.416	0.010	4	B
1033.01	'Sr 2'	-0.353	0.598	232	A
1033.02	'Fe 1'	-2.343	0.010		C

Figure 62: Identification of Sr II

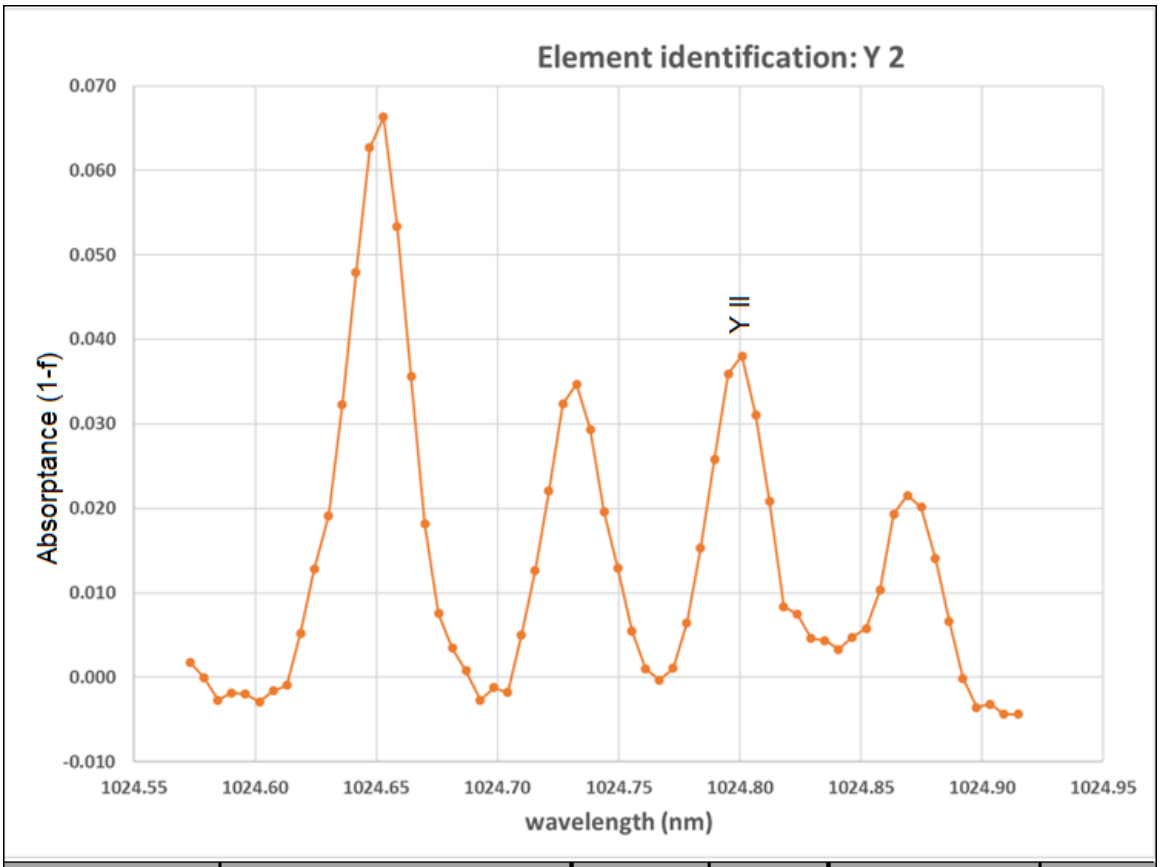

λ(nm)	Description	log gf	cdepth	EW (mA)	Match
1024.63	CN 3-2R_{1}62.5	-1.772	0.006	3	B
1024.65	U			17	F
1024.73	U			10	F
1024.80	'Y 2'	-1.823	0.036	11	B
1024.87	CN 2-1R_{2}73.5	-1.297	0.011	6	B

Figure 63: Identification of Y II

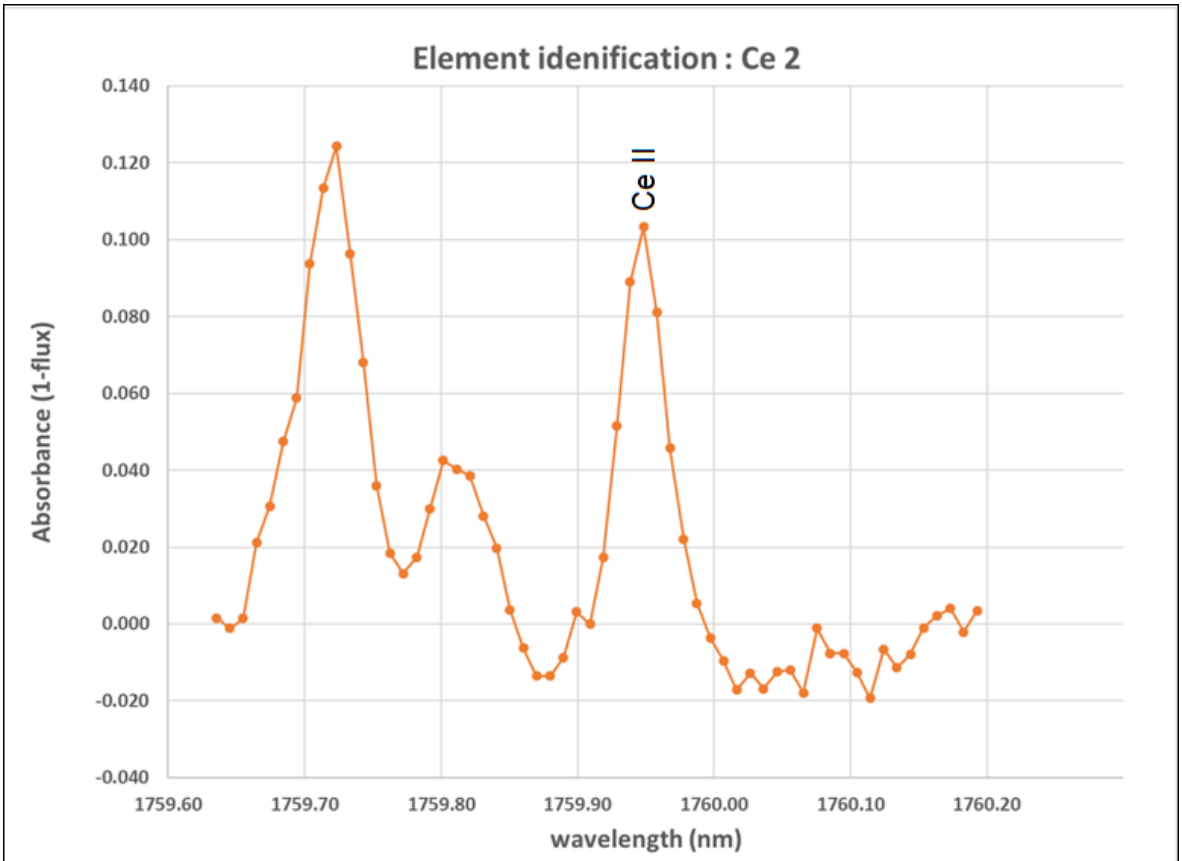

λ(nm)	Description	log gf	cdepth	EW (mA)	Match
1759.70	'C 1'	-1.090	0.087	0	B
1759.73	Fe1			63	E
1759.73	OH 2-0P_{2e}20.5	-4.899	0.011	5	B
1759.75	CO 5-2P70	-4.906	0.006	3	B
1759.80	'Fe 1'	-2.281	0.005	0	C
1759.82	'Si 1'	-2.054	0.167	19	A
1759.85	CO 9-6P36	-5.957	0.008	4	B
1759.95	Ce 2			41	F

Figure 64: Identification of Ce II

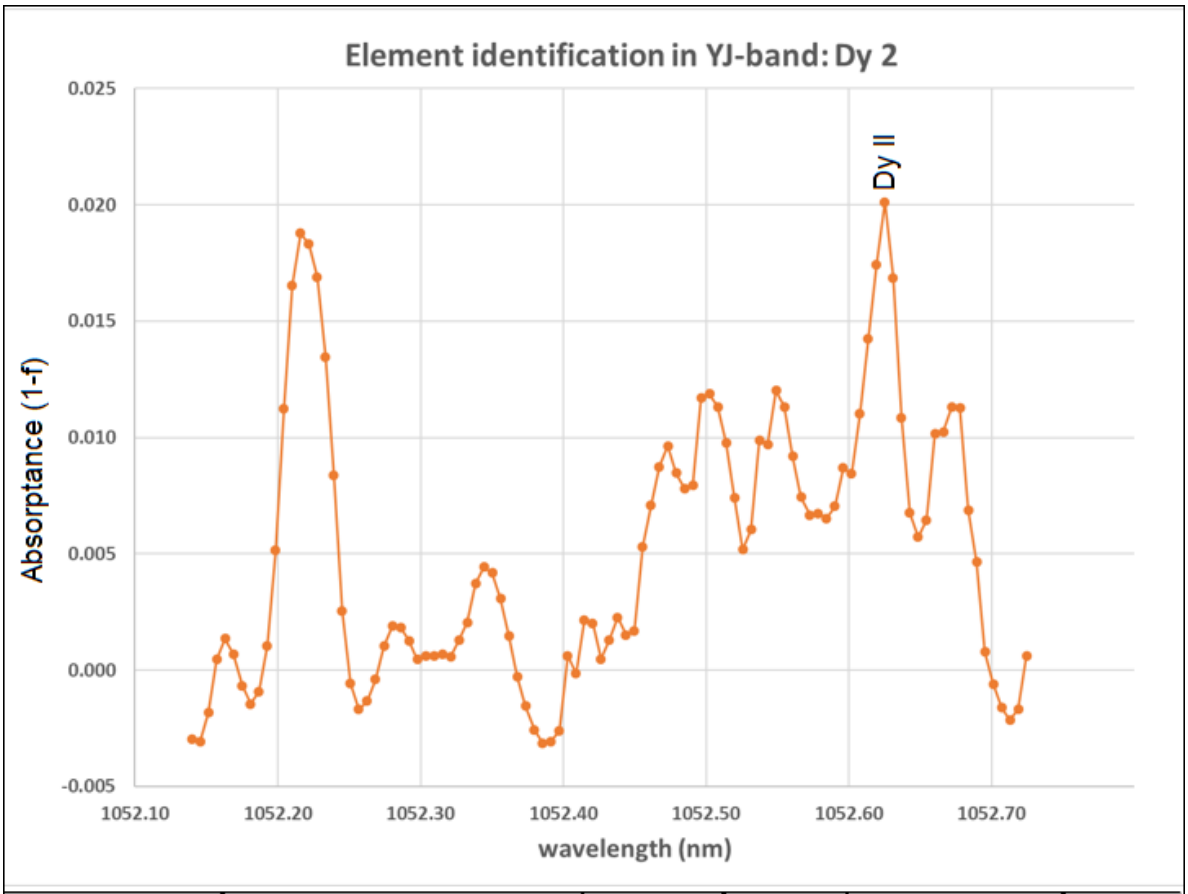

λ(nm)	Description	log gf	cdepth	EW (mA)	Match
1052.17	'Fe 1'	-1.149	0.025	0	C
1052.22	U+'Ni 1'			7	F
1052.34	U+'V 1'			1	F
1052.46	CN 3-2P_{2}56.5	-1.839	0.007	4	B
1052.50	U+'Cr 1'			3	F
1052.55	CN 2-1R_{2}82.5	-1.247	0.005	3	B
1052.63	'Dy 2'	-0.45	0.014	6	B
1052.67	U+'Sc 1'			3	F

Figure 65: Identification of Dy II

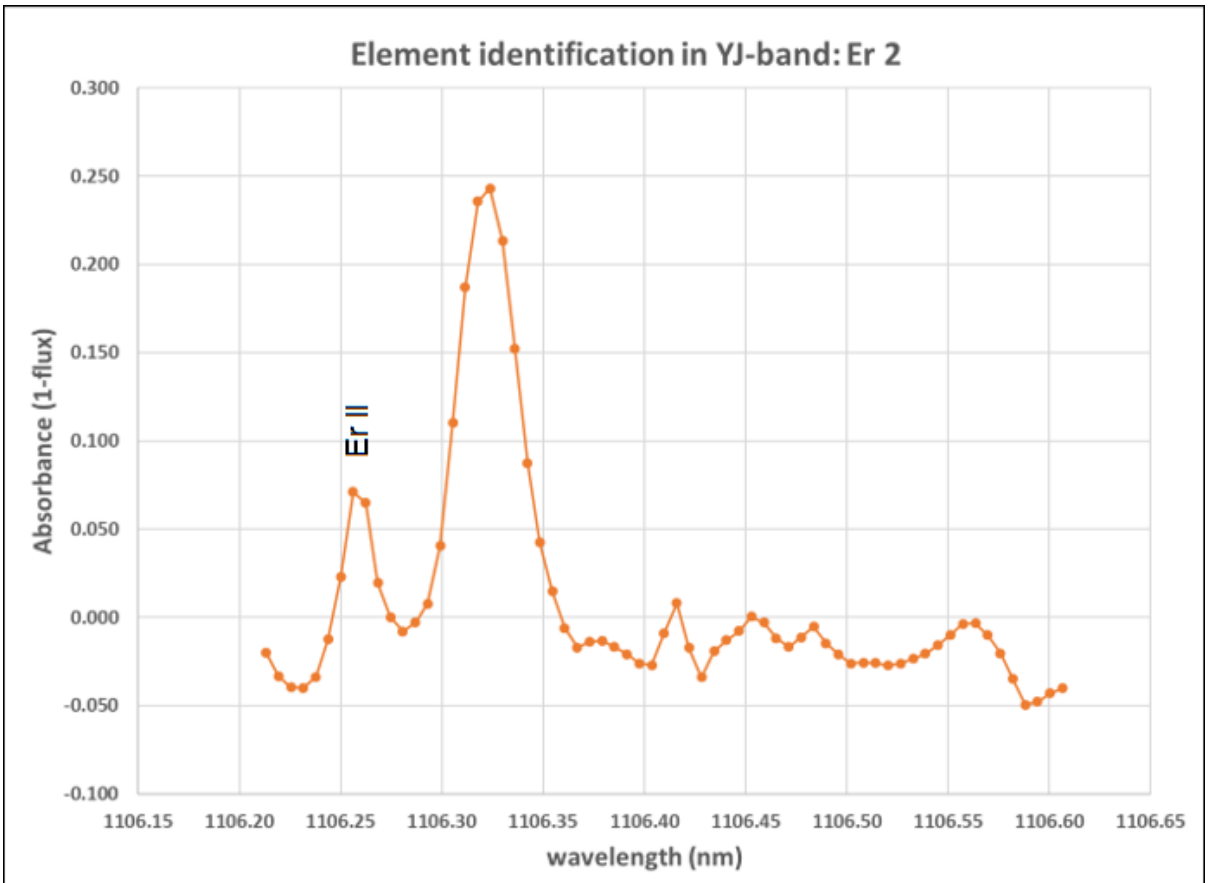

λ(nm)	Description	log gf	cdepth	EW (mA)	Match
1106.26	'Er 2'	-0.640	0.007	11	B
1106.32	CN 0-0Q_{12}18.5	-2.248	0.071	36	B
1106.33	CN 0-0P_{1}11.5	-2.043	0.106	50	A
1106.44	'Fe 1'	-2.707	0.007	0	C

Figure 66: Identification of Er II

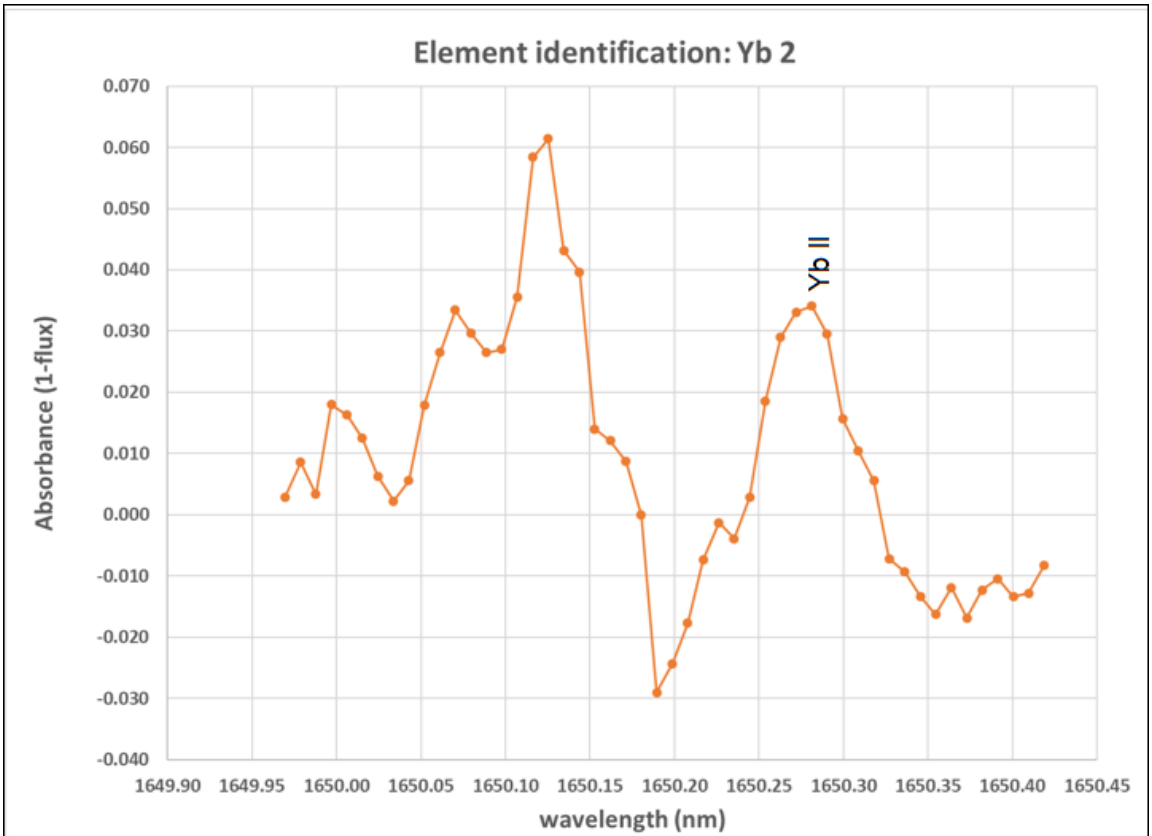

λ(nm)	Description	log gf	cdepth	EW (mA)	Match
1650.01	CO 7-4R7	-6.816	0.009	5	A
1650.06	'C 1'	-1.826	0.005	0	C
1650.08	'Ni 1'	-1.069	0.035	7	B
1650.08	CO 5-2P26	-7.090	0.013	6	A
1650.09	'C 1'	-1.52	0.009	0	C
1650.11	'Fe 1'	-3.437	0.007	0	C
1650.12	CN 3-4P_{1}35.5	-2.404	0.007	4	B
1650.13	CN 1-2P_{1}59.5	-1.486	0.045	24	A
1650.19	'Fe 1'	-2.465	0.049	0	C
1650.24	CO'	-5.645	0.006	0	C
1650.28	CO 7-4R59	-5.639	0.015	7	A
1650.29	'Yb 2'	-0.64	0.065	10	B
1650.36	'Ni 1'	-0.863	0.033	0	C

Figure 67: Identification of Yb II

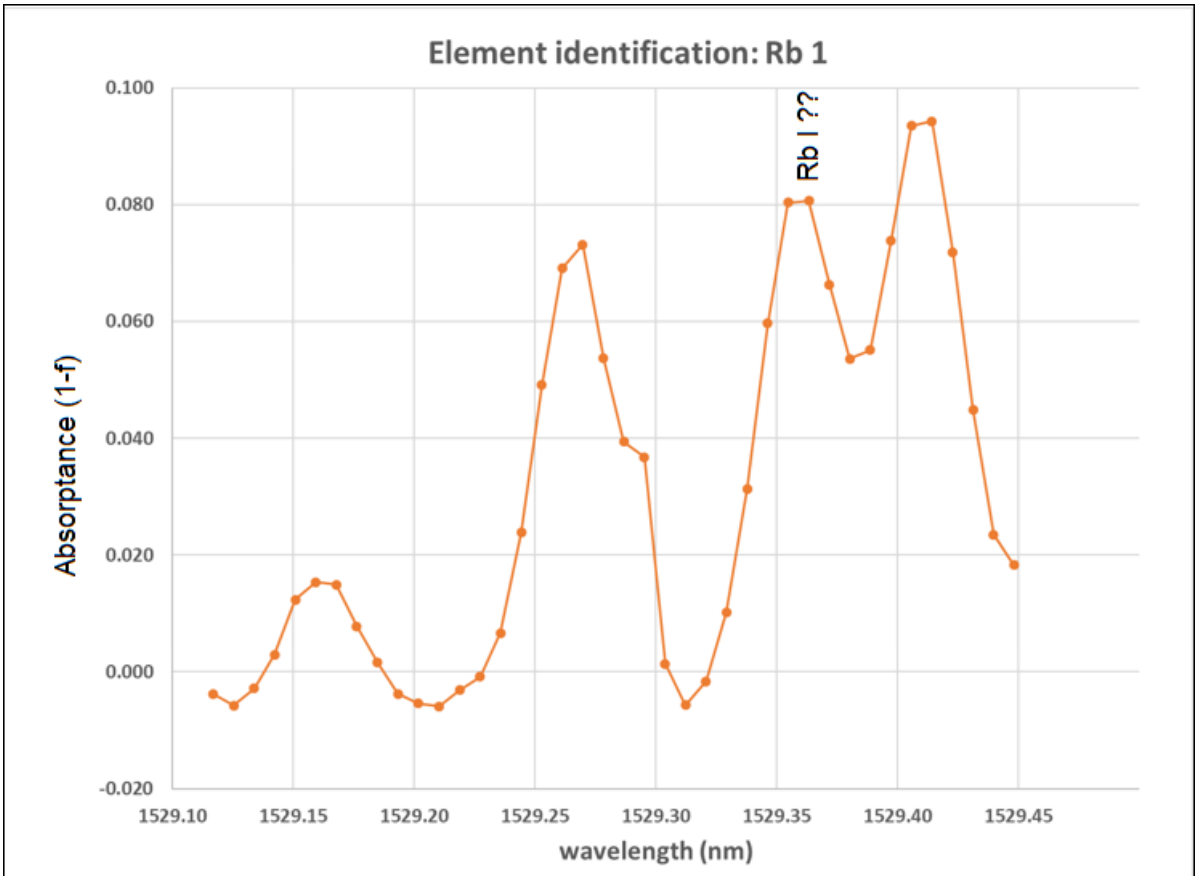

λ(nm)	Description	log gf	cdepth	EW (mA)	Match
1529.17	'Fe 1'	-1.252	0.086	5	B
1529.26	'Rb 1'	-0.535	0.007	0	C
1529.27	CN 1-2R_{2}53.5	-1.51	0.046	30	A
1529.37	'Rb 1'	0.42	0.041	6	B
1529.38	'Fe 1'	-1.036	0.116	28	A
1529.42	'Fe 1'	-0.837	0.162	39	A

Figure 68: Identification of Rb I

7.2.2 Identification of Molecules

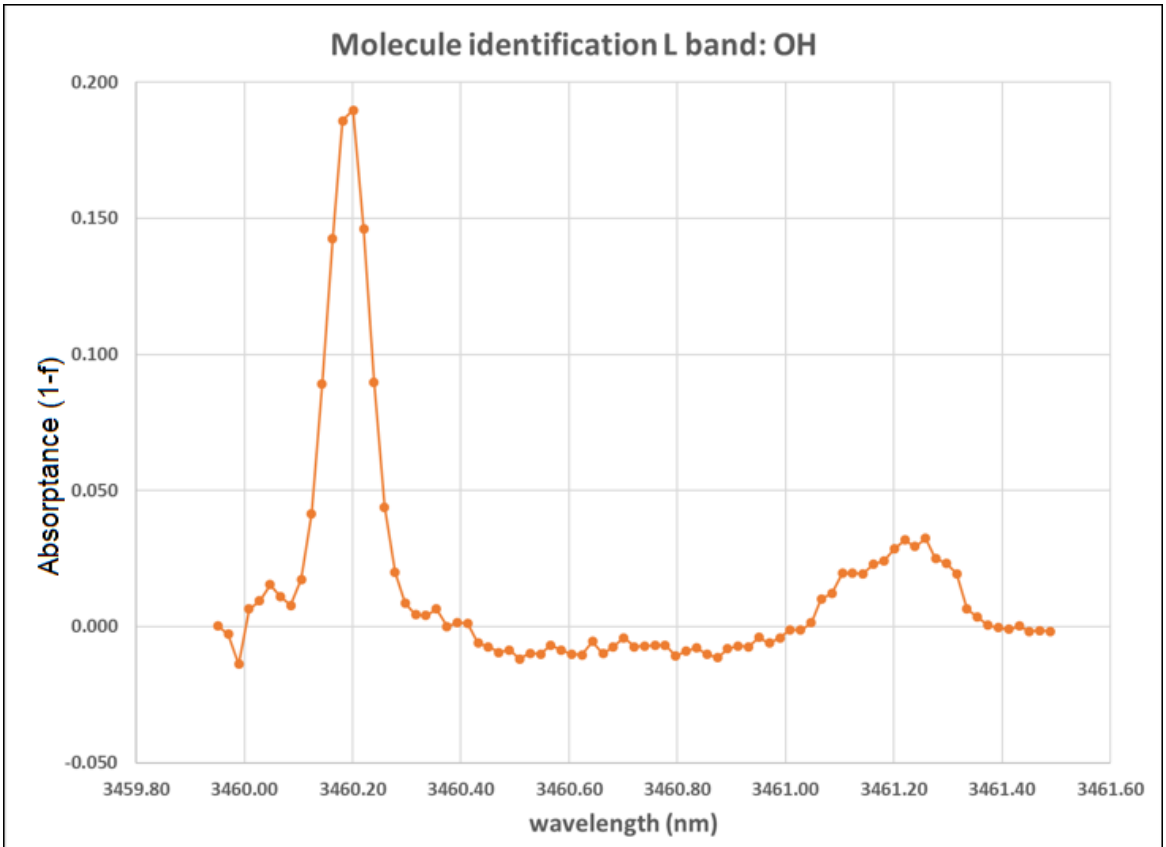

λ(nm)	Description	log gf	cdepth	EW (mA)	Match
3460.20	OH 1-0P_{1f}15.5	-4.025	0.129	190	A
3461.13	'CH 1'	-2.968	0.015	18	B
3461.22	CH 2-1R17 & R21	-2.94	0.016	19	A
3461.26	'CH 1'	-2.862	0.011	13	B
3461.32	'CH 1'	-2.839	0.011	13	B

Figure 69: Identification of OH molecule

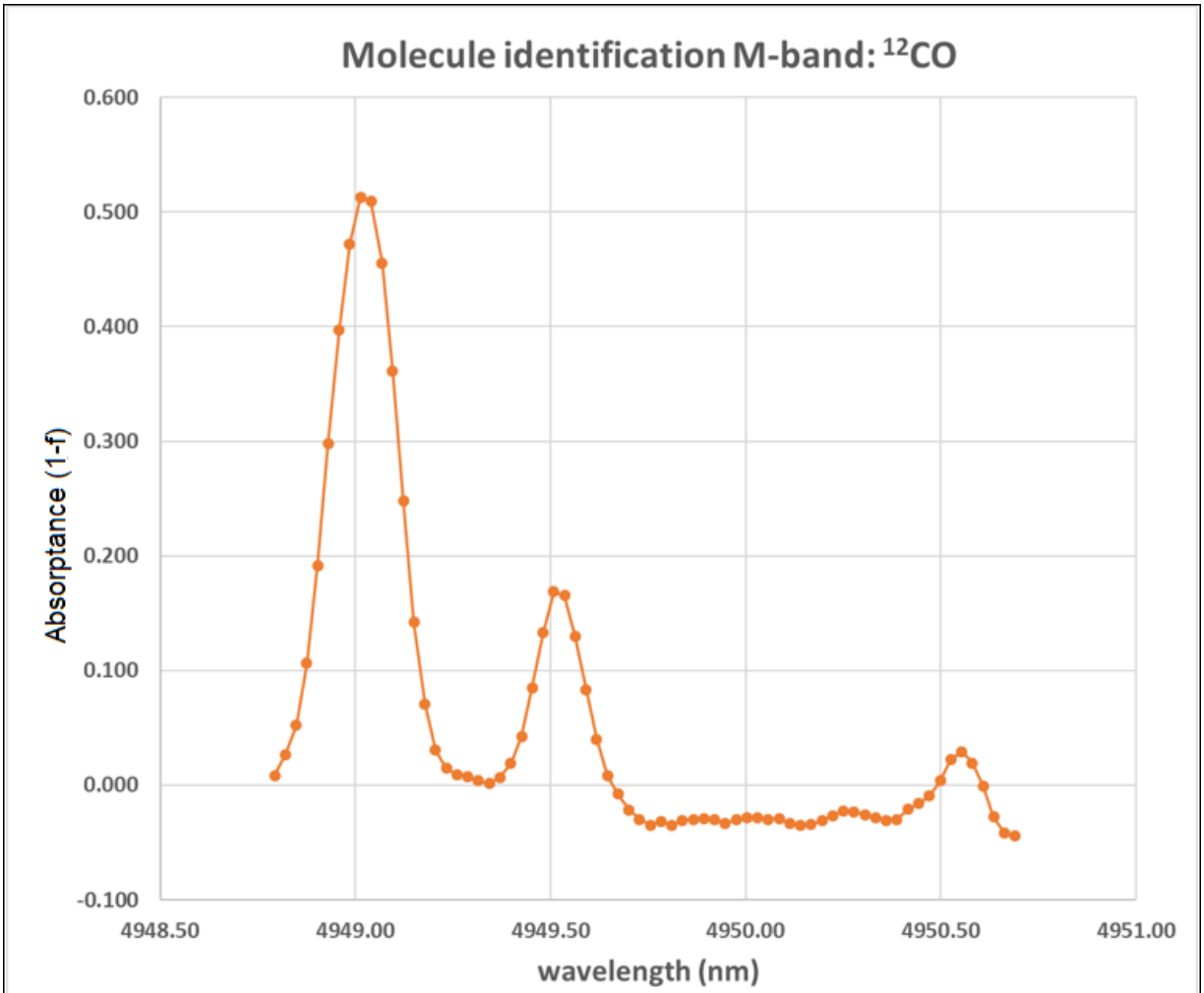

λ(nm)	Description	log gf	cdepth	EW (mA)	Match
4949.02	CO 2-1P23	-3.369	0.477	1074	A
4949.52	CO 10-9R40	-2.425	0.236	243	A
4950.27	'CO'	-5.457	0.018	0	C
4950.45	'CO'	-5.246	0.009	0	C
4950.56	^{13}CO 9-8R48	-4.328	0.021	21	A

Figure 70: Identification of ^{12}CO molecule

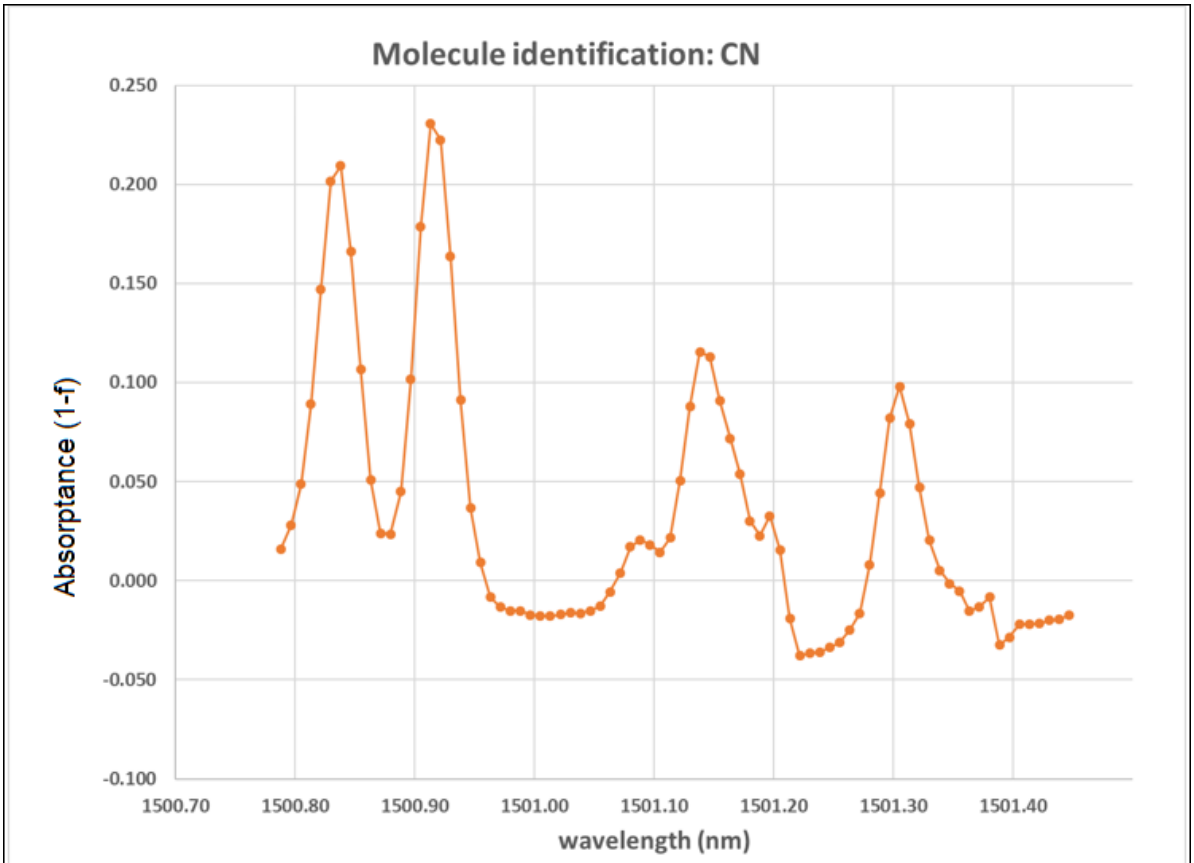

λ(nm)	Description	log gf	cdepth	EW (mA)	Match
1500.84	CN 1-2Q_{1}32.5	-1.448	0.123	68	A
1500.86	'Fe 1'	-1.191	0.077	22	B
1500.92	CN 0-1Q_{1}49.5	-1.208	0.161	92	A
1501.09	'Cr 1'	-0.719	0.007	5	B
1501.11	'Ca 1'	-1.656	0.013	0	C
1501.11	'Cr 1'	-3.739	0.011	0	C
1501.11	'Ni 1'	-1.534	0.005	0	C
1501.13	Fe 1'	-2.006	0.014	0	C
1501.15	CN 1-2P_{2}24.5	-1.907	0.065	55	A
1501.20	U+'Fe 1'			5	E
1501.31	CN 1-2R_{1}44.5	-1.588	0.058	32	A
1501.35	'Fe 1'	-0.383	0.261	0	C

Figure 71: Identification of ^{12}CN molecule

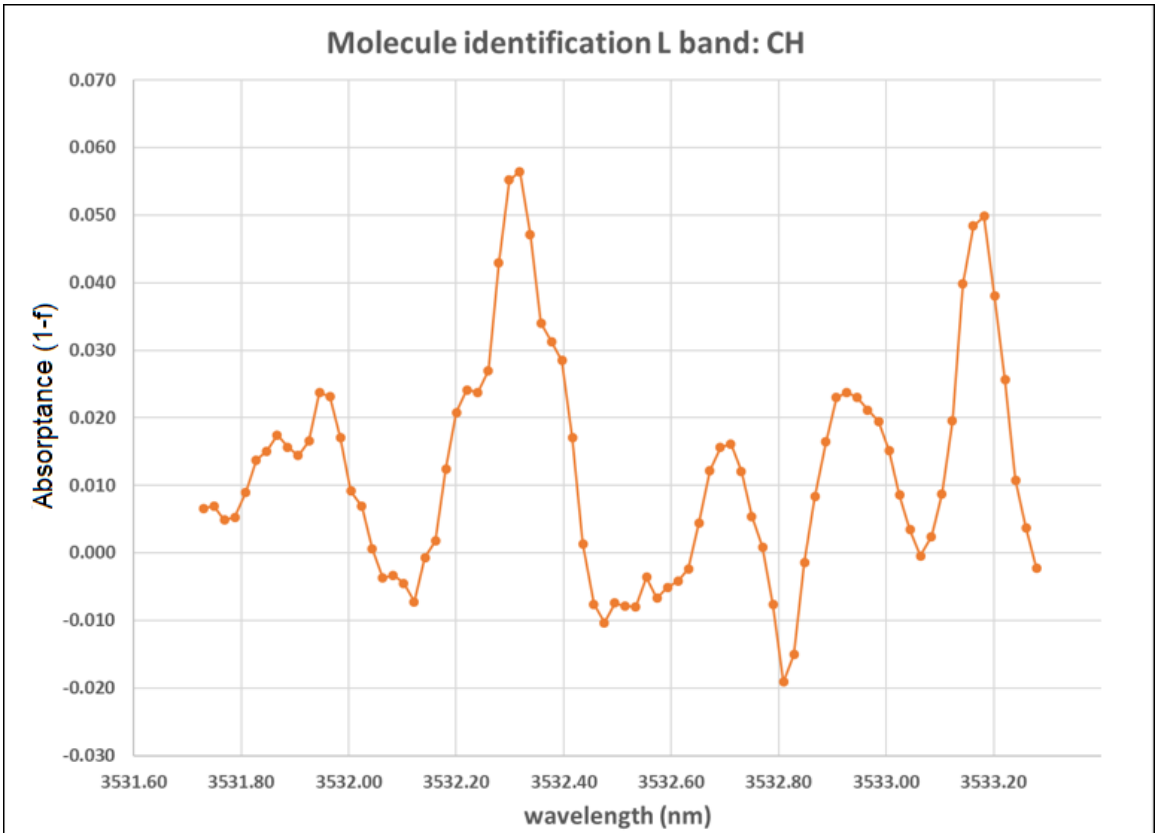

λ(nm)	Description	log gf	cdepth	EW (mA)	Match
3531.88	'Fe 1'	-5.045	0.024	15	B
3532.00	CH 2-1R_{2f}9.5	-3.214	0.018	22	A
3532.23	CH 2-1R_{1e}10.5	-3.171	0.019	12	A
3532.32	U			72	F
3532.72	CH 2-1R_{2e}9.5	-3.214	0.018	13	A
3532.93	CH 2-1R_{1f}10.5	-3.171	0.019	32	A
3533.19	'Si 1'	-0.195	0.119	48	A

Figure 72: Identification of ^{12}CH molecule

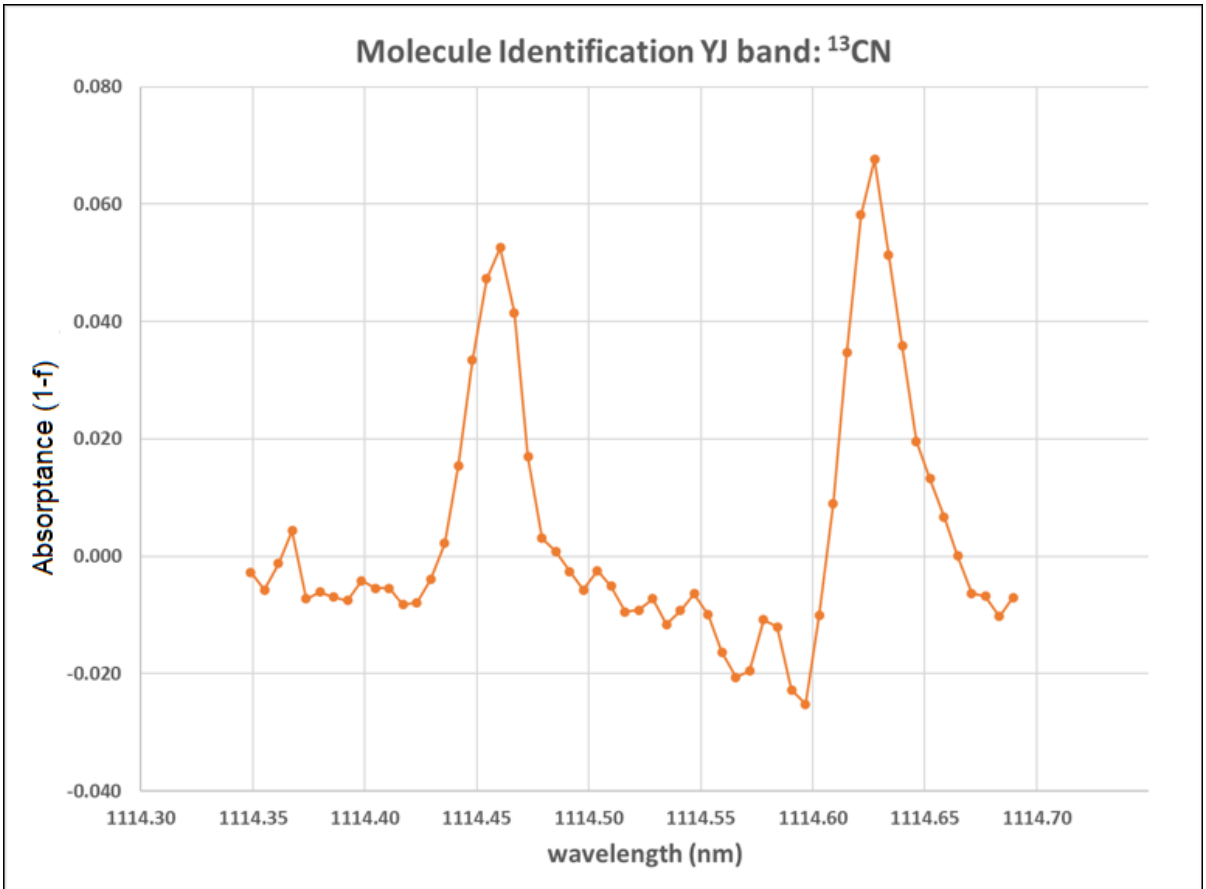

λ(nm)	Description	log gf	cdepth	EW (mA)	Match
1114.41	'Fe 1'	-1.537	0.010	0	C
1114.47	^{13}CN 0-0Q_{2}28.5			13	E
1114.47	'Fe 1'	-3.189	0.020	0	C
1114.64	CN 0-0^{o}P_{12}13.5	-2.629	0.030	18	A

Figure 73: Identification of ^{13}CN molecule

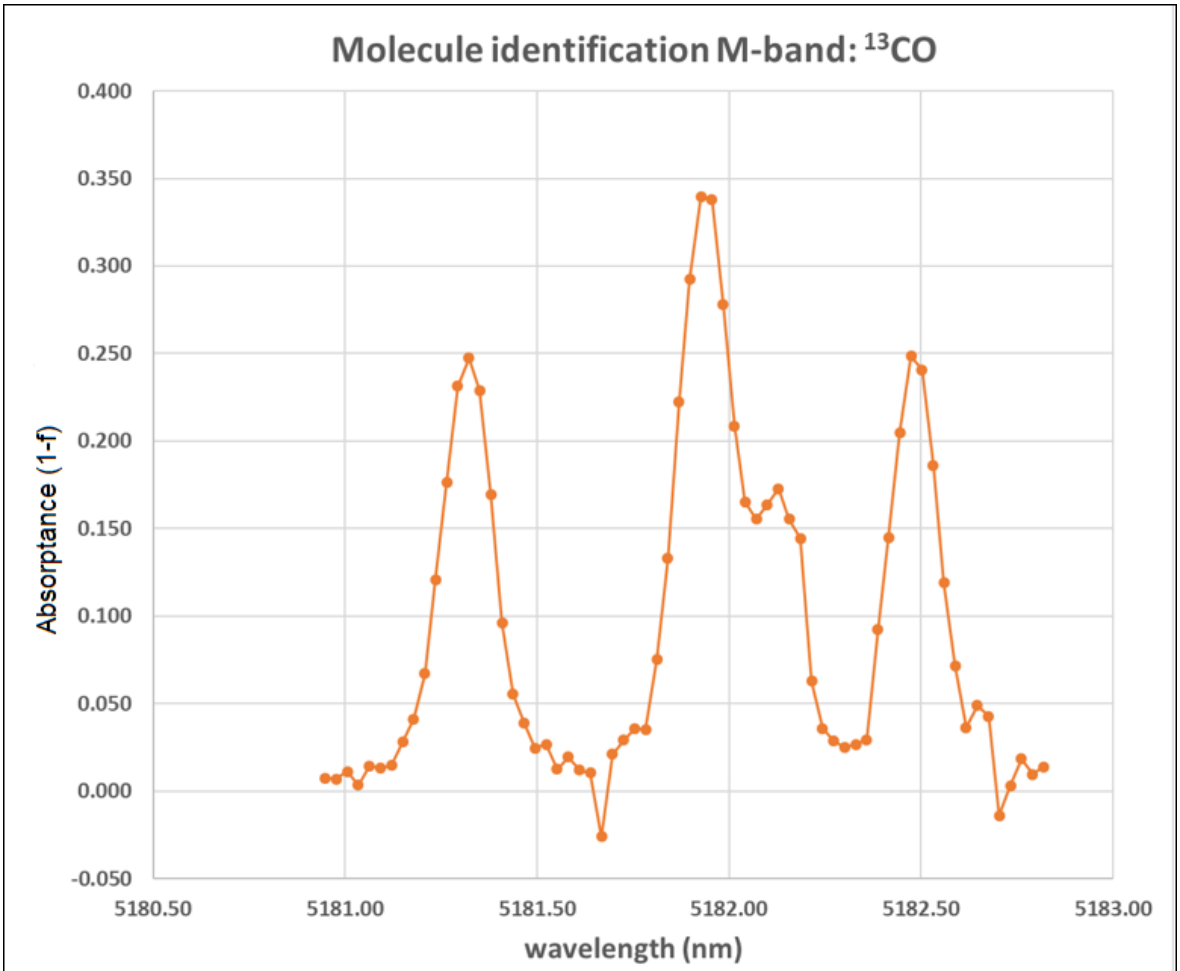

λ(nm)	Description	log gf	cdepth	EW (mA)	Match
5181.30	^{13}CO 4-3P25	-5.03	0.189	444	B
5181.87	CO 9-8P1	-4.028	0.104	154	B
5181.92	^{13}CO 1-0P39	-5.401	0.240	354	B
5181.92	CO 11-10R14	-2.848	0.191	282	B
5182.10	^{13}CO 6-5P11	-5.175	0.073	108	B
5182.46	CO 8-7P8	-3.253	0.256	430	A

Figure 74: Identification of ^{13}CO molecule

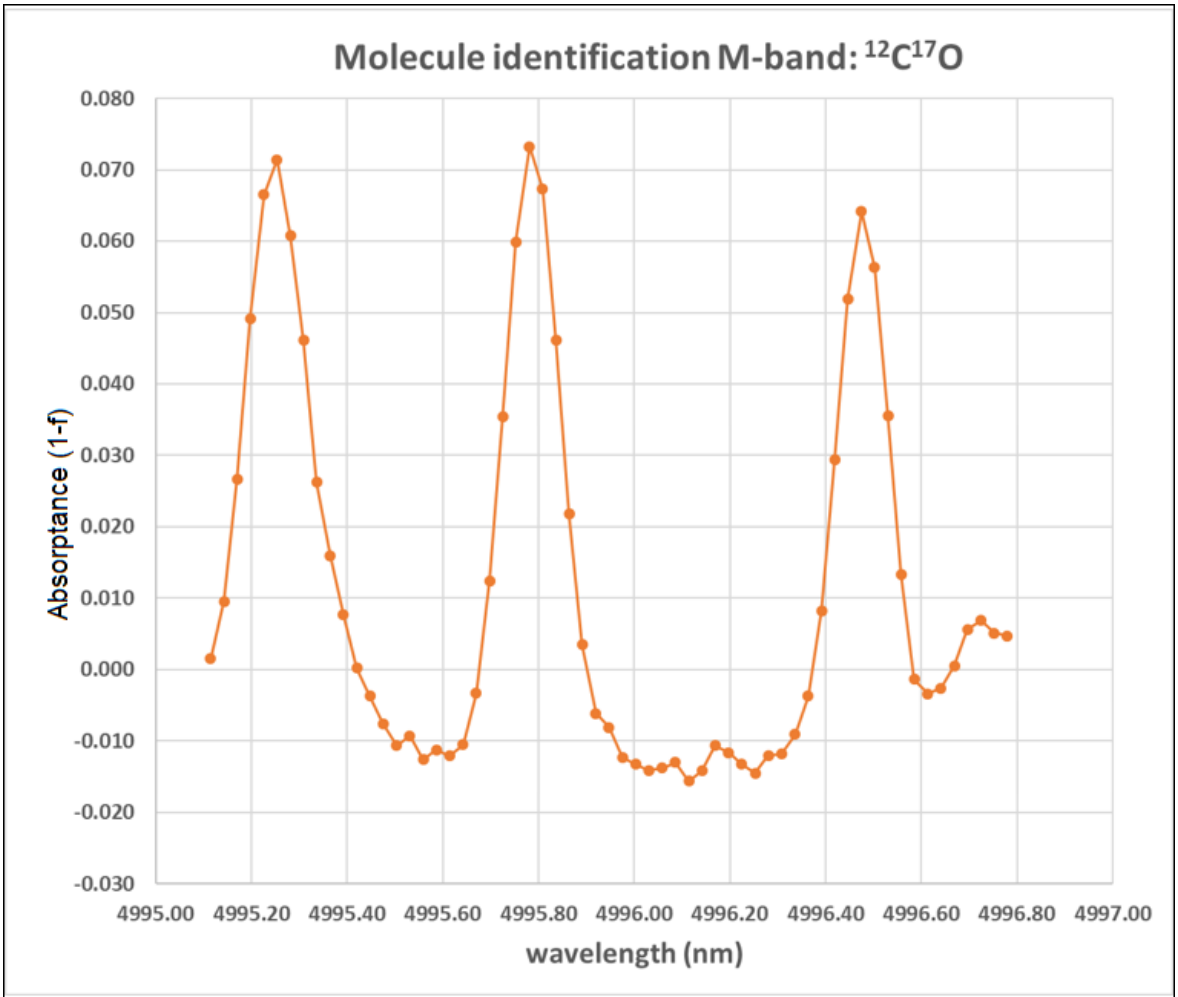

λ(nm)	Description	log gf	cdepth	EW (mA)	Match
4995.25	C^{17}O 3-2P16	-6.775	0.018	104	B
4995.40	'CO'	-5.358	0.010		C
4995.79	^{13}CO 9-8R38	-4.433	0.027	89	A
4996.48	CO 12-11R67	-2.138	0.078	72	A

Figure 75: Identification of $^{12}C^{17}O$

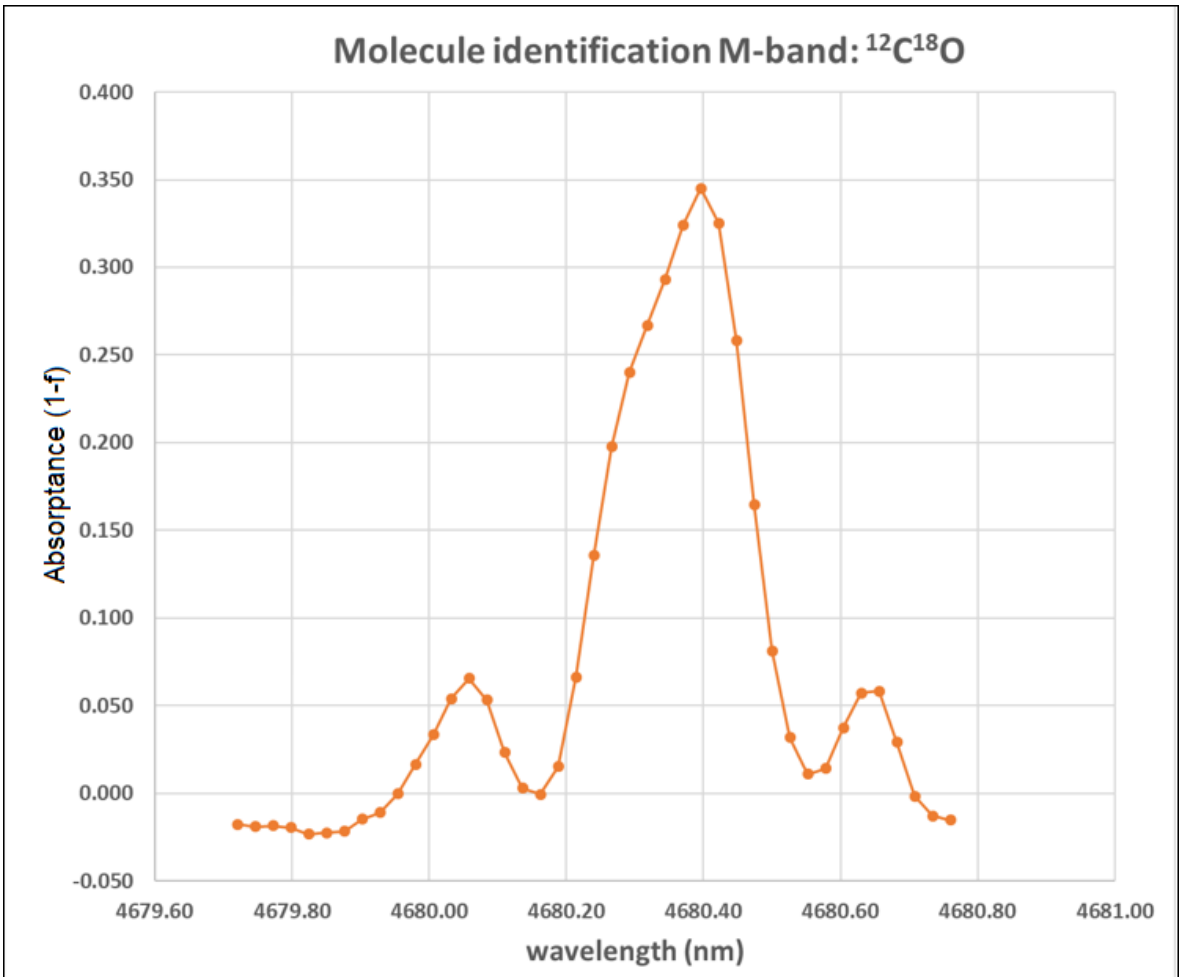

λ(nm)	Description	log gf	cdepth	EW (mA)	Match
4680.07	C^{18}O 1-0R12	-6.57	0.120	65	A
4680.26	CO 7-6R111	-2.091	0.027	32	B
4680.29	CO 7-6R61	-2.358	0.285	335	A
4680.40	^{13}CO 2-1R19	-5.333	0.273	321	A
4680.55	C^{18}O 5-4R57	-5.213	0.025	32	B
4680.65	C^{18}O 3-2R30	-5.712	0.114	55	B

Figure 76: Identification of $^{12}C^{18}O$

7.2.3 Identification of Unknowns

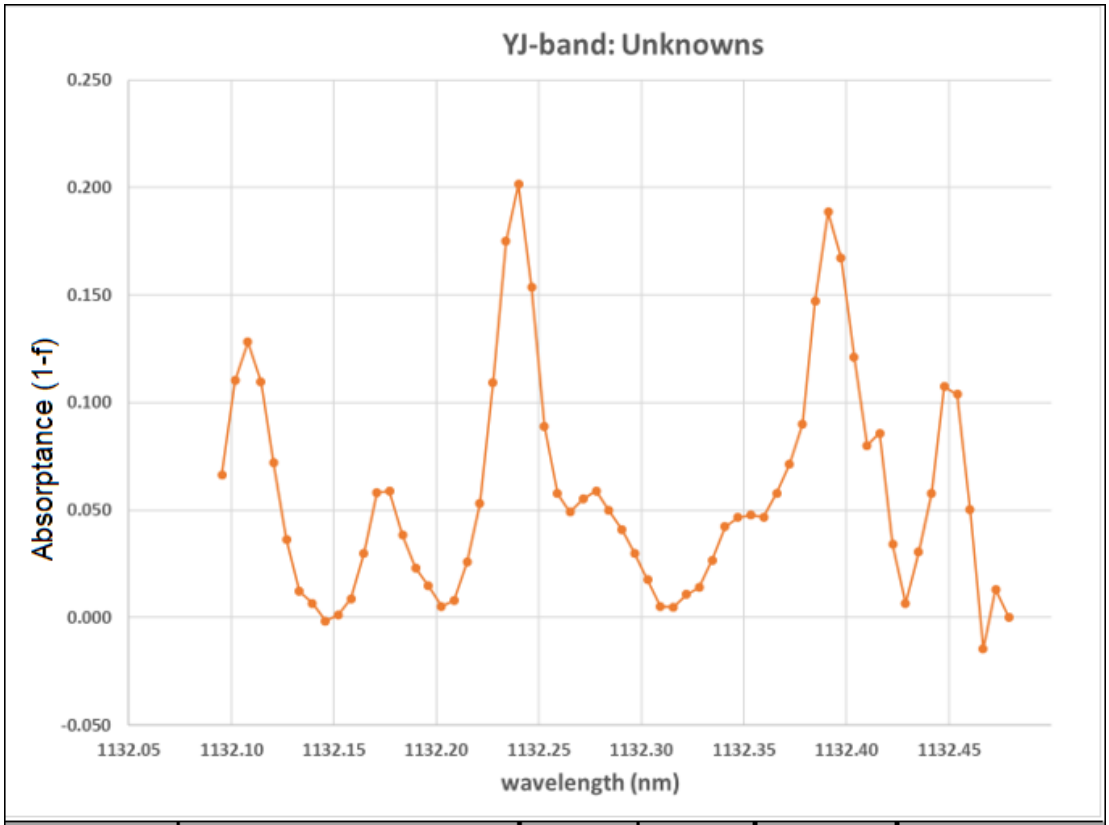

λ(nm)	Description	log gf	cdepth	EW (mA)	Match
1132.10	CN 1-1Q_{1}7.5	-2.951	0.009	6	B
1132.11	U			30	F
1132.14	'Co 1'	-1.437	0.081	0	C
1132.18	U (Co 1 shifted?)			14	F
1132.25	U			58	F
1132.26	'Fe 1'	-1.712	0.016	0	C
1132.28	CN 1-1R_{1}23.5	-2.633	0.013	12	B
1132.29	CN 1-1P_{2}8.5	-3.243	0.005	4	B
1132.36	CN 1-1Q_{2}8.5	-2.886	0.011	7	B
1132.39	CN 1-1R_{2}25.5	-2.605	0.013	8	B
1132.40	U			66	F
1132.44	'Fe 1'	-1.642	0.008	0	C
1132.45	U			22	F
1132.48	'Fe 1'	-1.877	0.027	0	C

Figure 77: Unknowns in YJ band

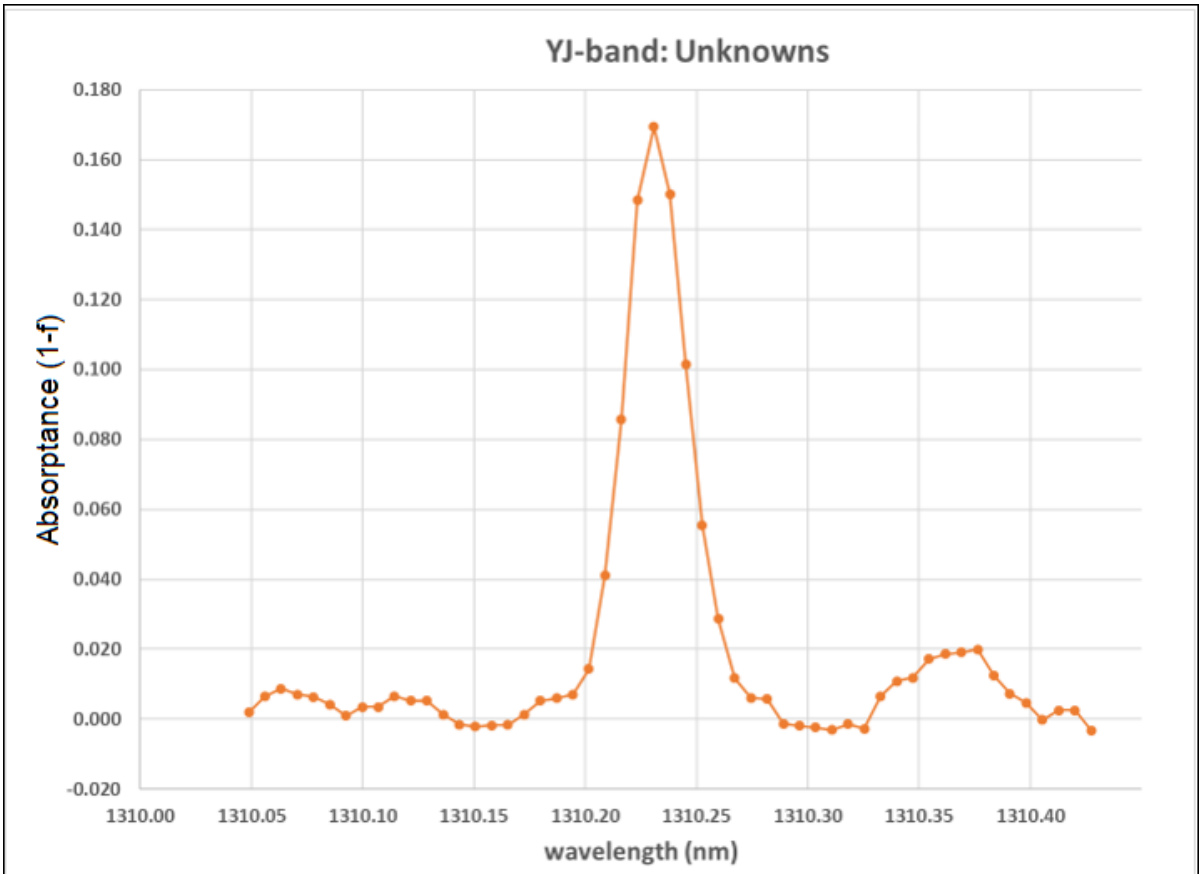

λ(nm)	Description	log gf	cdepth	EW (mA)	Match
1310.20	'Ni 1'	-1.781	0.007	0	C
1310.24	U('Fe 1')			61	E
1310.34	'Sc 1'	-1.323	0.009	3	C
1310.38	CN4-4Q_{1}50.5	-1.518	0.008	6	B

Figure 78: Unknowns in YJ band (continued)

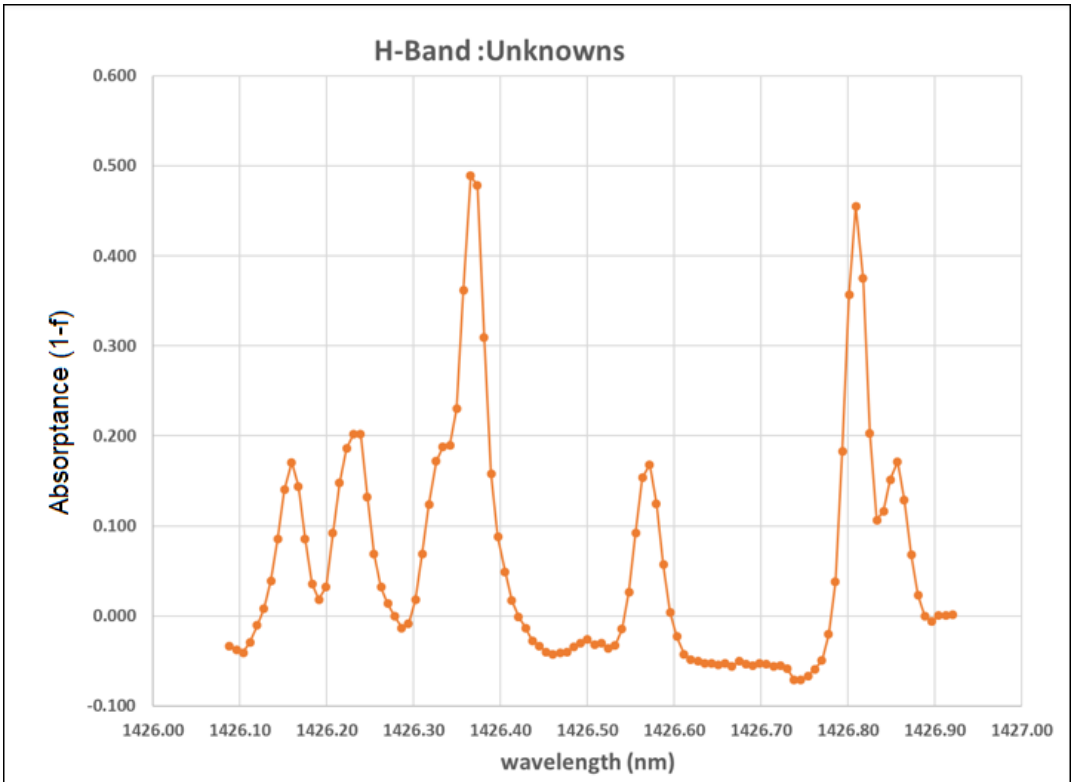

λ(nm)	Description	log gf	cdepth	EW (mA)	Match
1426.16	U			58	F
1426.21	CN 0-1R_{12}16.5	-2.751	0.019	10	B
1426.24	CN 0-1Q_{1}17.5	-1.702	0.152	78	B
1426.28	'Fe 1'	-1.905	0.024	0	C
1426.32	CN 0-1P_{1}9.5	-2.53	0.034	18	B
1426.34	'Ca 1'	-0.554	0.189	0	B
1426.34	CN 0-1P_{1}9.5	-2.427	0.042	22	B
1426.37	U			185	F
1426.38	'Ca 1'	-1.458	0.037	0	B
1426.39	'Fe 1'	-1.778	0.011	0	C
1426.40	'Fe 1'	-0.839	0.102	23	B
1426.42	'Co 1'	0.599	0.034	0	C
1426.57	CN 0-1R_{1}31.5	-1.692	0.110	50	B
1426.81	U			134	F
1426.86	CN 0-1R_{2}32.5	-1.684	0.104	54	B

Figure 79: Unknowns in HI band

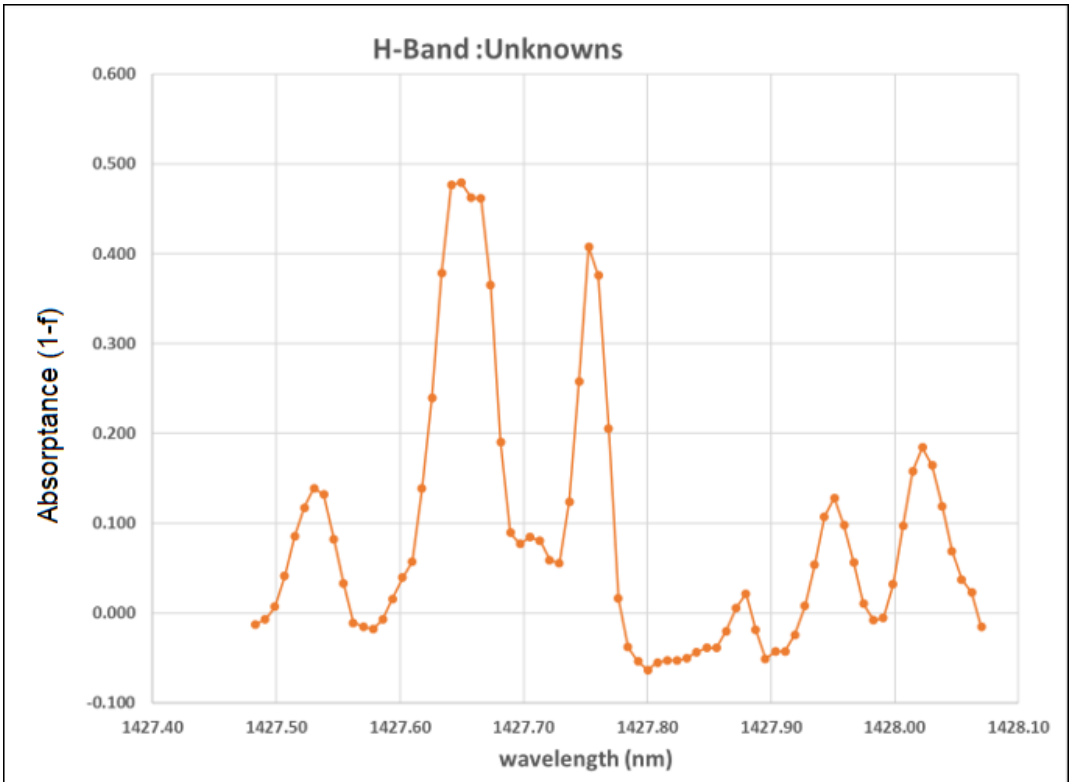

λ(nm)	Description	log gf	cdepth	EW (mA)	Match
1427.52	'Ni 1'	-1.269	0.009		C
1427.52	CN 0-1P_{1}10.5	-2.518	0.035	21	B
1427.54	CN 0-1Q_{1}18.5	-2.363	0.048	29	B
1427.65	U			258	F
1427.65	'Ni 1'	-0.225	0.032	0	B
1427.67	'P 1'	0	0.008	0	C
1427.72	CN 0-1P_{2}13.5	-2.175	0.067	35	B
1427.74	'Fe 1'	-1.954	0.013	0	C
1427.75	U			114	F
1427.83	'Fe 1'	-1.852	0.008	0	C
1427.88	U			0	F
1427.95	U			37	F
1427.96	'Fe 1'	-2.212	0.008	0	C
1428.02	U			68	F

Figure 80: Unknowns in H band (continued)

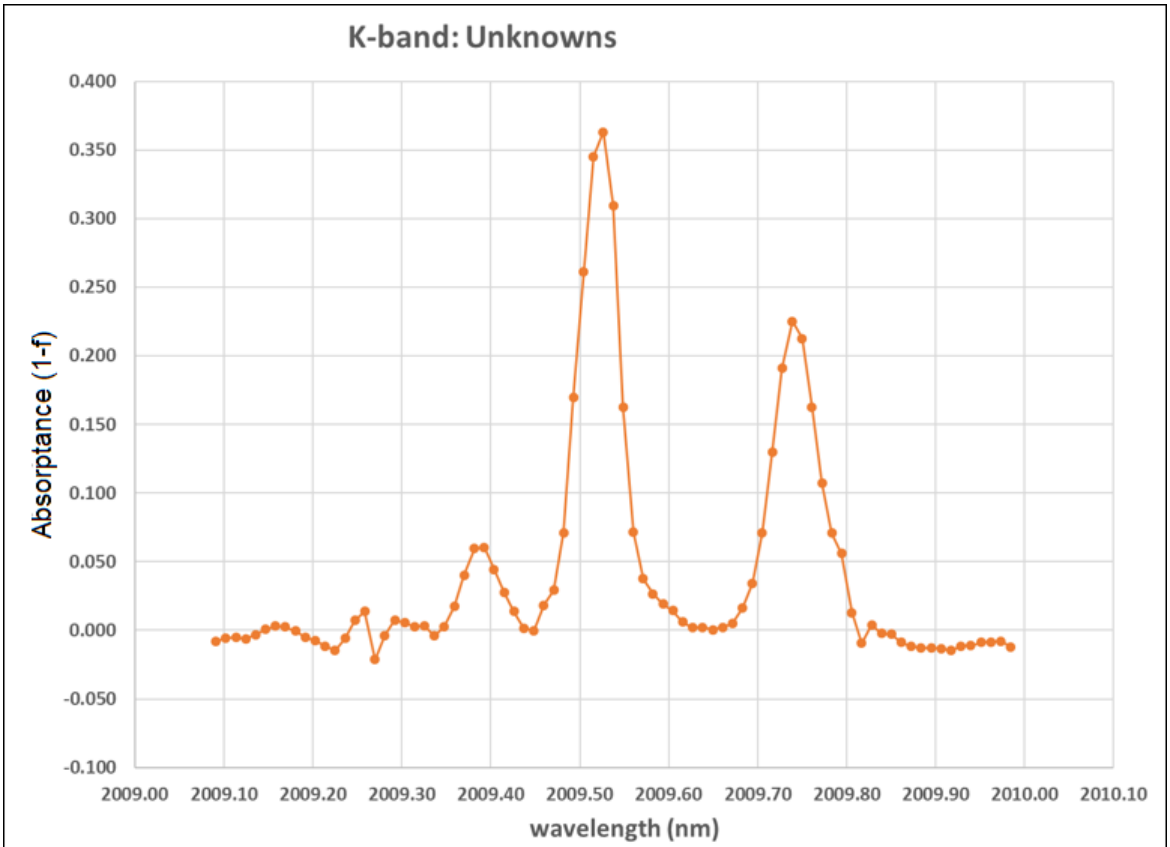

λ(nm)	Description	log gf	cdepth	EW (mA)	Match
2009.40	CN 0-2Q_{2}23.5	-2.253	0.043	30	A
2009.39	'Ti 1'	0.187	0.009	0	C
2009.53	U			213	F
2009.70	'Fe 1'	-1.674	0.026	0	C
2009.73	'Fe 1'	-0.862	0.085	0	B
2009.75	'Fe 1'	0.07	0.377	145	A

Figure 81: Unknowns in K band

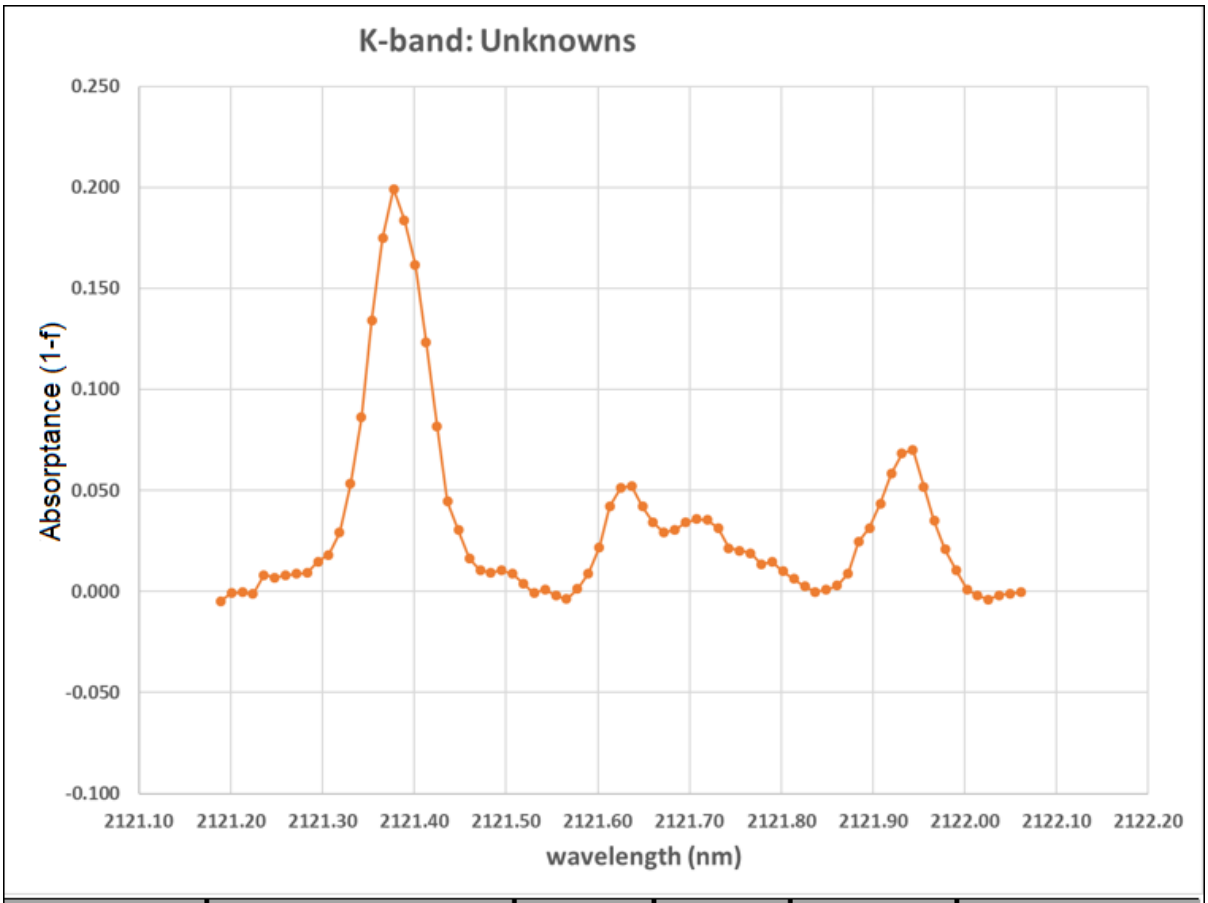

λ(nm)	Description	log gf	cdepth	EW (mA)	Match
2121.27	'Cr 1'	-2.854	0.009	0	C
2121.38	U+Al1?			163	E
2121.39	'Mg 1'	-2.036	0.064	0	B
2121.63	CN 0-2Q_{2}47.5	-1.924	0.029	33	A
2121.67	CN 0-2R_{1}60.5	-2.105	0.010	8	B
2121.73	'C 1'	-0.067	0.073	25	A
2121.95	'Mg 1'	-1.559	0.150	51	A

Figure 82: Unknowns in K band (continued)

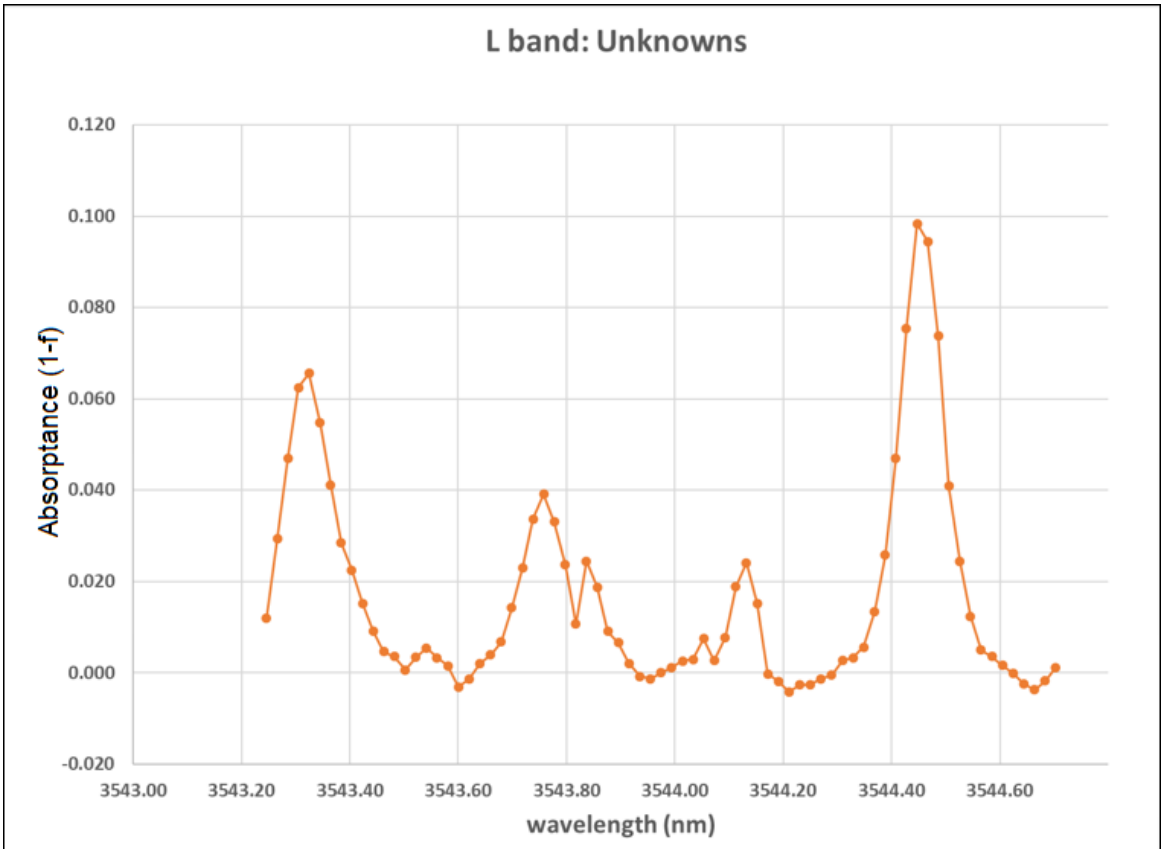

λ(nm)	Description	log gf	cdepth	EW (mA)	Match
3543.32	U			79	F
3543.43	'Fe 1'	-1.025	0.020		C
3543.76	U+Sc1?			37	F
3543.84	U			14	F
3544.13	U			13	F
3544.43	U			103	F

Figure 83: Unknowns in L band

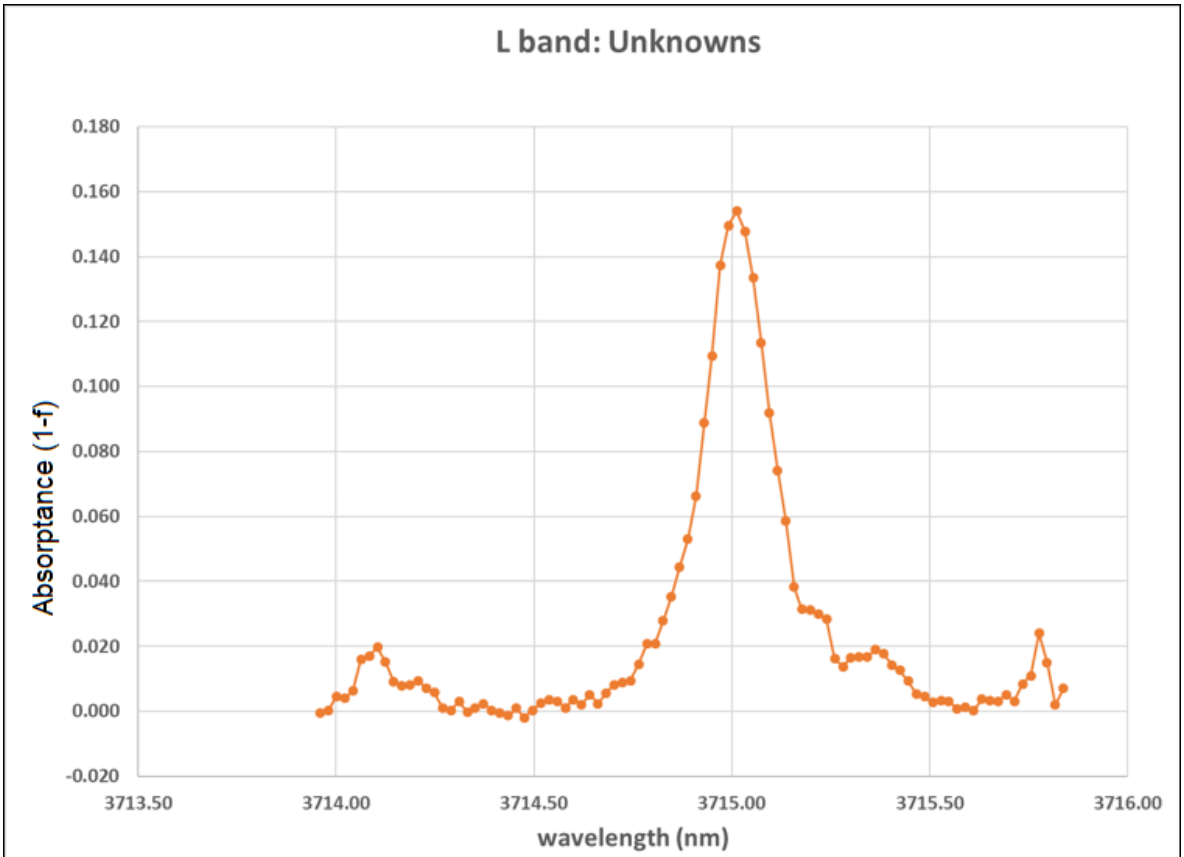

λ(nm)	Description	log gf	cdepth	EW (mA)	Match
3714.11	OH 4-3P_{1f}10.5	-4.041	0.012	20	A
3714.23	'Fe 1'	-1.993	0.007	6	B
3715.01	U+C1			364	E
3715.78	U			13	F

Figure 84: Unknowns in L band (continued)

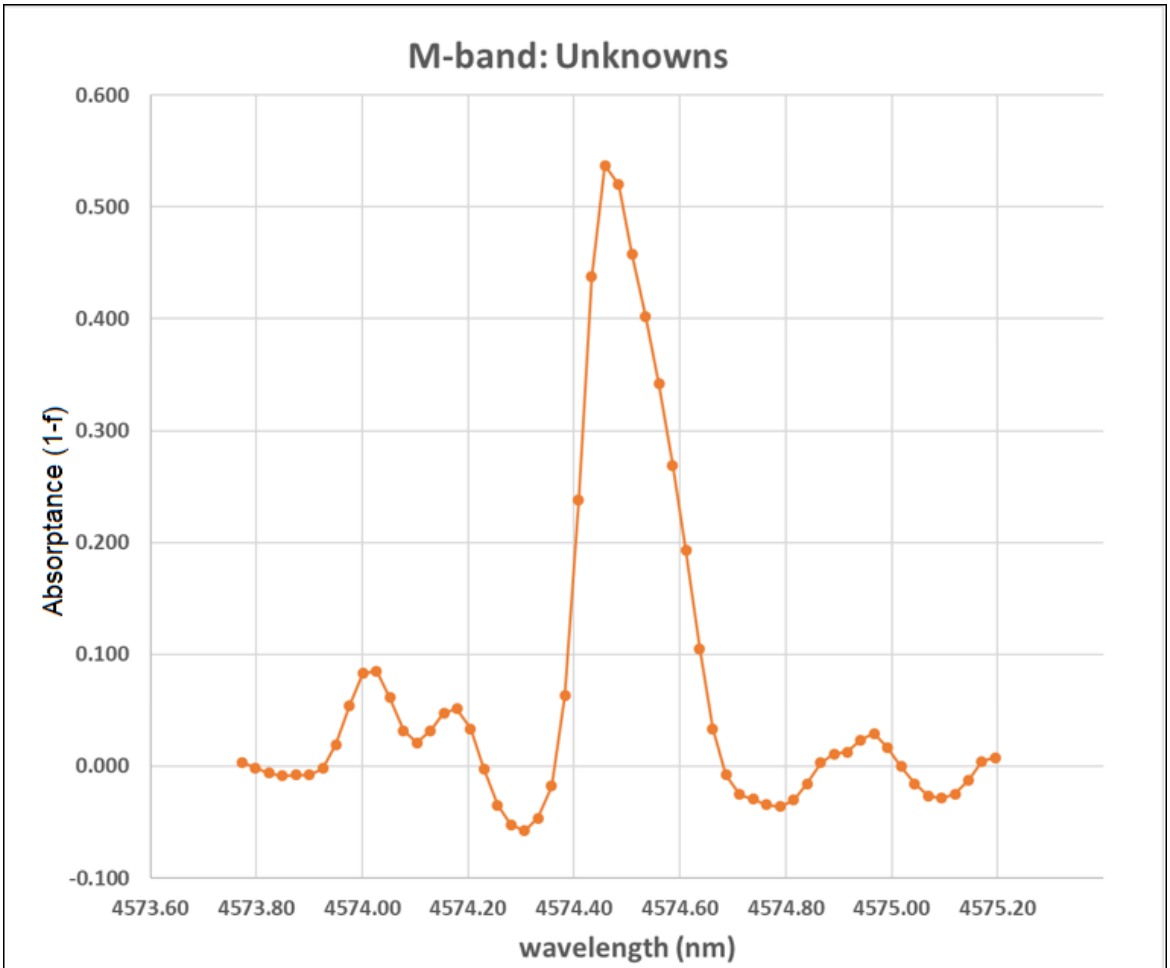

λ(nm)	Description	log gf	cdepth	EW (mA)	Match
4574.03	C^{18}O 1-0R29	-6.189	0.162	90	A
4574.20	C^{18}O 2-1R40	-5.75	0.134	47	B
4574.40	'Ca 1'	0.261	0.077	0	B
4574.44	'CO'	-5.137	0.008	0	C
4574.46	U			644	F
4574.54	^{13}CO 4-3R74	-4.431	0.066	49	B
4574.54	^{13}CO'	-2.181	0.028	21	B
4574.57	^{13}CO 2-1R38	-5.026	0.272	201	A
4574.98	C^{18}O 3-2R54	-5.443	0.068	24	A

Figure 85: Unknowns in M band

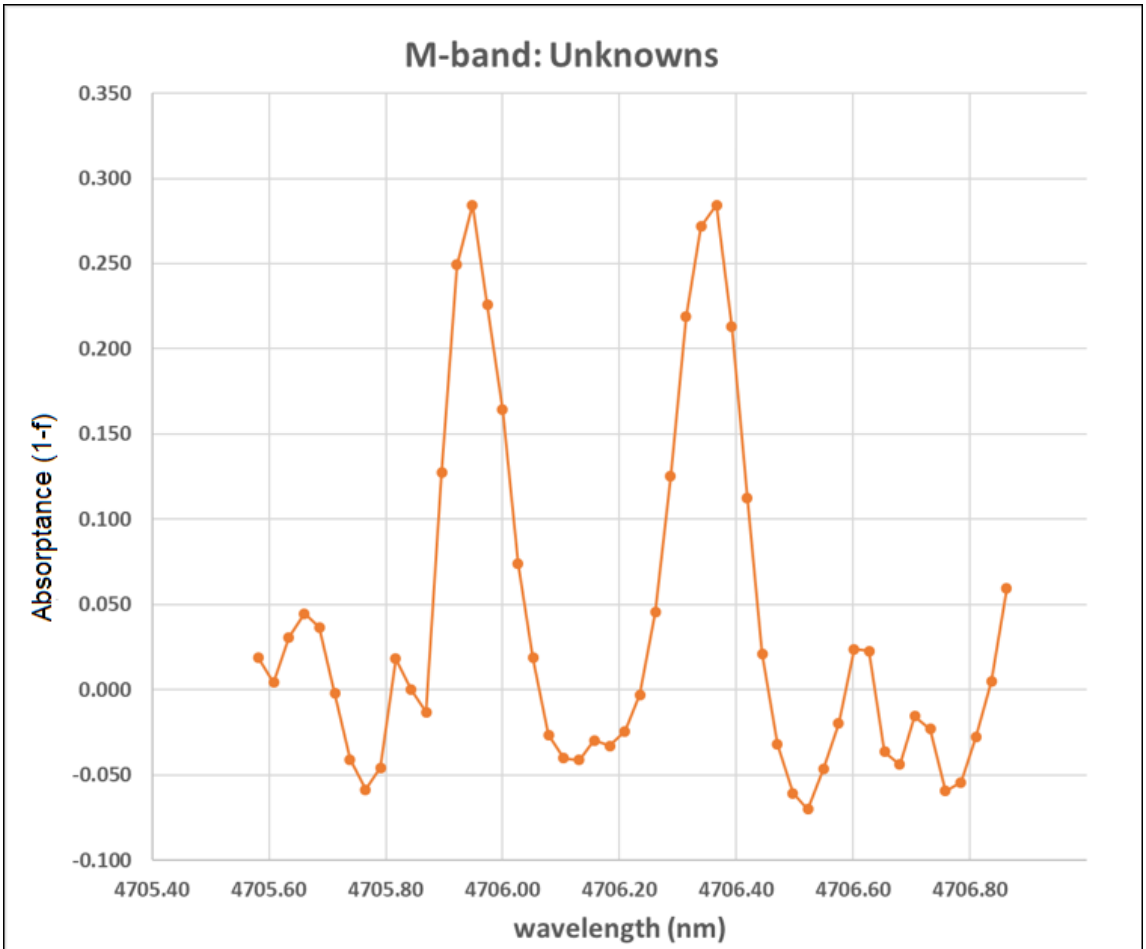

λ(nm)	Description	log gf	cdepth	EW (mA)	Match
4705.62	'CO'	-2.061	0.011	11	B
4705.68	C^{17}O 3-2R17	-6.689	0.023	24	B
4705.95	U			299	F
4706.16	C^{18}O 6-5R71	-5.042	0.007		C
4706.24	'Fe 1'	-1.108	0.024		C
4706.37	^{13}CO 3-2R24	-5.063	0.250	338	A

Figure 86: Unknowns in M band (continued)

7.2.4 Overlay spectra 10 Leo and Arcturus

The log gf and cdepth values refer to the VALD extract stellar model (castelli_ap00k2_T04750G30.krz with solar abundances, see Table 10).

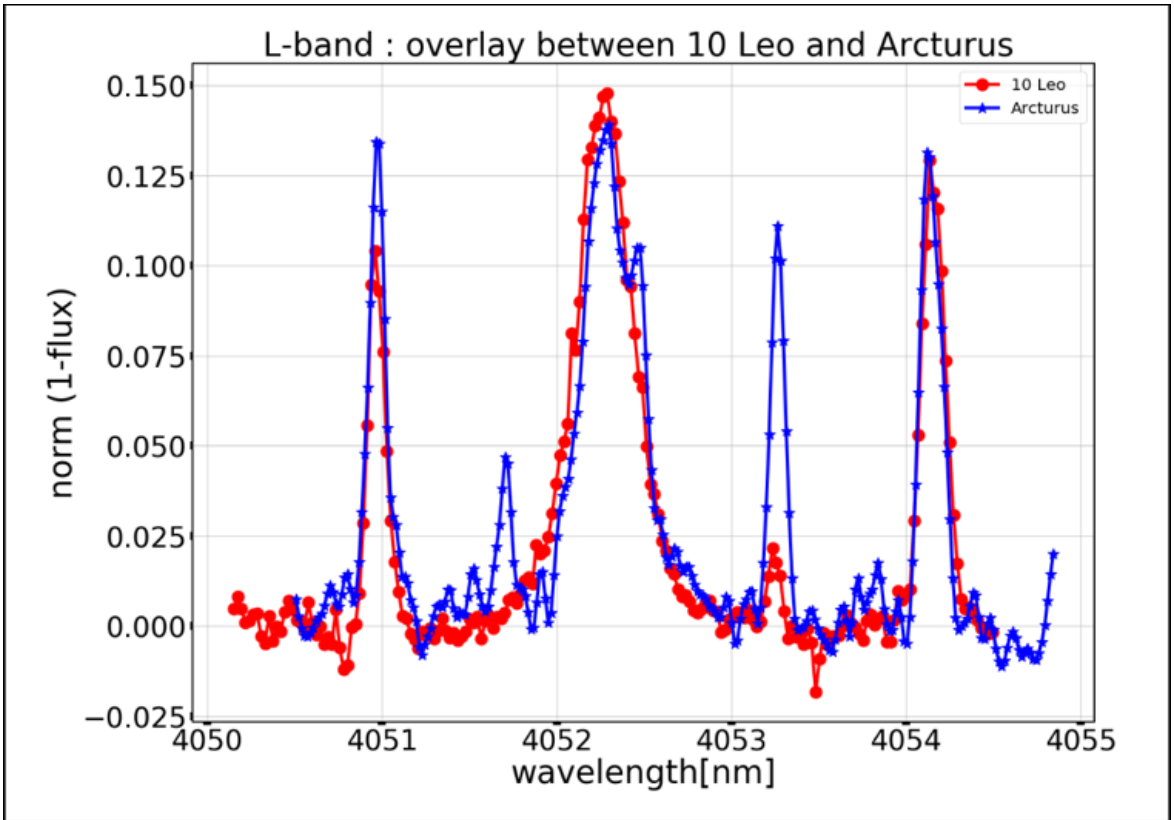

λ(nm)	Description	log gf	cdepth	EW (mA)	Match
4050.29	SiO 3-1R48			2	E
4050.47	SiO 2-0R16			3	E
4050.83	'Fe 1'	-0.802	0.012		C
4050.96	'Si 1'	0.085	0.145	130	A
4051.37	'Fe 1'	-0.405	0.028		C
4051.73	SiO 3-1R46			6	E
4052.00	'Si 1'	-1.115	0.011	7	B
4052.29	'H 1'	1.521	0.099	625	A
4052.47	SiO 3-1R45				G
4053.23	OH 4-3P_{2f}14.5	-3.751	0.010	18	A
4053.95	U			4	F
4054.14	'Si 1'	-0.171	0.171	213	A
4054.23	'Fe 1'	0.100	0.117		B

Figure 87: H I in 10 Leo and Arcturus

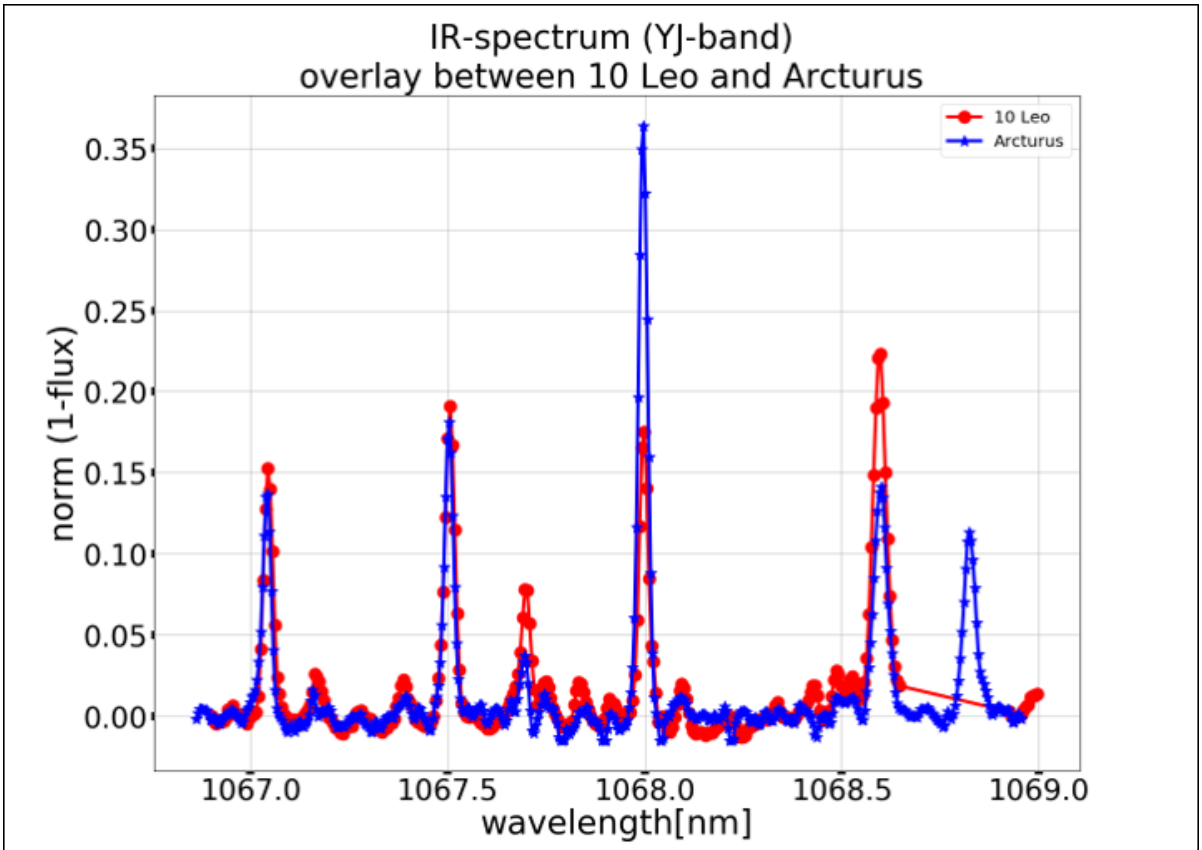

λ(nm)	Description	log gf	cdepth	EW (mA)	Match
1067.04	'Cr 1'	-1.481	0.283	29	A
1067.16	'Fe 1'	-0.962	0.035	7	B
1067.39	'Fe 1'	-1.064	0.031	6	B
1067.51	'Cr 1'	-1.354	0.325	53	A
1067.70	'Fe 1'	-0.466	0.098	21	B
1067.74	CN 2-1Q_{2}78.5	-0.975	0.014	8	A
1067.83	CN 3-2Q{21}78.5			5	F
1068.00	'Ti 1'	-2.522	0.381	52	A
1068.09	U			4	F
1068.49	CN 2-1Q_{1}79.5	-0.970	0.014	8	A
1068.60	'C 1'	0.079	0.161	93	A

Figure 88: C I in 10 Leo and Arcturus

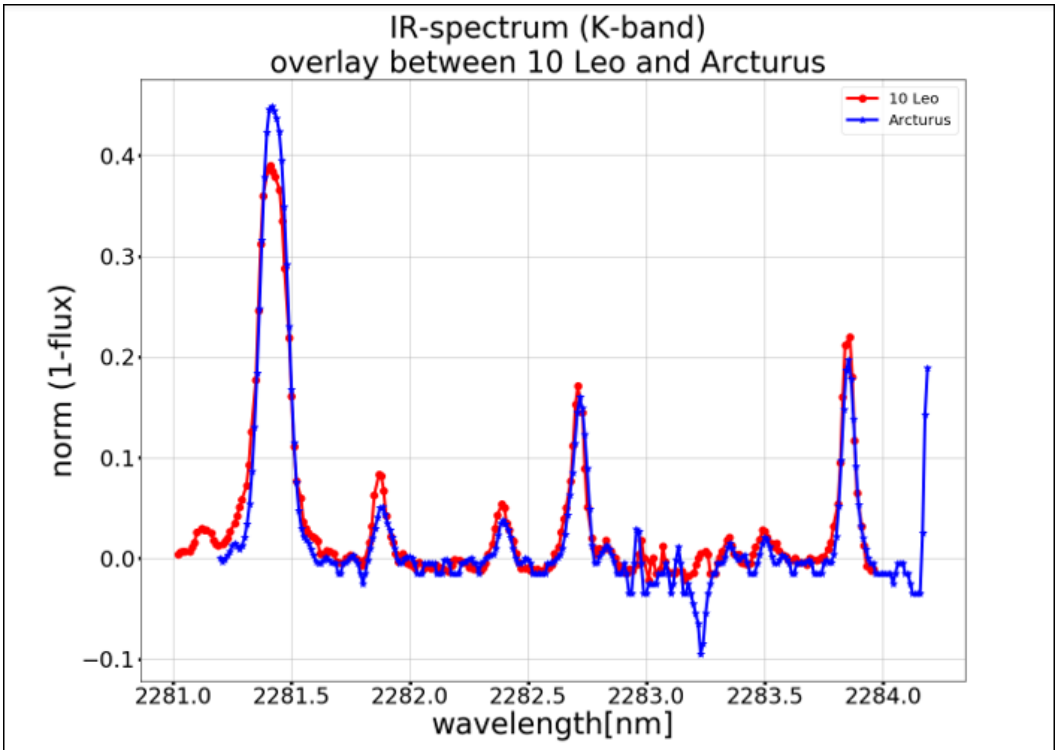

λ(nm)	Description	log gf	cdepth	EW (mA)	Match
2281.40	'Mg 1'	0.018	0.424		B
2281.40	'Mg 1'	-1.044	0.258		B
2281.40	'Mg 1'	-1.046	0.258		B
2281.40	'Mg 1'	-2.595	0.018		B
2281.43	'Mg 1'	-0.143	0.406	665	A
2281.43	'Mg 1'	-1.23	0.215		B
2281.45	'Mg 1'	-0.313	0.386		B
2281.88	'Fe 1'	-0.901	0.272	54	A
2282.39	CN 2-4Q_{1}42.5	-1.614	0.022	25	B
2282.43	**CN 0-2P_{2}56.5**	-2.158	0.009	10	B
2282.67	**CN 0-2Q_{1}67.5**	-1.767	0.011	9	B
2282.73	'Ca 1'	-0.396	0.310	113	A
2283.25	'Fe 1'	-1.646	0.047	2	B
2283.36	CN 2-4Q_{2}43.5	-1.614	0.020	8	B
2283.50	**CN 1-3Q_{1}56.5**	-1.57	0.020	16	B
2283.86	'Fe 1'	-1.269	0.366	152	A

Figure 89: Mg I in 10 Leo and Arcturus

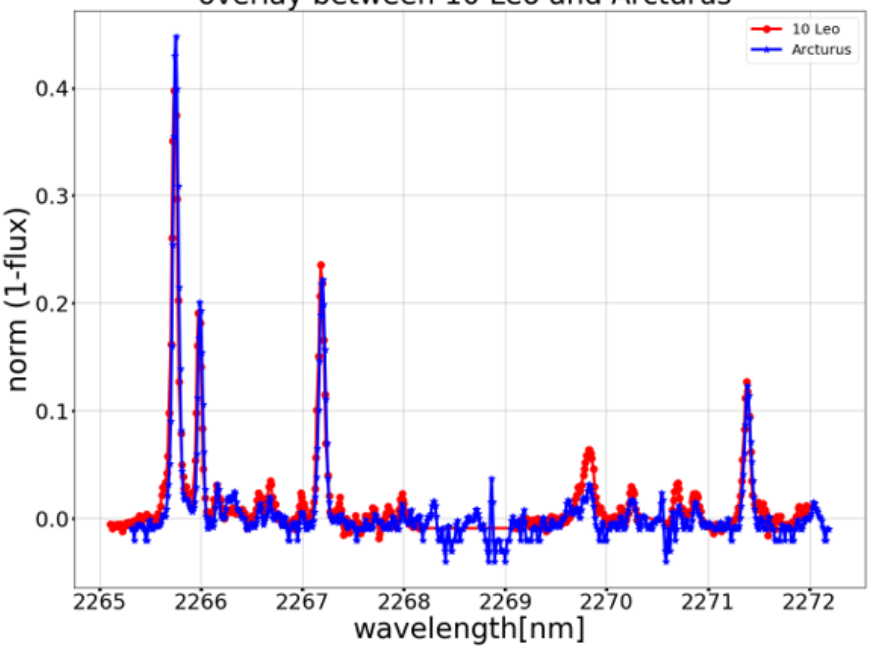

λ(nm)	Description	log gf	cdepth	EW (mA)	Match
2265.73	'Ca 1'	0.847	0.471	339	A
2265.97	'Ca 1'	-0.216	0.338	133	A
2266.15	'S 1'	-1.2	0.045	19	A
2266.31	'Sc 1'	-1.875	0.031	4	B
2266.56	**CN 0-2P_{1}55.5**	-2.169	0.011	10	B
2266.68	**CN 1-3Q_{1}54.5**	-1.587	0.022	19	B
2266.98	CN 2-4P_{2}31.5	-2.089	0.012	10	B
2267.18	'Si 1'	-0.68	0.277	183	A
2267.84	'Ni 1'	-1.159	0.067	4	B
2267.98	**CN 1-3P_{1}44.5**	-1.996	0.017	12	B
2269.77	'Si 1'	-1.56	0.047	68	B
2269.83	CN 2-4Q_{1}40.5	-1.636	0.024	25	B
2270.24	CN 2-4Q_{2}41.5	-1.636	0.022	16	B
2270.70	'Al 1'	-1.673	0.048	23	A
2270.90	**CN 1-3P_{2}44.5**			12	A
2271.39	'S 1'	0.44	0.231	95	A

Figure 90: Ca I in 10 Leo and Arcturus

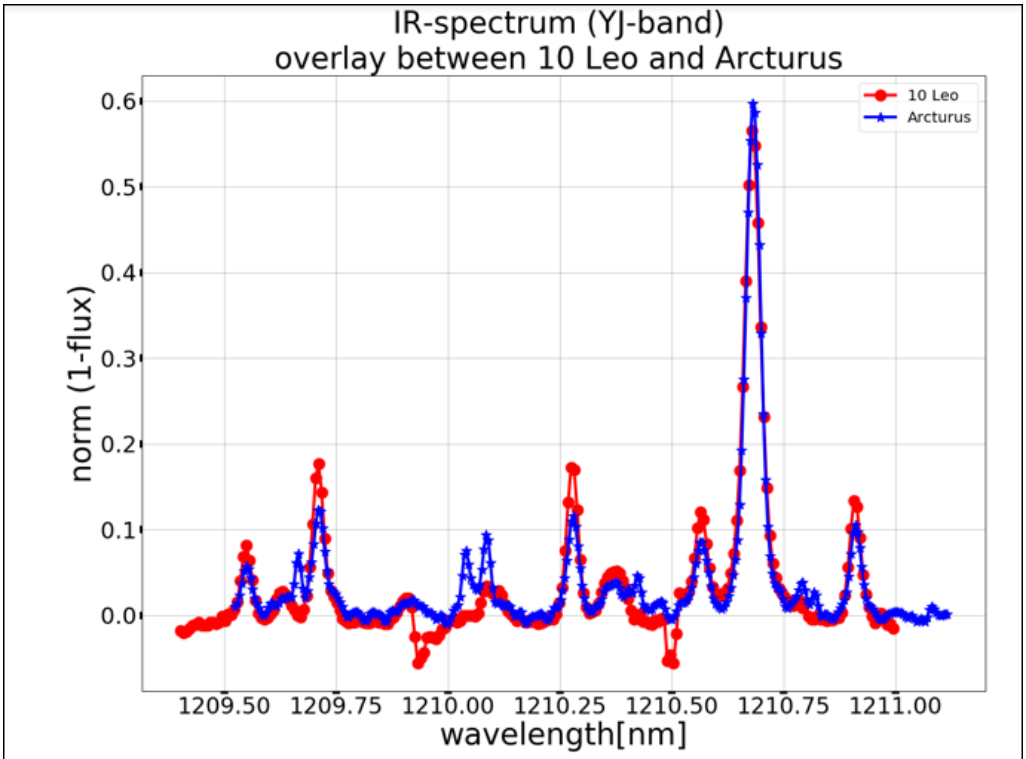

λ(nm)	Description	log gf	cdepth	EW (mA)	Match
1209.55	'Fe 1'	-2.369	0.011	23	E
1209.63	CN 3-3Q_{1}20.5	-2.140	0.013	6	B
1209.71	CN 0-0P_{1}59.5	-1.176	0.100	55	A
1210.09	Ce 2			9	F
1210.11	'Fe 1'	-2.599	0.024	5	B
1210.28	CN 0-0Q_{2}67.5	-0.807	0.110	55	A
1210.37	'Si 1'	-1.127	0.061	9	B
1210.38	'Si 1'	-2.154	0.033	5	B
1210.38	CN 3-3Q_{2}22.5	-2.094	0.013	9	B
1210.40	CN 3-3R_{1}32.5	-2.195	0.008	5	B
1210.52	CN 1-1Q_{2}56.5	-1.958	0.012	4	B
1210.56	'Si 1'	-0.694	0.143	47	A
1210.68	'Si 1'	-0.350	0.520	276	A
1210.91	'Ca 1'	-0.305	0.206	41	A
1210.94	'Ni 1'	-0.19	0.043		C

Figure 91: Si I in 10 Leo and Arcturus

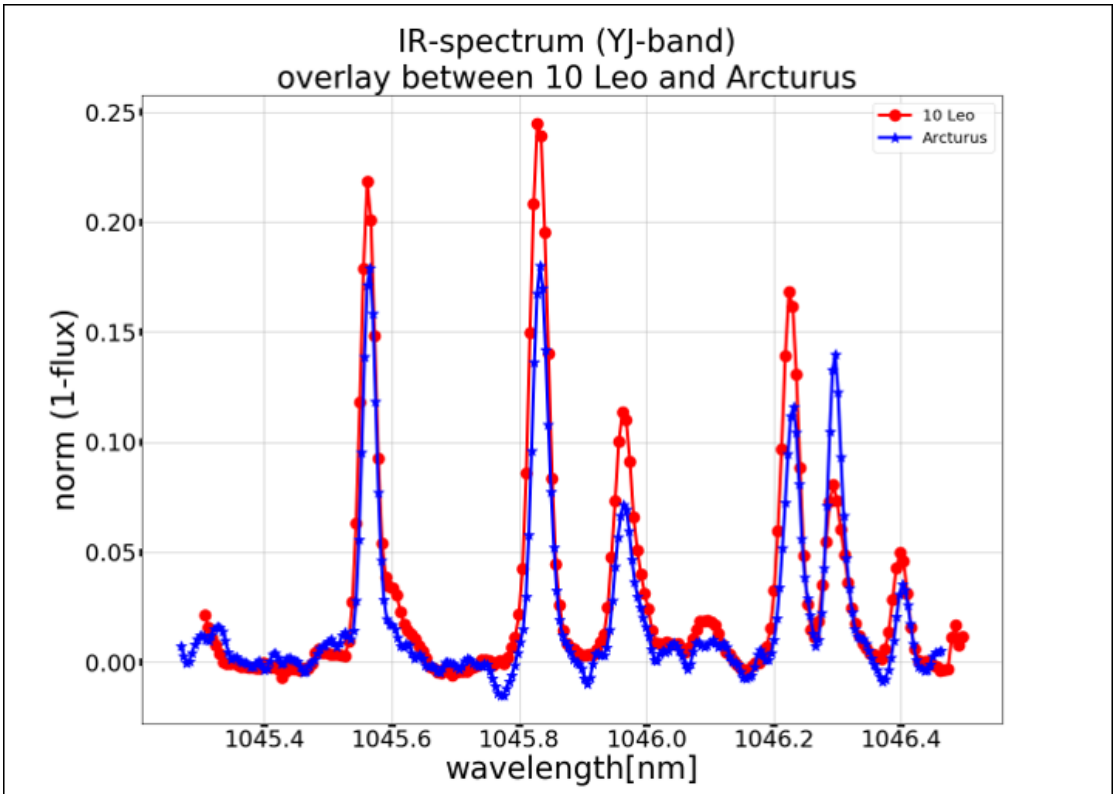

λ(nm)	Description	log gf	cdepth	EW (mA)	Match
1045.56	'Fe 1'			69	E
1045.60	'Fe 1'	-2.05	0.021	9	B
1045.83	'S 1'	0.250	0.223	70	A
1045.83	'Fe 1'	-0.908	0.195	20	B
1045.96	CN 2-1R_{2}80.5	-1.258	0.007	4	B
1045.96	'S 1'	-0.447	0.115	40	A
1045.98	'Fe 1'	-2.064	0.018	5	B
1046.08	CN 3-2Q_{1}62.5	-1.482	0.011	6	B
1046.10	'Fe 1'	-1.752	0.033	2	B
1046.22	'S 1'	0.030	0.187	58	A
1046.29	'Ti 1'	-1.399	0.146	21	A
1046.31	CN 2-1P_{2}64.5	-1.373	0.019	11	B
1046.40	CN 1-0P_{2}73.5	-1.172	0.026	14	A

Figure 92: S I in 10 Leo and Arcturus

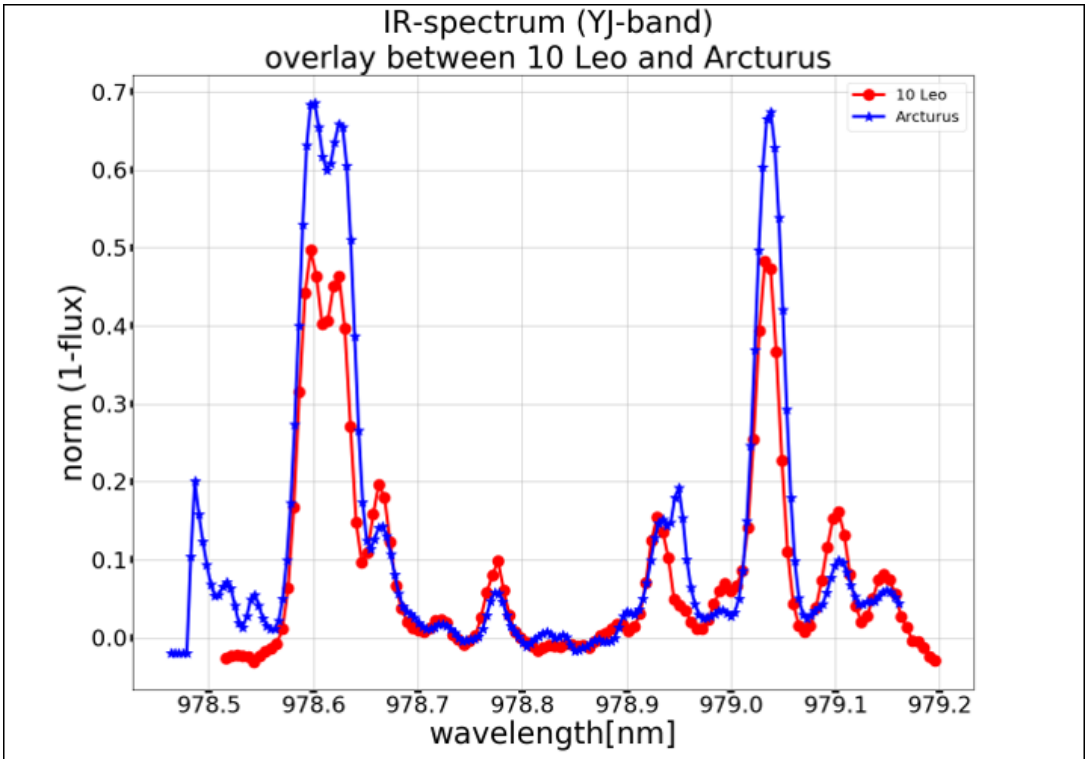

λ(nm)	Description	log gf	cdepth	EW (mA)	Match
978.60	'Ti 1'	-1.428	0.634	130	A
978.62	'Ti 1'	-1.617	0.605	125	A
978.66	'Fe 1'	-1.212	0.236	45	A
978.72	'Ca 1'	-1.104	0.039	5	B
978.78	CN 1-0R_{2}66.5	-1.199	0.043	20	A
978.93	'Fe 1'	-1.676	0.244	35	A
978.96	CN 3-2R_{2}34.5	-2.036	0.015	8	B
978.99	CN 3-2Q_{1}24.5	-1.915	0.028	10	B
979.00	CN 3-2Q{12}16.5	-2.883	0.005	2	B
979.01	CN 3-2P_{1}17.5	-2.436	0.011	4	B
979.03	'Ti 1'	-1.444	0.634	94	A
979.04	CN 1-0Q_{1}58.5	-0.964	0.129	47	B
979.09	'Fe 1'	-2.146	0.047	15	B
979.10	CN 2-1Q_{2}44.5	-1.229	0.089	37	A

Figure 93: Ti I in 10 Leo and Arcturus

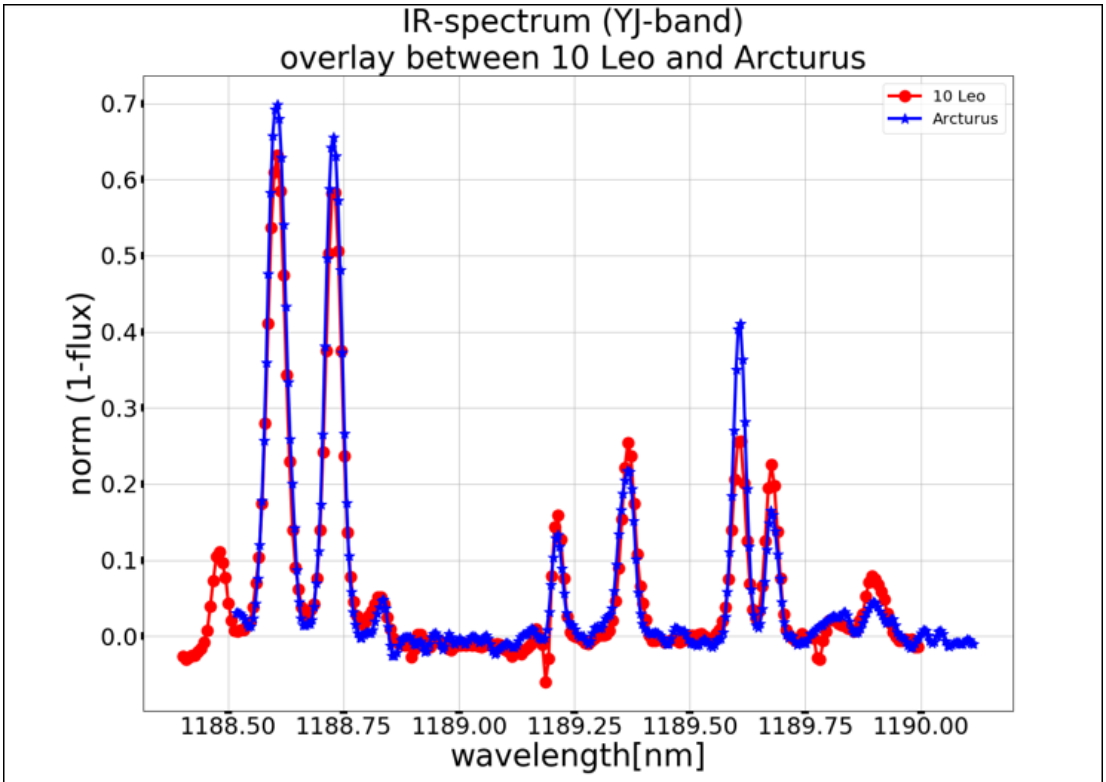

λ(nm)	Description	log gf	cdepth	EW (mA)	Match
1188.61	'Fe 1'	-1.668	0.738	325	A
1188.65	'Ca 1'	-1.332	0.024		C
1188.73	'Fe 1'	-2.083	0.689	267	A
1188.82	'Si 1'	-1.581	0.024	20	A
1189.21	CN 0-0P_{1}53.5	-1.225	0.125	41	A
1189.36	CN 1-1Q_{1}49.5?	-2.018	0.017	11	B
1189.37	'Fe 1'	-0.544	0.261	33	A
1189.37	'Si 1'	-2.222	0.192	51	B
1189.41	'Ca 1'	-1.170	0.033		C
1189.61	'Ti 1'	-1.730	0.401	73	A
1189.62	'C 1'	-0.277	0.052	18	B
1189.68	CN 0-0Q_{2}61.5	-0.848	0.147	74	A
1189.82	'Co 1'	-0.889	0.177	7	B
1189.89	'C 1'	-0.008	0.067	38	A

Figure 94: Fe I in 10 Leo and Arcturus

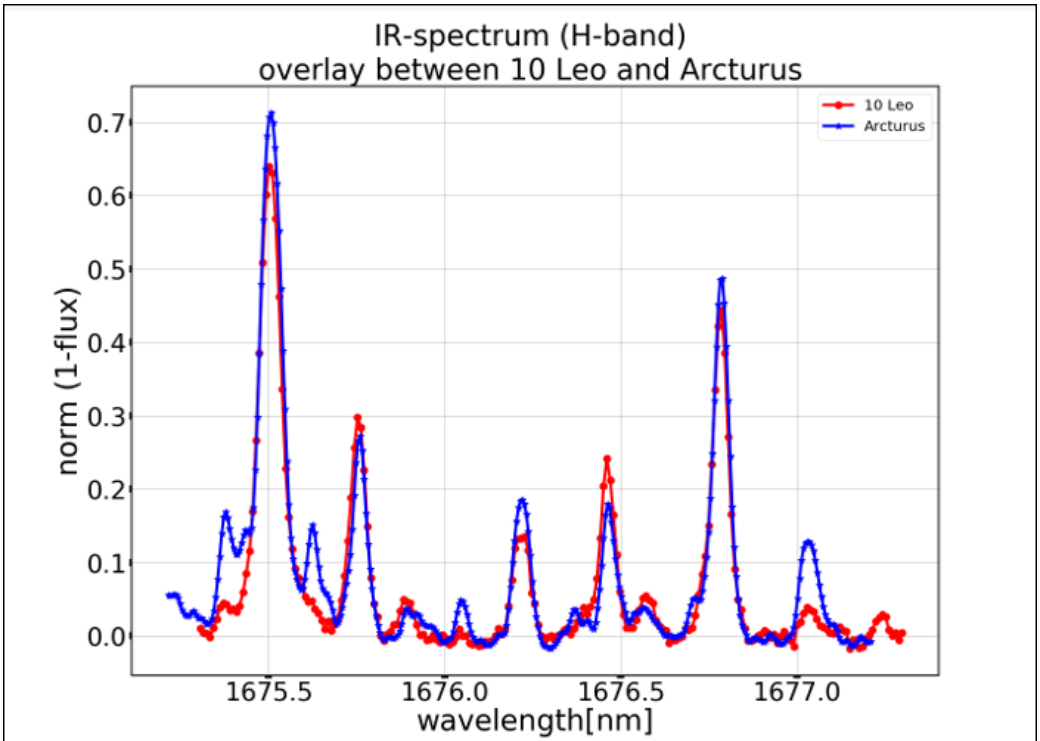

λ(nm)	Description	log gf	cdepth	EW (mA)	Match
1675.37	OH 4-2P_{1e}8.5	-4.683	0.018	7	A
1675.49	'Fe 1'	-1.635	0.036	9	B
1675.50	'Al 1'	0.408	0.618	520	A
1675.59	'Fe 1'	-1.935	0.054	17	B
1675.63	OH 4-2P_{1f}8.5	-4.683	0.018	7	A
1675.75	'Fe 1'	0.407	0.495	173	A
1675.88	CN 1-2P_{1}63.5	-1.456	0.036	24	A
1676.04	CO 8-5R63	-5.372	0.009		D
1676.23	'Co 1'	-0.923	0.440	82	B
1676.46	Fe1			122	E
1676.57	'Ni 1'	-0.307	0.150	29	A
1676.74	CN 0-1P_{1}72.5	-1.349	0.040	25	B
1676.79	'Al 1'	-0.55	0.549	241	A
1677.03	CO 8-5R64	-6.642	0.012	7	B
1677.04	CO 7-4P16	-5.360	0.011	7	B
1677.05	CO 6-3P29	-6.719	0.012	7	B

Figure 95: Co I in 10 Leo and Arcturus

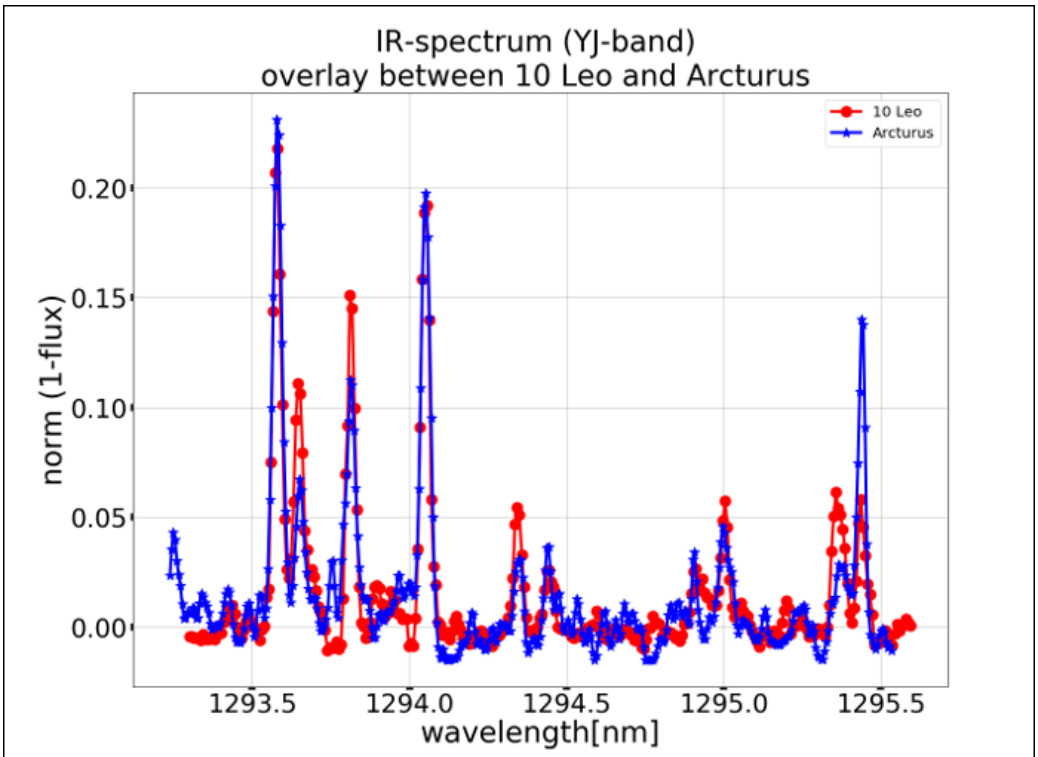

λ(nm)	Description	log gf	cdepth	EW (mA)	Match
1293.58	'Ni 1'	-2.523	0.414	70	A
1293.59	CN 4-4P_{2}36.5	-1.983	0.006	4	B
1293.65	'Fe 1'	-1.548	0.206	43	A
1293.69	CN 3-3P_{2}49.5	-2.037	0.006	4	B
1293.82	'Fe 1'	-0.948	0.243	46	A
1293.90	CN 4-4Q_{2}44.5	-1.575	0.011	6	B
1294.06	'Cr 1'	-1.896	0.320	66	A
1294.34	CN 0-0Q_{2}86.5	-0.697	0.032	17	A
1294.44	'Si 1'	-1.282	0.050	4	A
1294.45	CN 3-3Q_{1}58.5	-1.649	0.007	5	B
1294.91	U			8	F
1295.00	U			18	F
1295.06	'Cr 1'	-2.462	0.009	4	B
1295.36	CN 0-0Q_{1}87.5	-0.692	0.032	23	A
1295.44	'Ti 1'	-0.569	0.059	18	A

Figure 96: Ni I in 10 Leo and Arcturus

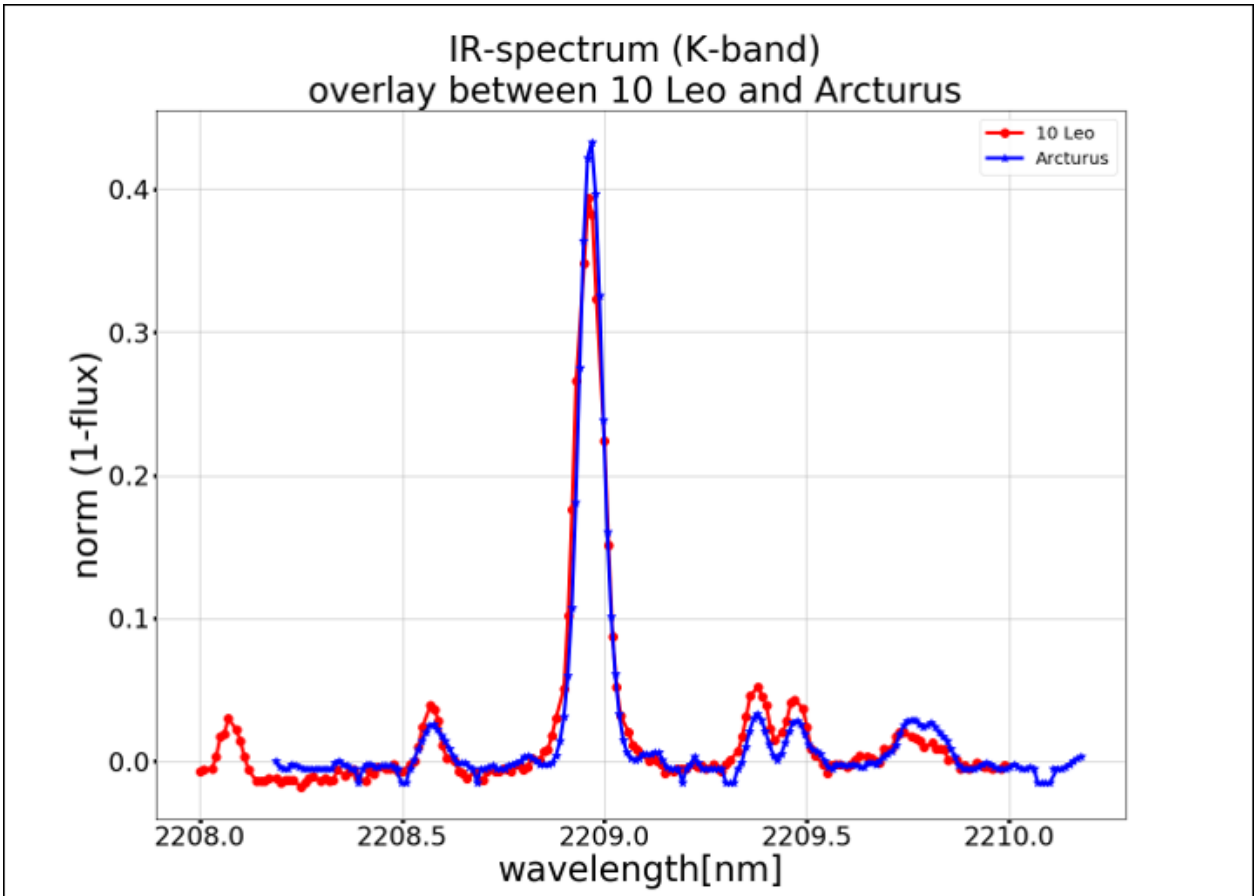

λ(nm)	Description	log gf	cdepth	EW (mA)	Match
2208.57	'Fe 1'	-1.404	0.138	19	A
2208.96	'Na 1'	-0.013	0.485	331	A
2209.38	**CN 1-3Q_{2}46.5**	-1.658	0.029	32	A
2209.41	'Fe 1'	-1.685	0.049		C
2209.47	CN 2-4Q_{1}28.5	-1.801	0.025	27	B
2209.65	'Ca 1'	-1.528	0.046		C
2209.73	CN 2-4P_{2}21.5	-2.29	0.011	9	B
2209.74	'V 1'	-0.754	0.123	12	A

Figure 97: Na I in 10 Leo and Arcturus

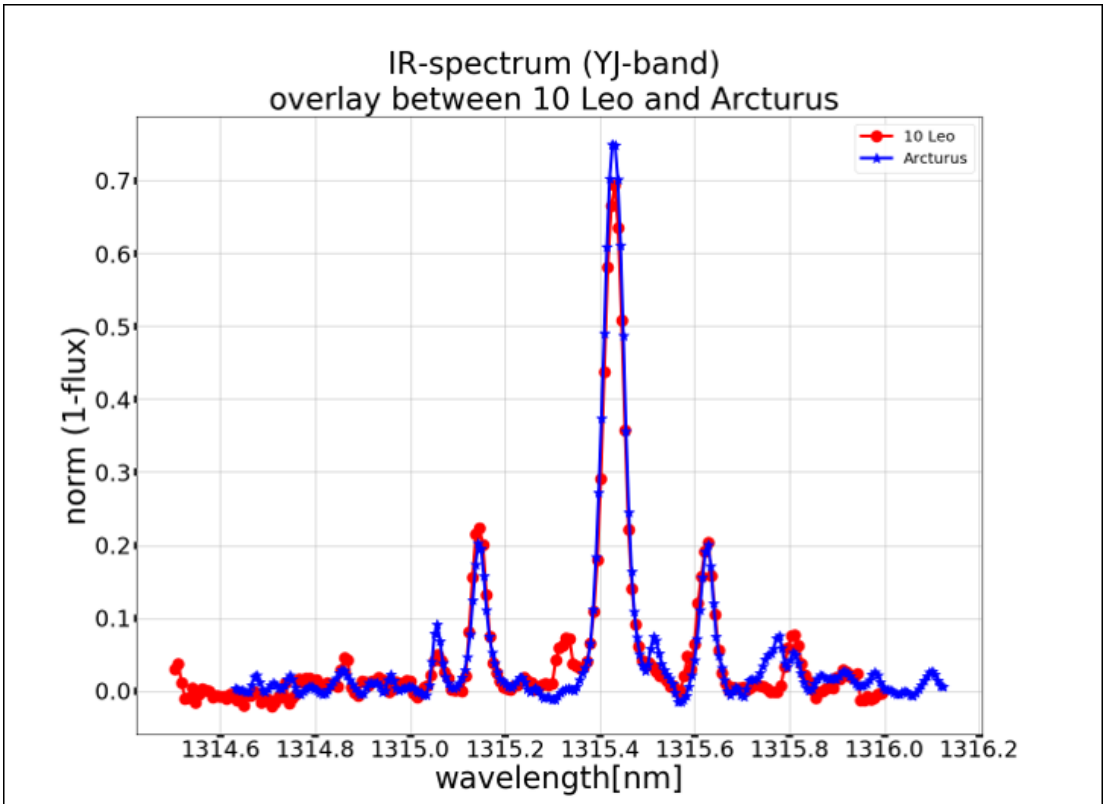

λ(nm)	Description	log gf	cdepth	EW (mA)	Match
1314.86	'Fe 1'	-3.296	0.068	10	B
1315.06	CN 0-0P_{1}82.5	-1.028	0.027	15	B
1315.15	'Fe 1'	-0.814	0.282	86	A
1315.24	CN 4-4Q_{2}51.5	-1.509	0.009		B
1315.33	CN 4-4P_{2}43.5	-1.9	0.007	31	B
1315.34	U				F
1315.41	'Zn 1'	0.121	0.051		B
1315.43	'Al 1'	-0.030	0.579	377	A
1315.52	U			18	F
1315.58	U				F
1315.63	'Si 1'	-2.504	0.211	80	A
1315.81	'Si 1'	-0.997	0.121	28	B
1315.91	U			9	F

Figure 98: Al I in 10 Leo and Arcturus

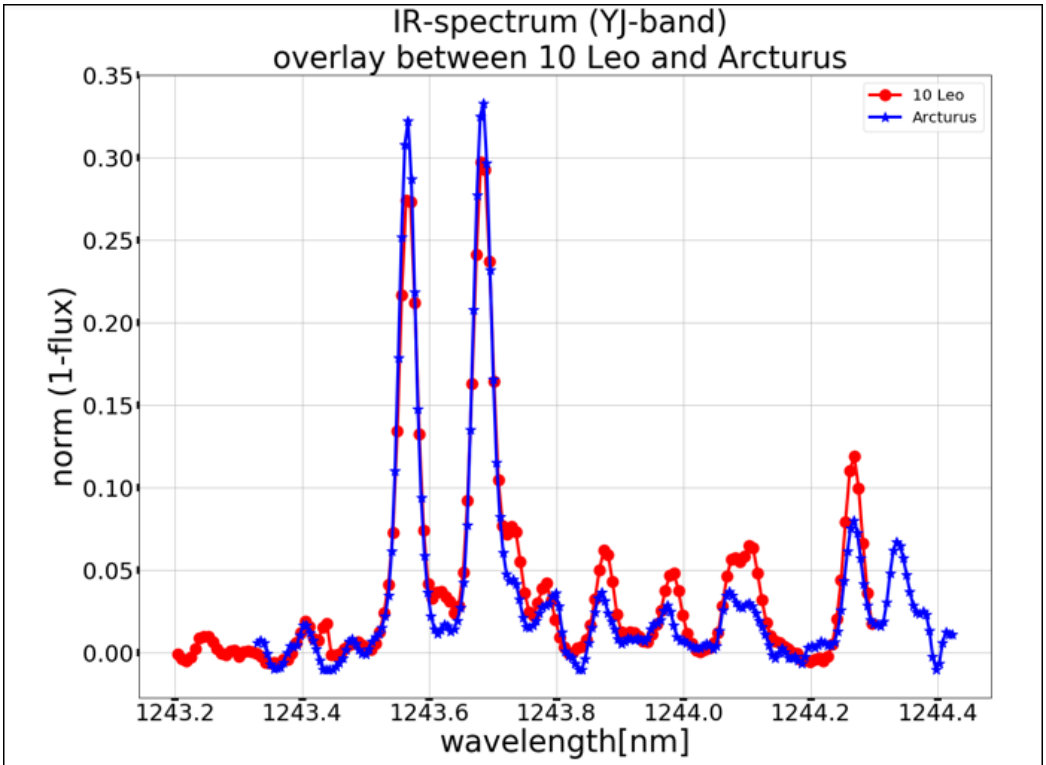

λ(nm)	Description	log gf	cdepth	EW (mA)	Match
1243.40	CN 4-4Q_{2}18.5	-1.994	0.010	5	B
1243.49	CN 3-3R_{2}50.5	-2.004	0.005	2	B
1243.57	'K 1'	-0.439	0.323	107	A
1243.62	'Fe 1'	-1.239	0.092	9	B
1243.68	'Mg 1'	-0.967	0.354	127	A
1243.73	'Ca 1'	-0.066	0.136	25	B
1243.78	CN 4-4Q_{1}16.5	-2.053	0.010	12	B
1243.87	CN 4-4R_{1}28.5	-2.056	0.008	16	F
1243.92	CN 4-4R_{2}29.5	-2.048	0.007	4	B
1243.94	'Ni 1'	0.077	0.070		C
1243.97	CN 1-1P_{1}58.5	-2.257	0.007	5	B
1243.99	CN 4-4P_{1}9.5			10	F
1244.08	U			18	F
1244.10	U			25	F
1244.27	CN 0-0P_{2}67.5	-1.117	0.063	33	A

Figure 99: K I in 10 Leo and Arcturus

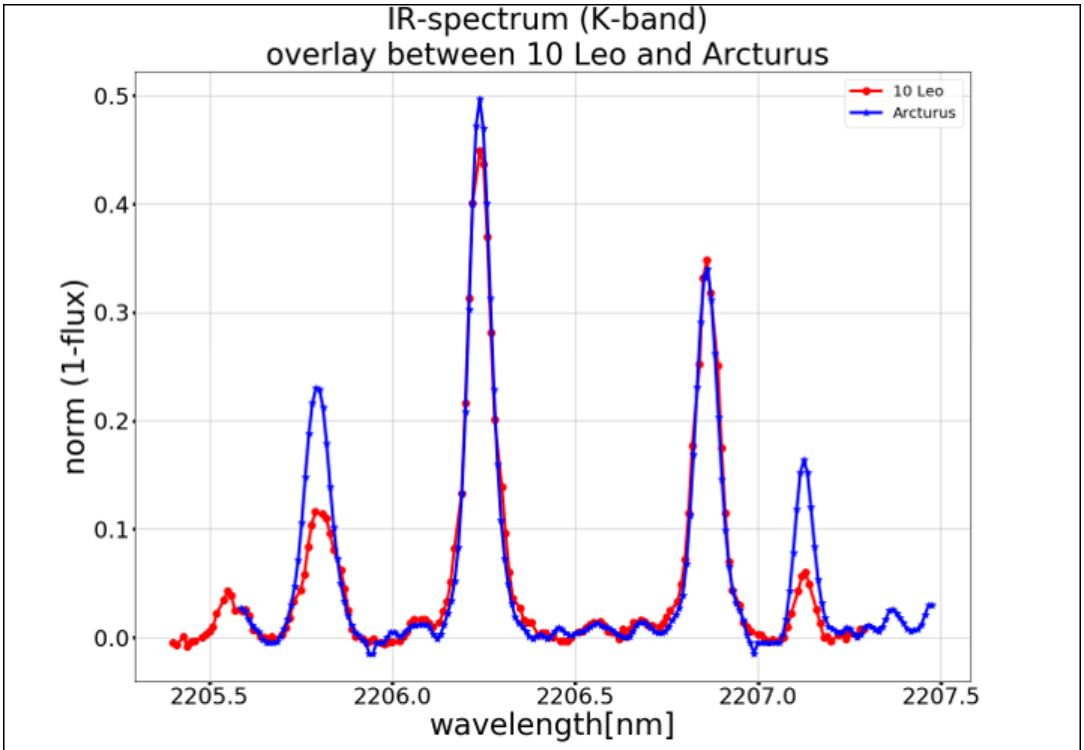

λ(nm)	Description	log gf	cdepth	EW (mA)	Match
2205.73	CN 2-4R_{2}42.5	-1.912	0.011	9	B
2205.77	'Fe 1'	-1.720	0.011		C
2205.78	'Fe 1'	-2.100	0.019		C
2205.79	'Sc 1'	-0.838	0.227	109	A
2205.81	'Si 1'	-2.170	0.014		C
2205.83	'Ni 1'	-1.422	0.064	6	B
2206.06	**CN 1-3R_{2}58.5**	-1.846	0.009	11	B
2206.24	'Na 1'	0.287	0.505	395	A
2206.28	CN 2-4Q_{2}29.5	-1.800	0.026	25	B
2206.53	'Na 1'	-1.674	0.014		C
2206.55	'Fe 1'	-2.775	0.024	2	B
2206.57	CN 2-4P_{1}18.5	-2.363	0.009	8	B
2206.68	CN 2-4R_{1}41.5	-1.908	0.012	8	B
2206.86	'Si 1'	0.538	0.424	305	A
2207.13	'Sc 1'	-1.058	0.168	34	A

Figure 100: Sc I in 10 Leo and Arcturus

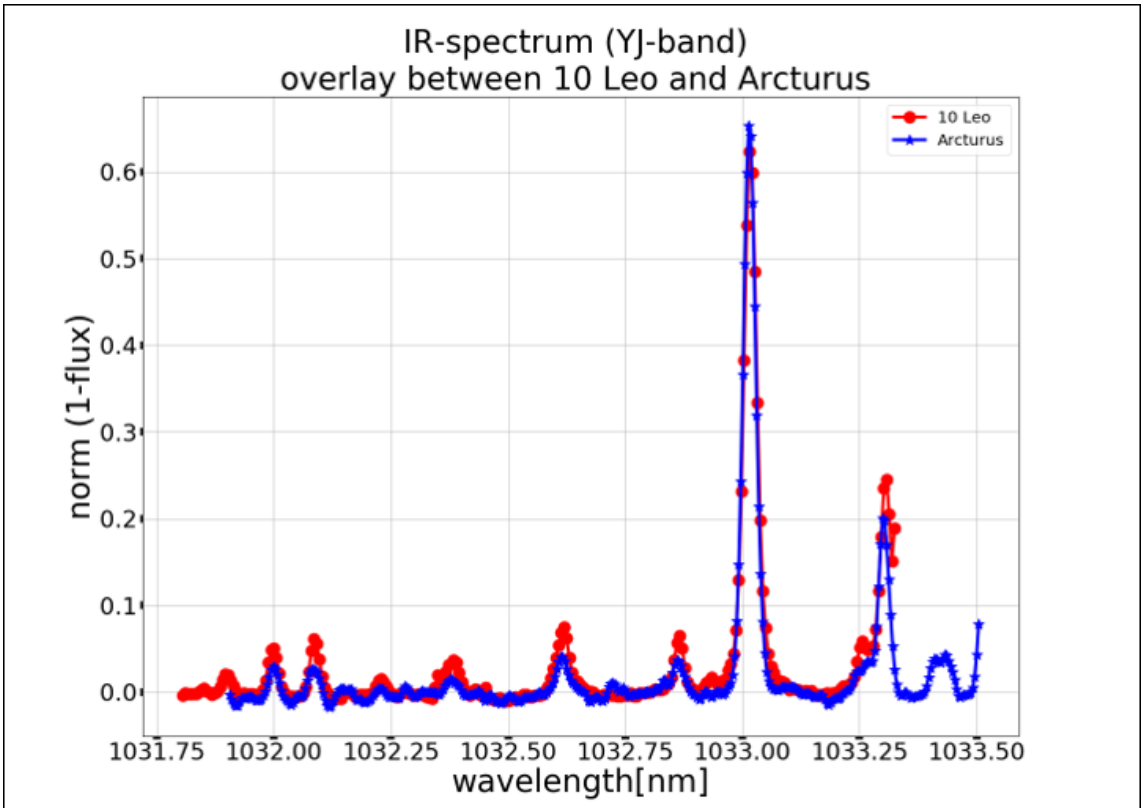

λ(nm)	Description	log gf	cdepth	EW (mA)	Match
1032.00	CN 2-1P_{1}60.5	-1.404	0.026	12	A
1032.09	CN 2-1Q_{2}67.5	-1.042	0.032	15	A
1032.23	CN 3-2P_{1}49.5	-1.903	0.009	3	B
1032.37	CN 3-2Q_{2}56.5	-1.527	0.013	7	B
1032.38	'Ni 1'	-0.562	0.048	7	A
1032.62	CN 1-0P_{2}69.5	-1.197	0.035	16	A
1032.65	'Ni 1'	-4.018	0.035	10	B
1032.80	'Cr 1'	-1.375	0.014		C
1032.87	CN 2-1Q_{1}68.5	-1.036	0.032	17	A
1033.01	'Sr 2'	-0.353	0.598	232	A
1033.27	'Y 2'	-1.760	0.040	13	B
1033.27	CN 3-2Q_{1}57.5	-1.519	0.013	7	A
1033.31	'Ni 1'	-0.982	0.320	83	A

Figure 101: Sr II in 10 Leo and Arcturus

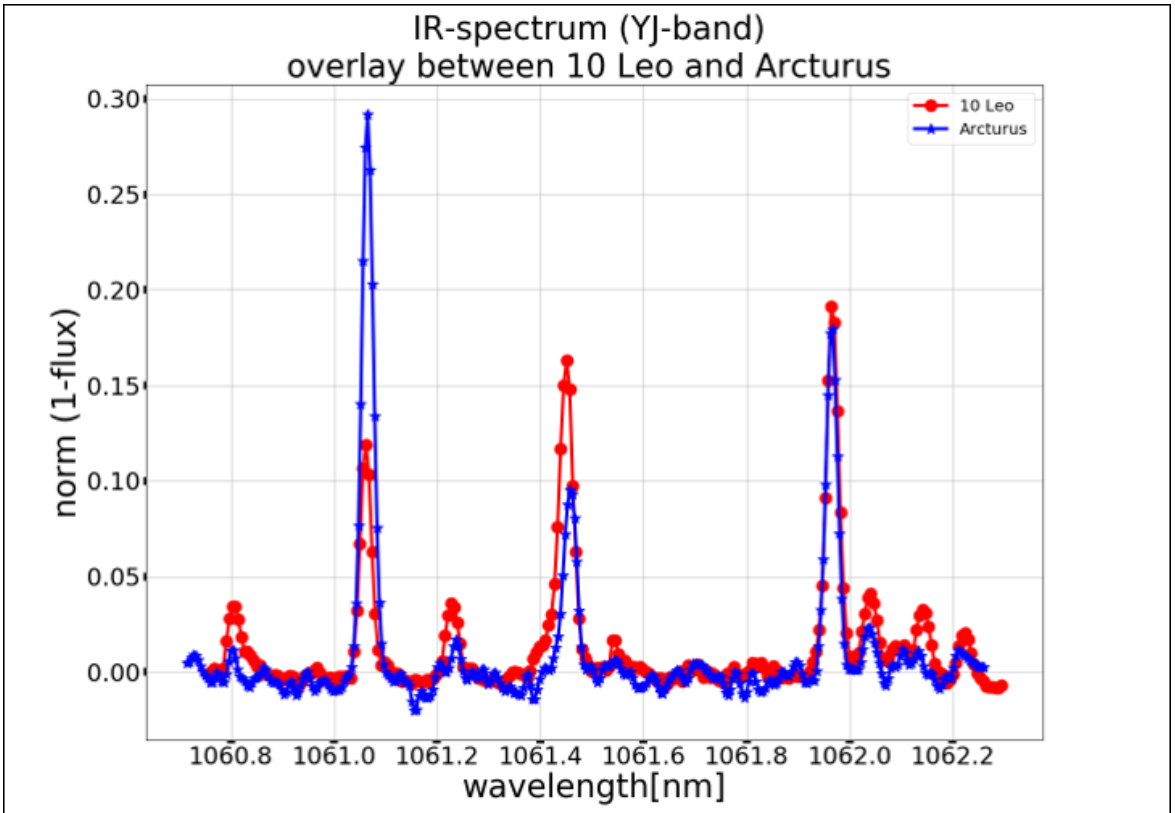

λ(nm)	Description	log gf	cdepth	EW (mA)	Match
1060.81	'Y 2'	-1.960	0.028	10	B
1061.06	'Ti 1'	-2.697	0.318	32	A
1061.23	CN 1-0P_{2}77.5	-1.148	0.021	10	A
1061.40	CN 3-2P_{2}59.5	-1.815	0.005	3	B
1061.44	CN 2-1Q_{1}77.5	-0.981	0.016	8	B
1061.45	U			14	F
1061.45	'Fe 1'	0.021	0.192	35	B
1061.96	'Fe 1'	-3.127	0.320	59	A
1062.04	CN 1-0P_{1}78.5	-1.144	0.021	14	A
1062.08	'Fe 1'	-0.336	0.107		C
1062.14	CN 1-0Q_{2}85.5			10	F
1062.22	Ce 2			5	F

Figure 102: Y II in 10 Leo and Arcturus

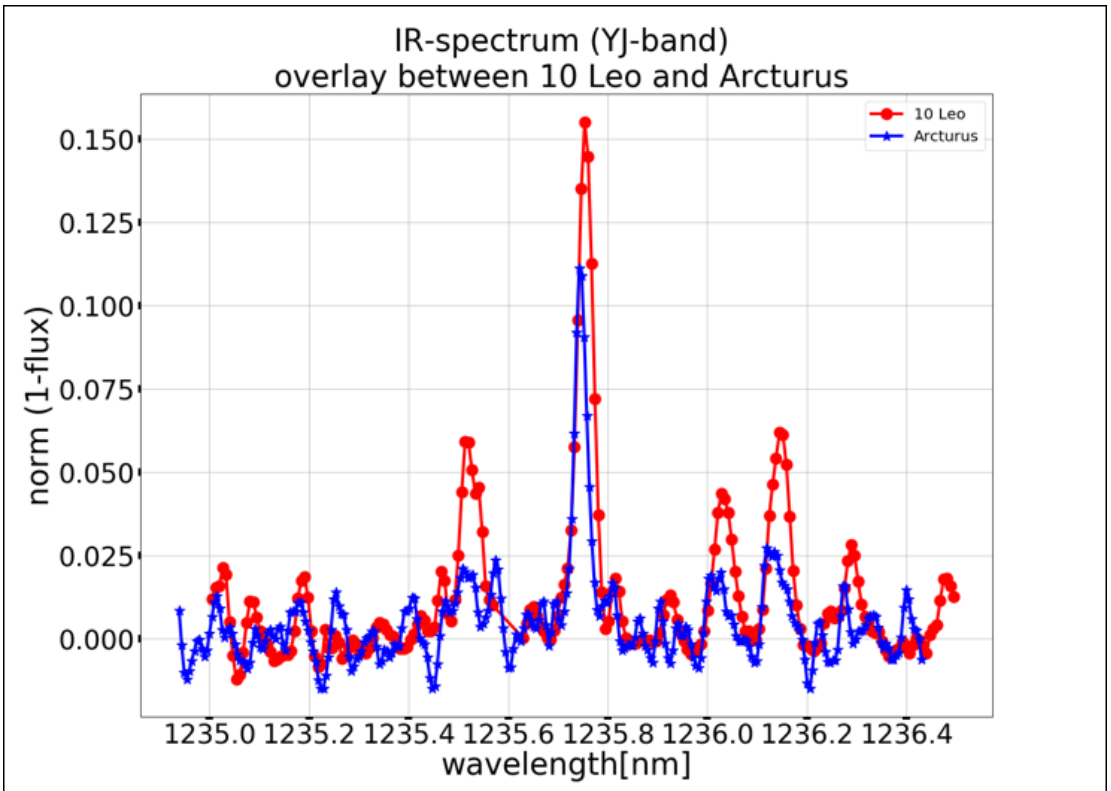

λ(nm)	Description	log gf	cdepth	EW (mA)	Match
1235.03	'CN 1'	-2.337	0.007	7	B
1235.09	'C 1'	-0.486	0.009	2	B
1235.18	CN 4-4R_{1}16.5	-2.278	0.006	2	B
1235.19	CN 1-1P_{2}55.5	-2.302	0.005	2	B
1235.47	U			4	F
1235.52	U			27	F
1235.75	CN 0-0R_{2}83.5	-1.006	0.020	12	B
1235.75	CN 0-0P_{2}65.5	-1.130	0.071	42	A
1235.82	CN 3-3R_{1}47.5	-2.028	0.007	4	B
1235.93	CN 3-3P_{1}29.5	-2.292	0.008	4	B
1236.03	CN 3-3Q_{1}37.5	-1.851	0.015	13	B
1236.04	CN 4-4R_{1}18.5	-2.250	0.007	6	B
1236.15	Ce 2			29	F
1236.29	CN 3-3Q_{2}37.5	-1.851	0.013	10	B

Figure 103: Ce II in 10 Leo and Arcturus

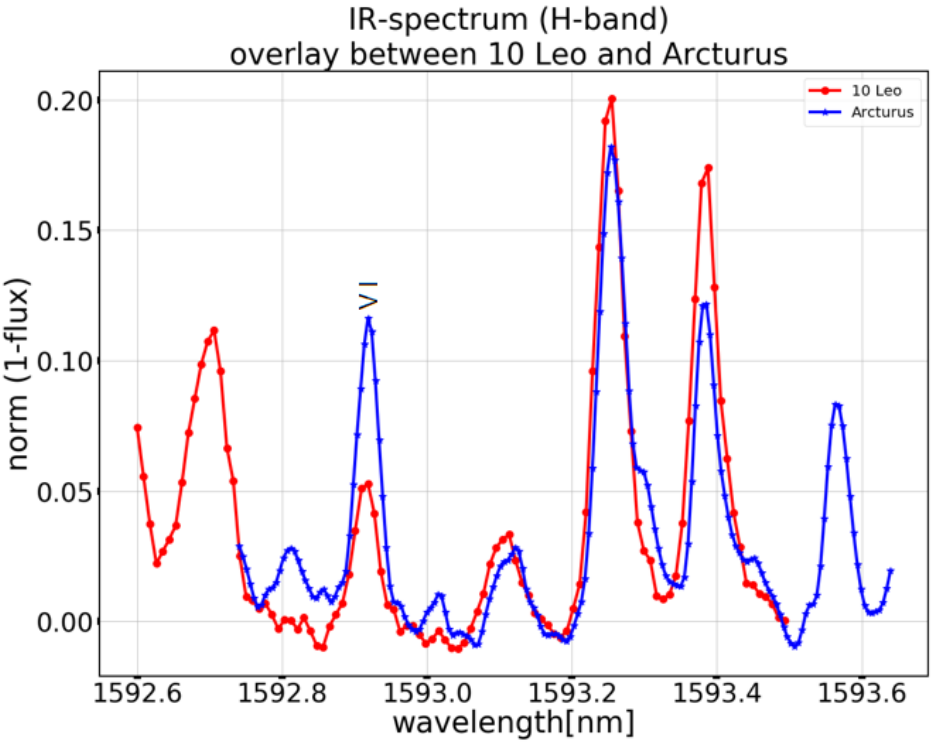

λ(nm)	Description	log gf	cdepth	EW (mA)	Match
1592.91	'Fe 1'	-1.589	0.023	6	B
1592.92	'V 1'	-1.108	0.155	15	A
1592.98	'Fe 1'	-1.115	0.110		C
1593.09	'Ti 1'	-3.298	0.008		C
1593.11	'Fe 1'	-3.427	0.048	16	B
1593.26	'Fe 1'	-0.680	0.358	97	A
1593.30	'Fe 1'	-0.478	0.327		C
1593.31	CO 4-1R67	-6.525	0.009	4	B
1593.38	'Fe 1'	-0.383	0.326	81	A
1593.42	'Fe 1'	-0.328	0.357		C

Figure 104: V I in 10 Leo and Arcturus

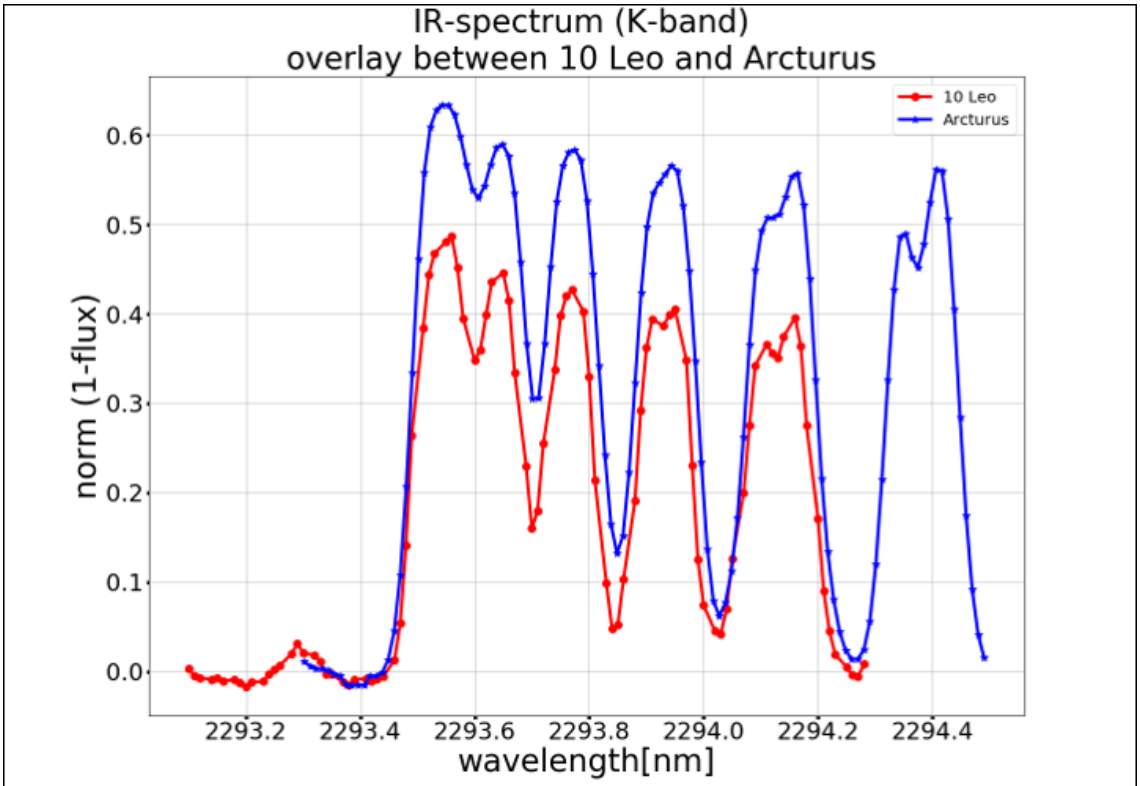

λ(nm)	Description	log gf	cdepth	EW (mA)	Match
2293.52	CO 2-0R51	-5.257	0.395	156	B
2293.53	CO 2-0R50	-5.268	0.399	157	B
2293.56	CO 2-0R52	-5.245	0.390	154	B
2293.57	CO 2-0R49	-5.28	0.404	159	B
2293.63	CO 2-0R53	-5.234	0.384	151	B
2293.65	CO 2-0R48	-5.292	0.408	163	B
2293.75	CO 2-0R54	-5.222	0.380	150	B
2293.77	CO 2-0R47	-5.305	0.413	163	B
2293.91	CO 2-0R55	-5.211	0.374	219	B
2293.95	CO 2-0R46	-5.317	0.417	245	B
2294.08	'Si 1'	-1.382	0.261		B
2294.09	CN 1-3P_{1}47.5	-1.965	0.015		B
2294.11	CO 2-0R56	-5.2	0.369	216	B
2294.17	CO 2-0R45	-5.33	0.422	247	B
2294.35	CO 2-0R57	-5.189	0.362	199	B
2294.41	CO 2-0R44	-5.342	0.425	233	B

Figure 105: ^{12}CO 2-0 Bandhead in 10 Leo and Arcturus

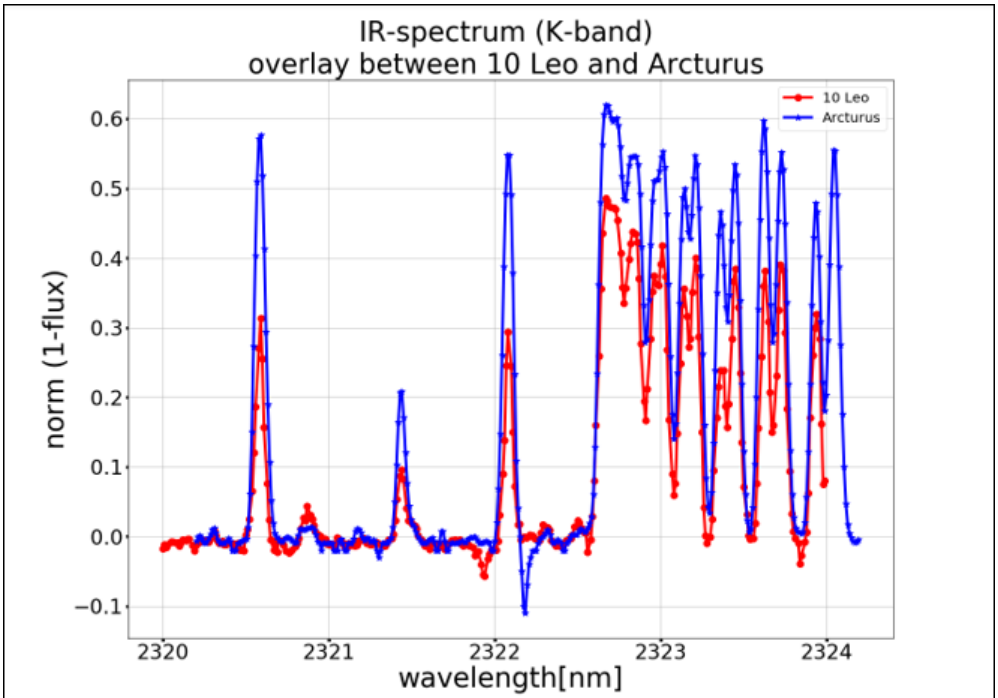

λ(nm)	Description	log gf	cdepth	EW (mA)	Match
2320.59	CO 2-0R14	-5.913	0.414	173	A
2320.87	CN 3-5Q_{1}30.5			24	F
2321.44	CO 2-0R87	-4.908	0.085	56	A
2322.08	CO 2-0R13	-5.946	0.407	168	A
2322.29	'Fe 1'	-1.662	0.011	8	B
2322.51	'Ni 1'	0.411	0.073	11	B
2322.65	CO 3-1R50	-4.789	0.434	181	B
2322.67	CO 3-1R51	-4.777	0.43	180	B
2322.69	CO 3-1R49	-4.801	0.438	183	B
2322.72	CO 3-1R52	-4.766	0.425	178	B
2322.76	CO 3-1R48	-4.813	0.441	184	B
2322.82	CO 3-1R53	-4.754	0.42	176	B
2322.87	CO 3-1R47	-4.825	0.444	186	B
2322.96	CO 3-1R54	-4.743	0.415	173	B
2323.01	CO 3-1R46	-4.837	0.447	187	B
2323.04	CO 2-0R88	-4.899	0.077	32	B
2323.14	CO 3-1R55	-4.732	0.409	224	B
2323.21	CO 3-1R45	-4.849	0.450	247	B
2323.36	CO 3-1R56	-4.721	0.403	204	B
2323.45	CO 3-1R44	-4.862	0.453	229	B
2323.62	CO 2-0R12	-5.981	0.401	166	B

Figure 106: ^{12}CO 3-1 Bandhead in 10 Leo and Arcturus

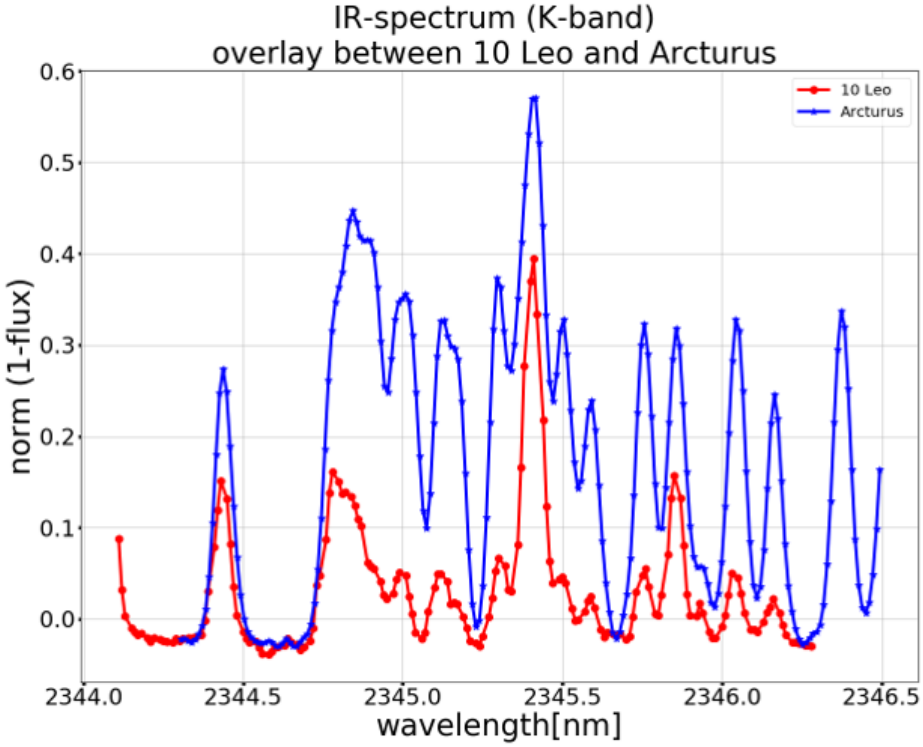

λ(nm)	Description	log gf	cdepth	EW (mA)	Match
2344.43	CO 3-1R82	-4.473	0.153	82	A
2344.78	'Ti 1'	-1.63	0.381	167	A
2344.82	^{13}CO 2-0R52	-7.194	0.012	10	B
2344.85	^{13}CO 2-0R51	-7.206	0.012	10	B
2344.86	^{13}CO 2-0R53	-7.183	0.012	10	B
2344.90	^{13}CO 2-0R50	-7.217	0.012	10	B
2344.94	^{13}CO 2-0R54	-7.171	0.010	9	B
2344.99	^{13}CO 2-0R49	-7.229	0.012	11	B
2345.02	^{13}CO 2-0R55	-7.16	0.010	9	B
2345.10	**CN 0-2Q_{2}72.5**	-1.736	0.007	5	B
2345.12	^{13}CO 2-0R48	-7.241	0.013	15	B
2345.17	^{13}CO 2-0R56	-7.149	0.009	10	B
2345.29	^{13}CO 2-0R47	-7.254	0.014	8	B
2345.30	CO 2-0R0	-7.303	0.055	33	B
2345.42	CO 3-1R17	-5.343	0.456	272	B
2345.51	^{13}CO 2-0R46	-7.266	0.014	8	B
2345.59	^{13}CO 2-0R58	-7.128	0.009	8	B

Figure 107: ^{13}CO 2-0 Bandhead in 10 Leo and Arcturus

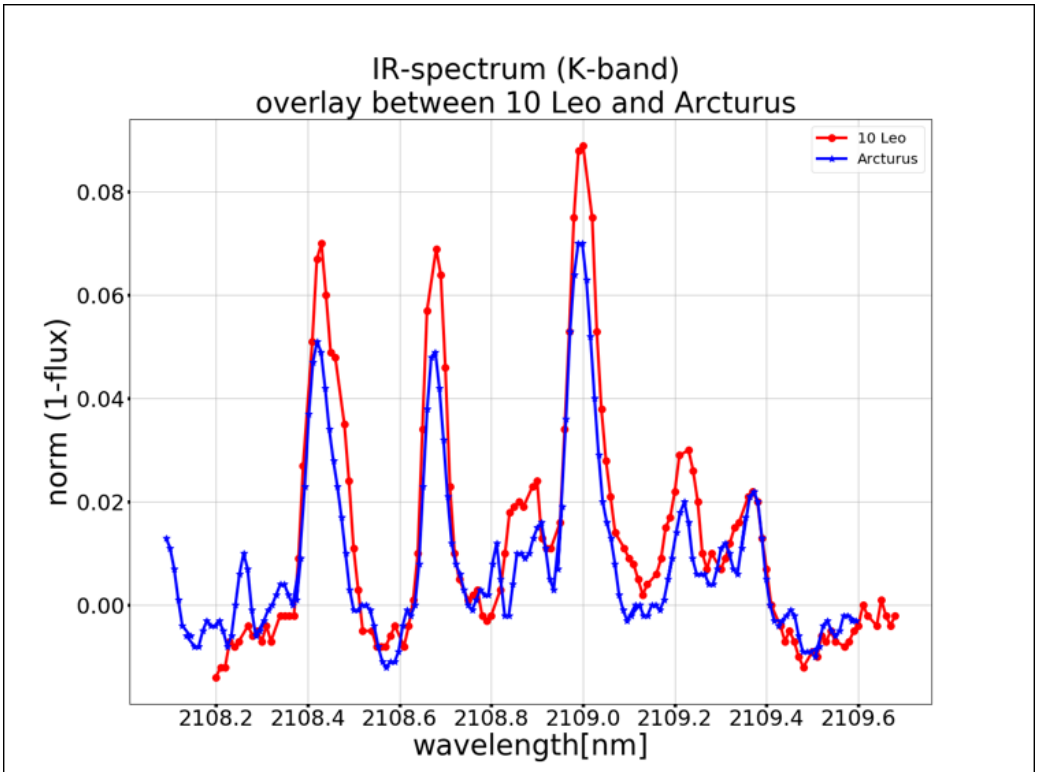

λ(nm)	Description	log gf	cdepth	EW (mA)	Match
2108.43	CN 1-3Q_{1}26.5	-1.92	0.042	35	A
2108.48	**CN 1-3R_{1}40.5**	-2.004	0.020	18	A
2108.68	CN 1-3Q_{2}27.5	-1.902	0.040	37	A
2108.86	**CN 0-2R_{1}58.5**	-2.12	0.010	10	B
2108.90	CN 0-2P{12}27.5			8	C
2109.00	CN 0-2Q_{2}45.5	-1.944	0.031	71	A
2109.04	'Si 1'	-1.324	0.049		B
2109.23	'Si 1'	-1.294	0.053	23	B
2109.33	CN 1-3Q_{12}16.5	-2.935	0.006	5	B
2109.34	'Fe 1'	-2.435	0.021		B
2109.37	**CN 1-3P_{1}17.5**	-2.478	0.015	11	A

Figure 108: CN in 10 Leo and Arcturus

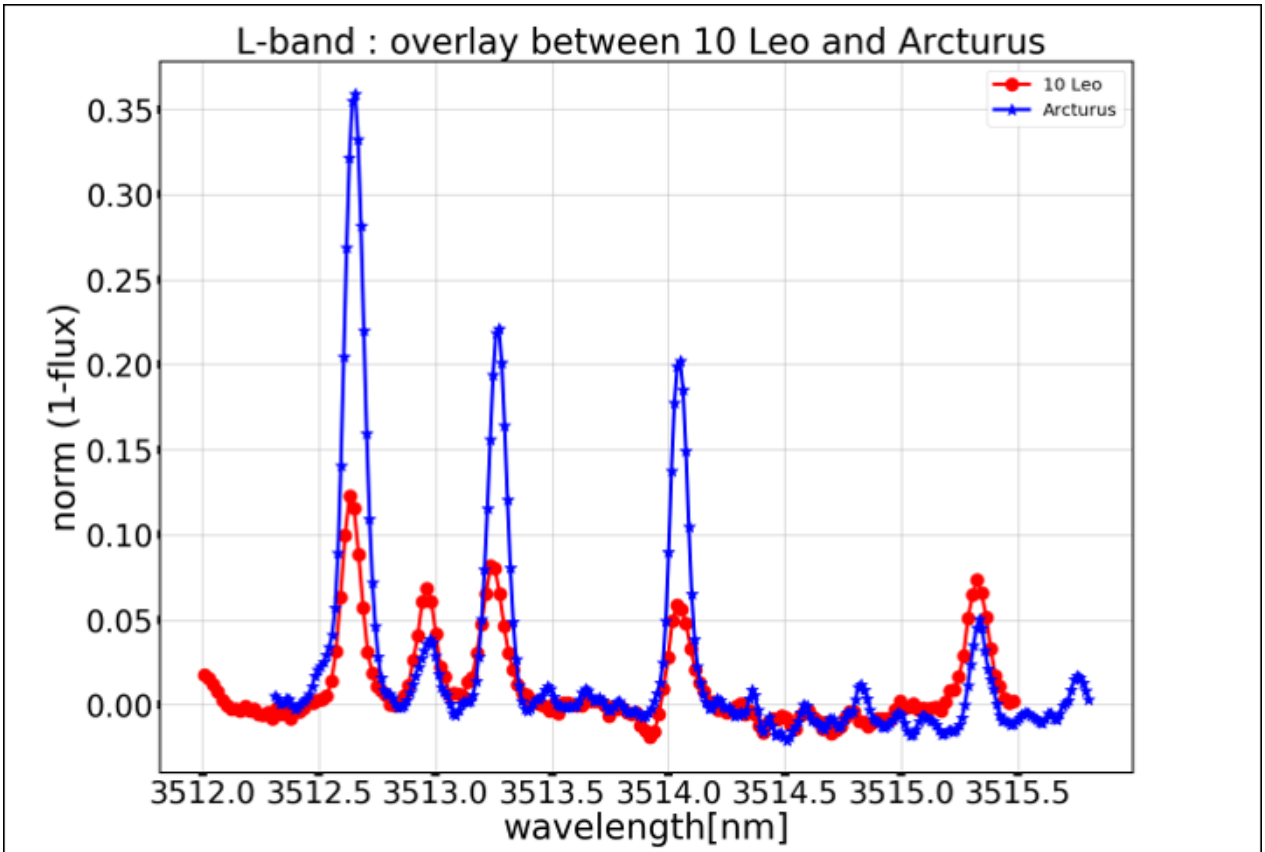

λ(nm)	Description	log gf	cdepth	EW (mA)	Match
3512.34	'Fe 1'	-0.28	0.049		C
3512.57	'Fe 1'	-0.896	0.013		C
3512.63	OH 2-1P_{1f}13.5	-3.91	0.083	131	A
3512.96	'Fe 1'	0.381	0.143	70	B
3513.24	OH 3-2P_{2f}9.5	-4.077	0.033	103	A
3513.26	'Si 1'	-0.006	0.143	103	B
3513.67	'Al 1'	-1.314	0.015		C
3513.90	'Si 1'	-1.93	0.006		C
3514.04	OH 3-2P_{2e}9.5	-4.077	0.032	63	A
3514.58	'Fe 1'	-5.64	0.006		C
3514.66	'Si 1'	-1.582	0.007		C
3515.15	'Fe 1'	-0.77	0.017		C
3515.33	U			85	F

Figure 109: OH in 10 Leo and Arcturus

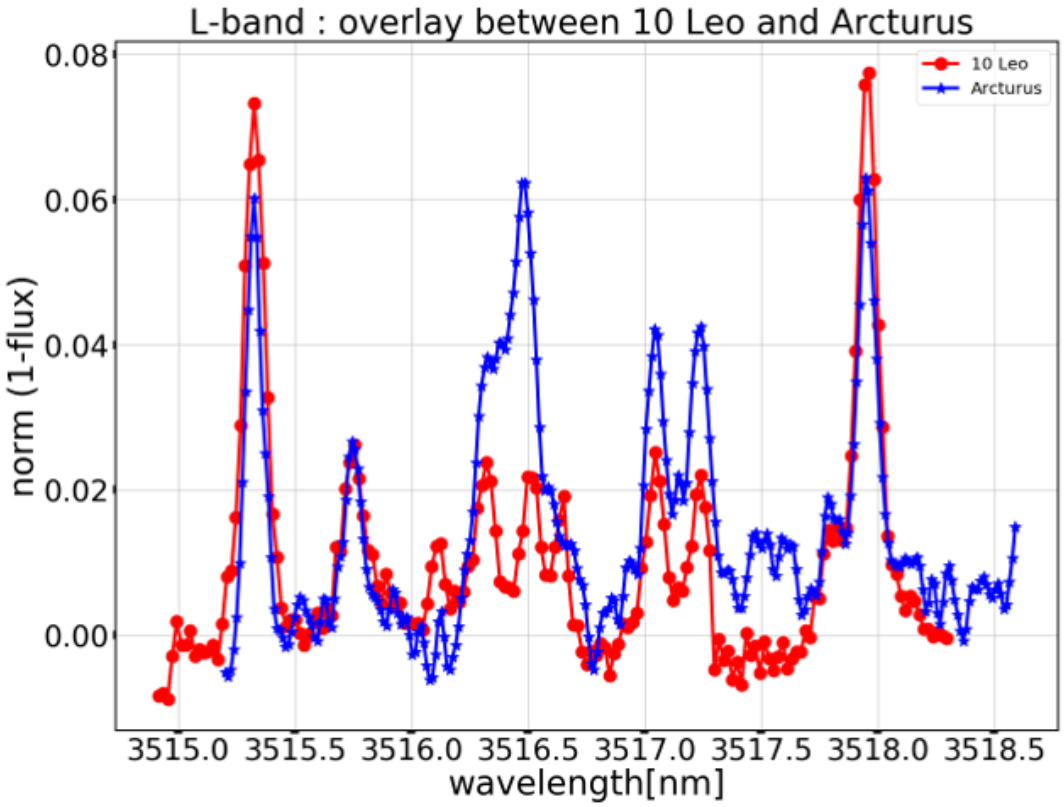

λ(nm)	Description	log gf	cdepth	EW (mA)	Match
3515.33	U			85	F
3515.76	'Si 1'	-0.534	0.056	34	B
3515.83	'Fe 1'	-1.141	0.086		C
3515.91	'Fe 1'	-2.397	0.007		C
3516.32	'CH 1'	-3.171	0.018	26	A
3516.52	'CH 1'	-3.131	0.019	23	A
3516.65	U			13	F
3517.04	'CH 1'	-3.171	0.018	24	A
3517.24	'CH 1'	-3.131	0.020	19	A
3517.79	'Si 1'	-0.957	0.040	9	B
3517.96	'Fe 1'	0.494	0.159	94	B

Figure 110: CH in 10 Leo and Arcturus

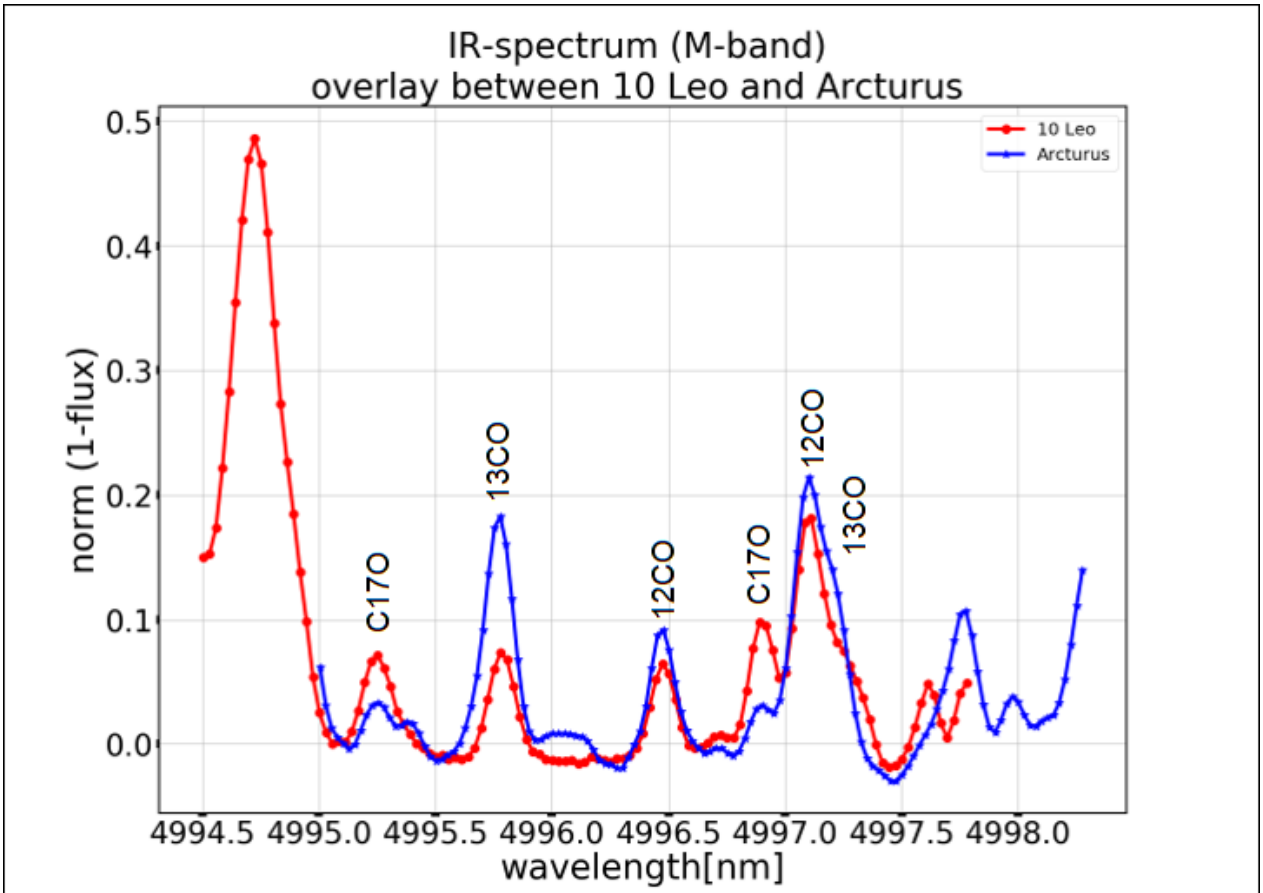

λ(nm)	Description	log gf	cdepth	EW (mA)	Match
4995.25	C^{17}O 3-2P16	-6.775	0.018	106	B
4995.79	^{13}CO 9-8R38	-4.433	0.027	89	A
4996.48	CO 12-11R67	-2.138	0.078	72	A
4996.76	C^{18}O7-6R18	-5.599	0.015	5	C
4996.91	C^{17}O 2-1P22	-6.813	0.030	121	B
4997.11	CO 10-9R31	-2.539	0.241	307	A
4997.23	^{13}CO 10-9R53	-4.248	0.010	40	A
4997.27	C^{17}O 4-3P10	-6.855	0.008	32	B

Figure 111: ^{12}CO,^{13}CO and $C^{17}O$ in 10 Leo and Arcturus

7.3 Software Applications

7.3.1 Python

Python program for overlay of observed spectrum with two models.

```
"""
K-Band:1958nm-2528nm (Leo);1961nm-2500nm (model)
"""
import numpy as np
import matplotlib.pyplot as plt
#------enter parameter for wavelength interval-----
lower_boundary=2449.5#lower wavelength border (nm)
upper_boundary=2452.5#Higher wavelength border (nm)
wavelength_LL1_K_shift=-0.01#shift of model spectrum 1 (nm)
wavelength_LL2_K_shift=-0.01#shift of model spectrum 2 (nm)
flux_shift1=+0.00 # shifts flux of model spectrum 1
flux_shift2=+0.00 # Shifts flux of model spectrum 2
id='K_Overlay'+str(lower_boundary)+'-'+str(upper_boundary)#ID(plot)
#------source data ------------------------------------
filename1='Leo10_KBand.txt'        # data source for 10 Leo
data1 = np.loadtxt(filename1)
filename2='model_10 Leo_LL1_K.txt' # data source for model 1
data2 = np.loadtxt(filename2)
filename3='model_10 Leo_LL2_K.txt' # data source for model 2
data3 = np.loadtxt(filename3)
x1list=data1[1:,0]       #list of wavelength (10 Leo)
x2list=data2[1:,0]       #list of wavelength (model 1)
x3list=data3[1:,0]       #list of wavelength (model 2)
#-------Find records for wavelength interval------------
a = np.searchsorted(x1list, lower_boundary)
b = np.searchsorted(x1list, upper_boundary)
c = np.searchsorted(x2list, lower_boundary)
d = np.searchsorted(x2list, upper_boundary)
e = np.searchsorted(x3list, lower_boundary)
f = np.searchsorted(x3list, upper_boundary)
#----norm.flux and wavelength for wavelength  interval   ----
wavelength_Leo    = data1[a:b, 0] #10 Leo-observed
flux_Leo          = data1[a:b, 1] #10 Leo-observed
wavelength_LL1_K  = data2[c:d, 0] #model 1
flux_LL1_K        = data2[c:d, 1] #model 1
wavelength_LL2_K  = data3[e:f, 0] #model 2
flux_LL2_K        = data3[e:f, 1] #model 2
#--------plot parameter ----------
plt.rcParams['figure.figsize'] = 20,10 #size of plot
fig=plt.figure();plt.figure()
plt.title("IR-spectrum (K-band) \noverlay between 10 Leo and models ",
                                    fontsize=20)
plt.xlabel("wavelength[nm]--->", fontsize =15)
plt.ylabel("norm flux--->", fontsize =15)
plt.grid(True)
plt.plot(wavelength_Leo,flux_Leo,'r-o', label='10 Leo')
plt.plot(wavelength_LL1_K+wavelength_LL1_K_shift,flux_LL1_K+flux_shift1
                                    ,'g-*', label='LL1K')
plt.plot(wavelength_LL2_K+wavelength_LL2_K_shift,flux_LL2_K+flux_shift2
                                    ,'bx', label='LL2K')
plt.legend(loc=0,fontsize=15)
plt.savefig(id+"nm.png");plt.show()
```

Python program for standardization and cleanup

```
# -*- coding: utf-8 -*-
"""
clean-up of data
YJ-Band:962nm-1344nm
@author: Manfred
"""
import numpy as np
import math
import matplotlib.pyplot as plt
#--------------------load file----------
bf = np.loadtxt('Arcturus_YJBand.txt')# data source for Arcturus
bf[:,0] = bf[:,1]     #puts first column as wavelength
lambdalist=bf[:,1]*1 #may convert units, e.g. 10 for A
fluxlist=bf[:,7]      #puts second column as flux
fluxlist=[1 if math.isnan(x)else x for x in fluxlist]
fluxlist=[1 if x>1.05 else x for x in fluxlist]
fluxlist=[0 if x<0 else x for x in fluxlist]
#---------------------------------------
np.savetxt("lambdalist.txt",lambdalist, fmt='%.4f') #formats wavelength
np.savetxt("fluxlist.txt",fluxlist, fmt='%.4f') #formats flux
#--writes modified flux to output file, e.g. ArcturusYJ.txt-
with open('ArcturusYJ.txt', 'w') as file3: #writes textfile
    with open('lambdalist.txt', 'r') as file1:
        with open('fluxlist.txt', 'r') as file2:
            for line1, line2 in zip(file1, file2):
                print(line1.strip(), line2.strip(), file=file3)
#-----check of output file----------
be=np.loadtxt('ArcturusYJ.txt')
print('number of records in input file  :', len(bf))
print('number of records in output file :', len(be))
# optional plot-----------------------
plt.title("IR-spectrum baed on raw data",fontsize=20)
plt.xlabel("wavelength[nm]--->", fontsize =15)
plt.ylabel("norm flux--->", fontsize =15)
plt.grid(True)
plt.plot(lambdalist,bf[:,7],'r-o', label='raw')
plt.show()
plt.title("IR-spectrum based on processed data",fontsize=20)
plt.xlabel("wavelength[nm]--->", fontsize =15)
plt.ylabel("norm flux--->", fontsize =15)
plt.grid(True)
plt.plot(be[:,0],be[:,1],'b-o', label='raw')
plt.show()
```

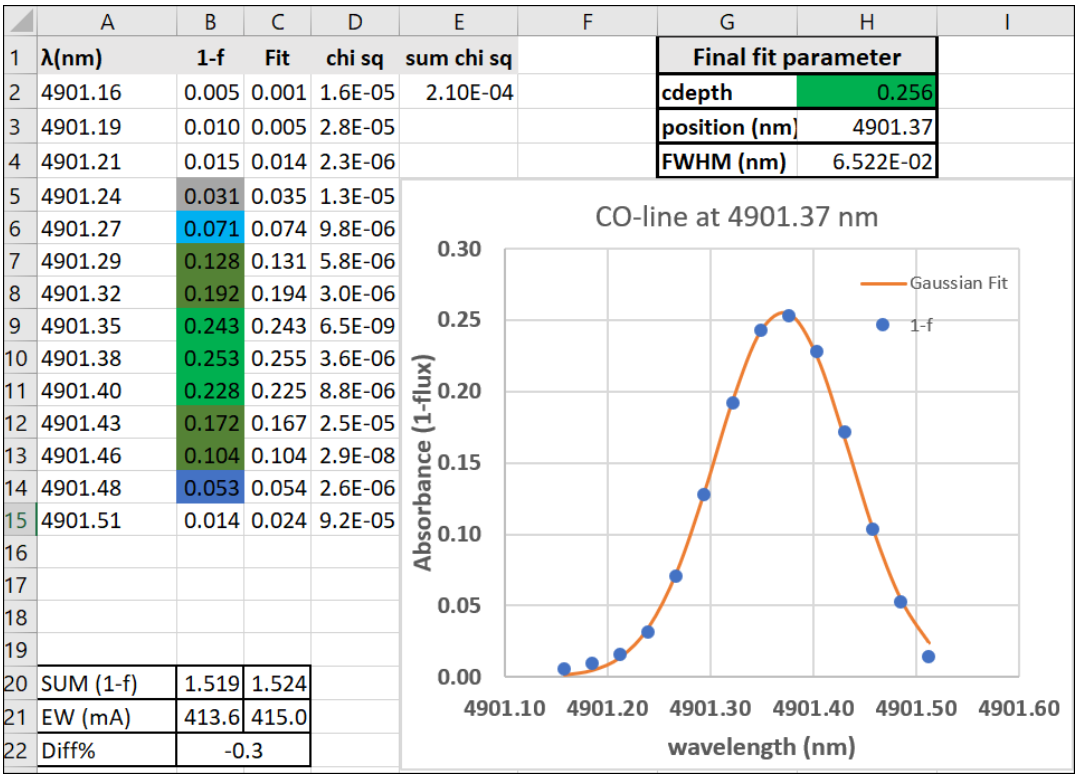

	A	B	C	D	E	F	G	H	I
1	λ(nm)	1-f	Fit	chi sq	sum chi sq		Final fit parameter		
2	4901.16	0.005	0.001	1.6E-05	2.10E-04		cdepth	0.256	
3	4901.19	0.010	0.005	2.8E-05			position (nm)	4901.37	
4	4901.21	0.015	0.014	2.3E-06			FWHM (nm)	6.522E-02	
5	4901.24	0.031	0.035	1.3E-05					
6	4901.27	0.071	0.074	9.8E-06					
7	4901.29	0.128	0.131	5.8E-06					
8	4901.32	0.192	0.194	3.0E-06					
9	4901.35	0.243	0.243	6.5E-09					
10	4901.38	0.253	0.255	3.6E-06					
11	4901.40	0.228	0.225	8.8E-06					
12	4901.43	0.172	0.167	2.5E-05					
13	4901.46	0.104	0.104	2.9E-08					
14	4901.48	0.053	0.054	2.6E-06					
15	4901.51	0.014	0.024	9.2E-05					
16									
17									
18									
19									
20	SUM (1-f)	1.519	1.524						
21	EW (mA)	413.6	415.0						
22	Diff%	-0.3							

Figure 112: View of customized Excel spreadsheet using solver tool for gaussian fit

.

7.3.2 Excel solver tool for Gauß fit

The columns for 1-flux (observed value) and corresponding wavelengths are copied to a separate worksheet. A third column (fit column) and fourth column (chi square) are added to calculate the fit and the square of differences between observed and fitted value. The fit is based on the formula for a gaussian curve with the parameter for position, FWHM and cdepth. All chi square values are added and the solver attempts to minimize this sum using initial estimates for the variable parameter. The newly calculated parameter are automatically updating the fit column and subsequently produce a new sum of chi square. The observed and fitted curve are visualized in the same spreadsheet to check the quality of the line profile and its match to the fitted curve. The parameter can be manually adjusted to achieve the best fit. Finally the sum of the fitted 1-f values is converted to the equivalent width. Figure 112 provides part of a screenshot for a typical gaussian line fit.

7.3.3 Synth3

Synth3 program (Kochukhov, 2012) is written in Fortran 77, which ensures portability to all major computer platforms and straightforward interfacing with alternative software modules. It calculates a synthetic spectrum for a given model atmophere using a**.krz file** embedded in the VALD extracted stellar spectrum. The program runs under Linux with the executable **Synth3.Linux**.

7.3.4 BinMag2

BinMag2 is an IDL code designed to produce graphical comparison of observed and stellar spectra computed by Synth/SynthMag/Synmast/Synth3/SME spectrum synthesis codes (Kochukhov, 2018). It reads observations in *.asc and *.fits formats and synthetic spectra in *.out or *.prf (specific intensity/flux) formats. BinMag applies radial velocity shift and broadening to the theoretical spectra to account for the effects of stellar rotation, radial-tangential macroturbulence and instrumental "smearing". It calculates EWs and provides annotated (element/molecule identification) plots of observed spectra and synthetic spectra. BinMag2 plots are available for a simultaneous selection of up to six synthetic spectra and six observational spectra.